

Core Testing and Numerical Simulation of Well Logs for the Upper Coastal Plains and Llano Uplift Aquifers

Texas Water Development Board Contract Number 2248302663

Prepared for:

Texas Water Development Board

Prepared by:

Dr. Mohamed Bennis

Dr. Carlos Torres-Verdín

Dr. Zoya Heidari

The University of Texas at Austin

August 2023

Texas Water Development Board Contract Number 2248302663

Final Report: Core Testing and Numerical Simulation of Well Logs for the Upper Coastal Plains and Llano Uplift Aquifers

This page is intentionally blank.

CONTENTS

1	EXECUTIVE SUMMARY.....	5
2	LIST OF CORES AND WELL LOGS	6
3	CORE LOCATION, LITHOLOGY AND HYDROGEOLOGIC INTERVALS	8
4	PHOTOGRAPHS AND BASIC CORE DESCRIPTIONS	11
4.1	Upper Coastal Plains: Queen City Formation.....	11
4.2	Upper Coastal Plains: Wilcox Formation	12
4.3	Upper Coastal Plains: Carrizo Formation	16
4.4	Upper Coastal Plains: Jackson and Yegua Formation	18
4.5	Llano Uplift: Ellenburger and San Saba Formations	19
4.6	Llano Uplift: Hickory Formations	24
5	CORE SAMPLE ANALYSES	26
5.1	Methods and Equipment	26
5.2	Photographs of Core Plugs.....	28
5.3	Results of Core Analysis in the Upper Coastal Plains	30
5.4	Results of Core Analysis in the Hickory Aquifer at the Llano Uplift.....	49
5.5	Results of Core Analysis in the Ellenburger and San Saba aquifers at the Llano Uplift	59
6	NUMERICAL SIMULATION OF WELL LOGS	71
6.1	The Header of a Well Log.....	71
6.2	Depth Matching of Well Logs	72
6.3	Geothermal Gradients at the Llano Uplift and Upper Coastal Plains	73
6.4	Water Salinity Estimation Methods	74
6.5	Numerical Simulations of Well Logs.....	76
6.6	Assessment of Porosity in the Hickory Formation in Well #A01.....	77
6.7	Assessment of Salinity, Porosity, and Shale Concentration in the Lower Wilcox Formation in Well #B04 Using UTAPWeLS.....	78
6.8	Assessment of Porosity and Lithology in the Ellenburger and San Saba Formations in Well #A02 81	
6.9	Assessment of Porosity and Lithology in the Ellenburger and San Saba Formations in Well #A03 83	
6.10	Assessment of Salinity and Porosity in the Hickory Formation in Well #A05.....	85
6.11	Assessment of Salinity, Porosity, and Shale Concentration in the Upper Wilcox Formation in Well #B06 Using Calculations.....	87
6.12	Assessment of Mineralogy in the Llano Uplift Based on Nuclear Logs in Well #A04.....	88
6.13	Assessment of petrophysical properties of the Ellenburger and San Saba Formations in Well #A04 91	
6.14	Assessment of the Radial Length of invasion in Oil-Bearing Carrizo Sandstones in well #B01 Using UTAPWeLS	95

Texas Water Development Board Contract Number 2248302663

Final Report: Core Testing and Numerical Simulation of Well Logs for the Upper Coastal Plains and Llano Uplift Aquifers

7 CONCLUSIONS..... 97

8 REFERENCES 98

APPENDIX A – DIGITIZED WELL LOGS..... 100

APPENDIX B – PULSE DECAY PERMEABILITY MEASUREMENTS 123

APPENDIX C – NORMALIZED MAGNETIZATION DECAY MEASUREMENTS AND NMR T₂ DISTRIBUTIONS 131

APPENDIX D – WATER PERMEABILITY MEASUREMENTS 150

APPENDIX E – A SIMPLE CORRELATION BETWEEN T₂ CUTOFF AND T_{2LM} 156

APPENDIX F – ARCHIE’S POROSITY EXPONENT OF DUAL POROSITY ROCKS..... 159

1 EXECUTIVE SUMMARY

The Texas Water Development Board (TWDB) Brackish Resources Aquifer Characterization System (BRACS) department contracted this work as part of their data collection efforts for their studies on the brackish groundwater resources of the Upper Coastal Plains and Llano Uplift aquifers. For this project, we located, described, photographed, and measured petrophysical properties for the Upper Coastal Plains and Llano Uplift aquifers from multiple cores managed by the Bureau of Economic Geology. The core descriptions include lithology, mineralogy, hydrogeologic units, bedding thickness, color, sedimentary structures, and other significant features. We conducted laboratory measurements on multiple core samples which were obtained from different rock types. The core descriptions and photographs are available by request from the TWDB BRACS department. We performed nuclear magnetic resonance (NMR), helium porosimetry, core-flood, pulse-decay, and electrical measurements on the core samples to quantify basic rock properties such as total porosity, permeability, and electrical properties.

In addition, we assessed formation water salinity by numerical simulations of well logs of multiple wells to accurately estimate rock and fluid properties of the different formations of both hydrogeologic units. We digitized all available image files of well logs into LAS files. The well log LAS files and the simulation model files are available on request from the TWDB BRACS department.

2 LIST OF CORES AND WELL LOGS

The Texas Water Development Board (TWDB) provided the University of Texas at Austin (UT Austin) a list of known wells with core, core depths, geophysical log picks for the aquifers of interest, and well information. The formations of interest in the Upper Coastal Plains are Jackson, Yegua, Queen City, Carrizo, and Wilcox. The formations of interest in the Llano Uplift are Ellenburger, San Saba, and Hickory. **Figure 1** shows a summary of the 16 cores under consideration in this study. The total number of core boxes is approximately 600.

Figure 2 shows the available well logs in each well. The most common well logs are gamma ray (GR), spontaneous potential (SP), and resistivity. The well logs named SFL, NPHI, RHOB, PEF and DT correspond to shallow resistivity, neutron porosity, bulk density, photoelectric factor, and sonic logs. Well logs from 23 wells were digitized and plotted along with the core depths and well log picks for the aquifers of interest. Plots of the digitized well logs are available in **APPENDIX A**. Considering the complexity of names given to some wells, we attributed new identification names (LOG_UT) to all the wells in this study where AXX and BXX designate well in the Llano Uplift and Upper Coastal Plains, respectively. There are only 4 wells (#A02, #A04, #B03, and #B10) that have resistivity and porosity (density, neutron, and/or sonic) logs.

Core #	Fm	Accession Number	Box Count	Top Depth (ft)	Bottom Depth (ft)	Fm top (ft)	Fm bottom (ft)	Fm	Fm top (ft)	Fm bottom (ft)	Fm
Upper Coastal Plains											
1	Queen City	C01440	12	324	579	~360	425	Queen City			
2	Carrizo	C00535	6	545	586	510	665	Carrizo			
3	Lower Wilcox	C00839	8	4390	4450.2	4330-4600	5340	Lower Wilcox			
4	Upper Wilcox	C04523	5	8025	8066.5	8050	8310	Upper Wilcox			
5	Upper Wilcox	C01543	7	3448	3508	2740	3630	Upper Wilcox			
6	Lower Wilcox	C09032	26	4610	6066	4000-4025	6060	Lower Wilcox			
7	Jackson & Yegua	V21533	1	108	3269	1240	2350	Jackson	2350	~3500	Yegua
Llano Uplift											
8	San Saba	C01694	11	6266	6882	6260	6880	San Saba			
9	Ellenburger	B02380	1	3660	3755	3760	>3875	Ellenburger			
10	Ellenburger	C00421	12	2518	5344	3735	>4660	Ellenburger			
11	Ellenburger	C06479	174	50	1688	868	1490	Ellenburger	1490	>1688	San Saba
12	Ellenburger & San Saba	C06484	174	0	1617	515-600	900-1000	Ellenburger	900-1000	1250	San Saba
13	Ellenburger & San Saba	C06457	141	428	1784	820	1220	Ellenburger	1220	1715	San Saba
14	Hickory	C00115	5	2835	3333	3230	>3333	Hickory			
15	Hickory (outcrop)	C00087	22	40	299	0		Hickory			
16	Hickory	C00086	26	60	366	~120	>371	Hickory			

Figure 1. List of cores and corresponding wells in the Llano Uplift and Upper Coastal Plains.

*Texas Water Development Board Contract Number 2248302663
Final Report: Core Testing and Numerical Simulation of Well Logs for the Upper Coastal Plains and Llano Uplift Aquifers*

Core #	Formations	LOG_ID	LOG_UT	GR	SP	Resistivity	SFL	NPHI	RHOB	PEF	DT
Upper Coastal Plains											
1	Queen City	Q663_01	B02		SP	Dual Induction (2)					
2	Carrizo	Q448_001-LOG8	B01		SP	Dual Induction (2) and Lateral (1)					
		Q34b_041	B04	GR	SP	Dual Induction (2)					
3	Lower Wilcox	4131947	B03	GR	SP	Dual Induction (2)	SFL				DT
4	Upper Wilcox	4212300590	B05		SP	Dual Induction (2)					
		Q9a_177	B06	GR	SP	Dual Induction (2)					
5	Upper Wilcox	Q9b_177	B07	GR	SP	Dual Induction (2)					
		Q83_255_log2	B09		SP	Dual Laterolog (2)					
6	Lower Wilcox	25534747	B08	GR/Cal							
7	Jackson & Yegua	4229733226	B10	GR	SP	Dual Induction (2)	SFL	NPHI	DPHI		
Llano Uplift											
		18810_4216500034	A09		SP	Dual Induction (2) and Lateral (1)					
8	San Saba	6427_Q10_4201900016	A10		SP	Dual Laterolog (2)					
9	Ellenburger	4226530099	A08	GR	SP	Dual Induction (2)	SFL				
		70274_4219330256	A12	GR	SP	AIT-H (5)					
10	Ellenburger	38639_4219300071	A11		SP	Dual Induction (2)	SFL				
		19330266	A13	GR	SP	AIT-H (10)					
		7465_30730494	A03		SP	Dual Induction (2) and LL8 (1)					
11	Ellenburger	30731189	A04	GR	SP	AIT-M (5)		TNPH	DPHZ	PEF	
12	Ellenburger & San Saba	7345_30730837_912	A01	GR	SP	Dual Induction (1) and Lateral (1)					
		7365_30730920_918	A02	GR					RHOB		
13	Ellenburger & San Saba	7460_878	A06		SP	Dual Induction (1) and Lateral (1)					
14	Hickory	6433_Q2_265	A07		SP	Dual Induction (2) and Lateral (1)					
15	Hickory (outcrop)										
16	Hickory	Q31_307	A05	GR		Res (1)					

Figure 2. List of cores and corresponding well logs in the Llano Uplift and Upper Coastal Plains. The most common well logs are resistivity, followed by SP and GR.

3 CORE LOCATION, LITHOLOGY AND HYDROGEOLOGIC INTERVALS

UT Austin gained access to available core data at the Austin Core Research Center (Austin CRC) and at the Bureau of Economic Geology (BEG), coordinated with the core librarian to rent a table, and followed their procedures for viewing and sampling. The core facility provided UT Austin with a list of cores of interest.

Figure 3 shows the geographical location of cores selected for analysis. **Figure 4** shows the stratigraphy associated with the Upper Coastal Plains aquifers. This sequence stratigraphy was obtained from the TWDB report 385 (Meyer et al., 2020). **Figure 5** presents stratigraphy associated with the Llano Uplift aquifers. This sequence stratigraphy was obtained from the TWDB contract report 0604830614 (D.B. Stephens & Associates, 2007).

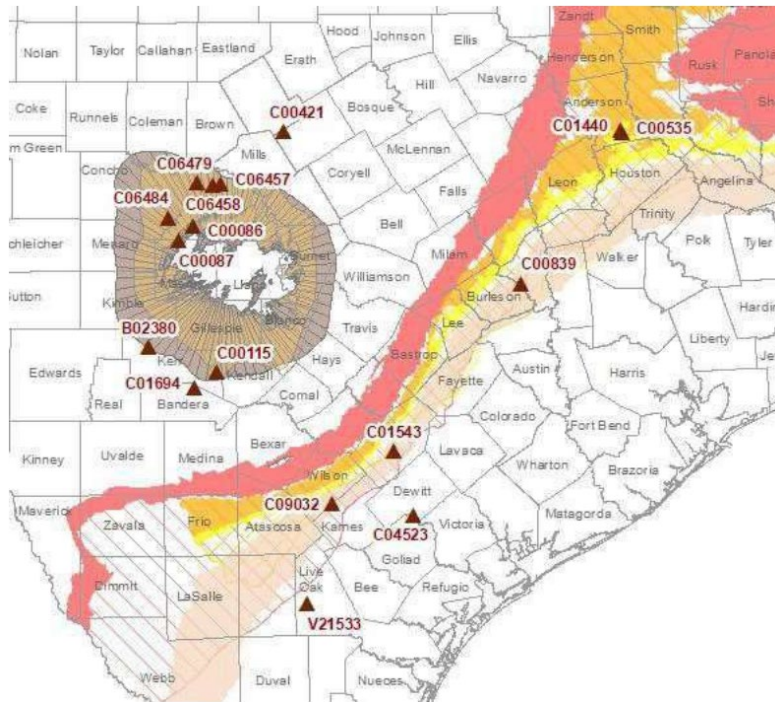


Figure 3. Locations of wells selected for core analysis along with the corresponding accession numbers. All the cores are stored at the Bureau of Economic Geology (BEG) in Austin, Texas.

Epoch	Group	Formation	USGS aquifer name	Texas aquifer name	Aquifer system
Eocene	Jackson	Caddell	Vicksburg-Jackson confining unit	Yegua-Jackson Aquifer	Upper Coastal Plains
		Moodys Branch			
		Hiatus			
	Claiborne	Yegua	Upper Claiborne Aquifer	Confining unit	
		Cook Mountain	Middle Claiborne		
		Hiatus	confining unit	Sparta Aquifer	
		Sparta Sand	Middle Claiborne Aquifer		
		Weches		Confining unit	
		Hiatus		Queen City Sand	
		Reklaw			
		Hiatus	Lower Claiborne confining unit	Confining unit	
		Carrizo Sand	Lower Claiborne – upper Wilcox Aquifer		
		Hiatus			
	Sabinetown				
	Wilcox	Rockdale	Middle Wilcox Aquifer		
Seguin					
Midway		Wills Point			Midway confining unit
Paleocene					

Figure 4. Stratigraphic column showing the epochs, formations, and hydrogeologic units of the Upper Coastal Plains aquifers as shown in TWDB report 385 (Meyer et al., 2020).

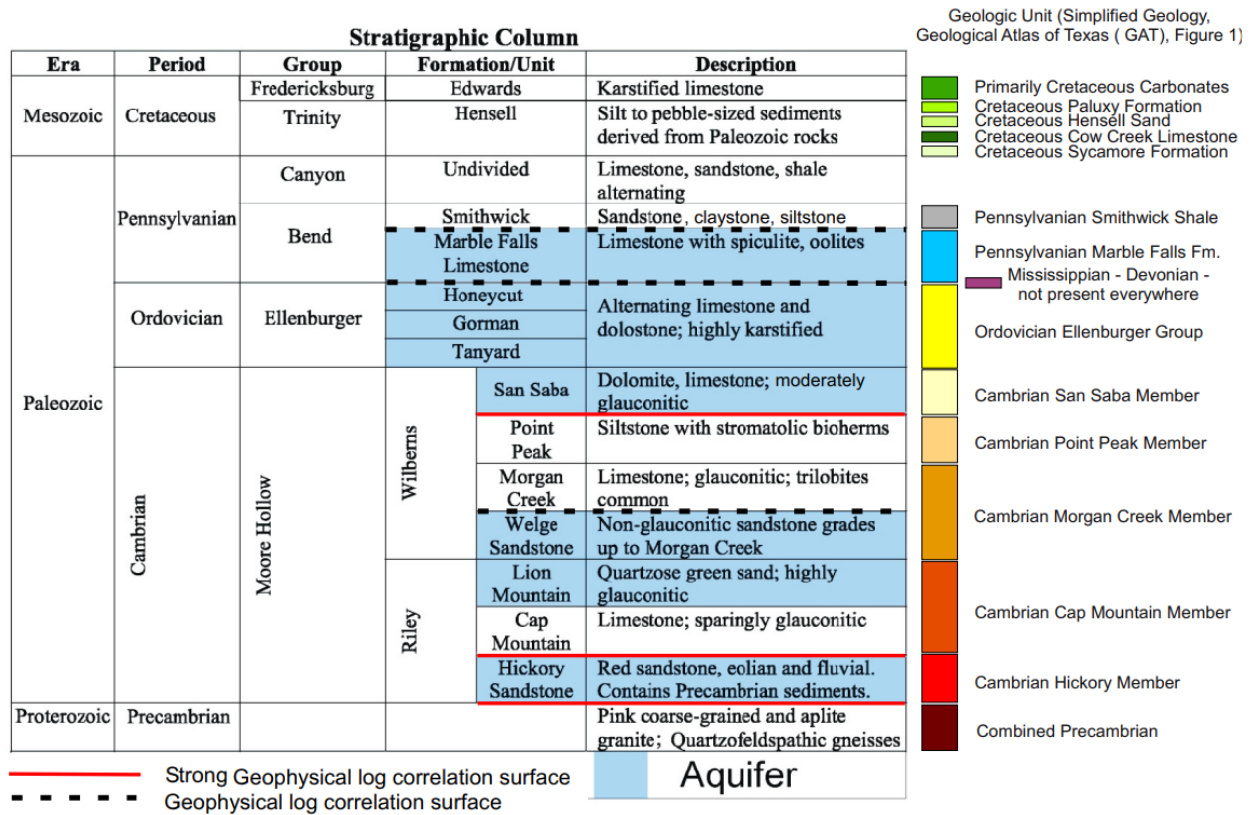


Figure 5. Stratigraphic column showing the era, period, group, formation, and description of the Llano Uplift aquifers as shown in TWDB report 0604830614 (D.B. Stephens & Associates, 2007).

4 PHOTOGRAPHS AND BASIC CORE DESCRIPTIONS

This section includes core photographs of 16 total cores available at the Austin Core Research Center. Figure 6 shows the list of cores that have been laid out and photographed. Each report indicates facies lithology, depth of intervals, geological formation, hydrogeologic unit, sedimentary structures, color, and a brief description of grain size, distribution, texture, mineralogy, and geological features. Core quality was assessed, and the best cores were selected for sampling and laboratory analysis.

Core #	Fm	Accession Number	Box Count	Core Quality	Comments
Upper Coastal Plains					
1	Queen City	C01440	12	Bad	Brittle
2	Carrizo	C00535	6	Bad	Oil saturated
3	Lower Wilcox	C00839	8	Good	
4	Upper Wilcox	C04523	5	Good	
5	Upper Wilcox	C01543	7	Good	
		C09032	26	Very Good	
6	Lower Wilcox				
7	Jackson & Yegua	V21533	1	Bad	Powder
Llano Uplift					
8	San Saba	C01694	11	Good	
9	Ellenburger	B02380	1	Bad	Cuttings
10	Ellenburger	C00421	12	Good	
11	Ellenburger	C06479	174	Very Good	
12	Ellenburger & San Saba	C06484	174	Very Good	
13	Ellenburger & San Saba	C06457	141	Very Good	
14	Hickory	C00115	5	Very Good	
15	Hickory (outcrop)	C00087	22	Very Good	
16	Hickory	C00086	26	Very Good	

Figure 6. List of cores in the Llano Uplift and Upper Coastal Plains.

4.1 Upper Coastal Plains: Queen City Formation

Core #1 representing the Queen City formation is of poor quality. **Figure 7** shows a photograph of two boxes from core #1 (C01440). The sandstones from the Queen City formation exhibit a brown color and are very brittle. Shale layers exhibit a medium grey color and are fractured along bedding planes. The tight reddish-brown rocks correspond to siderite nodules.

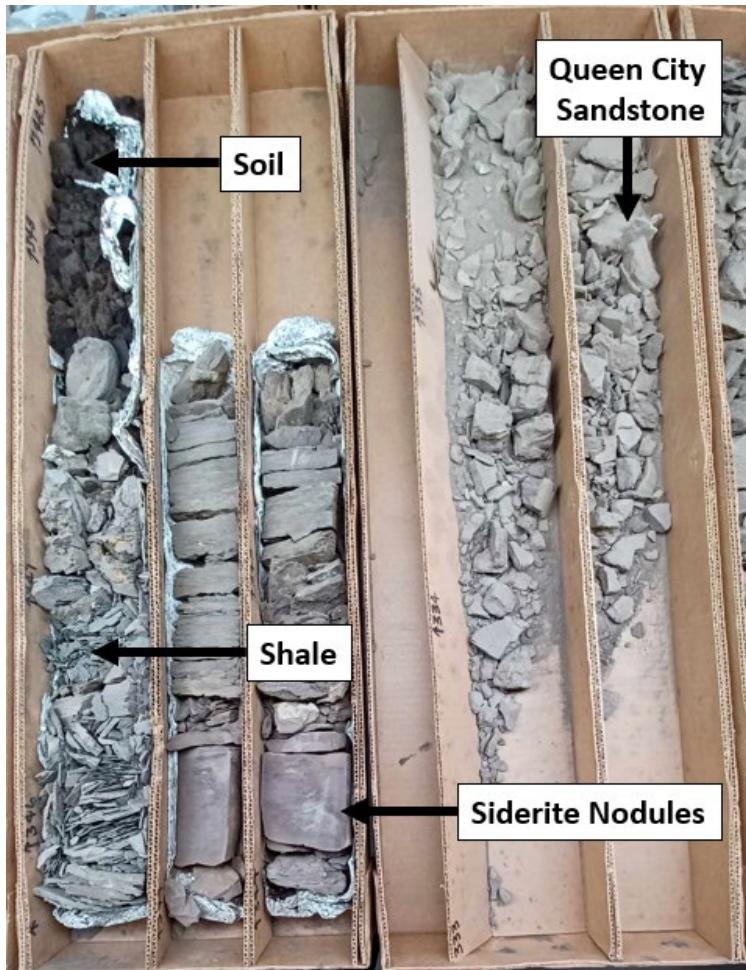


Figure 7. Photograph of two boxes from core #1 (C01440) representing the Queen City formation. The facies include light brown sandstones, reddish-brown tight siderite nodules, dark brown soil, and medium grey shale fractured along bedding planes. The sandstones are extremely brittle, making them unsuitable for sampling and laboratory analysis.

4.2 Upper Coastal Plains: Wilcox Formation

The Wilcox group includes the following facies:

- Cross-stratified sandstone
- Cross-strata with mud drapes
- Structureless sandstone with mud clasts
- Structureless sandstone with Ophiomorpha
- Hummocky cross stratification
- Ripple stratification with double mud drapes
- Very fine-grained sandstone with ripples
- Laminated mudstone
- Flaser bedding with syneresis cracks
- Wavy bedding
- Lenticular beddings with syneresis cracks
- Indistinctive bioturbation
- Soft sediment deformation

- Coal

Figure 8 shows all 26 boxes available for core #6 (C09032) where the lower Wilcox formation and the overlying shale (Big Shale) are highlighted in red and blue. **Figure 9** shows the boundary between pure shale (Big Shale) and shaly sandstone (lower Wilcox) at 4616 ft. **Figure 10** shows that multiple core plugs have been taken from core #6 in the past, and that core plugs were taken primarily in shale-free and homogeneous sandstones (Box 16). **Figure 11** shows the variability of core plugs taken with depth and core depth gaps. Most core plugs were taken in the past from the shale-free sandstones at the bottom section of the core.



Figure 8. Photograph of all 26 boxes of core #6 (C09032). Each box is composed of 3 rows and can hold up to 9 ft of core. The lower Wilcox formation is highlighted in red, and the overlying shale (Big Shale) is highlighted in blue.

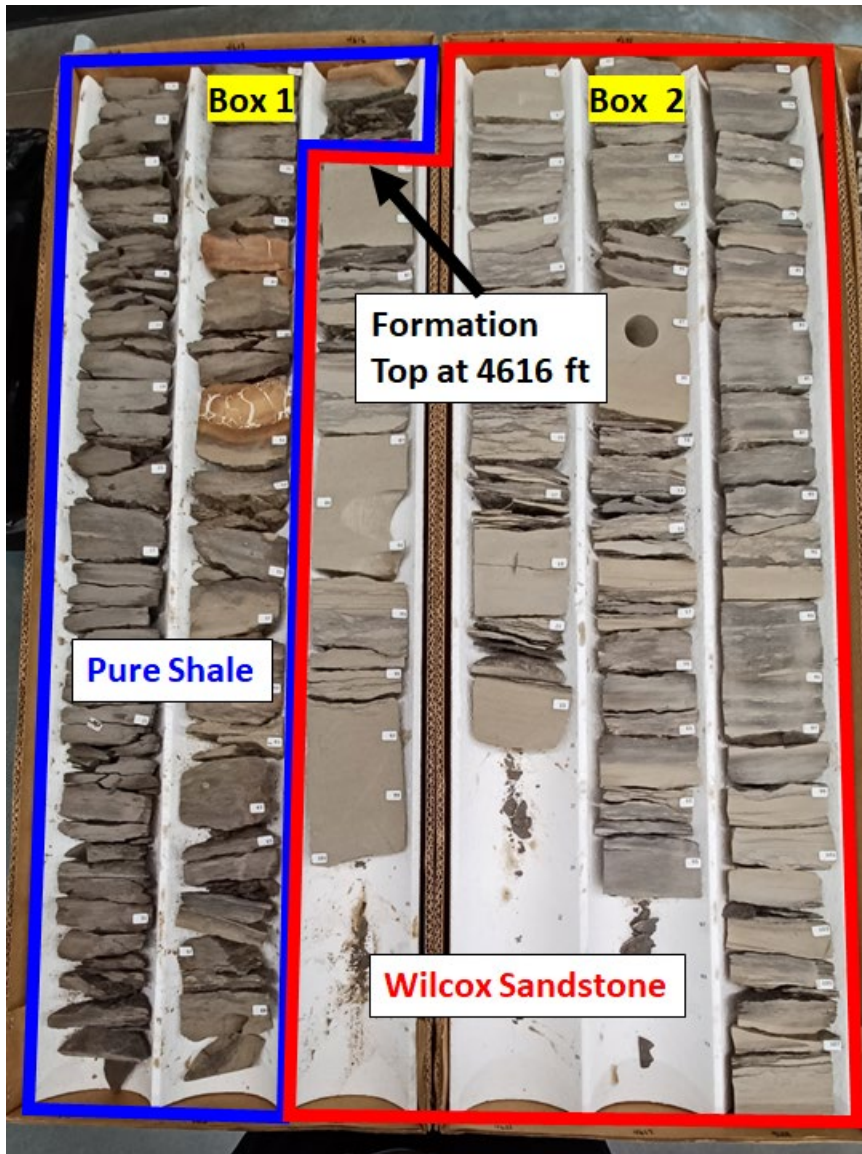


Figure 9. Photograph of boxes #1 and #2 of core #6 (C09032). The lower Wilcox formation is highlighted in red, and the overlying shale (Big Shale) is highlighted in blue. Wilcox formation top is located at a depth of 4616 ft.

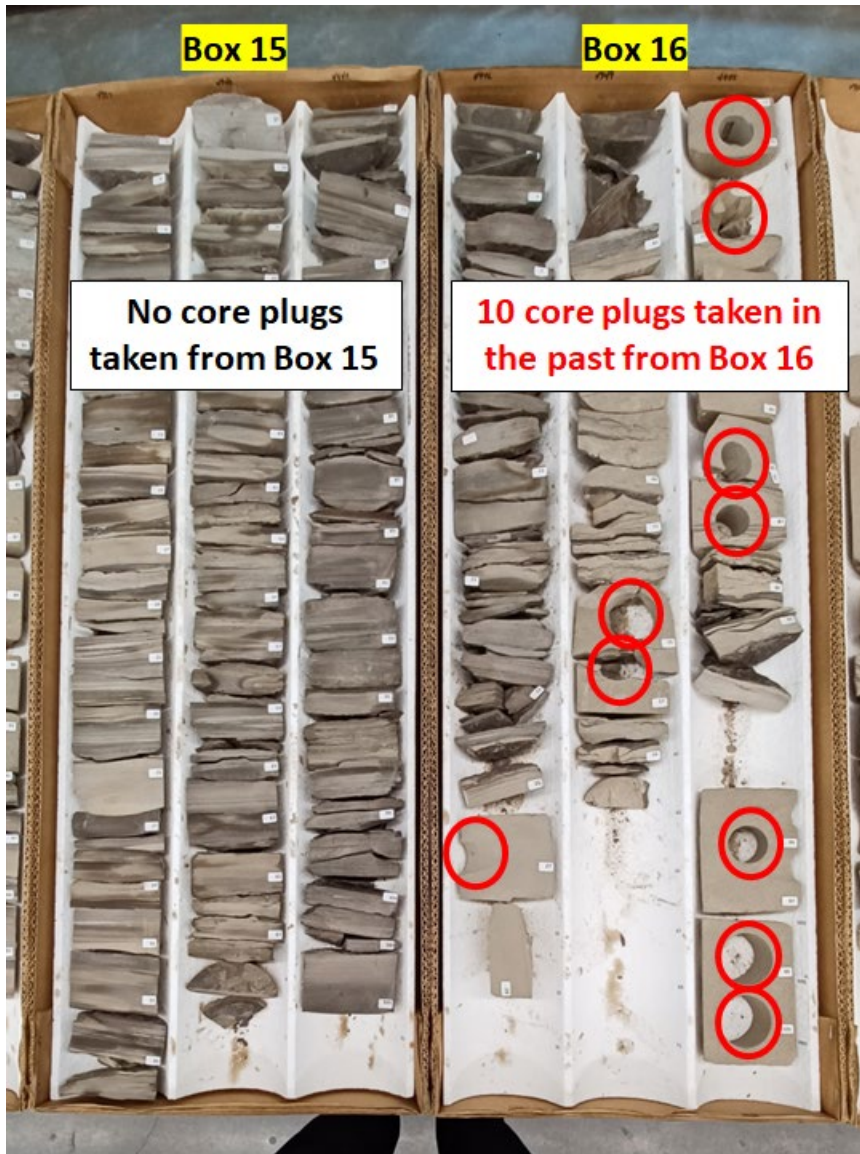


Figure 10. Photograph of boxes #15 and #16 of core #6 (C09032) from the Wilcox formation. Box #15 is composed of laminated shaly sandstones whereas box #16 is composed of clean sandstones. In the past, most core plugs were taken from clean sandstones, as indicated by the red circles.

Box #	Top Depth (ft)	Bottom Depth (ft)	Gap Top (ft)	Gap Bottom (ft)	Gap Length (ft)	Core Plugs #
1	4610	4619				4
2	4619	4628				1
3	4628	4637				1
4	4637	4646				1
5	4646	4658	4652	4655	3	6
6	4658	4667				8
7	4860	4869	4667	4860	193	3
8	4869	4878				5
9	4878	4887				3
10	4887	4896				1
11	4896	4905				1
12	4905	4914				1
13	4914	4928	4914	4928	14	2
14	4928	4937				3
15	4937	4946				0
16	4946	4955				10
17	4955	4964				16
18	4964	4973				7
19	4973	4982				7
20	4982	6021	4983	6015	1032	7
21	6021	6030				8
22	6030	6039				8
23	6039	6048				8
24	6048	6057				3
25	6057	6066				7
26	6066	6075				7

Figure 11. Summary of properties of core #6 (C09032) from the Wilcox formation. The last column lists the number of core plugs that were taken from each box in the past by previous studies. Based on visual inspection, the number of core plugs correlates with the volumetric concentration of shale. Indeed, the lower the shale concentration, the larger the number of samples taken. Therefore, this example illustrates biased sampling made by previous studies.

4.3 Upper Coastal Plains: Carrizo Formation

Carrizo sandstones in core #2 are oil saturated and were easily identified thanks to the strong smell of oil. **Figure 12** shows a photograph of two boxes from core #2 (C00535). The sandstones exhibit a dark brown color. The sandstones are loosely consolidated (resembling soil) and were held together with aluminum foil. **Figure 13** shown SP and resistivity logs across the Carrizo formation in well #B01. The high resistivity readings indicate the presence of oil. The separation between shallow- and deep-sensing resistivity logs indicates the presence of mud-filtrate invasion.



Figure 12. Photograph of two boxes from core #2 (C00535) representing the Carrizo formation. The sandstones are loosely consolidated and exhibit a strong smell due to the presence of oil.

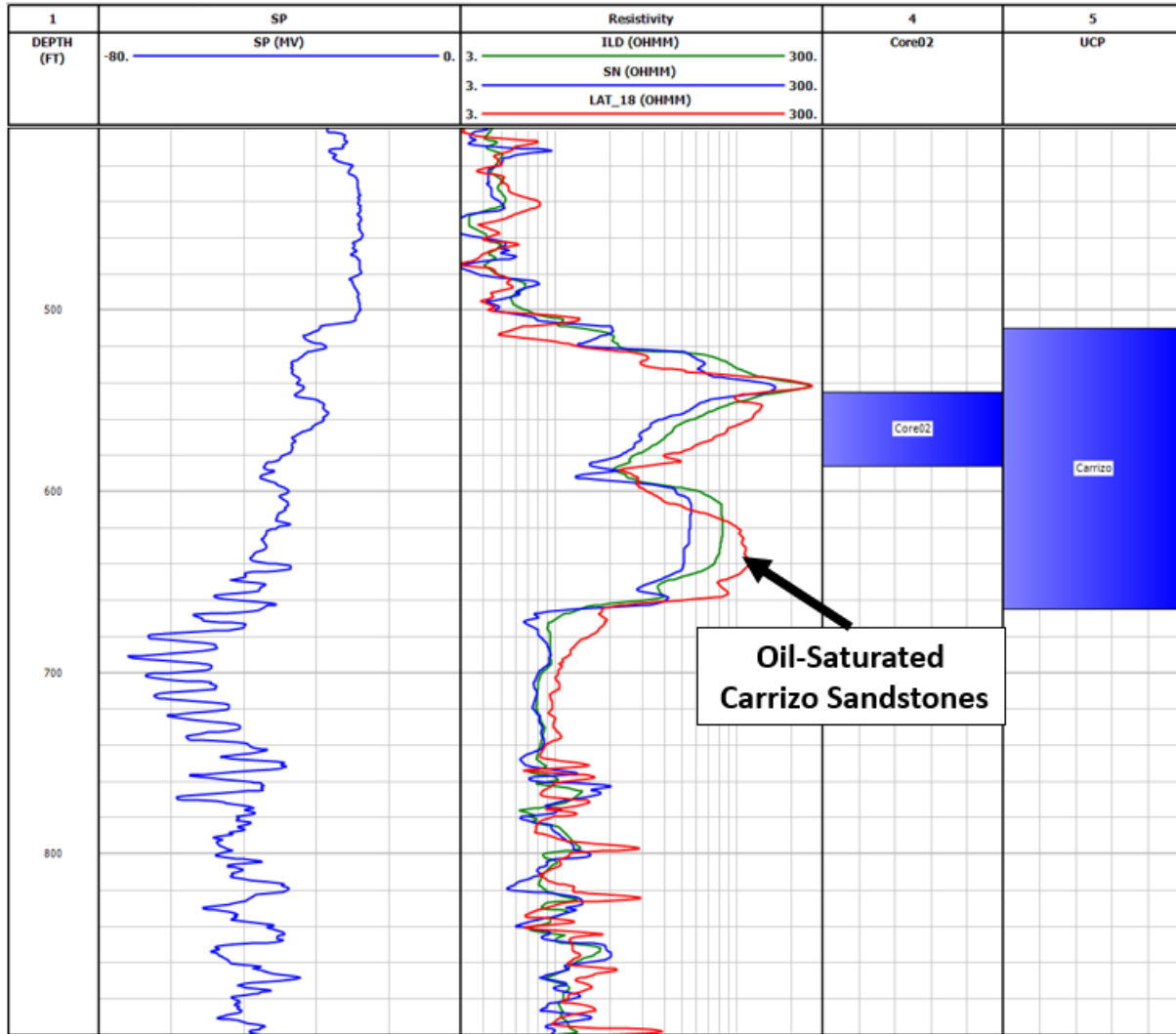


Figure 13. Well logs of well #B01. The high resistivity reading between 520 ft and 660 ft indicates the presence of oil in the Carrizo sandstones. The separation between the deep-, medium-, and shallow-sensing resistivity logs (red, green, and blue curves, respectively) indicates the presence of mud-filtrate invasion. Track 1: depth. Track 2: SP log. Track 3: resistivity logs. Track 4: cored interval. Track 5: formation zones.

4.4 Upper Coastal Plains: Jackson and Yegua Formation

Core #7 representing the Jackson & Yegua formations is of poor quality and stored in glass vials. Figure 14 shows a photograph of five glass vials from core #7 (V21533). The sandstones from the Jackson and Yegua formations exhibit tan, light brown, and light grey colors. The rock samples are too small and damaged, making them unsuitable for laboratory analysis.



Figure 14. Photograph of five glass vials from core #7 (V21533) representing the Jackson & Yegua formations.

4.5 Llano Uplift: Ellenburger and San Saba Formations

The Ellenburger and San Saba formations are represented by six cores from which cores #11, #12, and #13 are very long (more than 140 boxes each) and are of good quality. The three most common lithologies are (1) tight limestones and dolostones, (2) vuggy limestones and dolostones, and (3) chert. The limestones exhibit white to light grey colors. The dolostones exhibit tan to light grey colors with dolomite crystals on the surface of the vugs. Chert (made of silica SiO_2) exhibits a green color and occurs as layered deposits. The presence of calcium carbonate and dolomite minerals is tested using hydrogen chloride (HCl) acid. Chert does not react with HCl. **Figures 15 to 18** show different facies encountered in the Ellenburger and San Saba formations. **Figure 19** shows the distribution of vuggy porosity on cores #11 (top) and #13 (bottom) based on visual inspection. The top of the Ellenburger formation exhibits tight limestones. Rocks with the best storage and flow properties (large vugs) are in the middle and at the bottom of the cores. **Figure 20** shows an example of well logs (SP and resistivity) of well #A03 from the Llano Uplift. The Ellenburger and San Saba formations show a distinct well log signature (High resistivity and low SP) compared to the underlying and overlying formations. The core associated with this well is core #11.

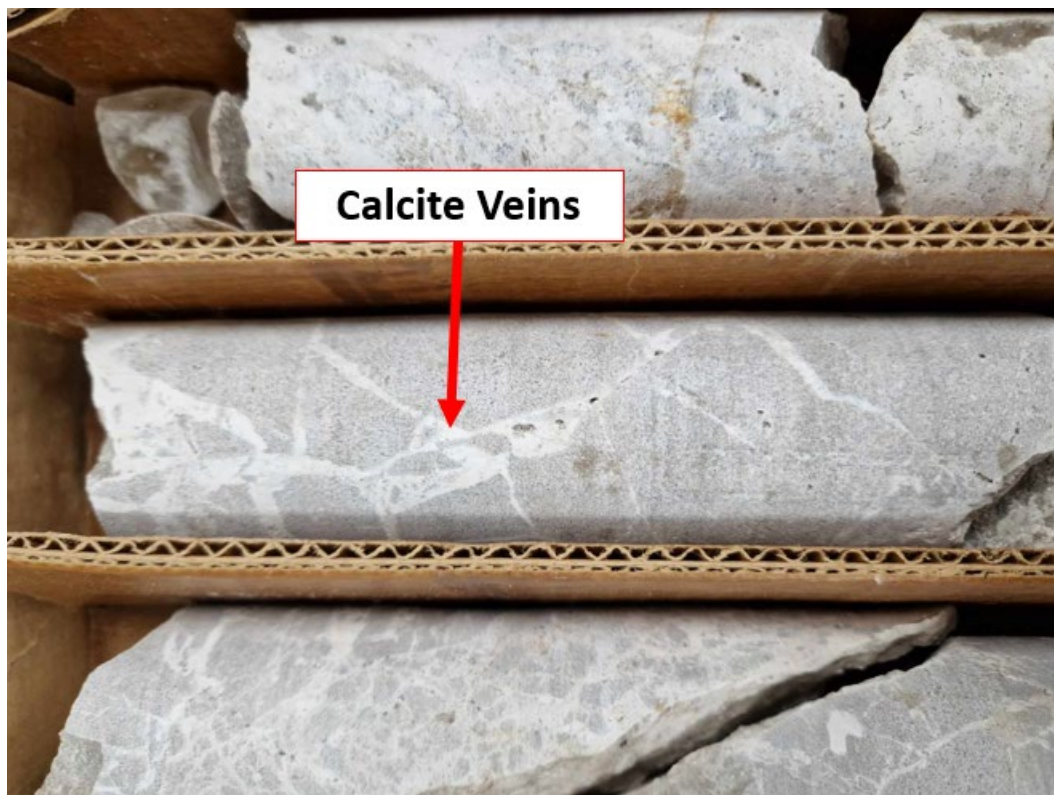


Figure 15. Photograph of a naturally fractured dolostone from the Ellenburger formation with white calcium carbonate veins. The diameter of the cores is 2 in.

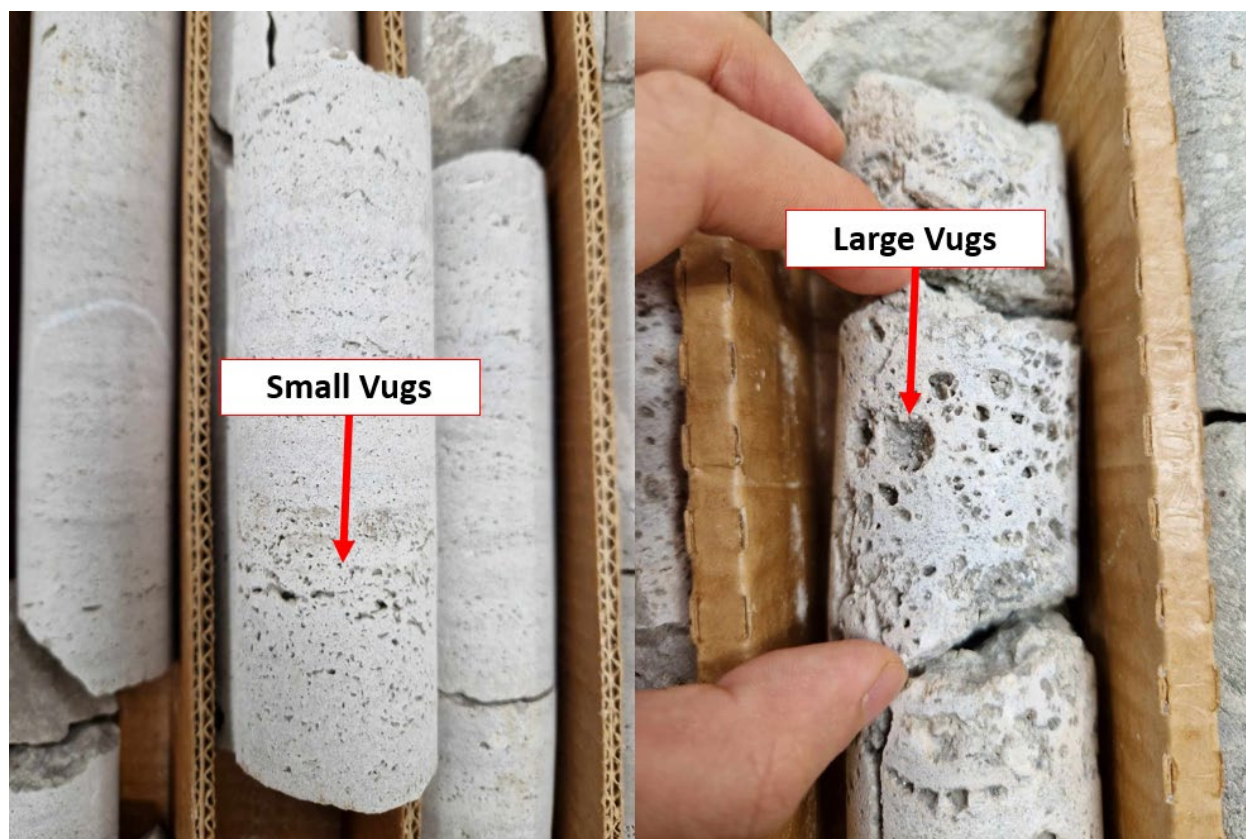


Figure 16. Photograph of dolostones with small (left) and large (right) vugs. The diameter of the cores is 2 in.



Figure 17. Photograph of dolomite crystals inside a large vug from the Ellenburger formation. The diameter of the cores is 2 in.

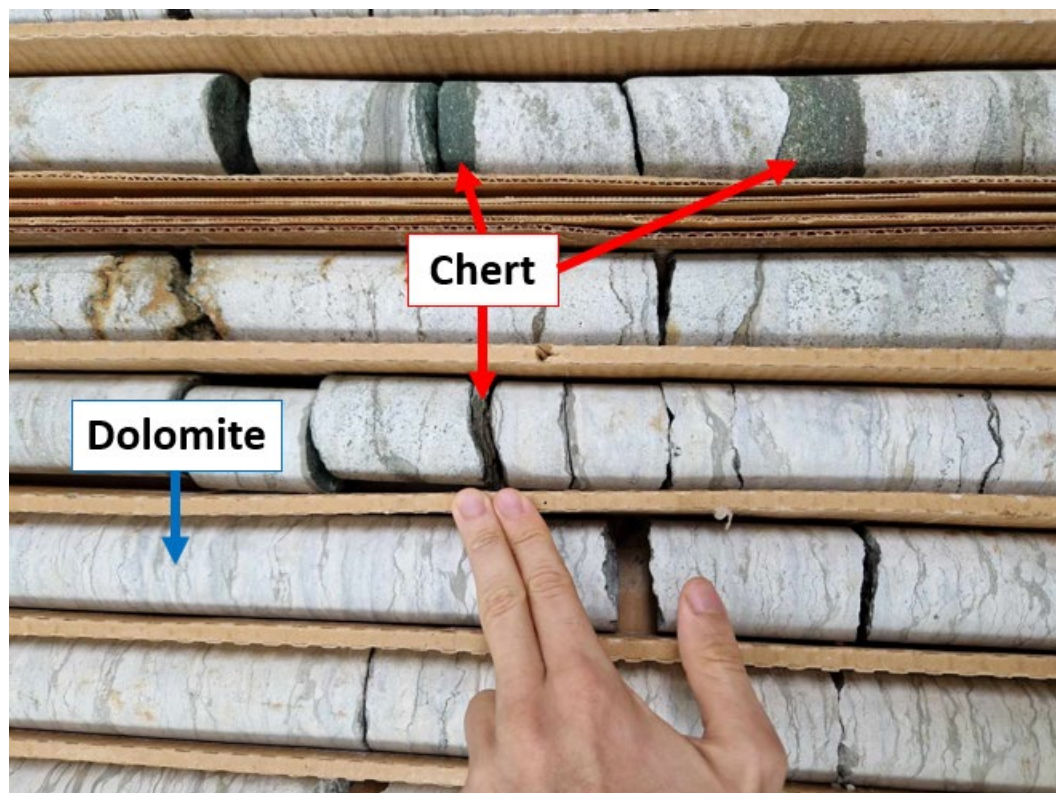


Figure 18. Photograph of dolostone from San Saba with interlayers of green chert. The diameter of the cores is 2 in.

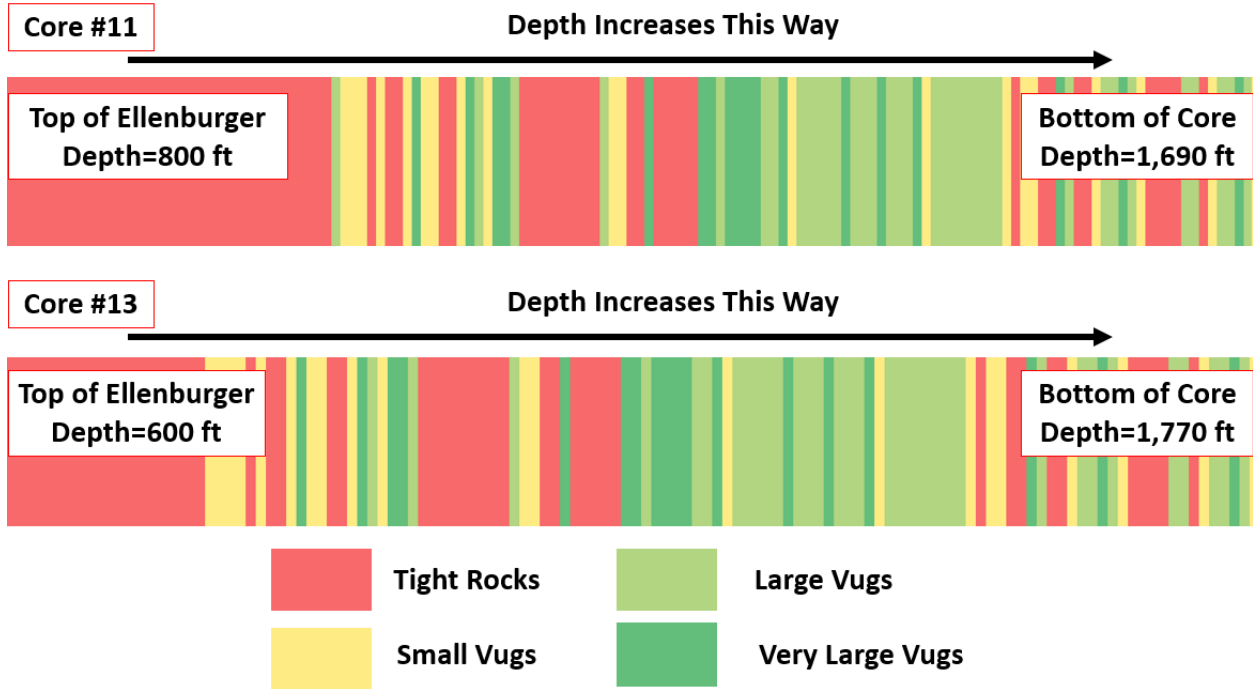


Figure 19. Distribution of vugs and their sizes on cores #11 (top) and #13 (bottom) based on visual inspection. The core is represented horizontally where the top of the Ellenburger formation is located to the left and the bottom of the core is located to the right. The top of the Ellenburger formation exhibits tight limestones. Rocks with the best storage and flow properties (large vugs) are in the middle and at the bottom of the cores.

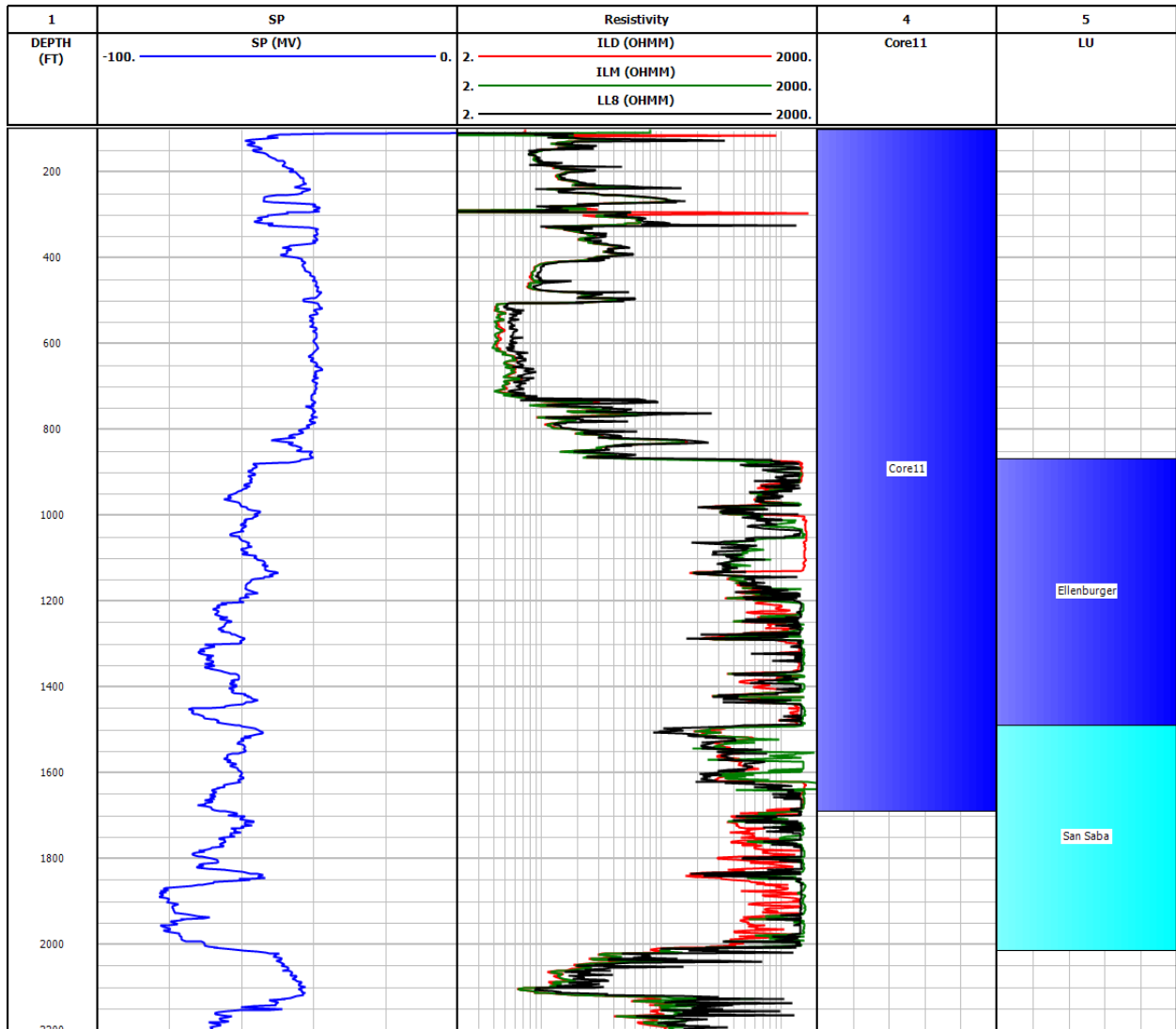


Figure 20. Well logs of well #A03. The Ellenburger and San Saba formations exhibit large resistivity values (over 1,000 ohm-m) due to low porosity (less than 0.1). Track 1: depth. Track 2: spontaneous potential (SP) log. Track 3: resistivity logs. Track 4: cored interval. Track 5: formation zones.

4.6 Llano Uplift: Hickory Formations

The Hickory sandstones exhibit a wide range of grain sizes. The color of the sandstones varies between red, yellow, grey, and beige. **Figure 21** shows sandstones from the Hickory formation that exhibit cross-laminations with medium and fine-grained layers.

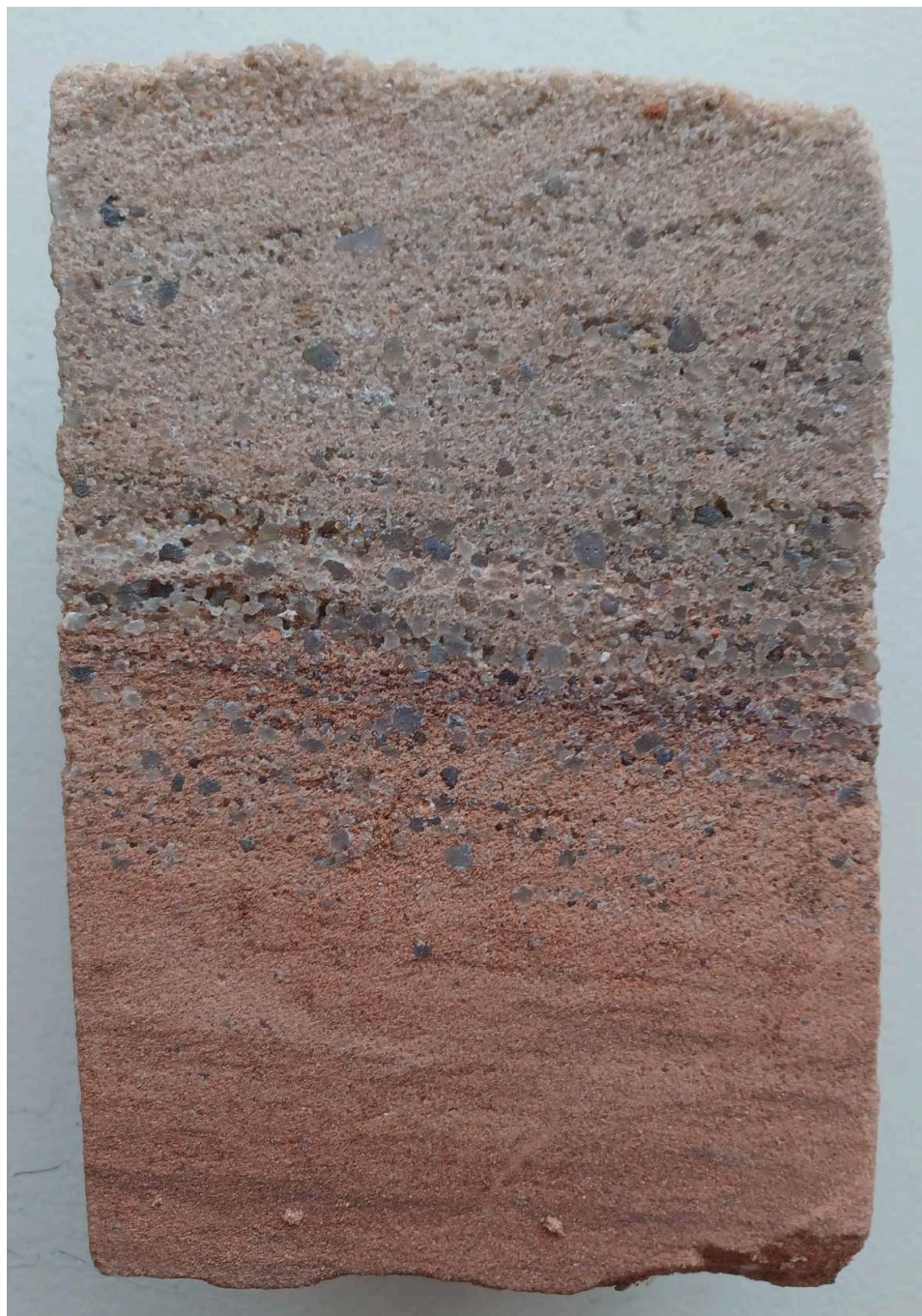


Figure 21. Photograph of a multi-layered rock from the Hickory sandstones obtained from Core #16 (C0087) at a depth of 626 ft. The upper section of the core is composed of medium-sized tan grains, the middle section is poorly sorted and composed of a mixture of fine, medium, and coarse grains. The bottom section is composed of light brick-red fine grains.

5 CORE SAMPLE ANALYSES

The main objective of this task is to analyze approximately 30 representative core samples of various rock types from the Llano Uplift and the Upper Coastal Plains. The petrophysical properties of interest include porosity, permeability, grain density, porosity exponent (m), and nuclear magnetic resonance (NMR) T_2 distribution.

5.1 Methods and Equipment

This section of the report presents the methodology and equipment used to obtain porosity, permeability, NMR, and electrical measurements in the core samples acquired in wells located in the Llano Uplift and the Upper Coastal Plains.

Step 1: Sample preparation

We cut core samples that represent the main rock types of the Llano Uplift and Upper Coastal Plains formations and analyzed them through laboratory measurements. Considering the geometrical constraints of some laboratory instruments, the diameter of all core plugs was set equal to 1.5 in.

Step 2: Drying core plugs

We dried the samples at 65°C for at least 48 hours to remove any moisture in them.

Step 3: Volume and weight measurements of dried core samples

The weight of dried core plugs was determined using a scale and the volume of the core plugs was calculated assuming a cylindrical shape.

Step 4: Helium porosity measurements

To measure the porosity of dried core samples, we used a helium porosimeter.

Step 5: Gas permeability measurements (pulse-decay method) for tight core samples

To measure the permeability of tight core plugs, we used the pressure-decay permeability measurement method. In this technique, the core sample is placed in a core holder connected to an upstream tank filled with nitrogen. Then, an upstream valve is opened, and the gas expands across the sample either to the atmosphere or vacuum. The differential pressure versus time is recorded and the permeability values are obtained through the data analysis procedure. Then, we used a GCTS pulse-decay permeameter (PDP) to obtain the permeability values for all core samples at room temperature (25°C). After we placed the dried core sample in a Hassle-type core holder, we applied a confining pressure of 1,400 psi around the core sleeve using a hydraulic oil pump. Next, we established a pore pressure of 800 psi using nitrogen (N_2) as the pore fluid. We allowed N_2 pressure to equilibrate before conducting any measurements on the core samples. After the pore pressure was equilibrated, we applied a small pressure pulse by decreasing the downstream pressure to 10 psi. Finally, we recorded the decline in the differential pressure and the increase in downstream pressure as the pressure pulse traveled through the core sample. The recorded data was processed to obtain the gas permeability using an in-house data processing algorithm based on the formulation introduced by Jones (1997). Gas permeability measurements are shown in **Appendix B**.

Step 6: Volumetric concentration of shale (image analysis)

We analyzed photographs of laminated shaly sandstones on the software FIJI ImageJ to estimate the volumetric concentration of shale. Laminations with dark colors indicate shales whereas laminations with light colors indicate sandstones.

Step 7: Saturating core plugs with brine

We saturated the core samples with 3 wt. % potassium chloride brine (KCl) to inhibit the clay and prevent core samples from swelling. We situated the core samples in vacuum equipment for 12 to 24 hours depending on the sample porosity and permeability. Finally, we introduced the brine to the samples in the vacuum and left them for 4 to 12 hours to be saturated. Some core samples get damaged when exposed to water. No further measurements can be conducted on these core samples.

Step 8: Weight measurements

The weight of saturated core plugs was determined using a scale. Weight measurements from dry and saturated core plugs were used to estimate porosity (density porosity) and grain density. To ensure consistency between the different measurements, density porosity values are compared to helium porosity measurements.

Step 9: Electrical measurements

Archie's equation is traditionally used to describe the relationship between formation resistivity, formation water resistivity, and formation porosity. The value of the porosity exponent (m) is rock-class dependent. In this study, we derived an average porosity exponent for each aquifer/formation (Wilcox, Hickory, Ellenburger and San Saba). We used multifrequency impedance analyzer equipment to measure the electrical resistivity, R_t (ohm-m), of core plugs. Brine resistivity, R_w (ohm-m), was measured using a portable conductivity meter and is approximately equal to 0.22 ohm-m at 69 degrees F. The measured electrical resistivity and the estimated porosity are then used through the application of Archie's model to estimate the porosity exponent (m). Formation factor, F (ohm-m/ohm-m), is given by:

$$F = \frac{R_t}{R_w} = \frac{a}{\phi^m}. \quad (\text{Equation 1})$$

The Winsauer coefficient (a) was assumed to be equal to 1.

Step 10: NMR measurements

NMR is a geophysical method used to assess porosity and pore-size distribution. NMR measurements can also be used to estimate irreducible water saturation and permeability. NMR instruments use strong magnets to create a static magnetic field, B_0 , that aligns (polarizes) the protons in the pore fluid from their resting (random) state to the direction of the imposed magnetic field. The protons then precess around B_0 at a frequency that is proportional to the strength of B_0 . A second oscillating magnetic field, B_1 , is then applied perpendicular to B_0 . This causes the protons to precess around B_1 as well as B_0 . The frequency of B_1 is swept over a range of values until it matches the frequency of precession of the protons around B_0 . At this point, energy is absorbed by protons, and they flip their spin direction. When B_1 is turned off, the protons return to their original state and emit energy at a frequency equal to their precession frequency around B_0 . We measured the relaxation time of the transverse magnetization decay (T_2) using a 2-MHz Magritek NMR Rock Core Analyzer with a CPMG pulse sequence. We set the interexperiment delay to 5s, the minimum signal-to-noise ratio (SNR) to 200, and the echo spacing to 100 μ s. We used an inversion algorithm to obtain the T_2 distribution of each fully brine-saturated core sample from the magnetization-decay measurements. NMR measurements are shown in **Appendix C**.

Step 11: Quality control of porosity measurements

To ensure consistency between the different measurements, NMR porosity is compared to helium porosity and density porosity.

Step 12: Water permeability measurements (brine core-flood method)

We used the brine core flood method to estimate the permeability of rock types with high and moderate permeabilities (larger than 1 mD). This method could not be applied to low-permeability (tight) samples due to the limitations on the required maximum brine pressure needed to penetrate the core plugs. Water permeability measurements are shown in **Appendix D**.

5.2 Photographs of Core Plugs

We cut a total of 49 core plugs. 20 core plugs are from the Upper Coastal Plains (core #1 to #20), 12 are from the Hickory formation (core #21 to #32), 10 are from the Ellenburger (core #42 to #50), and 7 are from San Saba (core #61 to #67). The diameter of each core plug is 1.5 in. Core plugs #1 and #41 were disregarded in the core analysis because they were cut too short. **Figures 22 to 24** show photographs of all the core plugs.

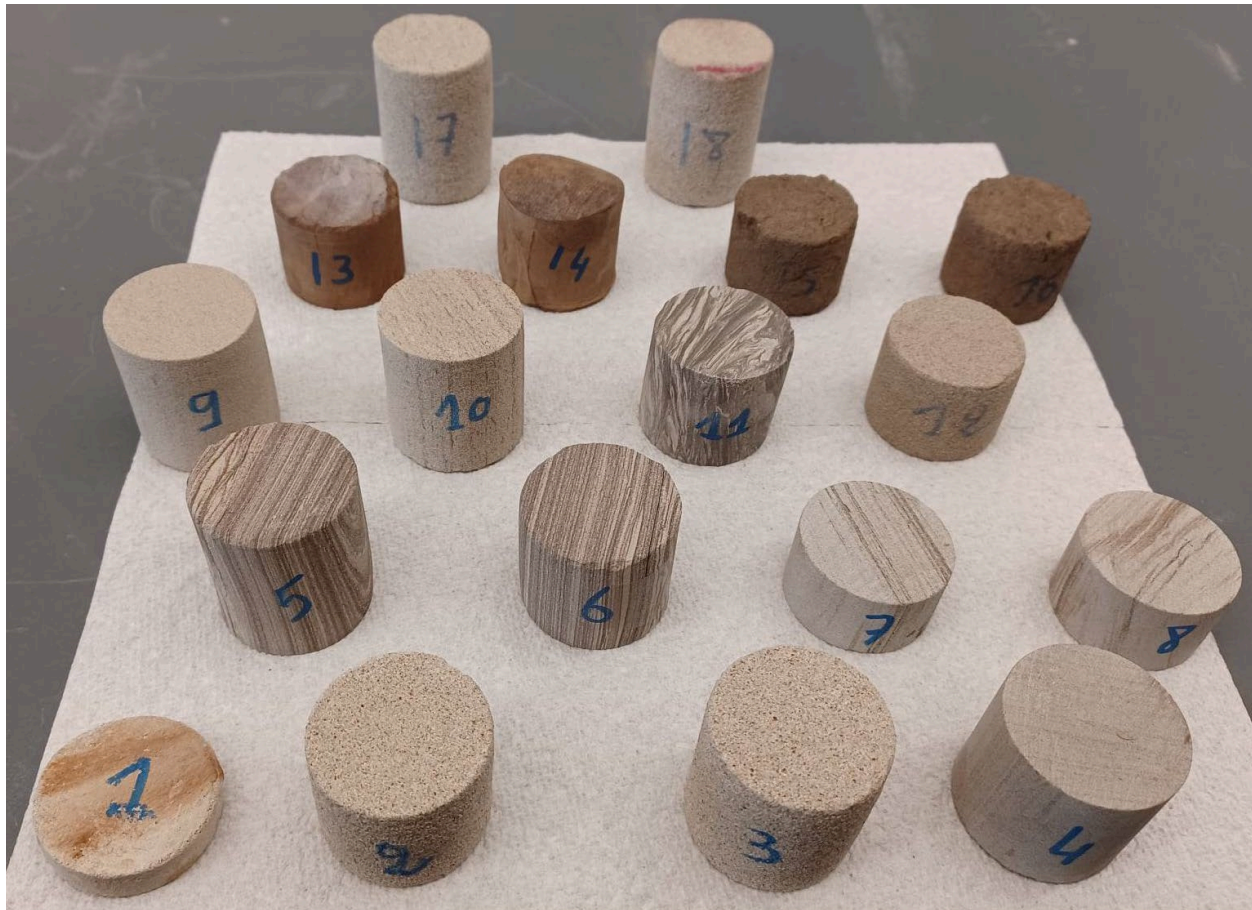


Figure 22. Core plugs from the Upper Coastal Plains formations (core plugs #1 to #18). Core plug #1 was disregarded in the core analysis because it was cut too short. The diameter of each core plug is 1.5 in.



Figure 23. Core plugs from the Upper coastal Plains formations (core plugs #19 and #20) and Hickory aquifer (core plugs #21 to #32). Core plug #41 from the Ellenburger formation was disregarded in the core analysis because it was cut too short. The diameter of each core plug is 1.5 in.



Figure 24. Core plugs from the Ellenburger (core plugs #42 to #50) and San Saba aquifers (core plugs #61 to #67). The diameter of each core plug is 1.5 in.

5.3 Results of Core Analysis in the Upper Coastal Plains

This section contains the results and observations for permeability, NMR, porosity, and electrical measurements performed on core plugs acquired from the Upper Coastal Plains.

Upper Coastal Plains: Rock sampling

Rock samples were obtained primarily from the Carrizo, upper Wilcox, and lower Wilcox formations. Cores from the Queen City formation were extremely brittle (Core #1 - C01440) and were damaged/fractured when sampling was attempted. Thus, samples from the Queen City formation were unsuitable for core analysis. Core #7 – V21533 is comprised of cuttings stored in glass vials. Sampling from Core #7 – V21533 was not permitted, preventing us from taking core samples of the Jackson and Yegua formations. Nonetheless, photos of all the cores were taken.

Upper Coastal Plains: Summary of measurements

Table 1 summarizes core measurement results.

Table 1. Summary of laboratory measurements in the Hickory formation. (*) estimated properties. Accession #: BEG well identification number. Core #: study core identification number. k : permeability. T_{2LM} : NMR T_2 logarithmic mean. $T_{2,Peak}$: NMR T_2 value at the peak. $S_{wr,Xms}$: estimated irreducible water saturation from NMR measurements. Archie's m : porosity exponent.

Plug #	Depth (ft)	Core #	Accession #	ϕ (fraction)	Grain Density (g)	k (mD)	T_{2LM} (ms)	$T_{2,Peak}$ (ms)	$S_{wr,Xms}$ (fraction)	Archie's m
17	4,441	7	C00839	0.281	2.59	161.7	189.7	446.7	0.278	1.74
18	4,441	7	C00839	0.288	2.62	139.1	189.9	501.2	0.283	2.01
2	4,410	3	C00839	0.292	2.62	127.4	178.3	446.7	0.277	1.85
3	4,410	3	C00839	0.287	2.62	177.6	171.9	446.7	0.286	1.75
9	4,397	1	C00839	0.308	2.67	66.8	83.96	199.5	0.334	1.85
10	4,398	1	C00839	0.283	2.66	23.24	54.03	177.8	0.383	1.85
12	3,479	4	C01543	0.300	2.62	80.88	80.64	141.3	0.368	1.92
19	3,479	4	C01543	0.289	2.64	92.39	76.61	158.5	0.338	1.89
20	3,478	4	C01543	0.296	2.60	115.8	78.44	158.5	0.379	1.86
5	4,394	1	C00839	0.169	2.71	0.2093	6.061	3.981	0.641	1.94
6	4,394	1	C00839	0.165	2.69	1.903	5.413	3.548	0.679	1.79
11	4,391	1	C00839	0.180	2.66	0.039	4.597	4.467	0.709	1.87
13	344	4	C01440	0.173	3.13	0.074*	2.499	1.778	0.755	2.13
4	8,035	2	C04523	0.058	2.67	0.001	4.567	4.467	0.735	1.65
7	3,500	6	C01543	0.088	2.69	0.010*	5.471	5.012	0.708	1.71

8	3,500	6	C01543	0.106	2.68	0.034	5.142	1.778	0.739	1.89
15	349	2	C00535	0.371	2.63	N/A	N/A	N/A	N/A	N/A
16	349	2	C00535	0.375	2.65	N/A	N/A	N/A	N/A	N/A

Upper Coastal Plains: Rock classes and facies

Table 2 summarizes rock properties per rock class and facies.

Table 2. Average petrophysical properties per rock classes in the Upper Coastal Plains.

Rock Class	Facies	Core plugs	ϕ (fraction)	k (mD)	Grain Density (g/cc)	Archie's m	T_{2LM} (ms)
I	Coarse-grained sandstones	2 – 3 – 17 – 18	0.29	151	2.61	1.84	182
II	Medium-grained sandstones	9 – 10 – 12 – 19 – 20	0.3	75.8	2.64	1.87	74.7
III	Laminated shaly sandstones	5 – 6	0.17	1.06	2.7	1.87	5.74
IV	Siltstones with ripples	11	0.18	0.04	2.66	1.87	4.60
V	Siderite nodules	13	0.17	0.05	3.13	2.13	2.50
VI	Grey siltstones	4 – 7 – 8	0.08	0.06	2.68	1.75	5.06
VII	Brown mudstones	15 – 16	0.37	N/A	2.64	N/A	N/A

Upper Coastal Plains: Grain density measurements

The median grain density is 2.65 g/cc. The highest grain density is equal to 3.13 g/cc and corresponds to a siderite nodule. The average grain density of laminated shaly sandstone (where the volumetric concentration of shale is approximately 50%) is 2.7 g/cc. The average grain density of medium- and coarse-grained sandstone is 2.63 g/cc. The average grain density of grey siltstones is 2.68 g/cc.

Upper Coastal Plains: Relationship between porosity and permeability

Figure 25 shows the relationship between porosity and permeability in the Upper Coastal Plains aquifers. The porosity and permeability of the best quality rocks (coarse-grained sandstones) is equal to 0.3 and 160 mD, respectively. The permeability of the fractured (damaged) sample (core plug #5) is one order of magnitude greater than the intact sample (core plug #6).

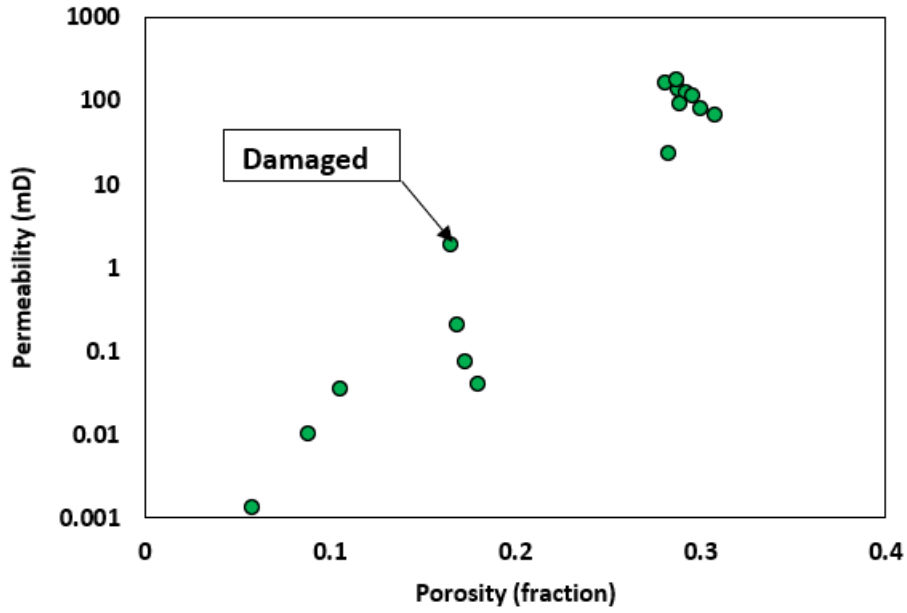


Figure 25. Relationship between porosity and permeability of core plugs from the Upper Coastal Plains aquifers. The fractured/damaged core plug exhibits a permeability that is one order of magnitude greater than similar unfractured rocks.

Upper Coastal Plains: NMR T_2 distributions and rock classes

Rocks from different classes exhibit distinct NMR signatures. **Figure 26** shows T_2 distributions of all core samples from the Upper Coastal aquifers. **Figures 27 to 32** show T_2 distributions of core samples belonging to rock classes I to VI, respectively. **Figure 33** shows the relationship between porosity, T_{2LM} , and facies.

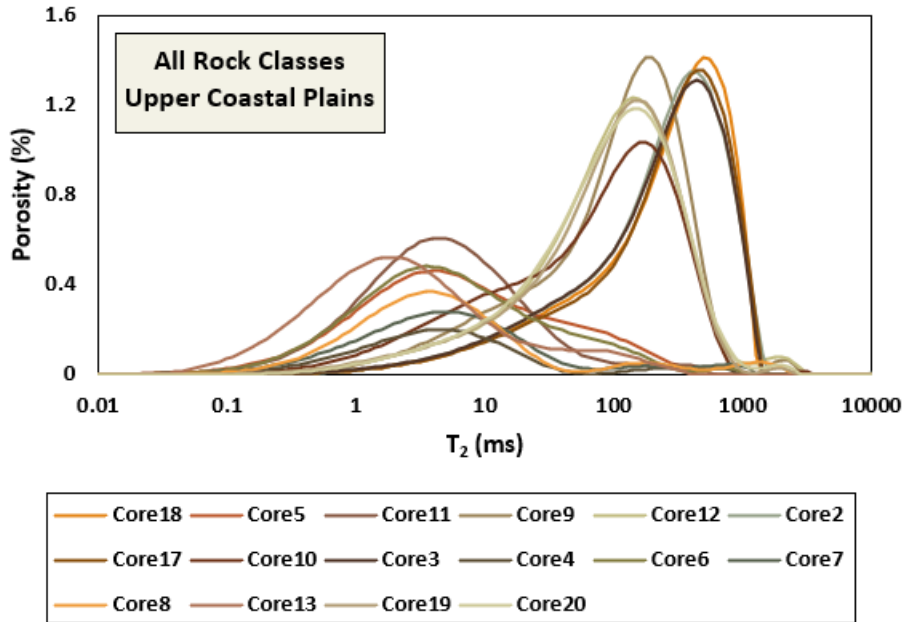


Figure 26. NMR T_2 distributions of all core samples from the Upper Coastal Plains aquifers.

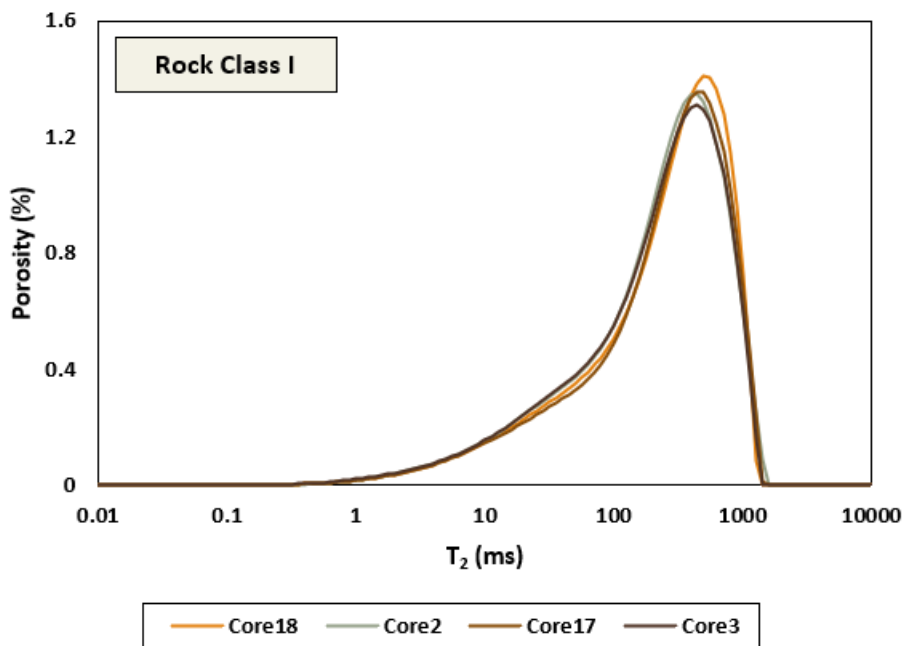


Figure 27. NMR T_2 distributions of coarse-grained sandstones (class I) from the Upper Coastal Plains aquifers.

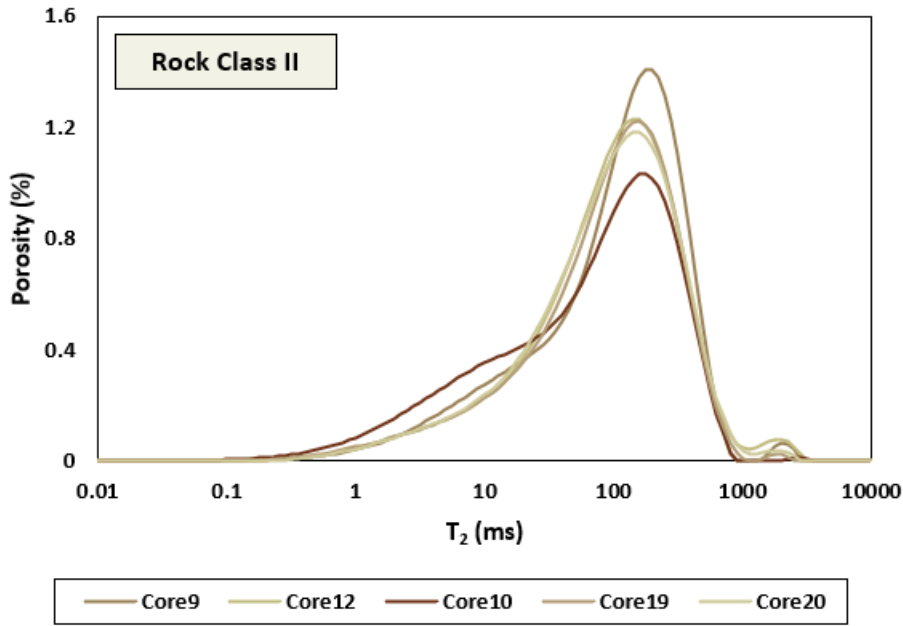


Figure 28. NMR T₂ distributions of medium-grained sandstones (class II) from the Upper Coastal Plains aquifers.

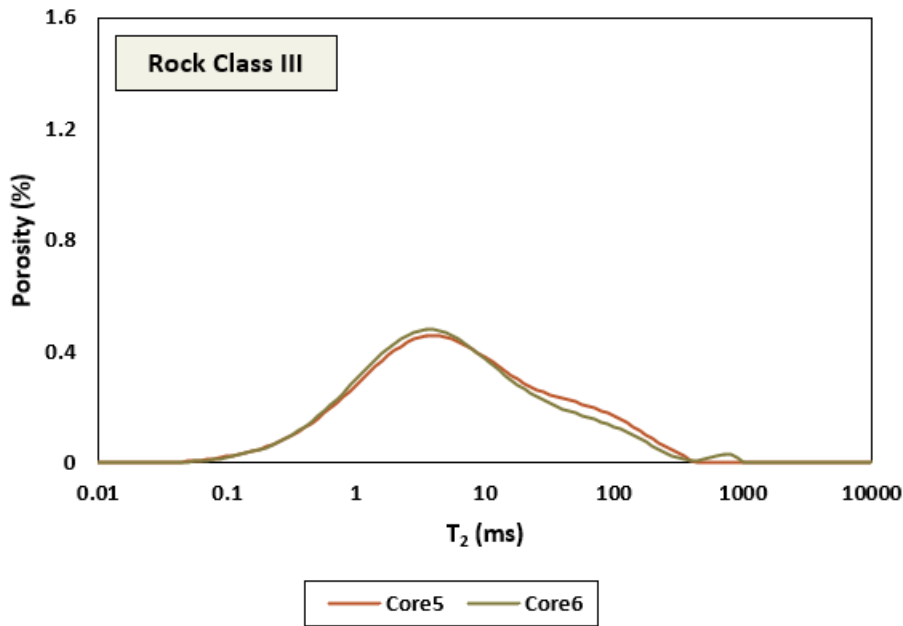


Figure 29. NMR T₂ distributions of laminated shaly sandstones (class III) from the Upper Coastal Plains aquifers.

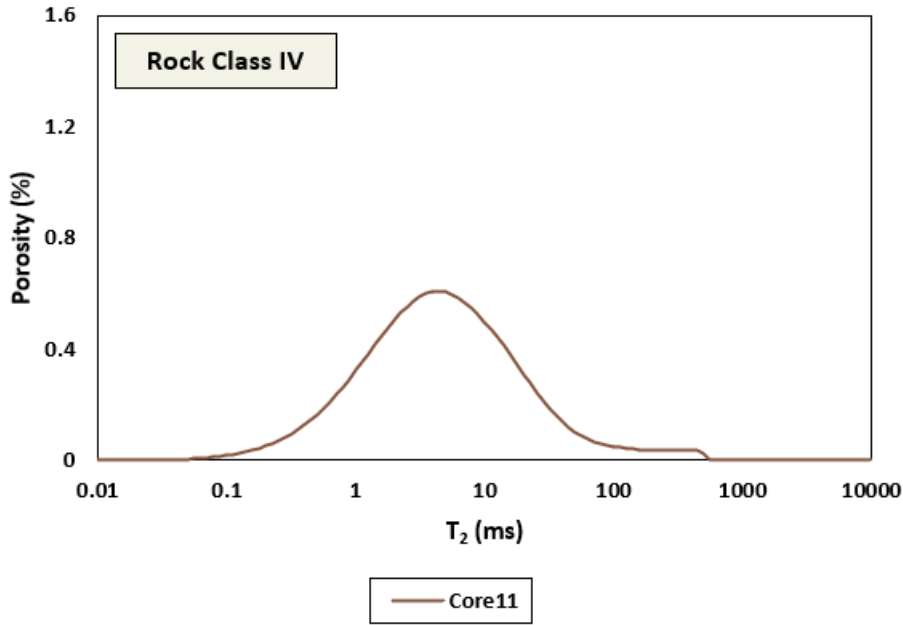


Figure 30. NMR T₂ distribution of siltstones with ripples (class IV) from the Upper Coastal Plains aquifers.

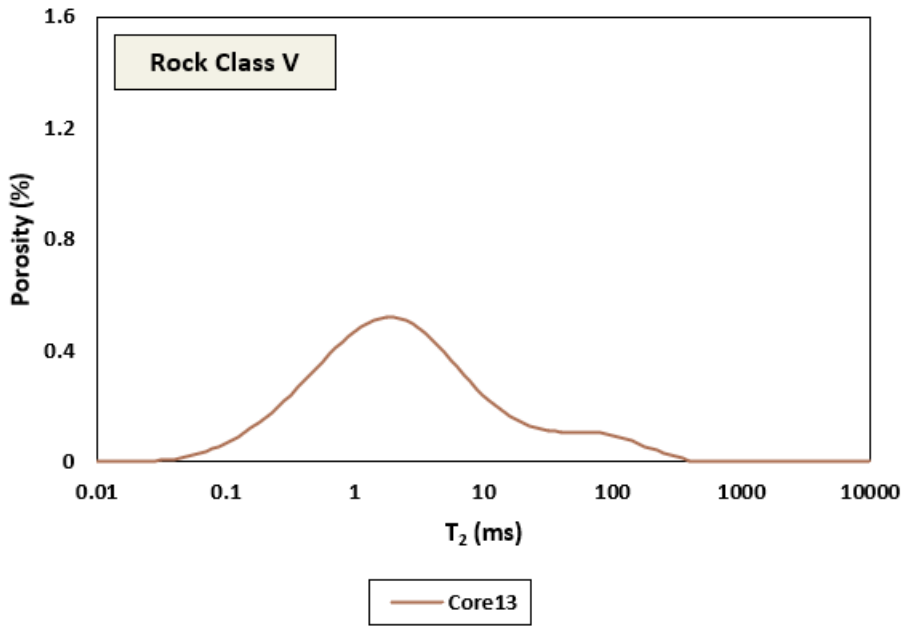


Figure 31. NMR T₂ distribution of siderite nodules (class V) from the Upper Coastal Plains aquifers.

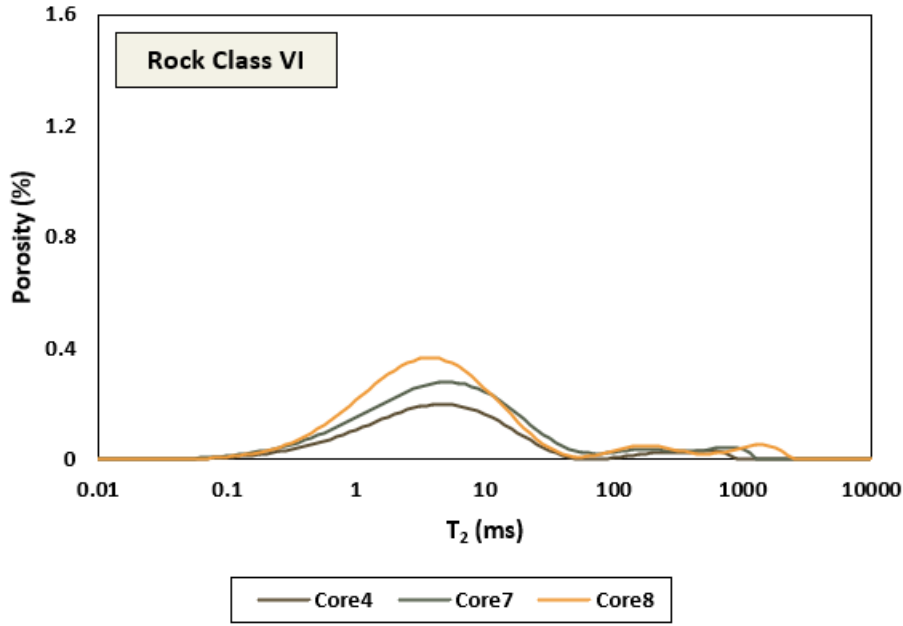


Figure 32. NMR T_2 distributions of grey siltstones (class VI) from the Upper Coastal Plains aquifers.

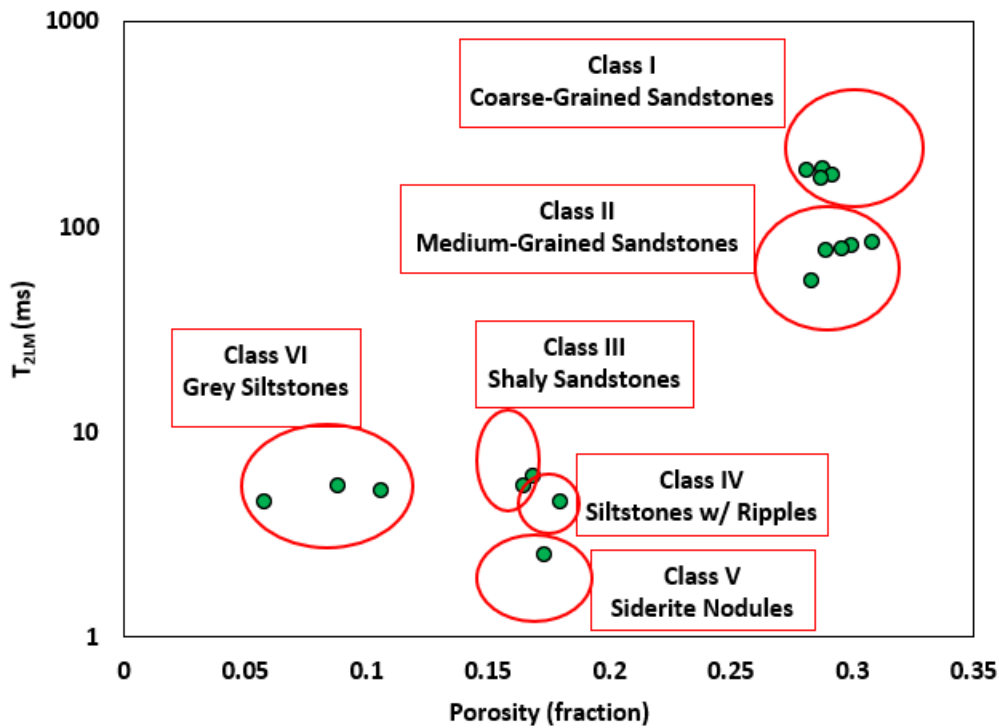


Figure 33. Relationship between porosity, T_{2LM} , and facies of all core plugs from the Upper Coastal Plains aquifers.

Upper Coastal Plains: Electrical properties

Figure 34 shows the relationship between formation factor and porosity. The average porosity exponent of all rock samples is equal to 1.85.

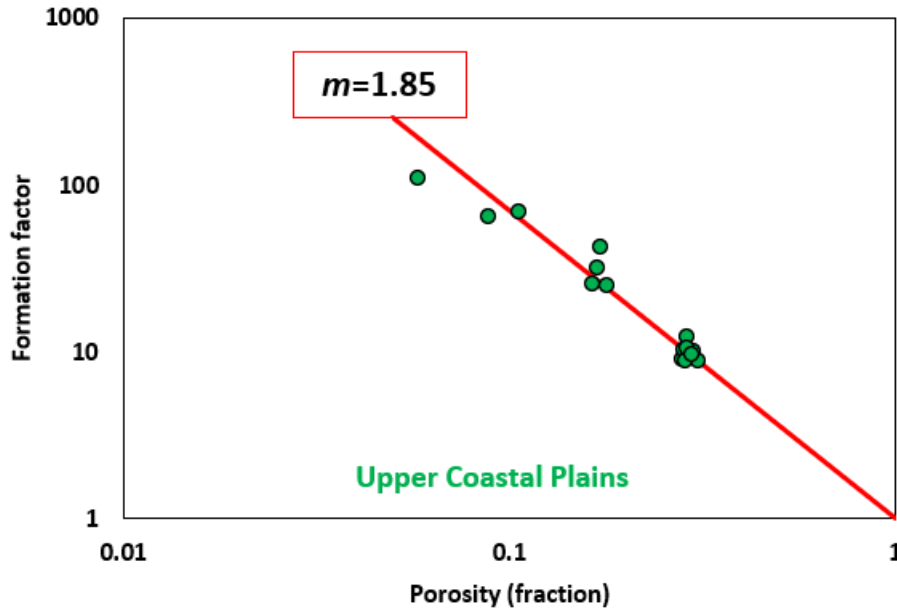


Figure 34. Relationship between formation factor and porosity of all core plugs from the Upper Coastal Plains aquifers. The red line corresponds to a porosity exponent equal to 1.85.

Upper Coastal Plains: Relationship between T_{2LM} and $T_{2,Peak}$

A non-negligible difference between T_{2LM} and $T_{2,Peak}$ (corresponding to the highest peak in the T_2 distribution) indicates the presence of a multimodal pore-size distribution. **Figure 35** shows the T_2 distribution of core #10 along with the corresponding T_{2LM} and $T_{2,Peak}$. **Figure 36** shows the relationship between T_{2LM} and modal $T_{2,Peak}$ for all core samples from the Upper Coastal Plains aquifers. In high-porosity and high-permeability rock samples, $T_{2,Peak}$ is greater than T_{2LM} , whereas in tight rocks, modal T_2 is smaller than T_{2LM} . The difference between modal T_2 and T_{2LM} is due to the presence of bimodal pore-size distributions in most rock samples.

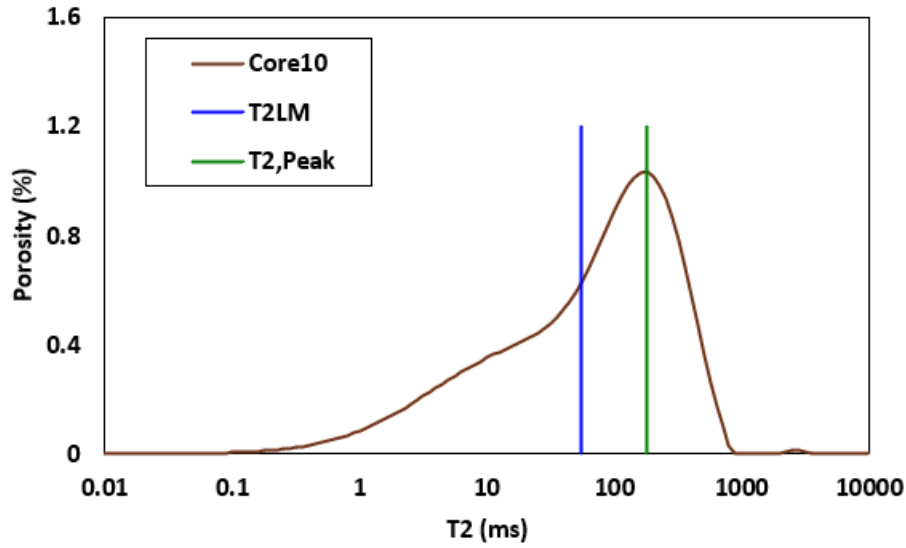


Figure 35. NMR T_2 distribution of core #10 along with the corresponding T_{2LM} (blue line) and $T_{2,Peak}$ (green line).

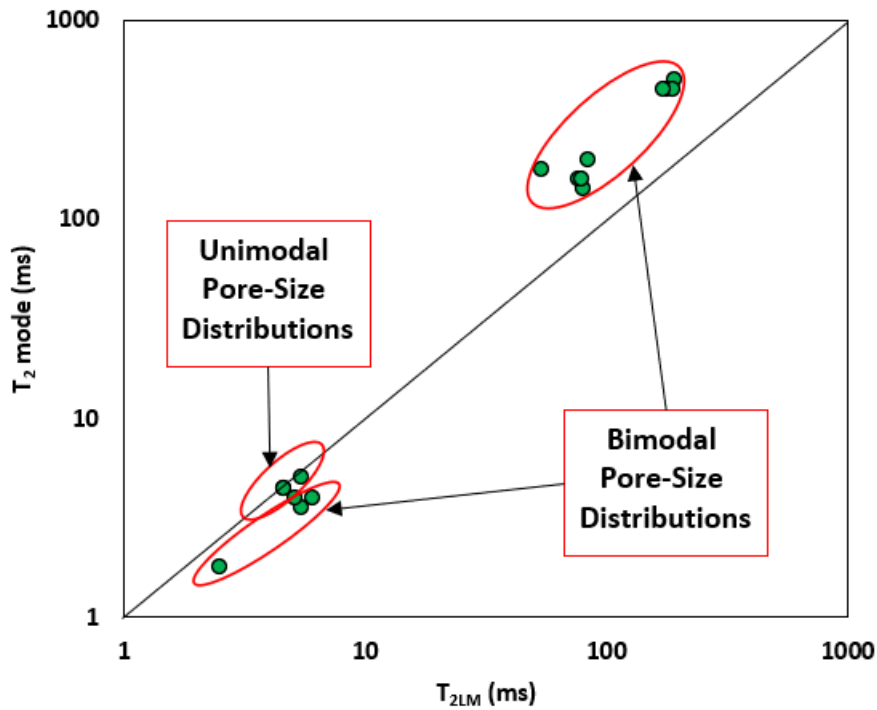


Figure 36. Relationship between T_{2LM} and modal $T_{2,Peak}$ of all core plugs from the Upper Coastal Plains aquifers.

Upper Coastal Plains: Irreducible water saturation from NMR measurements

Irreducible water saturation is estimated from NMR measurements using variable T_2 cutoff values (as a function of T_{2LM}) given by **Equation E-1** in **Appendix E**. **Figure 37** compares the estimated irreducible water saturation using variable T_2 cutoff values, $S_{wr,Xms}$, and a fixed T_2 cutoff equal to 33 ms (typical value of T_2 cutoff used in the literature for sandstones), $S_{wr,33ms}$. Note that these values of irreducible water saturation are mere approximations using NMR measurements; accurate assessment of irreducible water saturation would require additional laboratory measurements involving a centrifuge. **Figure 38** shows the relationship between T_{2LM} and irreducible water saturation, $S_{wr,Xms}$.

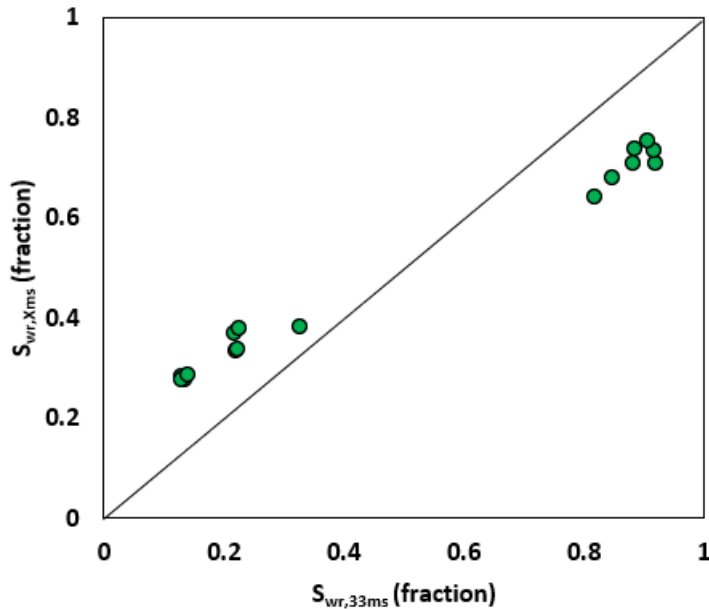


Figure 37. Relationship between irreducible water saturation from NMR measurements using a T_2 cutoff of 33 ms, $S_{wr,33ms}$, and variable T_2 cutoff values, $S_{wr,Xms}$, according to Equation E-1 in Appendix E.

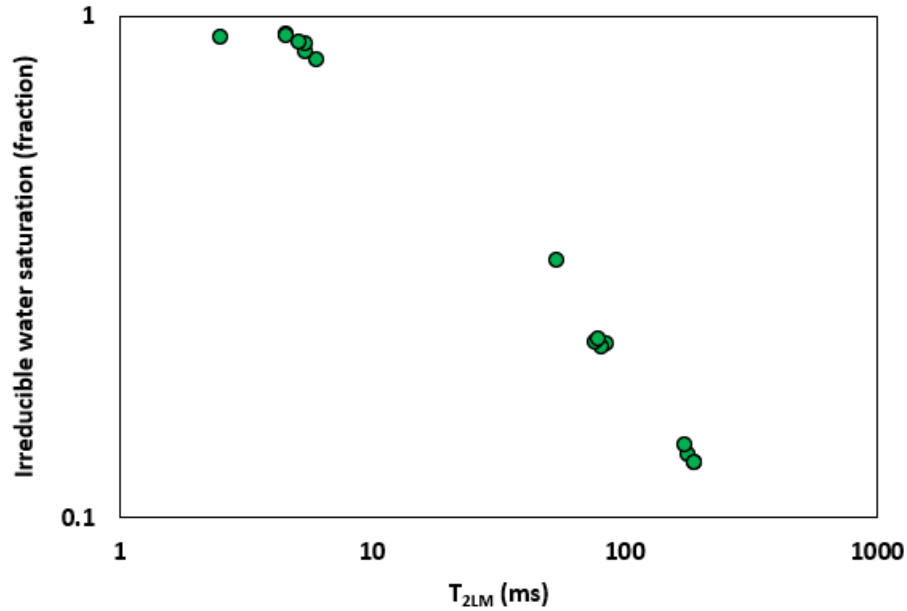


Figure 38. Relationship between T_{2LM} and irreducible water saturation on a log-log scale for all core plugs from the Upper Coastal Plains aquifers.

Upper Coastal Plains: Relationship between porosity and irreducible water saturation

The estimation of irreducible water saturation is crucial for identifying aquifer zones with flowing water. Irreducible water saturation typically decreases with increasing porosity for a given rock type. **Figure 39** shows the relationship between porosity and irreducible water saturation (derived from NMR measurements using variable T2 cutoff values according to **Equation E-1** in **Appendix E**). For porosity smaller than 0.16, S_{wr} is given by:

$$S_{wr} = 0.73. \quad (\text{Equation 2})$$

For porosity greater than 0.16, S_{wr} is given by:

$$S_{wr} = \frac{0.0601}{\phi^{1.373}}. \quad (\text{Equation 3})$$

Thus, core analysis indicates that aquifer rocks with non-negligible movable water saturations exhibit porosity values greater than 0.16.

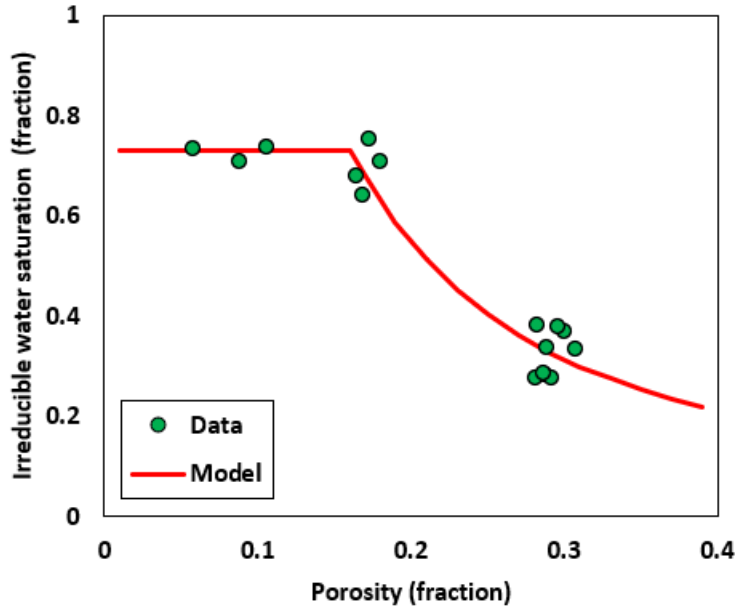


Figure 39. Relationship between porosity and irreducible water saturation in the Upper Coastal Plains aquifers. The red line is the model given by Equations 2 and 3.

Upper Coastal Plains: Permeability Models

The estimation of permeability based on NMR measurements is based on theoretical and core-calibrated models that show that permeability increases with increasing porosity and pore size. Several models are commonly used such as the Schlumberger-Doll-Research (SDR) model, Timur's model, and Timur-Coates (TC) model (Timur, 1968). These models assume that a good correlation exists between porosity, pore-body and pore-throat size, and pore connectivity. This assumption is generally valid in clastic rocks such as sandstones and shales. In carbonate rocks with complex pore structures, model-derived permeabilities may not be reliable. The permeability models include an NMR-derived pore-size parameter. In the Timur and Timur-Coates models, the pore-size parameter enters implicitly through $T_{2,cutoff}$, which determines irreducible water saturation. In the SDR model, the size parameter enters through the geometrical mean of the T_2 distribution, T_{2LM} . **Figure 40** shows the relationship between T_{2LM} and permeability. The calibrated SDR permeability model is given by:

$$k_{SDR} = 11.09\phi^{3.864}T_{2LM}^{1.446}. \quad (\text{Equation 4})$$

Figure 41 compares measured and SDR-based permeability.

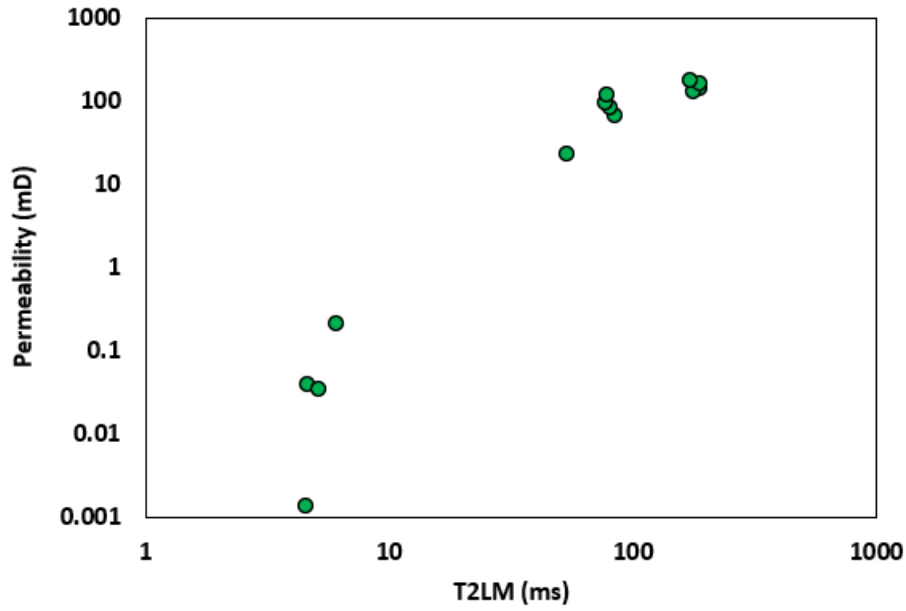


Figure 40. Relationship between T_{2LM} and permeability of all core plugs from the Upper Coastal Plains aquifers.

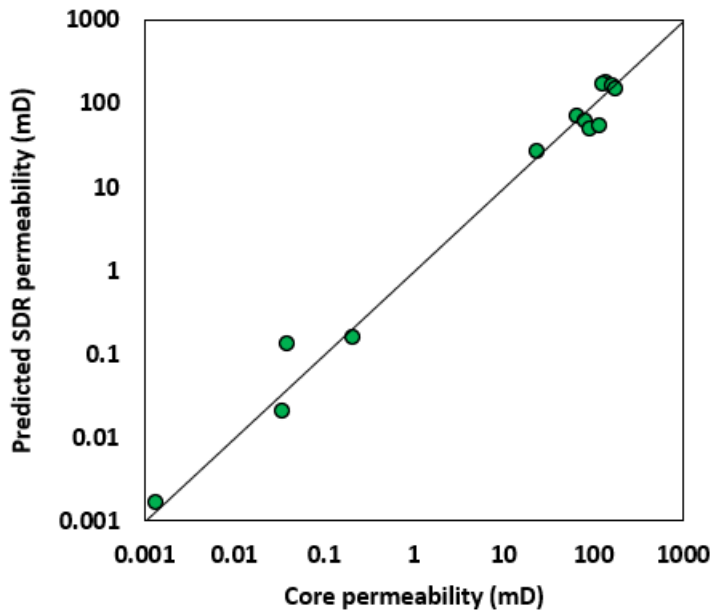


Figure 41. Comparison of measured core permeability and SDR-based estimated permeability given by Equation 4.

Figure 42 shows the relationship between S_{wr} and permeability. The calibrated Timur permeability model is given by:

$$k_T = 282.2 \frac{\phi^{4.767}}{S_{wr}^{4.29}}. \quad (\text{Equation 5})$$

Note that the fractured/damaged core plug #5 was not included in the calibration procedure. **Figure 43** compares measured and Timur-based permeability.

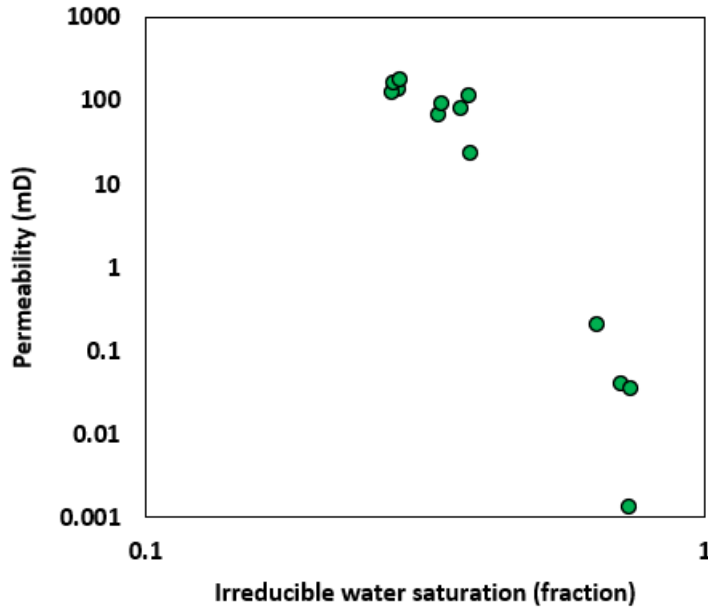


Figure 42. Relationship between irreducible water saturation and permeability on a log-log scale of all core plugs from the Upper Coastal Plains aquifers.

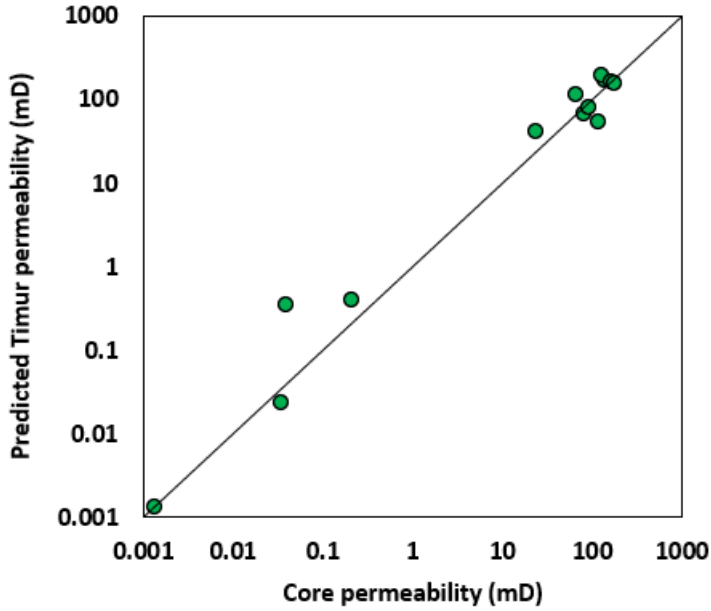


Figure 43. Comparison of measured core permeability and estimated Timur permeability given by Equation 5.

The calibrated Timur-Coates (TC) permeability model is given by:

$$k_{TC} = 578\phi^{3.411} \left(\frac{1-S_{wr}}{S_{wr}} \right)^{3.2} \quad \text{(Equation 6)}$$

Figure 44 compares measured and predicted permeabilities based on the calibrated Timur-Coates model. Note that the fractured/damaged core plug #5 was not included in the calibration. Among the three permeability models tested, the Timur-Coates model exhibits the lowest prediction error.

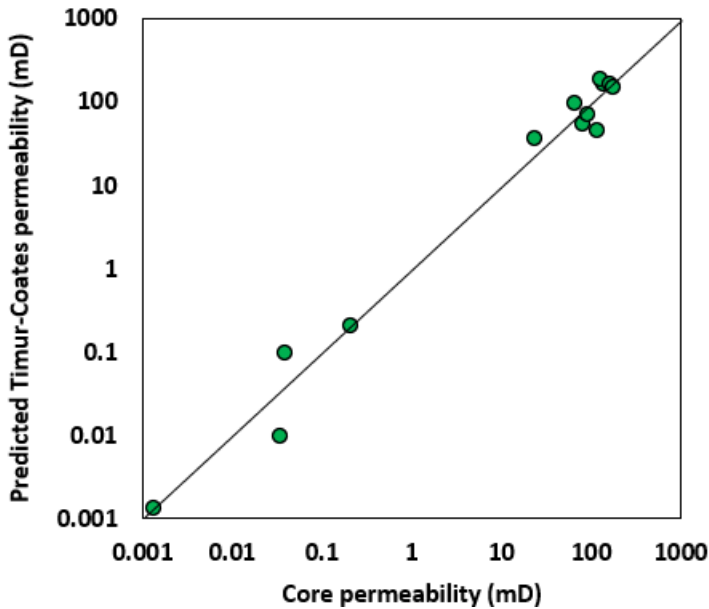


Figure 44. Comparison of measured core permeability and estimated Timur-Coates permeability given by Equation 6.

In the context of well log analysis, permeability estimation is challenging because irreducible water saturation estimates are not readily available from triple-combo logs. By combining **Equations 2, 3 and 6**, permeability can be estimated using porosity only. For porosity smaller than 0.16, permeability is given by:

$$k = 597\phi^{3.411} \left(\frac{1-0.73}{0.73} \right)^{3.2} \quad (\text{Equation 7})$$

For porosity greater than 0.16, permeability is given by:

$$k = 597\phi^{3.411} \left(\frac{1 - \frac{0.0065}{\phi^{2.722}}}{\frac{0.0065}{\phi^{2.722}}} \right)^{3.2} \quad (\text{Equation 8})$$

Figure 45 shows the porosity and permeability data along the model given by **Equations 7 and 8**.

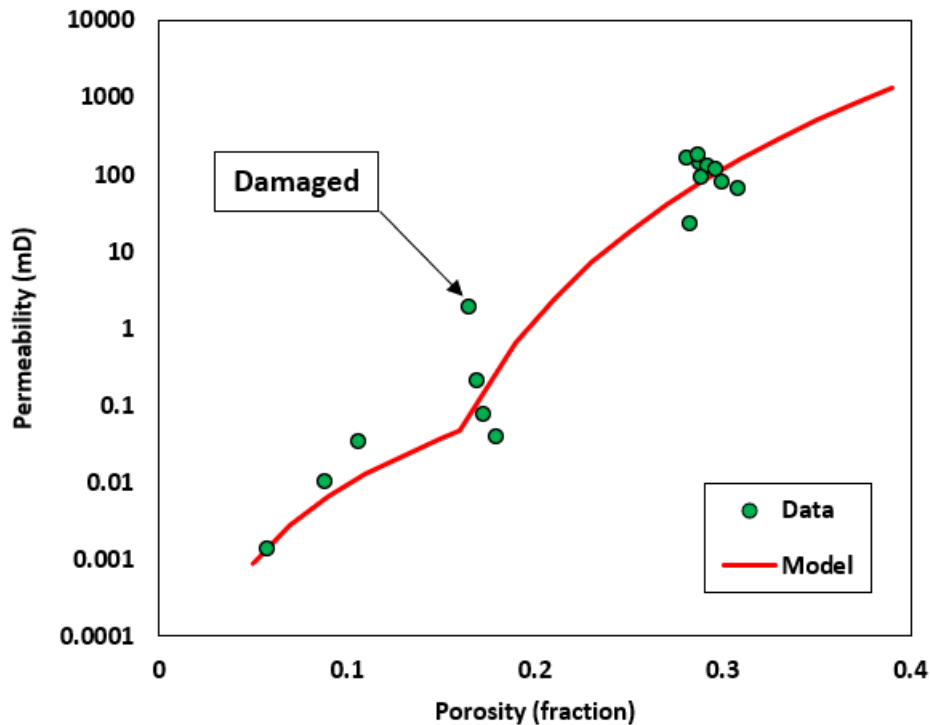


Figure 45. Relationship between porosity and permeability in the Upper Coastal Plains. The red curve is given by Equations 7 and 8.

Upper Coastal Plains: Effect of fractures on petrophysical properties

Core plugs #5 and #6 represent laminated shaly sandstones obtained from the same core at the same depth. Image analysis indicated that volumetric concentration of shale is around 50% where dark- and light-colored layers are associated to shale and sandstones, respectively. During sampling, core #6 was accidentally fractured where the fracture plane is parallel to bedding. **Figure 46** shows photographs of cores #5 and #6 where the arrow points towards the location of the fracture parallel to bedding plane. All

laboratory measurements were acquired on core #6 and compared to core #5 to evaluate the effects of induced fractures on the petrophysical properties of interest. **Table 3** compares the petrophysical properties of cores #5 and #6. While the two core plugs exhibit comparable porosity values (0.163 and 0.159), the presence of a fracture on core #6 yields larger permeability (a difference of one order of magnitude).

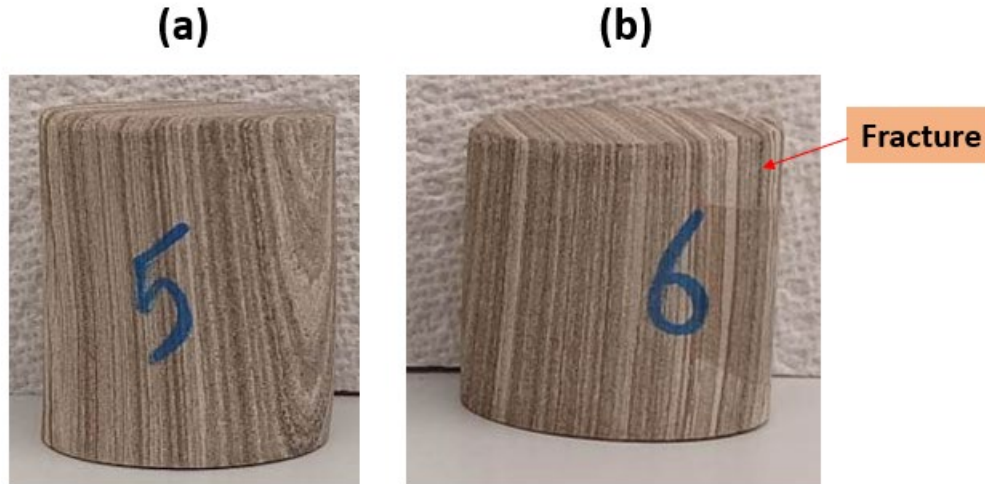


Figure 46. Photos of (a) core plug #5 and (b) fractured core plug #6. The fracture plane is parallel to bedding. The two pieces of core #6 were held together with transparent tape.

Table 3. Summary of petrophysical properties of core plugs #5 (intact) and #6 (fractured/damaged).

Plug #	Fractured ?	Φ (fraction)	k (mD)	F (-)	Archie's m	T_{2LM} (ms)	S_{wr} (fraction)
5	no	0.163	0.209	31.7	1.90	6.06	0.818
6	yes	0.159	1.90	25.4	1.76	5.41	0.847

Upper Coastal Plains: Data from TWDB Report 157 V3 (1976)

Figure 47 shows the relationship between porosity and permeability derived from the TWDB Report 157 v3 (1976). Samples from the Yegua, Carrizo, and Queen City formation are represented by blue, yellow, and green markers, respectively. The dashed red line corresponds to the best-fit line using a power law. **Figure 48** compares laboratory measurements from the TWDB Report 157 v3 (1976) and this study (red diamonds). The red curve corresponds to the permeability models given by **Equations 7 and 8**. For a given porosity, permeability measurements in this study are one order of magnitude smaller than values reported in the literature. In fact, we measured water permeability in this study, whereas previous studies measured air permeability. This explains the observed differences between the measurements.

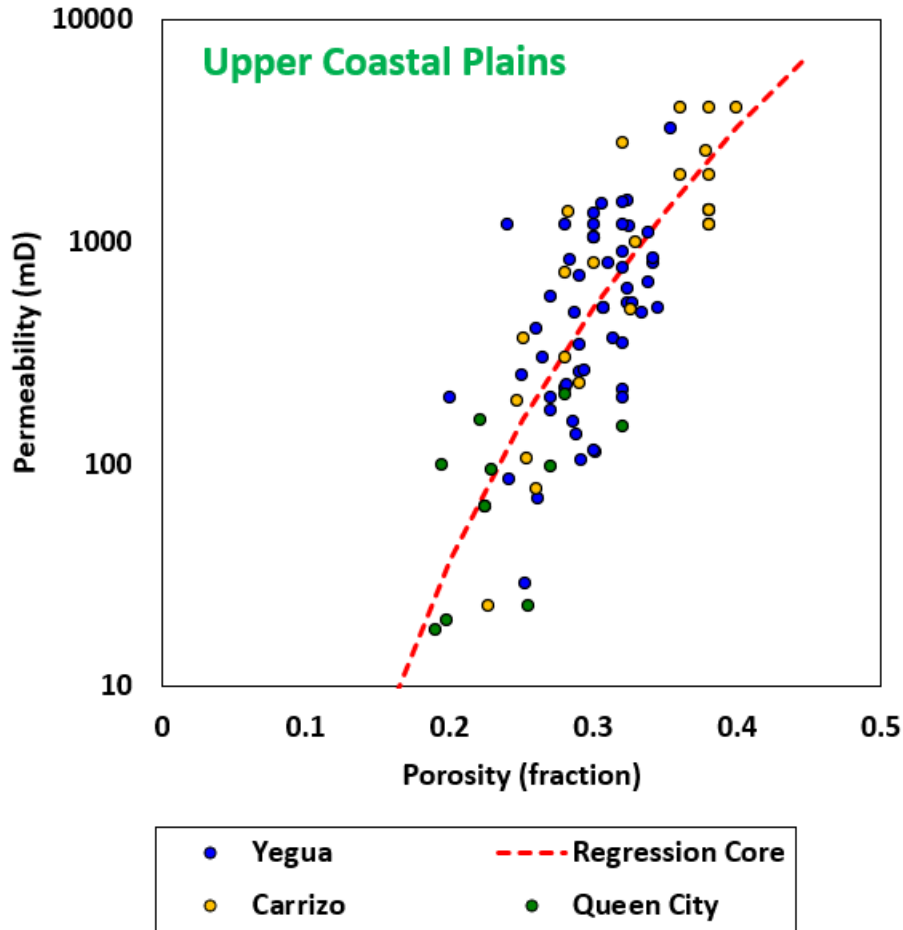


Figure 47. Relationship between porosity and permeability of core samples from the Upper Coastal Plains aquifers (Yegua, Carrizo, and Queen City). Data was obtained from the TWDB Report 157 V3 (1976). The dashed red line corresponds to the best-fit line using a power law.

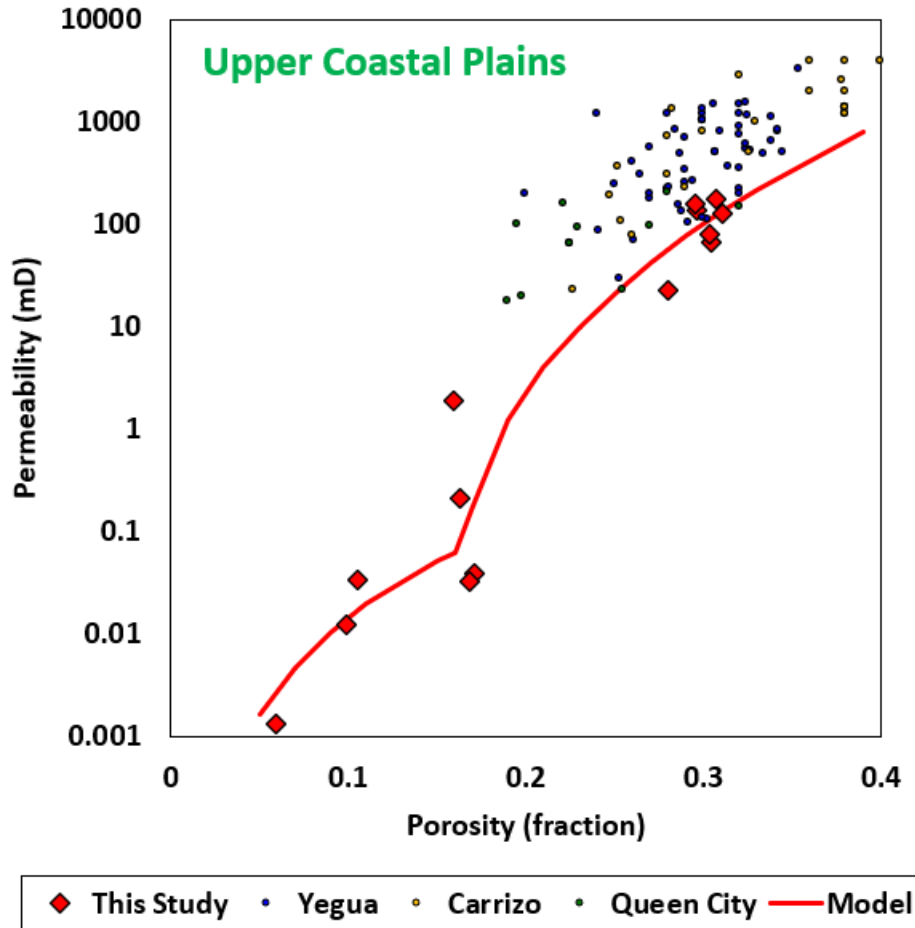


Figure 48. Comparison of core data obtained from the TWDB Report 157 V3 (1976) and this study (red diamonds). The red curve corresponds to the permeability models given by Equations 7 and 8. For a given porosity, permeability measurements in this study are one order of magnitude smaller than values reported in the literature. In fact, we measured water permeability in this study, whereas previous studies measured air permeability. This explains the observed differences between the measurements.

5.4 Results of Core Analysis in the Hickory Aquifer at the Llano Uplift

This section contains the results and observations for permeability, NMR, porosity, and electrical measurements performed on core plugs acquired from the Hickory aquifer at the Llano Uplift.

Hickory: Rock sampling

Rock samples from the Hickory formation were obtained from three wells. A total of 12 core plugs representing different facies were cut. Core #16 – C0086 is a shallow well in which laminated sandstones with variable grain sizes exhibit a yellowish color. Core #15 – C0087 is a shallow well in which laminated sandstones with variable grain sizes exhibit a reddish color (most likely due to the presence of hematite). Core #14 – C0115 is a deep well in which the Hickory formation is composed of grey siltstones with ripples.

Hickory: Summary of measurements

Table 4 summarizes core measurement results.

Table 4. Summary of laboratory measurements in the Hickory formation. (*) estimated properties. Accession #: BEG well identification number. Core #: study core identification number. k : permeability. T_{2LM} : NMR T_2 logarithmic mean. $T_{2,Peak}$: NMR T_2 value at the peak. $S_{wr,Xms}$: estimated irreducible water saturation from NMR measurements. Archie's m : porosity exponent.

Plug #	Depth (ft)	Core #	Accession #	ϕ (fraction)	Grain Density (g)	k (mD)	T_{2LM} (ms)	$T_{2,Peak}$ (ms)	$S_{wr,Xms}$ (fraction)	Archie's m
21	260	15	C0087	0.171	2.65	568.2	124.1	177.8	0.327	1.94
22	109	15	C0087	0.219	2.67	289.9	47.57	158.5	0.389	1.69
23	109	15	C0087	0.226	2.64	1820*	136.1	251.2	0.258	1.66
24	3,314	14	C0115	0.064	2.64	0.229	N/A	N/A	N/A	N/A
25	3,314	14	C0115	0.057	2.64	0.017	3.18	3.55	0.952	1.66
26	3,320	14	C0115	0.038	2.64	0.110	N/A	N/A	N/A	N/A
27	3,320	14	C0115	0.067	2.65	5.747	N/A	N/A	N/A	N/A
28	137	16	C0086	0.214	2.67	2605*	209.2	354.8	0.214	1.87
29	137	16	C0086	0.228	2.66	1347*	113.1	199.5	0.295	1.73
30	144	16	C0086	0.185	2.66	1075*	201.4	446.7	0.256	1.76
31	260	15	C0087	0.194	2.66	N/A	N/A	N/A	N/A	1.77
32	260	15	C0087	0.195	2.65	N/A	N/A	N/A	N/A	1.85

Hickory: Rock classes and facies

Table 5 summarizes rock properties per rock class and facies in the Hickory aquifer.

Table 5. Average petrophysical properties per rock classes in the Hickory aquifer.

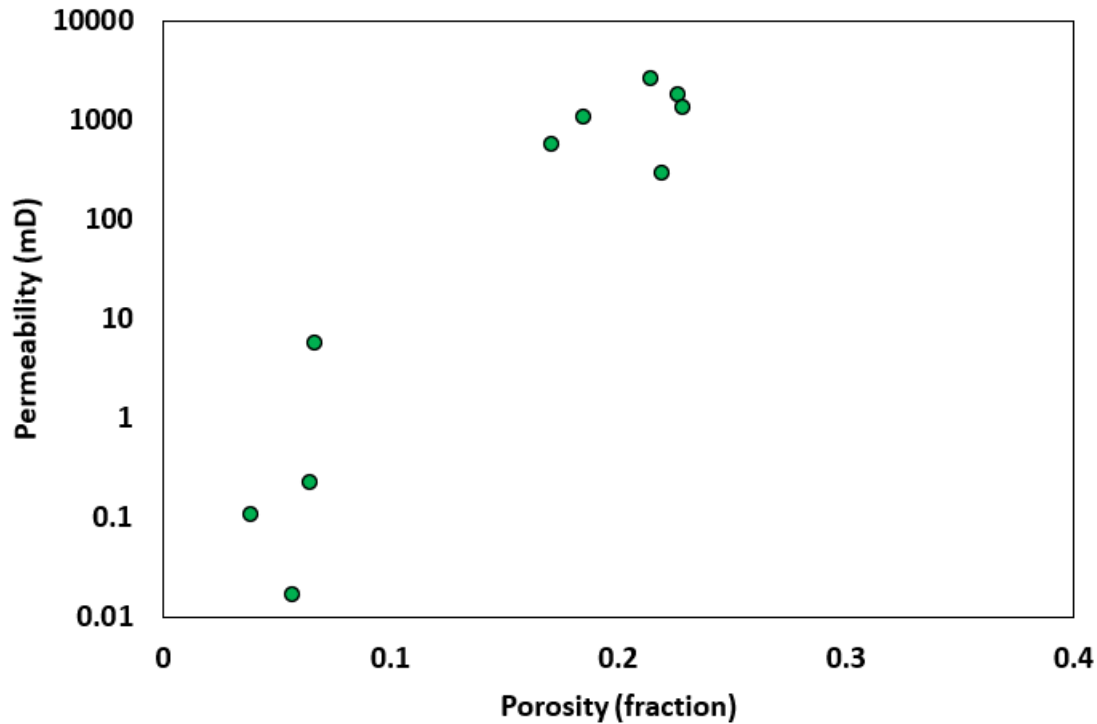
Rock Class	Facies	Core plugs	ϕ (fraction)	k (mD)	Grain Density (g/cc)	Archie's m	T_{2LM} (ms)
I	Coarse-grained sandstones	28 – 30 – 31 32	0.197	1,674	2.66	1.81	205
II	Medium-grained sandstones	21 – 23 – 29	0.208	1,245	2.65	1.78	156
III	Laminated sandstones with fine and medium-sized grains	22	0.219	1117	2.67	1.69	48
IV	Grey siltstones with ripples	24 – 25 – 26 – 27	0.057	0.22	2.64	1.66	3

Hickory: Grain density measurements

Grain density in the Hickory aquifer ranges from 2.64 to 2.67 g/cm with an average of 2.65 g/cc, which is the typical value of quartz.

Hickory: Relationship between porosity and permeability

Figure 49 shows the relationship between porosity and permeability in the Hickory aquifer. The porosity and permeability of the best quality rocks (coarse-grained sandstones) is equal to 0.2 and 1,700 mD, respectively.

**Figure 49. Relationship between porosity and permeability of core plugs from the Hickory aquifers.**

Hickory: NMR T_2 distributions and rock classes

Rocks from different classes exhibit distinct NMR signatures. **Figure 50** shows T_2 distributions of all core samples from the Hickory aquifers. **Figure 51 to 54** shows T_2 distributions of core samples belonging to the same rock class.

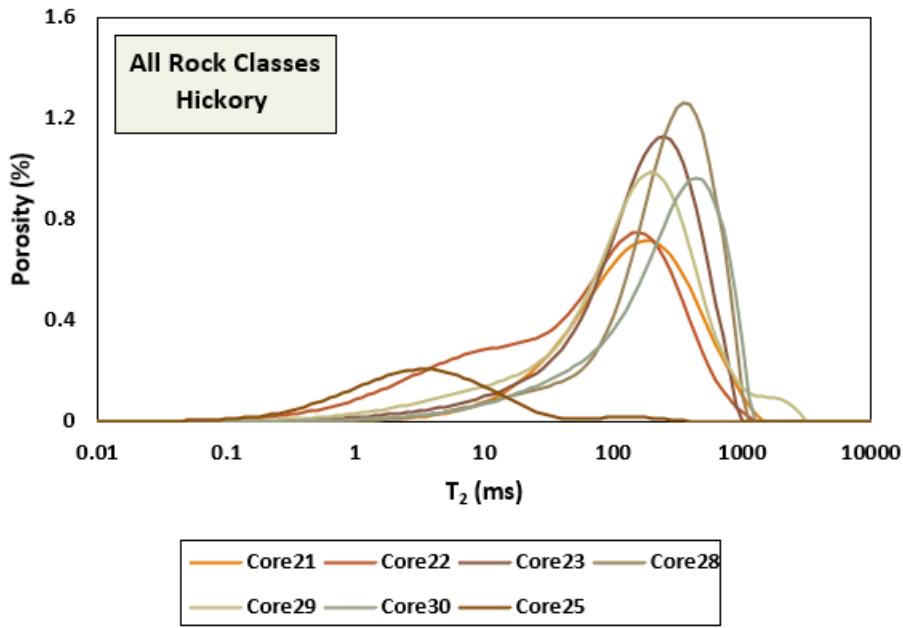


Figure 50. NMR T_2 distributions of all core plugs from the Hickory aquifer.

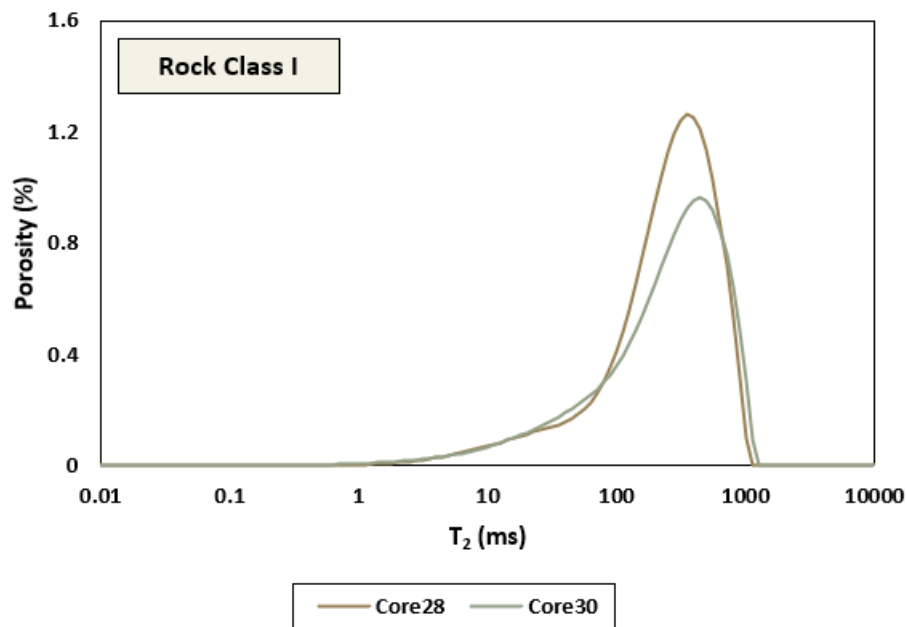


Figure 51. NMR T_2 distributions of coarse-grained sandstones (class I) from the Hickory aquifer.

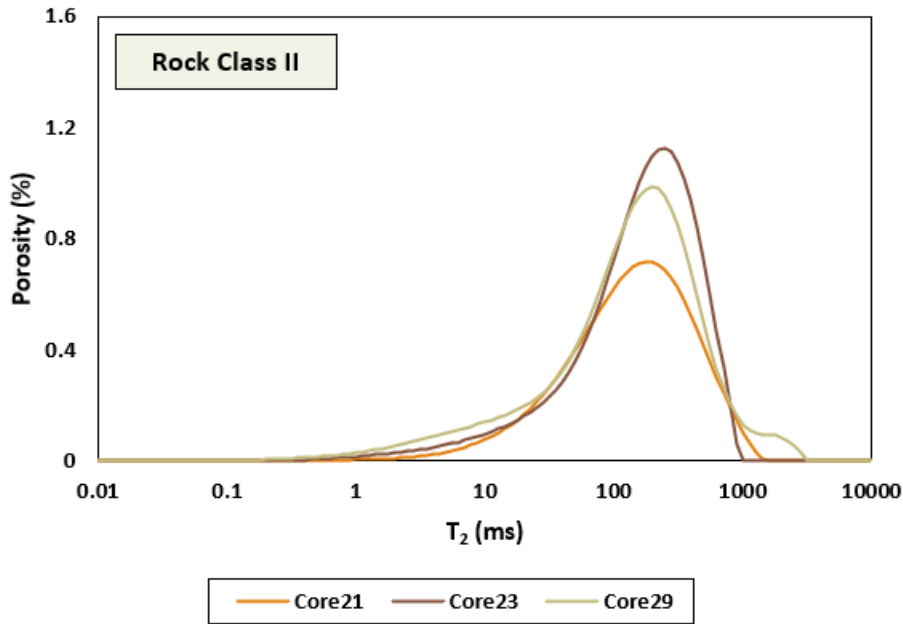


Figure 52. NMR T₂ distributions of medium sandstones (class II) from the Hickory aquifer.

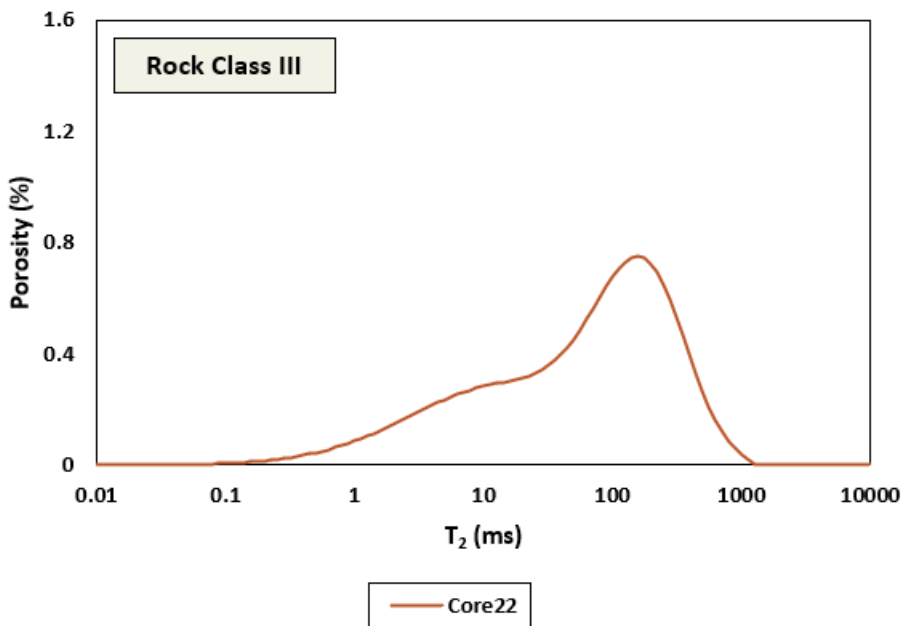


Figure 53. NMR T₂ distributions of laminated medium and fine-grained sandstones (class III) from the Hickory aquifer.

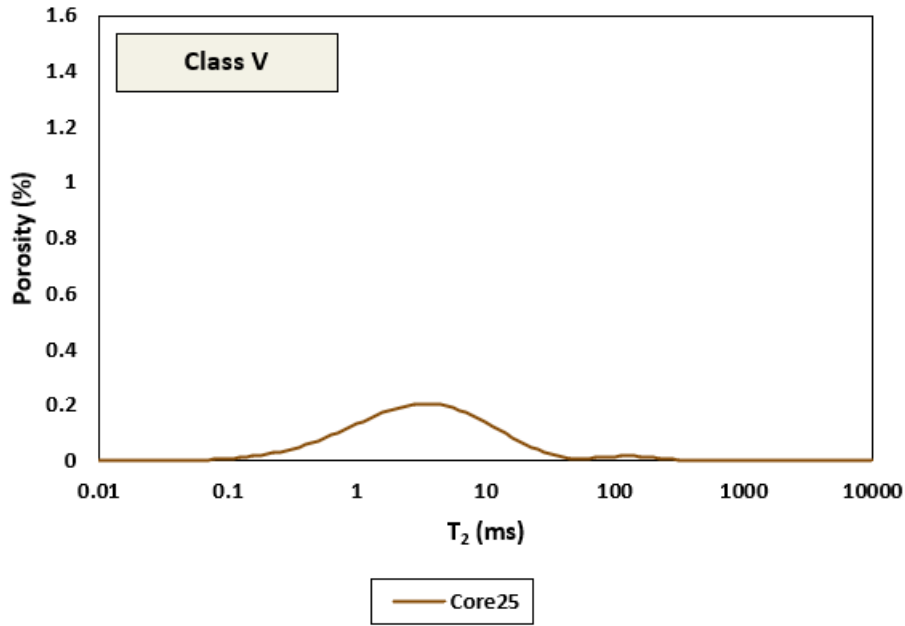


Figure 54. NMR T₂ distributions of grey siltstones (class IV) from the Hickory aquifer.

Hickory: Electrical properties

Figure 55 shows the relationship between formation factor and porosity. The average porosity exponent of all rock samples is equal to 1.77.

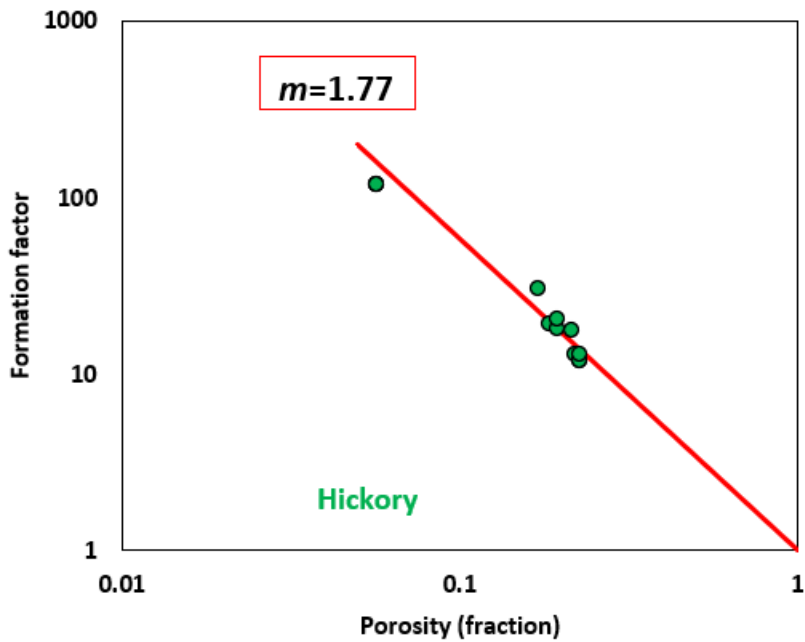


Figure 55. Relationship between formation factor and porosity of all core plugs from the Hickory aquifer. The red line corresponds to a porosity exponent equal to 1.77.

Hickory: Relationship between T_{2LM} and $T_{2,Peak}$

A non-negligible difference between T_{2LM} and $T_{2,Peak}$ (corresponding to the highest peak in the T_2 distribution) indicates the presence of a multimodal pore-size distribution. **Figure 56** shows the T_2 distribution of core #22 along with the corresponding T_{2LM} and $T_{2,Peak}$. **Figure 57** shows the relationship between T_{2LM} and modal $T_{2,Peak}$ for all core samples from the Hickory aquifer. In high-porosity and high-permeability rock samples, $T_{2,Peak}$ is greater than T_{2LM} , whereas in tight rocks, modal T_2 is smaller than T_{2LM} . The difference between modal T_2 and T_{2LM} is due to the presence of bimodal pore-size distributions in most rock samples. The bimodality of pore-throat size distributions in the Hickory aquifer is the result of intercalated sandstone layers of different grain sizes.

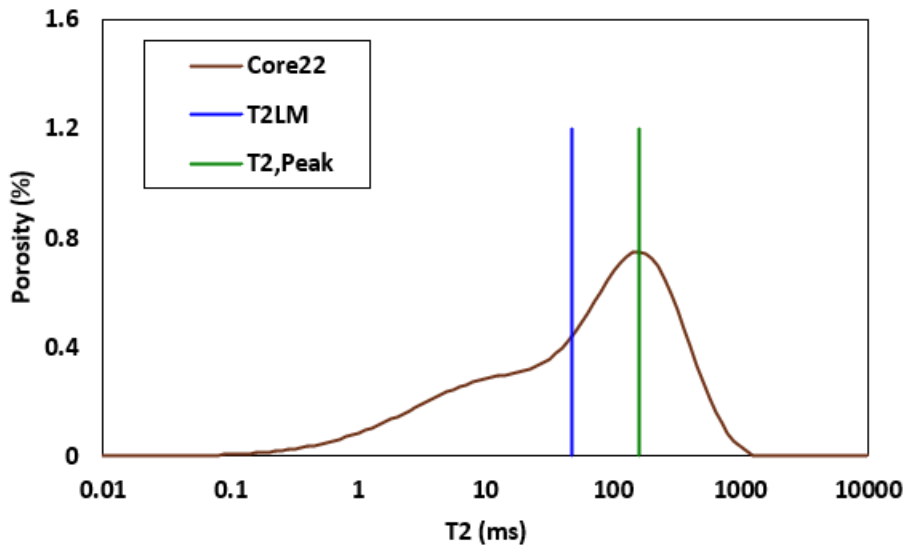


Figure 56. NMR T_2 distribution of core #22 along with the corresponding T_{2LM} (blue line) and $T_{2,Peak}$ (green line).

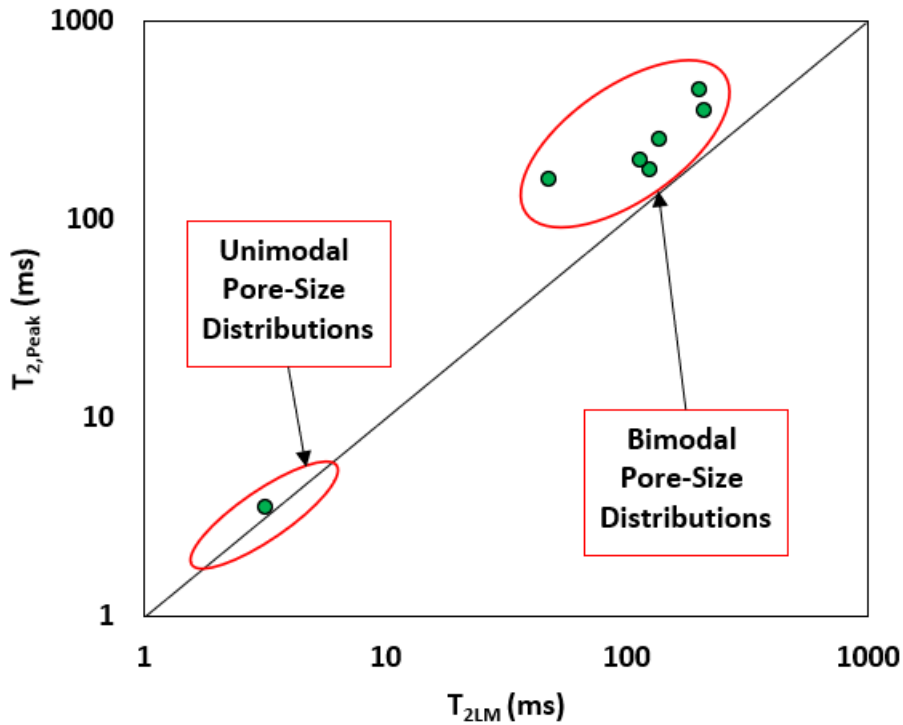


Figure 57. Relationship between T_{2LM} and modal $T_{2,Peak}$ of all core plugs from the Hickory aquifer.

Hickory: Irreducible water saturation from NMR measurements

Irreducible water saturation is estimated from NMR measurements using variable T_2 cutoff values (as a function of T_{2LM}) given by **Equation E-1** in **Appendix E**. **Figure 55** compares the estimated irreducible water saturation using variable T_2 cutoff values, $S_{wr,Xms}$, and a fixed T_2 cutoff equal to 33 ms (typical value of T_2 cutoff used in the literature for sandstones), $S_{wr,33ms}$. Note that these values of irreducible water saturation are mere approximations using NMR measurements; accurate assessment of irreducible water saturation would require additional laboratory measurements involving a centrifuge.

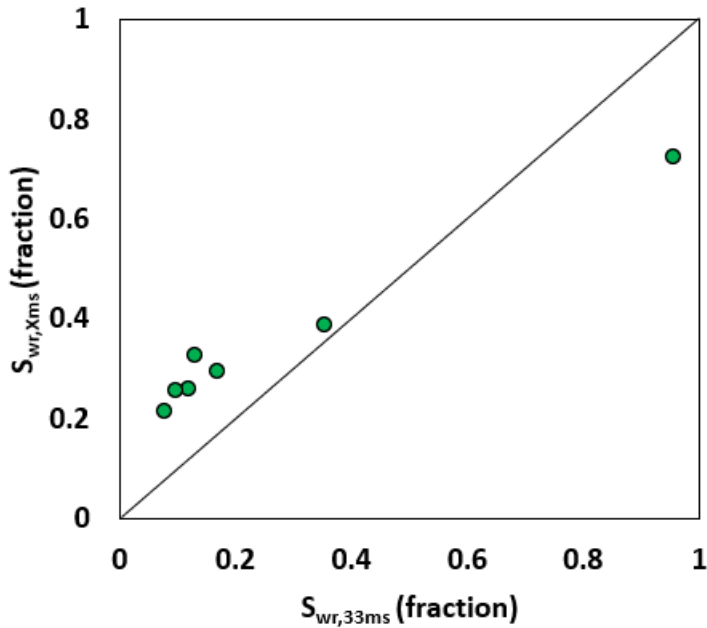


Figure 58. Relationship between irreducible water saturation from NMR measurements in the Hickory aquifer using a T_2 cutoff of 33 ms, $S_{wr,33ms}$, and variable T_2 cutoff values, $S_{wr,Xms}$, according to Equation E-1 in Appendix E.

Hickory: Relationship between porosity and irreducible water saturation

Figure 59 shows the relationship between porosity and irreducible water saturation (derived from NMR measurements using variable T_2 cutoff values according to **Equation E-1 in Appendix E**) in the Hickory formation. For porosity greater than 0.04, irreducible water saturation, S_{wr} , is given by:

$$S_{wr} = \frac{0.0945}{\phi^{0.701}} \quad (\text{Equation 9})$$

Accordingly, the irreducible water saturation is equal to 0.3 for high-porosity rocks. Irreducible water saturation is equal to 1 when porosity is smaller than 0.04. Note that these values of irreducible water saturation are mere approximations using NMR measurements; accurate assessment of irreducible water saturation would require additional laboratory measurements involving a centrifuge.

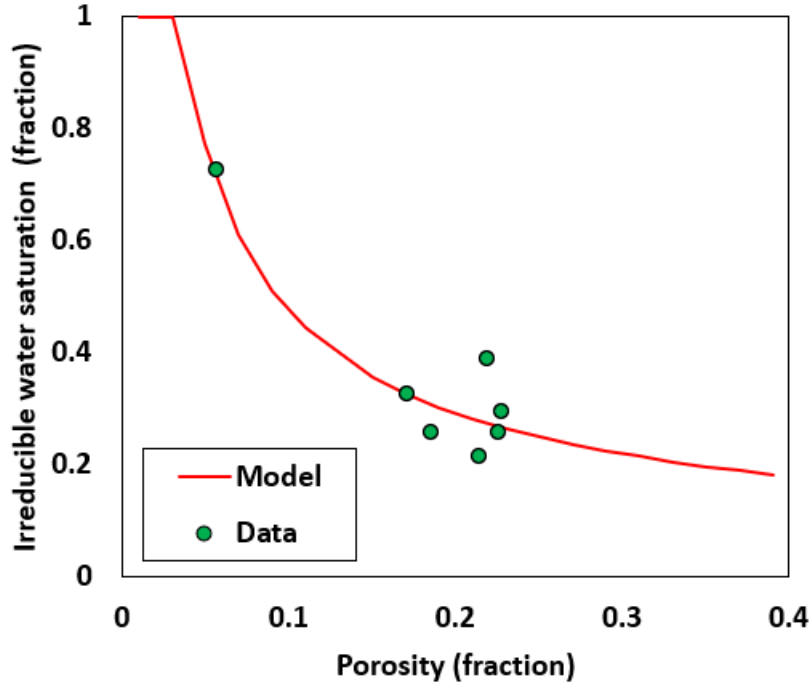


Figure 59. Relationship between porosity and irreducible water saturation (derived from NMR measurements using variable T_2 cutoff values according to Equation E-1 in Appendix E) in the Hickory formation. The red curve is given by Equation 9.

Hickory: Permeability Models

The calibrated SDR permeability model in the Hickory aquifer is given by:

$$k_{SDR} = 50\phi^4 T_{2LM}^2. \quad (\text{Equation 10})$$

The calibrated Timur permeability model in the Hickory aquifer is given by:

$$k_T = 35,000 \frac{\phi^4}{S_{wr}^2}. \quad (\text{Equation 11})$$

The calibrated Timur-Coates (TC) permeability model in the Hickory aquifer is given by:

$$k_{TC} = 23,000\phi^4 \left(\frac{1-S_{wr}}{S_{wr}} \right)^2 \quad (\text{Equation 12})$$

In the context of well log analysis, permeability estimation is challenging because irreducible water saturation estimates are not readily available from triple-combo logs. By combining **Equations 9** and **12**, permeability can be estimated using porosity only. For porosity greater than 0.04, permeability is given by:

$$k = 23,000\phi^4 \left(\frac{1 - \frac{0.0945}{\phi^{0.701}}}{\frac{0.0945}{\phi^{0.701}}} \right)^2 \quad (\text{Equation 13})$$

Figure 60 shows the porosity and permeability data along the model given by **Equation 13**.

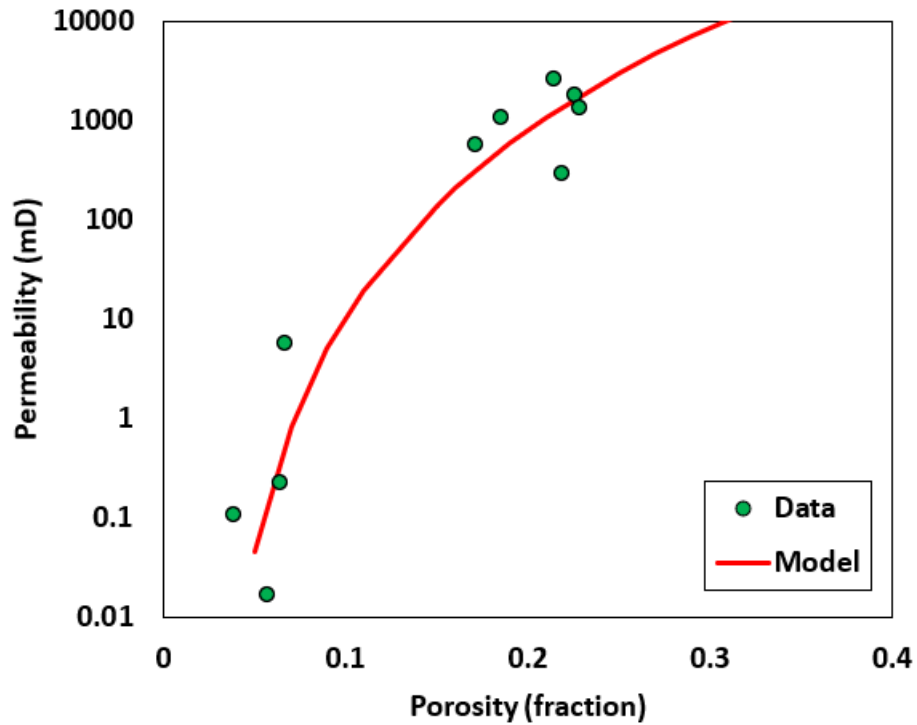


Figure 60. Relationship between porosity and permeability in the Hickory formation. The red curve is given by Equation 13.

Hickory: Effect of induced fractures on petrophysical properties

None of the core plugs were fractured (damaged) during core cutting. Thus, studying of the effects of fractures on permeability in the Hickory aquifers was not possible.

Hickory: Data from TWDB Report 157 V3 (1976)

No laboratory data (porosity and permeability) regarding the Hickory aquifer were found in the literature. Thus, we were not able to compare the results of our measurements to other studies.

5.5 Results of Core Analysis in the Ellenburger and San Saba aquifers at the Llano Uplift

This section contains the results and observations for permeability, NMR, porosity, and electrical measurements performed on core plugs acquired from the Ellenburger and San Saba aquifers at the Llano Uplift.

Ellenburger and San Saba: Rock sampling

Rock samples from the Ellenburger and San Saba formations were obtained from two wells. A total of 16 core plugs representing different facies were cut within the 3,059-6,301 ft depth range. Core #10 – C00421 and Core #8 – C01694 represent the Ellenburger and San Saba formations respectively. Depth intervals that exhibited green chert (SiO₂) were not sampled.

Ellenburger and San Saba: Summary of measurements

Table 6 summarizes core measurement results in the Ellenburger and San Saba aquifers.

Table 6 Summary of laboratory measurements in the Ellenburger and San Saba formations.

Plug #	Depth (ft)	Core #	Accession #	ϕ (fraction)	Grain Density (g)	k (mD)	T _{2LM} (ms)	T _{2,Peak} (ms)	$S_{wr,Xms}$	m
42	3,059	12	C00421	0.039	2.78	0.002055	174.10	251	0.358	1.86
43	3,059	12	C00421	0.034	2.78	0.000342	177.26	224	0.353	1.96
44	3,150	12	C00421	0.008	2.73	0.11028	33.30	14	0.565	1.33
45	3,150	12	C00421	0.011	2.73	0.071233	19.05	13	0.585	1.39
46	3,150	12	C00421	0.008	2.74	N/A	48.10	141	0.417	1.41
47	5,340	12	C00421	0.051	2.81	3.194	209.44	891	0.346	1.9
48	5,340	12	C00421	0.056	2.84	1.75752	280.38	1259	0.336	1.96
49	5,340	12	C00421	0.033	2.82	0.005549	157.31	126	0.378	1.83
50	3,970	12	C00421	0.047	2.83	1.3589	340.28	1585	0.343	2.03
61	6,269	8	C01694	0.006	2.73	0.003241	26.45	126	0.528	1.32
62	6,269	8	C01694	0.009	2.73	0.004779	25.75	126	0.534	1.38
63	6,273	8	C01694	0.007	2.70	0.000375	20.95	100	0.484	1.29
64	6,273	8	C01694	0.007	2.71	0.0000263	15.03	112	0.654	1.29
65	6,301	8	C01694	0.021	2.73	0.000717	N/A	N/A	N/A	N/A
66	6,301	8	C01694	0.005	2.72	0.001413	40.95	141	0.410	1.35
67	6,278	8	C01694	0.009	2.72	0.089527	26.13	126	0.481	1.39

Ellenburger and San Saba: Rock Classes and Facies

Table 7 summarizes rock properties per rock class and facies in the Ellenburger and San Saba aquifers. The color of the samples ranges from white to dark grey. Some samples exhibit cemented natural fractures and calcium carbonate veins. Rock samples with medium porosity (porosity ranging from 0.05 to 0.1) exhibit vuggy porosity.

Table 7. Average petrophysical properties per rock classes in the Hickory aquifer.

Rock Class	Facies	Core plugs	ϕ (fraction)	k (mD)	Grain Density (g/cc)	Archie's m	T_{2LM} (ms)
I	Medium-porosity carbonate rocks with bimodal pore size distribution	48 – 49 – 50	0.045	0.237	2.83	1.94	247
II	Medium-porosity carbonate rocks with unimodal pore size distribution	42 – 43 – 47	0.041	0.013	2.79	1.91	186
III	Low-porosity carbonate rocks	44 – 45 – 46 – 61 – 62 – 63 – 64 – 65 – 66 – 67	0.009	0.004	2.72	1.35	26.7

Ellenburger and San Saba: Grain density measurements

The grain density of core samples ranges from 2.70 to 2.84 g/cc. Considering that the grain density of limestones is 2.71 g/cc and the grain density of dolomites is 2.85 g/cc, the dominant mineral composition of the Ellenburger and San Saba formations is a mixture of limestone and dolomite.

Ellenburger and San Saba: Relationship between porosity and permeability

Figure 61 shows the relationship between porosity and permeability. The porosity and permeability of the best quality rocks (carbonate rocks with vuggy porosity) is about 0.05 and 3 mD, respectively. Tight rocks exhibit a porosity equal to 0.01 and a permeability that varies over several orders of magnitude depending on the presence or not of natural fractures.

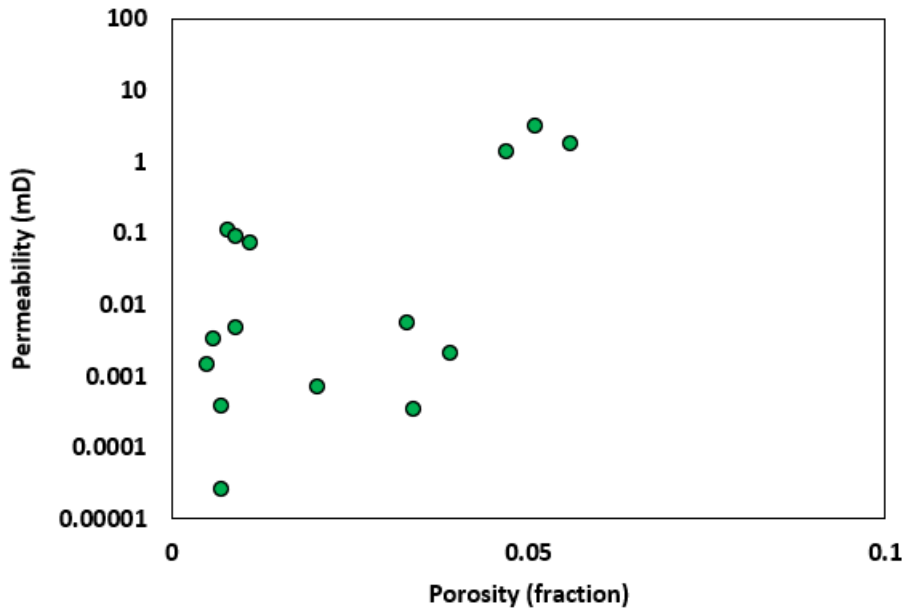


Figure 61. Relationship between porosity and permeability of core plugs from the Ellenburger and San Saba aquifers. NMR T_2 distributions of all core samples from the Ellenburger and San Saba aquifers.

Ellenburger and San Saba: NMR T_2 distributions and rock classes

Rocks from different classes exhibit distinct NMR signatures. **Figure 62** shows T_2 distributions of all core samples from the Upper Coastal aquifers. **Figure 63 to 65** show T_2 distributions of core samples belonging to the same rock class. **Figure 66** shows the relationship between porosity, T_{2LM} , and facies.

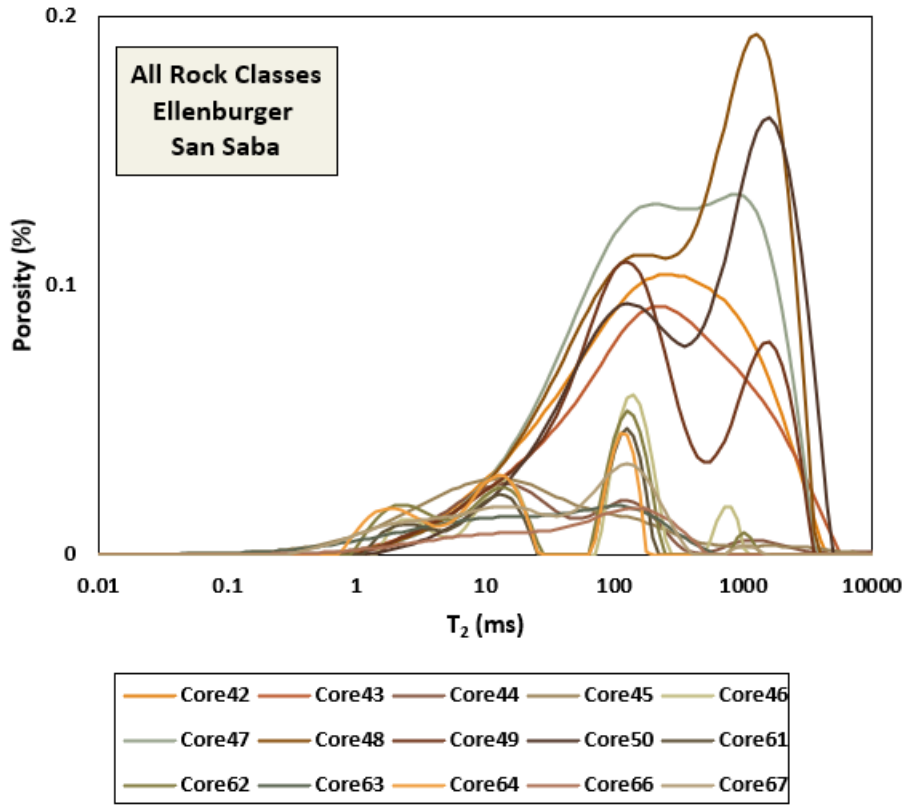


Figure 62. NMR T₂ distributions of all core samples from the Ellenburger and San Saba aquifers.

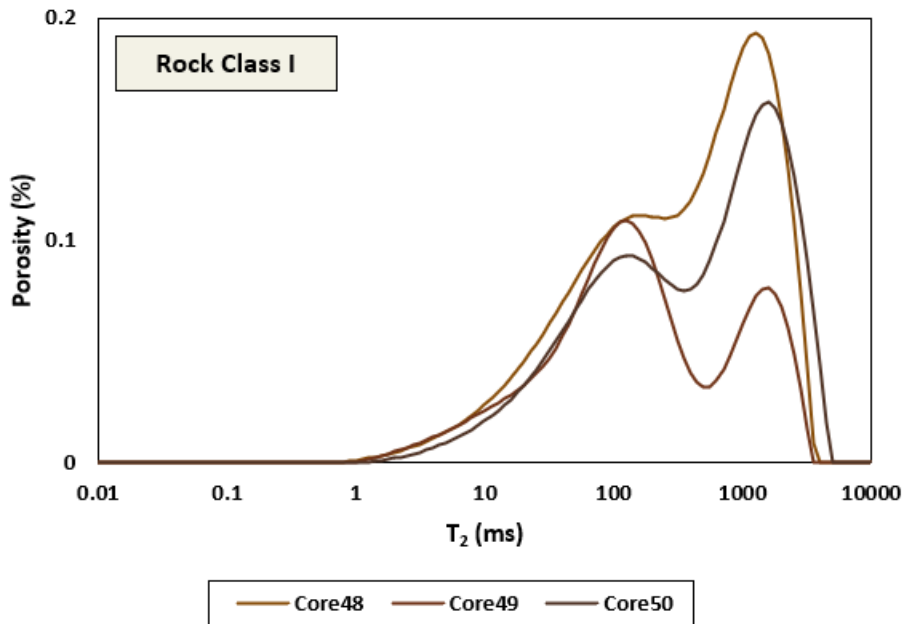


Figure 63. NMR T₂ distributions of carbonate rocks with multimodal vuggy porosity (class I) from the Ellenburger and San Saba aquifers.

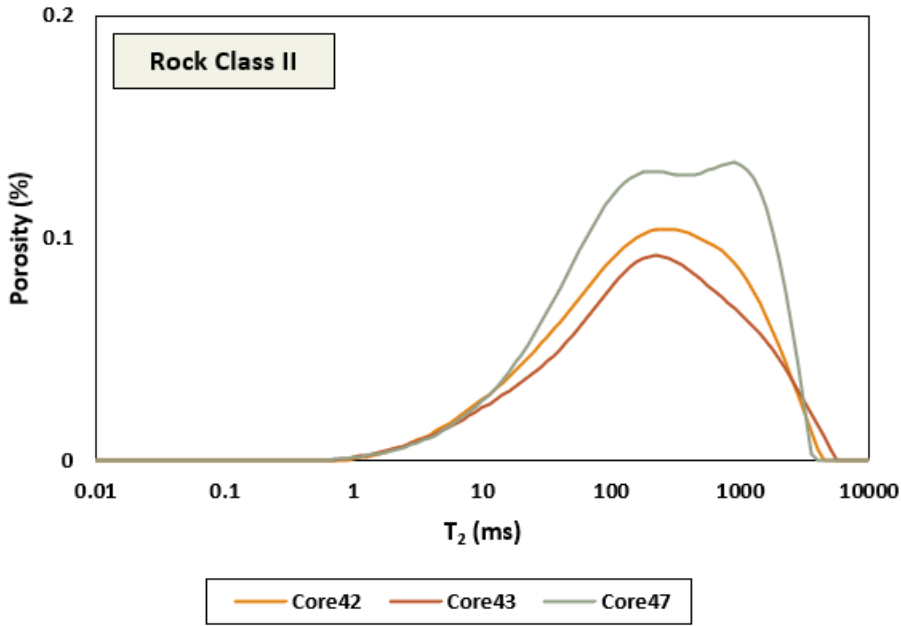


Figure 64. NMR T_2 distributions of carbonate rocks with unimodal vuggy porosity (class II) from the Ellenburger and San Saba aquifers.

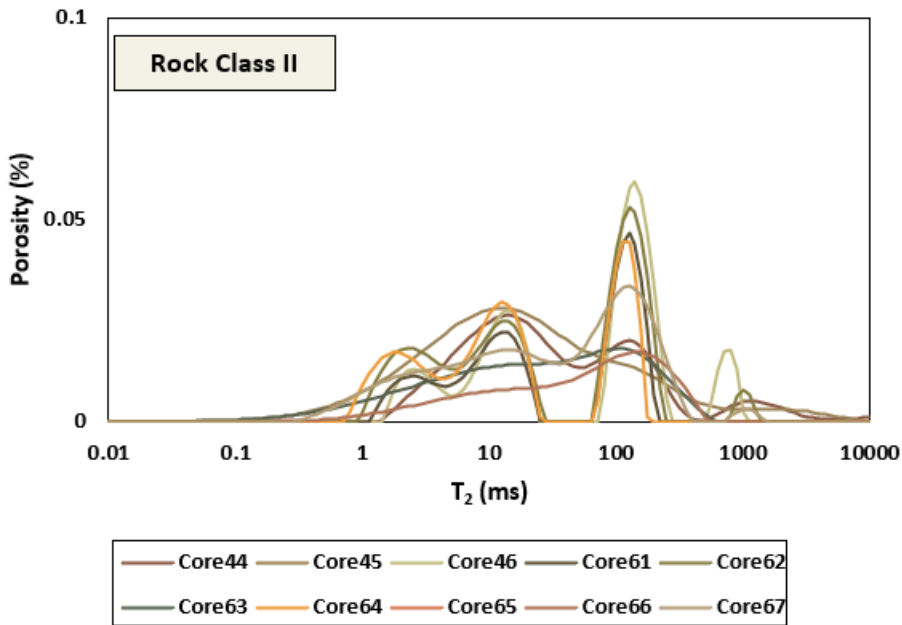


Figure 65. NMR T_2 distributions of tight carbonate rocks (class III) from the Ellenburger and San Saba aquifers.

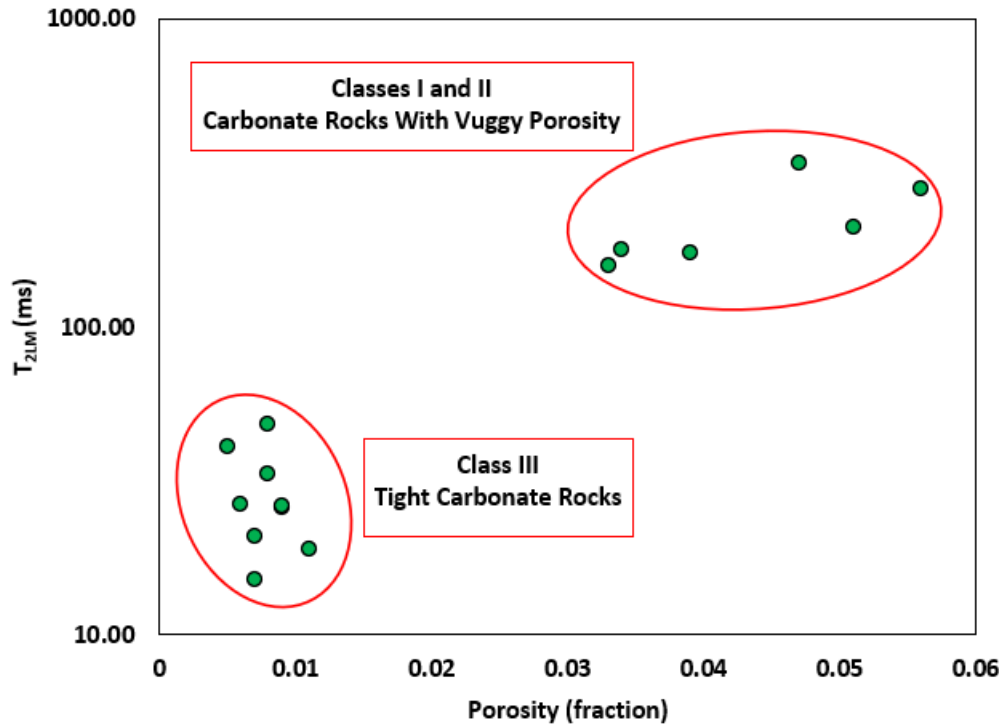


Figure 66. Relationship between porosity, T_{2LM} , and facies of all core plugs from the Ellenburger and San Saba aquifers.

Ellenburger and San Saba: Electrical properties

Figure 67 shows the relationship between formation factor and porosity. The average porosity exponent of relatively high-porosity rock samples is equal to 1.95, whereas the average porosity exponent of tight rocks is equal to 1.35. The abnormally low porosity exponent of the tight rocks indicates the presence of natural fractures or connected vugs that behave like a short circuit. This behavior was described by Serra (1989) and Aguilera (2003). For reservoirs with natural fractures or connected vugs, Serra's (1989) model is given by:

$$m = \frac{\log((\phi - \phi_2)^{m_b} + \phi_2^{m_f})}{\log(\phi)} \quad (\text{Equation 14})$$

where ϕ is total porosity, ϕ_2 is porosity of fractures or connected vugs, m_b is porosity exponent of the matrix, and m_f is porosity exponent of the fractures or connected vugs. Based on measurements acquired in this study, we used least-squares regression to estimate the parameters of Serra's (1989) model. Accordingly, ϕ_2 is equal to 0.001328, m_b is equal to 2.16, and m_f is set equal to 1. Figure 68 shows the relationship between water-filled porosity and porosity exponent where the green markers represent laboratory data whereas the blue line represents the calibrated Serra's (1989) model. We chose Serra's model in this study for its simplicity compared to Aguilera's (2003) model. For additional information, refer to **Appendix F**. Core description confirms the presence of natural fractures in the tight carbonate rocks of the Ellenburger and San Saba formations. Figure 69 shows a network of natural fractures cemented together with calcite. The colors of the matrix and calcium carbonate veins are tan and white, respectively.

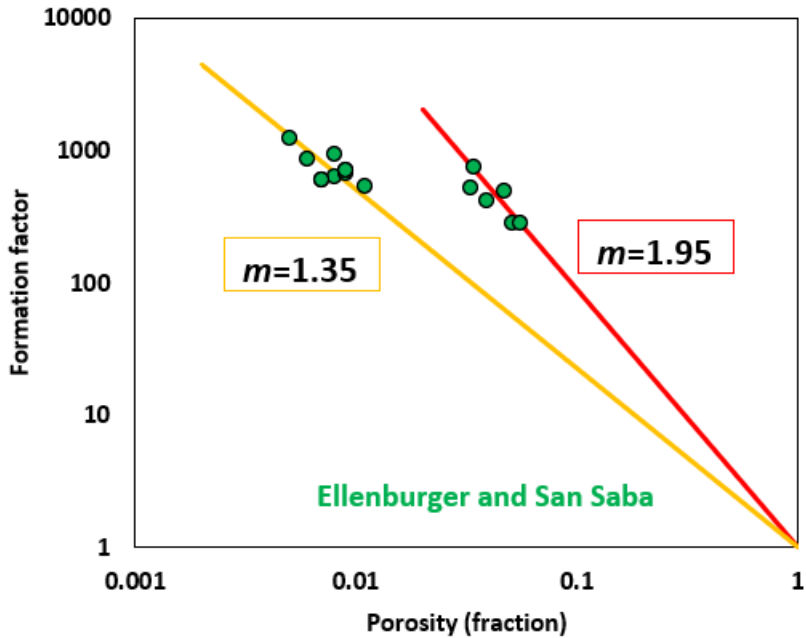


Figure 67. Relationship between formation factor and porosity of all core plugs from the Ellenburger and San Saba aquifers. The red and orange lines correspond to porosity exponents equal to 1.95 and 1.35, respectively.

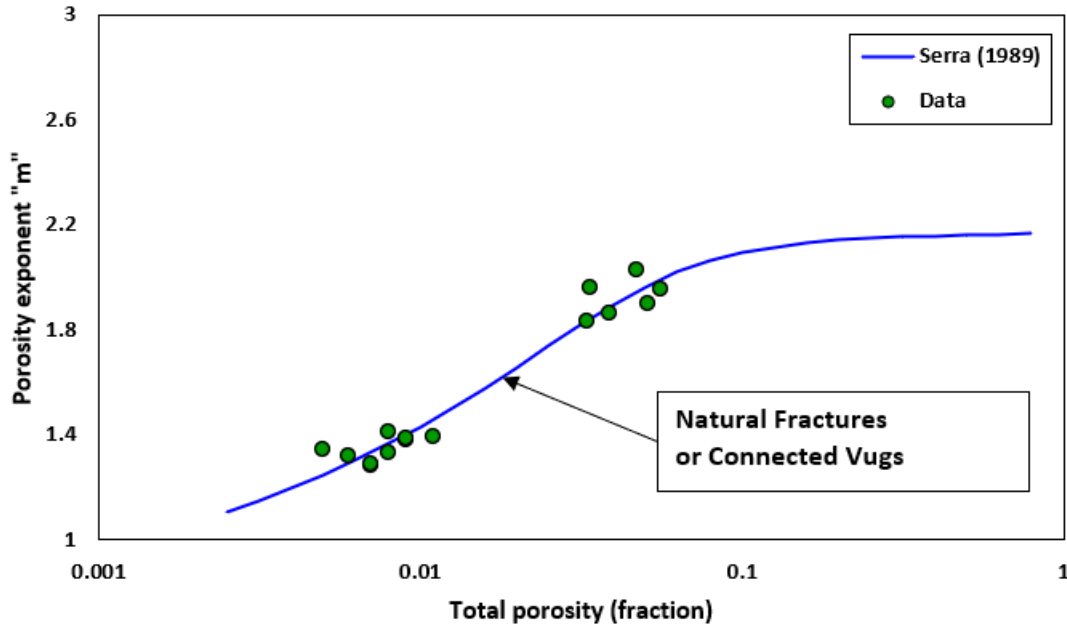


Figure 68. Relationship between total porosity and Archie's porosity exponent in the Ellenburger and San Saba aquifers. The green markers represent laboratory data whereas the blue line represents the calibrated Serra's (1989) model.



Figure 69. Photograph of a naturally fractured rock from the Ellenburger formation. The colors of the matrix and calcium carbonate veins are tan and white, respectively. The diameter of the cores is 2 in.

Ellenburger and San Saba: Relationship between T_{2LM} and $T_{2,Peak}$

A non-negligible difference between T_{2LM} and $T_{2,Peak}$ (corresponding to the highest peak in the T_2 distribution) indicates the presence of a multimodal pore size distribution. **Figure 70** shows the relationship between T_{2LM} and $T_{2,Peak}$ for all core samples from the Ellenburger and San Saba aquifers. Rock class II, represented by core samples #42 #43 and #47, exhibits a unimodal pore size distribution as indicated by the negligible difference between $T_{2,Peak}$ and T_{2LM} .

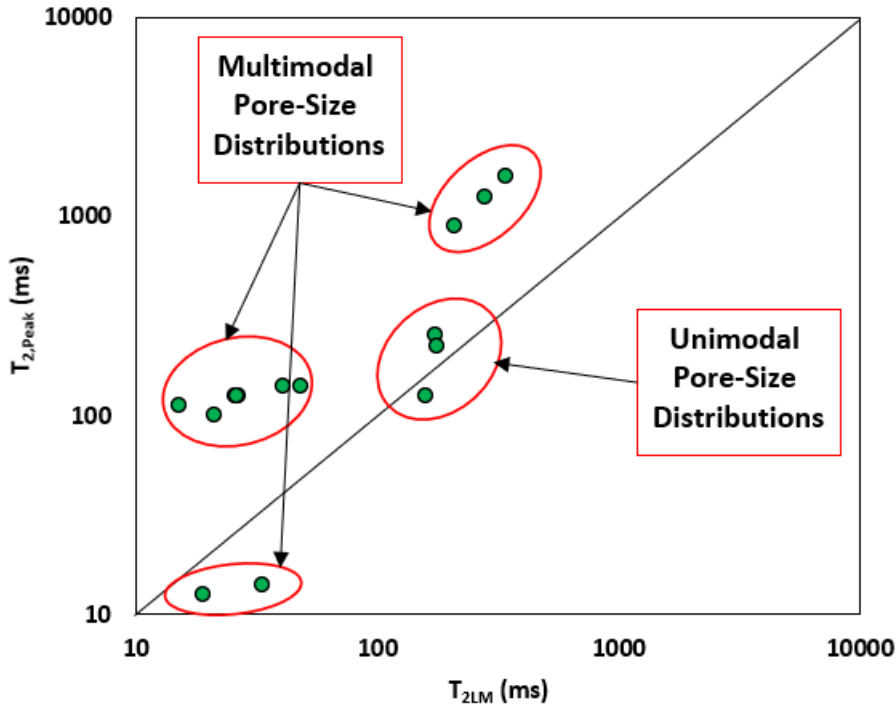


Figure 70. Relationship between T_{2LM} and modal $T_{2,Peak}$ of all core plugs from the Ellenburger and San Saba aquifers.

Ellenburger and San Saba: Irreducible water saturation from NMR measurements

Irreducible water saturation is estimated from NMR measurements using variable T_2 cutoff values (as a function of T_{2LM}) given by **Equation E-1** in **Appendix E**. **Figure 71** compares the estimated irreducible water saturation using variable T_2 cutoff values, $S_{wr,Xms}$, and a fixed T_2 cutoff equal to 92 ms (typical value of T_2 cutoff used in the literature for carbonate rocks), $S_{wr,92ms}$. Accordingly, the irreducible water saturation is equal to 0.35 for rock with porosity equal to 0.05. Note that these values of irreducible water saturation are mere approximations using NMR measurements; accurate assessment of irreducible water saturation would require additional laboratory measurements involving a centrifuge.

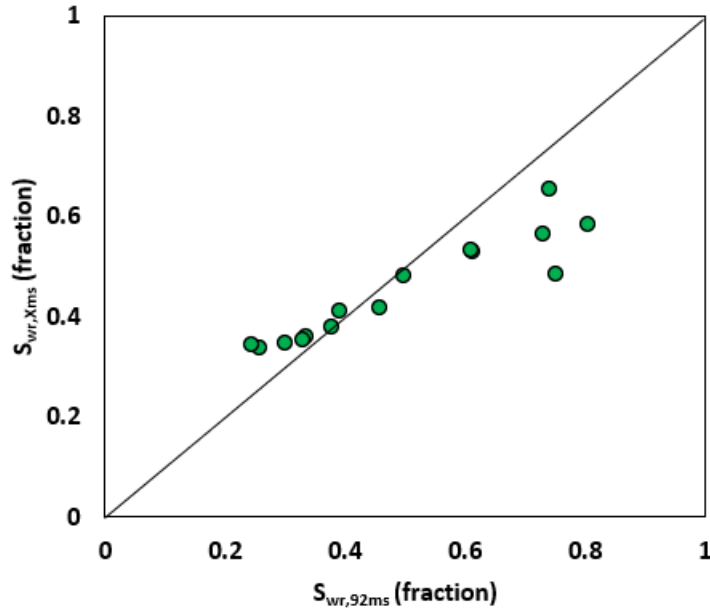


Figure 71. Relationship between irreducible water saturation from NMR measurements using a T_2 cutoff of 92 ms, $S_{wr,92ms}$, and variable T_2 cutoff values, $S_{wr,Xms}$, according to equation E-1 in Appendix E from the Ellenburger and San Saba aquifers.

Ellenburger and San Saba: Relationship between porosity and irreducible water saturation

Figure 72 shows the relationship between porosity and irreducible water saturation (derived from NMR measurements using variable T_2 cutoff values according to **Equation E-1** in **Appendix E**). Irreducible water saturation, S_{wr} , is given by:

$$S_{wr} = \frac{0.1921}{\phi^{0.198}} \quad (\text{Equation 15})$$

Accordingly, the irreducible water saturation is equal to 0.35 for medium-porosity rocks. Note that these values of irreducible water saturation are mere approximations using NMR measurements; accurate assessment of irreducible water saturation would require additional laboratory measurements involving a centrifuge.

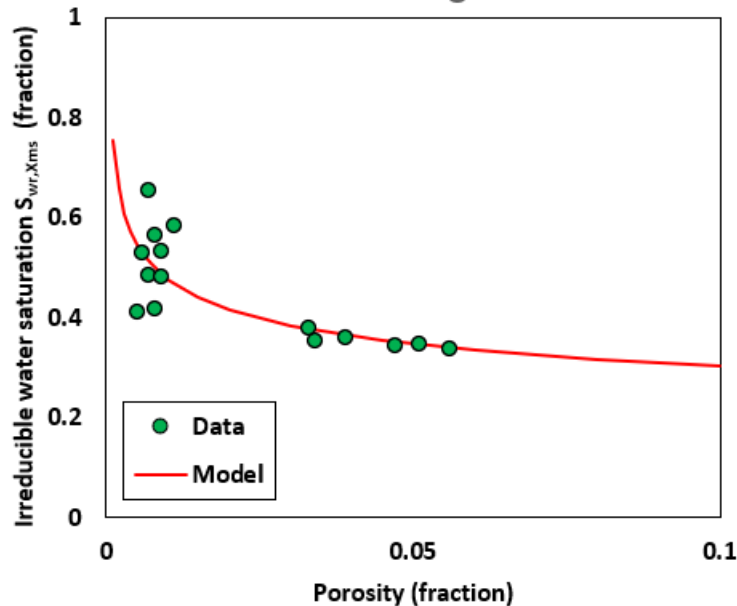


Figure 72. Relationship between porosity and irreducible water saturation in the Ellenburger and San Saba formations. The red curve is given by Equation 15.

Ellenburger and San Saba: Permeability Models

Laboratory measurements showed no clear correlations between permeability and NMR measurements (T_{2LM} and irreducible water saturation). Thus, we were not able to calibrate the traditional permeability models such as the SDR, Timur, and Timur-Coates models. These models assume that a good correlation exists between porosity, pore-body and pore-throat size, and pore connectivity. This assumption is generally not valid in carbonate rocks with complex pore structures (e.g., fractures, vugs, and non-connected porosity).

Ellenburger and San Saba: Effect of induced fractures on petrophysical properties

None of the core plugs were fractured (damaged) during core cutting. Thus, studying the effects of fractures on permeability in the Ellenburger and San Saba aquifers was not possible.

Ellenburger and San Saba: Data from TWDB Report 157 V3 (1976)

Figure 68 shows the relationship between porosity and permeability in the Ellenburger formation. Laboratory data obtained from the TWDB Report 157 V3 (1976) indicate that porosity in the Ellenburger formation is typically smaller than 0.05, which is consistent with porosity measurements acquired in this study. Permeability values in the TWDB Report 157 V3 (1976) vary between 1 and 100 mD. These values are greater than the permeability measurements acquired in this study. The median permeability-to-porosity ratio is equal to 667 mD, which corresponds to an equivalent pore radius of $0.81 \mu\text{m}$ ($\sqrt{667 * 9.87 * 10^{-16} \text{ m}^2} = 0.81 \mu\text{m}$).

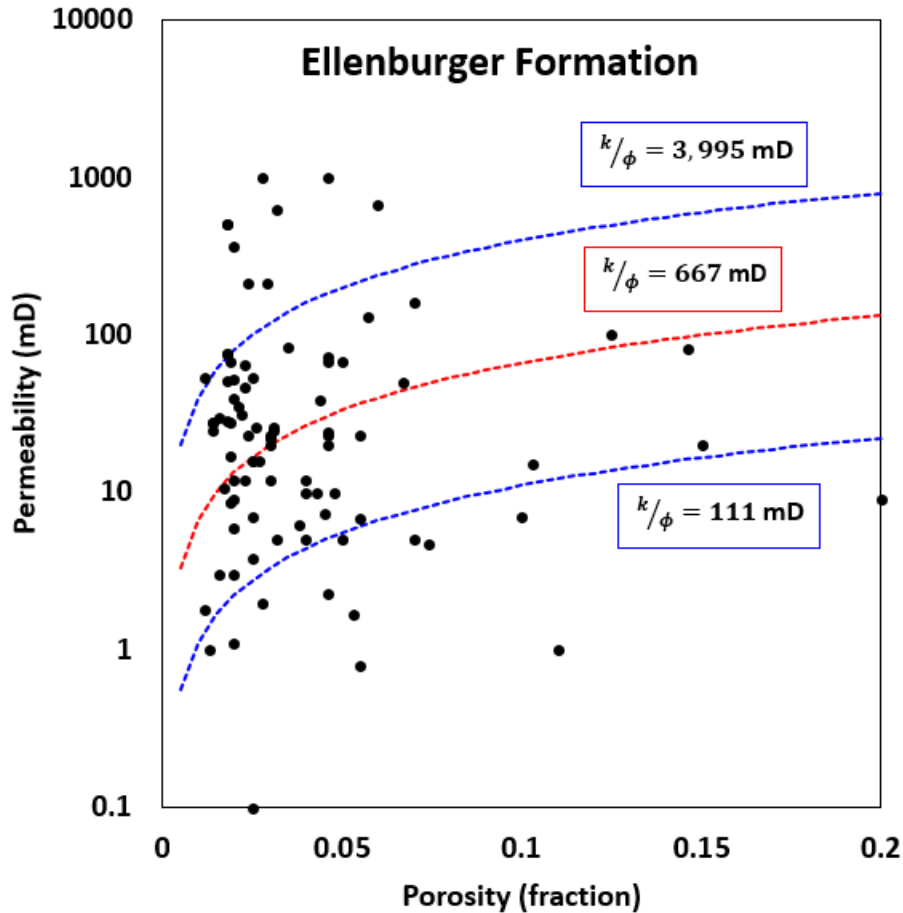


Figure 73. Relationship between porosity and permeability of core sample from the Ellenburger formation. Data was obtained from the TWDB Report 157 V3 (1976). The dashed red line corresponds to the median permeability-to-porosity ratio and the dashed blue lines correspond to standard deviation. The median permeability-to-porosity ratio is equal to 667 mD, which corresponds to an equivalent pore radius of 0.81 μm .

6 NUMERICAL SIMULATION OF WELL LOGS

The University of Texas at Austin's Petrophysical and Well Log Simulator (3D UTAPWeLS) is used to numerically simulate borehole measurements under various conditions (Voss et al., 2009). 3D UTAPWeLS can reproduce the various post-processing methods and configurations of the commercial tools used to acquire electrical, nuclear, and sonic logs. This software enables the generation of multi-layer models, honoring all petrophysical properties and available measurements. These models are referred to as earth models since they comprise physics related to rock and fluid dynamics. The numerical simulator also permits modeling the mud-filtrate invasion process. Indeed, 3D UTAPWeLS renders fully reliable petrophysical models to reproduce the well logs responses and provides fast and reliable methods for formation evaluation purposes (Bennis, 2022).

6.1 The Header of a Well Log

The header of a well log contains an itemized description of geographical, procedural, and borehole environmental variables associated with the acquisition of well logs. **Figure 74** shows an example of log header for modern triple-combo well logs acquired in a vertical well reaching the Ellenburger formation in McCulloch, Texas. The well was drilled with water-base mud and the maximum depth reached below the KB was over 2,959 ft with a recorded bottom-hole temperature of 110 °F. Mud-filtrate resistivity is 0.68 ohm-m at 96.3 °F, which corresponds to a salinity (NaCl) of 6,405 parts per million (ppm).

Schlumberger			
Company:		MERCURY OPERATING, LLC	
Well:		PLACID RIDGE #1	
Field:		WILDCAT	
County:		MCCULLOCH	State: TEXAS
County: MCCULLOCH Field: WILDCAT Location: 578' FSL & 1319' FWL Well: PLACID RIDGE #1 Company: MERCURY OPERATING, LLC	TCOM		
	578' FSL & 1319' FWL		Elev.: K.B. 1698.00 ft
	Sec: 293; Blk: 60; Abs: 740		G.L. 1686.00 ft
	Survey: H&TC RR CO		D.F. 1697.00 ft
Location:		Permanent Datum: Ground Level	Elev.: 1686.00 f
		Log Measured From: Kelly Bushing	12.00 ft above Perm.Datum
		Drilling Measured From: Kelly Bushing	
API Serial No.		Section:	Block: Abstract:
42-307-31189		293	60 740
Logging Date		02-Aug-2016	
Run Number		1A	
Depth Driller		2962.00 ft	
Schlumberger Depth		2959.00 ft	
Bottom Log Interval		2959.00 ft	
Top Log Interval		274.00 ft	
Casing Driller Size @ Depth		8.625 in @ 278.00 ft	
Casing Schlumberger		274 ft	
Bit Size		7.875 in	
Type Fluid In Hole		Chemical Gel	
MUD	Density	Viscosity	8.9 lbm/gal 40 s
	Fluid Loss	PH	8.3 cm3 9.5
	Source of Sample Active Tank		
RM @ Meas Temp		0.9 ohm.m @ 96.3 degF	
RMF @ Meas Temp		0.68 ohm.m @ 96.3 degF	
RMC @ Meas Temp		1.35 ohm.m @ 96.3 degF	
Source RMF		RMC	Calculated Calculated
RM @ BHT		RMF @ BHT	0.79 @ 110 0.6 @ 110
Max Recorded Temperatures		110 degF	
Circulation Stopped		Time	02-Aug-2016 15:00:00
Logger on Bottom		Time	02-Aug-2016 19:00:00
Unit Number	Location: 9116 Abilene, Texas		
Recorded By		Gaines Gibson	
Witnessed By		Chris Fourd	

Figure 74 Example of well log header for a well that was drilled with water-base mud in McCulloch County, Texas. The header indicates that the API Serial No. of the well is 42-307-31189 and that it was logged by Schlumberger in 2016. Note (1) the maximum depth with the corresponding bottom hole temperature and (2) measurements of electrical resistivity of drilling mud components.

6.2 Depth Matching of Well Logs

Well log interpretation starts with the verification of accurate depth matching of all measurements and implementation of corrections if necessary, including measurements which were acquired during different runs and with different tools, or in cases in which the cable tension and speed were uneven. Two given well logs are depth matched when their local minimum and maximum run depths are aligned. A depth-shifted well log is corrected by applying either a bulk depth shift (by moving a portion of the well log up or down by a fixed length) or by stretching and squeezing the well logs to depth match other reference logs.

6.3 Geothermal Gradients at the Llano Uplift and Upper Coastal Plains

Surface and bottom hole temperatures are key parameters for the estimation of geothermal gradients. Surface temperature at the well site is found on the well log header and is reported as mud, mud-filtrate, and/or mudcake temperature. In this study, surface temperature is set equal to 70 degrees Fahrenheit (F) for all the wells. Bottom hole temperature is found on the well log header either as a separate value or associated with a mud resistivity at the maximum recorded temperature. When a well is logged during multiple runs, with each run representing a different depth range, the bottom hole temperature of each run is usually recorded. **Figure 75** shows the increase of temperature with depth as recorded in the wells under study. Geothermal gradients in Llano Uplift and Upper Coastal Plains are equal to 0.011 and 0.017 degrees F/ft, respectively. Accordingly, formation temperature, T (F), at a given depth, z (ft), is expressed as follows:

$$T = T_s + G * z \quad (\text{Equation 16})$$

where G (F/ft) is geothermal gradient, T_s is surface temperature equal to 70 F, and z is vertical depth (ft). This equation is especially useful for cases in which temperature data are missing from well log headers.

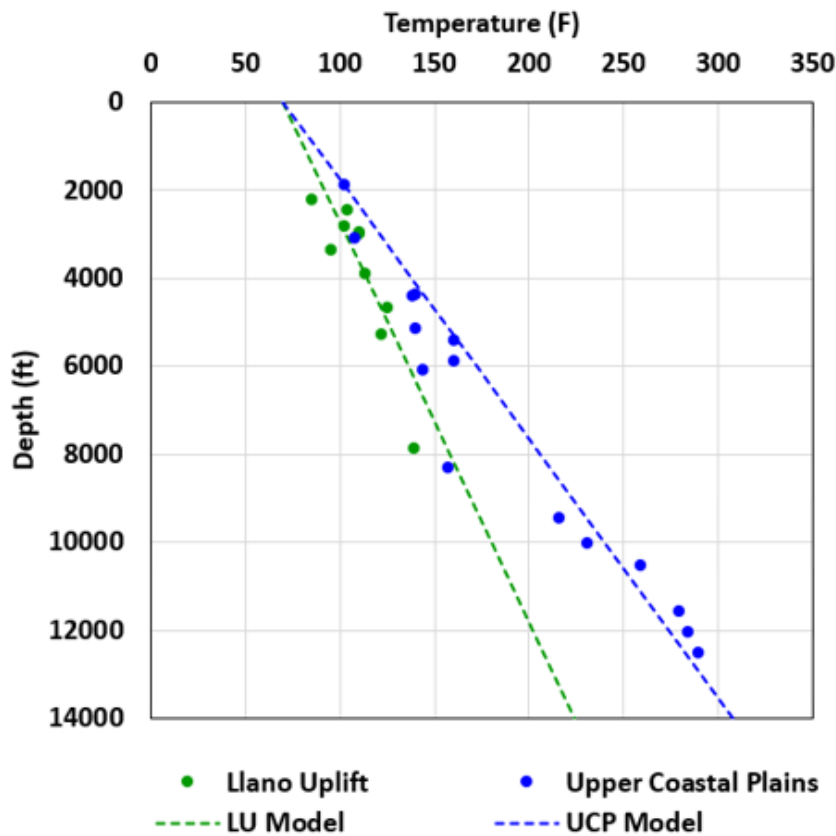


Figure 75. Measured bottomhole temperature (BHT) of wells drilled in the Llano Uplift (in green) and Upper Coastal Plains (in blue) as a function of vertical depth. The average surface temperature is 70 degrees Fahrenheit (F). The modeled geothermal gradients (dashed lines) in Llano Uplift and Upper Coastal Plains are equal to 0.011 and 0.017 degrees F/ft, respectively.

6.4 Water Salinity Estimation Methods

Formation water salinity is a key parameter in formation evaluation. However, its assessment is not trivial, and its significance is often underestimated. In aquifers, formation water salinity is a crucial property for classifying and monitoring water quality. This section presents basic information for several water salinity estimation methods, such as Archie's equation, Pickett plot, resistivity ratio, and spontaneous potential (SP) log. Most of the methods focus on computing formation water electrical resistivity (R_w) as a function of salt concentration and temperature (T), assuming clean aquifers to avoid the effect of clays on conductivity. In addition, if we assume that sodium chloride (NaCl) is the only salt dissolved in the formation water, we can use **Equations 17** and **18** to convert the electrical resistivity of water (R_w) to salt concentration ($[NaCl]_{ppm}$) at a given formation temperature (T in degrees F).

$$R_w = (0.0123 + \frac{3647.5}{[NaCl]_{ppm}^{0.955}}) (\frac{81.77}{T + 6.77}) \quad (\text{Equation 17})$$

$$[NaCl]_{ppm} = 10^{\left\{ \frac{3.562 - \log_{10} [R_w (\frac{T+6.77}{81.77}) - 0.0123]}{0.955} \right\}} \quad (\text{Equation 18})$$

Archie's equation

Archie's equation assumes a clean matrix and a fully saturated reservoir to calculate formation electrical resistivity, R_t (ohm-m) (Archie, 1942). Archie's equation is given by:

$$R_t = \frac{aR_w}{\phi^m S_w^n} \quad (\text{Equation 19})$$

where R_w is formation water resistivity (ohm-m), ϕ is porosity (fraction), S_w is water saturation, and a , m , and n are fitting parameters. The Winsauer factor, a , is assumed equal to 1. In the context of studying aquifers, rocks formations are fully water-saturated where S_w is equal to 1. Accordingly, water resistivity is given by:

$$R_w = R_t \phi^m \quad (\text{Equation 20})$$

In well log interpretation, porosity can be obtained from density, neutron porosity, and/or sonic logs. Porosity exponent, m , is obtained from core analysis. Formation resistivity is often obtained from the deep-sensing resistivity logs when the radial length of invasion is negligible. In the presence of deep mud-filtrate invasion, resistivity logs should be corrected for the effects of invasion using numerical simulations of borehole resistivity instruments in UTAPWeLS. The effect of mud-filtrate invasion on resistivity logs has been traditionally studied using a step radial resistivity profile corresponding to a piston-like flow model, which assumes a completely flushed-zone resistivity, R_{xo} , and a radial length of invasion, L_{xo} , beyond which lies the virgin formation of resistivity, R_t . Such a model embodies three unknown properties that, in theory, can be resolved using at least three independent resistivity logs exhibiting variable depths of investigation.

Porosity can also be derived using a Pickett plot. A Pickett plot is a graphical method that employs the logarithmic relation of formation resistivity, $\log(R_t)$, and porosity, $\log(\phi)$, to linearize Archie's equation and estimate formation water resistivity, R_w , by fitting the slope of the line, which is equal to the porosity exponent (m) (Aguilera, 1990).

Resistivity Ratio

The resistivity ratio method can be used to estimate formation water salinity for formations subject to mud-filtrate invasion. In porous and permeable beds, mud-filtrate displaces in-situ formation water, yielding a change in the formation electrical resistivity of the invaded zone. Borehole resistivity instruments exhibiting different volumes of investigation measure the electrical resistivity of the formation at different distances from the wellbore. Using the deep- and shallow-sensing resistivity logs, formation water resistivity can be calculated using a variant of Archie's equation given by:

$$R_w = R_{mf} \frac{R_t}{R_{xo}} \quad (\text{Equation 21})$$

where R_{mf} (ohm-m) is mud-filtrate resistivity at formation temperature and R_{xo} (ohm-m) is formation resistivity in the invaded zone. Note that it is important to convert mud-filtrate resistivity from surface to formation temperature. The conversion equation is given by:

$$R_{mf}(T_{Formation}) = R_{mf}(T_{Surface}) \frac{T_{Surface} + 6.77}{T_{Formation} + 6.77} \quad (\text{Equation 22})$$

where $T_{Formation}$ (F) and $T_{Surface}$ (F) are temperatures of the formation and at the surface, respectively.

It is a common assumption that the deep-sensing resistivity log provides a measure of the uninvaded (by mud filtrate) zone whereas the shallow sensing log provides a measure a measure of the flushed (invaded by mud filtrate) zone. These assumptions are very simplistic; Accurate estimations of R_{xo} and R_t require advanced numerical modeling capabilities as offered by UTAPWeLS.

Spontaneous Potential (SP) log

The spontaneous potential log measures the electrical potential generated from the salinity contrast between formation water and water-base mud-filtrate. This log is useful to estimate water salinity when there are thick permeable and clean (shale-free) formations with non-negligible differences in salt concentration between mud-filtrate and formation water. The static spontaneous potential (SSP) is given by:

$$SSP = SP_{log} - SP_{shale} \quad (\text{Equation 23})$$

where SP_{log} (in mV) is the SP measurements and SP_{shale} (in mV) is the shale baseline. An equivalent water resistivity, R_{we} (in ohm-m), is given by:

$$R_{we} = R_{mfe} 10^{-\frac{SSP}{K_{SP}}} \quad (\text{Equation 24})$$

where R_{mfe} (in ohm-m) is equivalent mud-filtrate resistivity. K_{SP} is a parameter that depends on ion mobility and temperature (T in degrees F) and is given by:

$$K_{SP} = 60 + 0.133T \quad (\text{Equation 25})$$

Note that R_{we} and R_{mfe} are equal to R_w and R_{mf} only in high-salinity solutions. Accurate estimation of water salinity from SP logs in low-salinity formations requires numerical modeling of SP logs in 3D UTAPWeLS. The use of numerical modeling is also important in the presence of non-zero irreducible water

saturation, the presence of shale, the presence of shoulder-bed effects, and the presence of deep mud-filtrate invasion.

6.5 Numerical Simulations of Well Logs

3D UTAPWeLS is used to construct multilayer earth models and perform numerical simulations of spontaneous potential (SP), resistivity, and nuclear (gamma ray (GR), density (RHOB), photoelectric factor (PEF, and neutron porosity (NPHI)) logs. The simulation method starts with the construction of stacked horizontal layers penetrated by a vertical well. Bed boundaries are detected based on the inflection point of well logs with the highest vertical resolution (e.g., density and shallow-sensing resistivity logs). Petrophysical properties, including porosity and shale concentration, are set across the petrophysical layers and the corresponding layer-by-layer physical properties (e.g., resistivity, density, migration length, and gamma ray) are calculated. In the presence of mud-filtrate invasion, radial boundaries are constructed away from the borehole wall to account for salinity differences between mud-filtrate and formation water (Bennis et al. 2023b).

Most well logs can be numerically simulated under specified formation properties and geometrical conditions, including well trajectory, borehole size, formation dip and azimuth, and bed boundaries. Several algorithms have been introduced for the rapid forward modeling of borehole measurements (resistivity, nuclear, sonic, and NMR) based on finite element methods and on the concept of spatial sensitivity functions that honor the physics of the measurements and incorporate instrument, borehole, and formation geometry. Numerical simulation of well logs is an efficient method to perform forward modeling and sensitivity analysis for a wide range of challenging conditions such as thin beds, anisotropy, complex mineralogy, and mud-filtrate invasion (Bennis et al., 2023a).

Numerical simulation of nuclear logs

Layer-by-layer gamma ray, GR (API), is given by:

$$GR = A_{WL}U_{ppm} + B_{WL}Th_{ppm} + C_{WL}K_{\%} \quad (\text{Equation 26})$$

where U_{ppm} , Th_{ppm} , and $K_{\%}$ are the volumetric concentrations of naturally occurring uranium (^{238}U), thorium (^{232}Th) and potassium (^{40}K) isotopes in rock formations. A_{WL} , B_{WL} , and C_{WL} are sensitivity coefficients that depend on tool design and borehole conditions. Sensitivity coefficients for the wireline (WL) GR Longhorn tool in a water-filled 8.5-in. borehole are: $A_{WL}=6.51$, $B_{WL}=2.71$, and $C_{WL}=14.23$. For a formation of known concentrations equal to 12 ppm of ^{238}U , 24 ppm of ^{232}Th and 4% of ^{40}K , GR is equal to 200 API. Layer-by-layer bulk density is calculated based on the solid and fluid compositions of the formation using linear mixing laws. Layer-by-layer photoelectric factor (PEF) and neutron migration length are estimated using The University of Texas at Austin's Nuclear Property calculator (UTNuPro). Subsequently, nuclear logs such as GR, density, neutron porosity, and PEF are numerically simulated using the WL Longhorn tools, which are designed to mimic the response of commercial logging tools (Ellis and Singer, 2007; Luycx et al., 2020).

Numerical simulation of resistivity logs

In shale-free formations, layer-by-layer formation resistivity is calculated using Archie's equation. In the presence of laminated shaly sandstones (such as those encountered in the Upper Coastal Plains aquifers), layer-by-layer formation resistivity, R_t (ohm-m), is calculated using a parallel circuit model given by:

$$R_t = \left[(1 - V_{sh}) \frac{\phi_s^m}{R_w} + \frac{V_{sh}}{R_{sh}} \right]^{-1} \quad (\text{Equation 27})$$

where V_{sh} is volumetric concentration of shale and R_{sh} is shale resistivity. ϕ_s is sandstone porosity given by:

$$\phi_s = \frac{\phi - V_{sh}\phi_{sh}}{1 - V_{sh}} \quad (\text{Equation 28})$$

where ϕ is total porosity and ϕ_{sh} is shale porosity. The corresponding apparent resistivity logs are obtained from the numerical simulation of the array induction tool, the dual induction tool, the array laterolog tool, or the dual laterolog tool.

6.6 Assessment of Porosity in the Hickory Formation in Well #A01

The temperature of the Hickory formation at 2,000 ft is approximately 92 degrees F (**Equation 16**). The resistivity of mud-filtrate at 92 degrees F is 1.66 ohm-m and the corresponding salinity (NaCl) is 2,600 parts per million (ppm). **Figure 76** shows the well logs acquired in this formation. The SP log exhibits negligible deflection with respect to the shale baseline, indicating that the mud filtrate and formation water have similar resistivity and salinity values. The top section of the Hickory formation exhibits low GR values indicating the presence of shale-free sandstones whereas the bottom section of the Hickory formation exhibit large oscillations in GR values indicating the presence of laminated shaly sandstones. In this case, the presence of mud-filtrate invasion would not cause a separation of resistivity logs with different volumes of investigation. Indeed, the medium- (ILD) and deep-sensing (LAT) resistivity logs exhibit negligible separation. We calculate porosity using Archie's equation and is given by:

$$\phi = \left(\frac{R_w}{R_t}\right)^{1/m} \quad (\text{Equation 29})$$

The ILD and LAT logs are used as formation resistivity. R_w and m are equal to 1.66 ohm-m and 1.77, respectively. Note that Archie's porosity exponent was obtained from core analysis. The estimated porosity values are displayed on track 5 of **Figure 71**. Porosity ranges between 0.05 and 0.2. Porosity is the highest in the top section of Hickory formation where the volumetric concentration of shale is the lowest (low GR values)

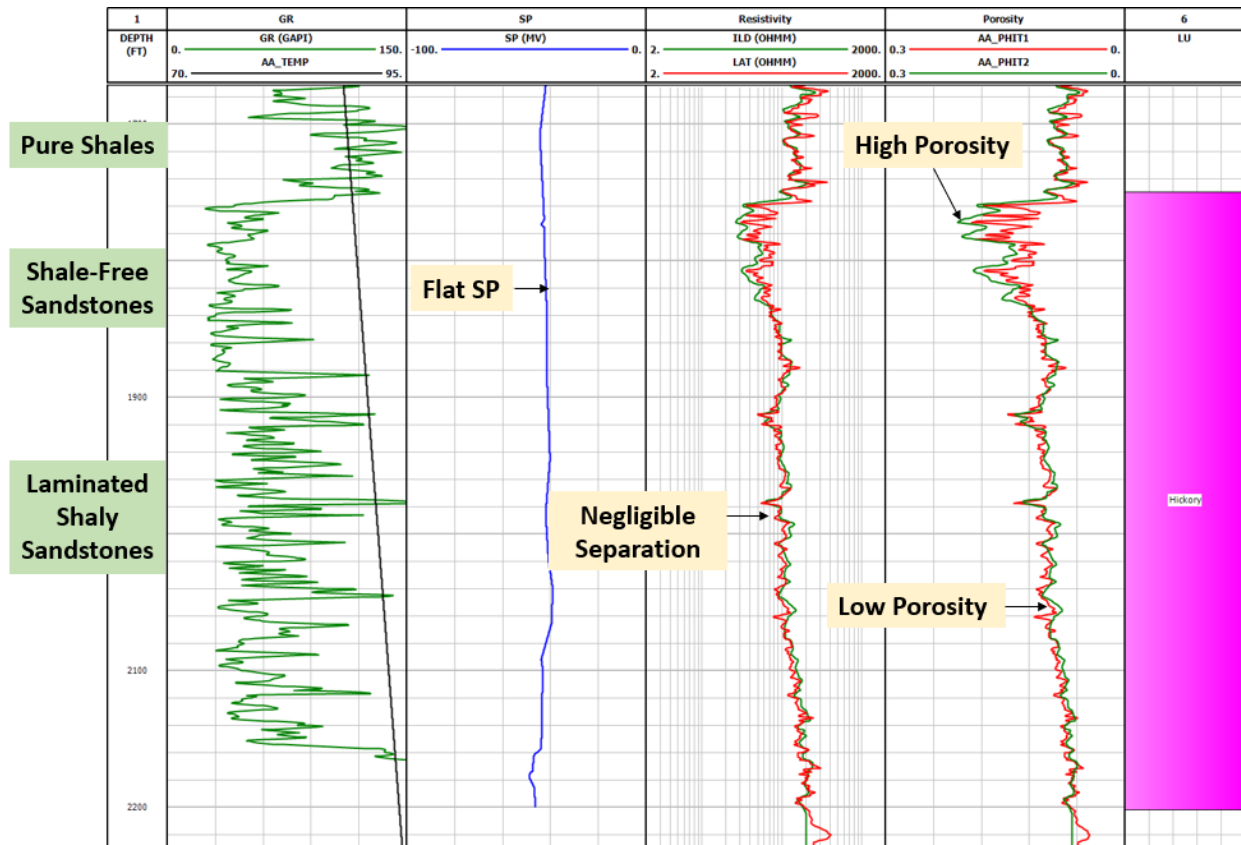


Figure 76. Well logs acquired in the Hickory formation in well #A01. Track 1: depth. Track 2: GR log and formation temperature. Track 3: SP log. Track 4: resistivity logs. Track 5: estimated porosity using ILD (green) and LAT (red) logs in Equation 29. Track 6: formation zones.

6.7 Assessment of Salinity, Porosity, and Shale Concentration in the Lower Wilcox Formation in Well #B04 Using UTAPWeLS

The Lower Wilcox formation consists of shale-free (clean) sandstones, pure shales, and laminated shaly sandstones. The salinity (NaCl) of mud-filtrate in well #B04 is 1,640 parts per million (ppm). The following sections describe the simulation method used to assess salinity, porosity and shale concentration within the 4400-4700ft and 4950-5200ft depth intervals in well #B04.

Numerical simulations within the 4950-5200 ft depth interval

The temperature of the Lower Wilcox formation at 5,100 ft is approximately 156 degrees F (**Equation 16**). **Figure 77** shows the well logs (GR, SP, and resistivity) acquired in this formation. The formation layer at 5094 ft is assumed to be a shale-free (clean) sandstone because it exhibits low GR values (approximately 55 API). The formation layer at 5,168 ft is assumed to be pure shale because it exhibits relatively high GR values (approximately 124 API). UTAPWeLS is used to estimate porosity, formation water salinity, and shale concentration by numerically simulating GR, SP, and resistivity logs. First, a multilayer earth model is built with laminated shaly sandstones. The inflection points of well logs are used to detect the boundaries between petrophysical layers. Then, formation salinity and volumetric concentration of shale are estimated by numerically simulating the SP log. Track 2 of **Figure 77** shows a good agreement between measured (black curve) and numerically simulated (red curve) SP logs. The SP of clean sandstones and pure shales

is -133 mV and -35 mV, respectively. The estimated formation water salinity (NaCl) is 35,000 parts per million (ppm). Track 5 of **Figure 77** shows the estimated layer-by-layer volumetric concentration of shale. Note that irreducible water saturation of shale-free (clean) sandstones is assumed to be negligible. Total and sandstone porosity values are estimated by numerically simulating the deep-sensing resistivity log. Layer-by-layer resistivity parallel to bedding planes (horizontal resistivity) is calculated using a parallel circuit model in which the resistivity of pure shales is assumed to be equal to 2 ohm-m. Based on core analysis, the porosity exponent is assumed equal to 1.85. Track 4 of **Figure 77** shows a good agreement between measured (black curve) and numerically simulated (red curve) deep-sensing resistivity logs. Track 6 of **Figure 77** shows the estimated layer-by-layer total (blue curve) and sandstone (red curve) porosity values. The porosity of pure shales is assumed to be equal to 0.1. The clean sandstone layer at 5,075 ft exhibits the largest porosity (approximately 0.35). Finally, the gamma ray log is numerically simulated. **Table 8** lists the assumed concentrations of potassium, thorium, and uranium in shale-free (clean) sandstones and pure shales (note that for more accurate numerical simulations of GR logs, laboratory GR measurements of clean sandstones and pure shales are required). Track 2 of **Figure 77** compares the measured (black curve) and numerically simulated (red curve) GR logs.

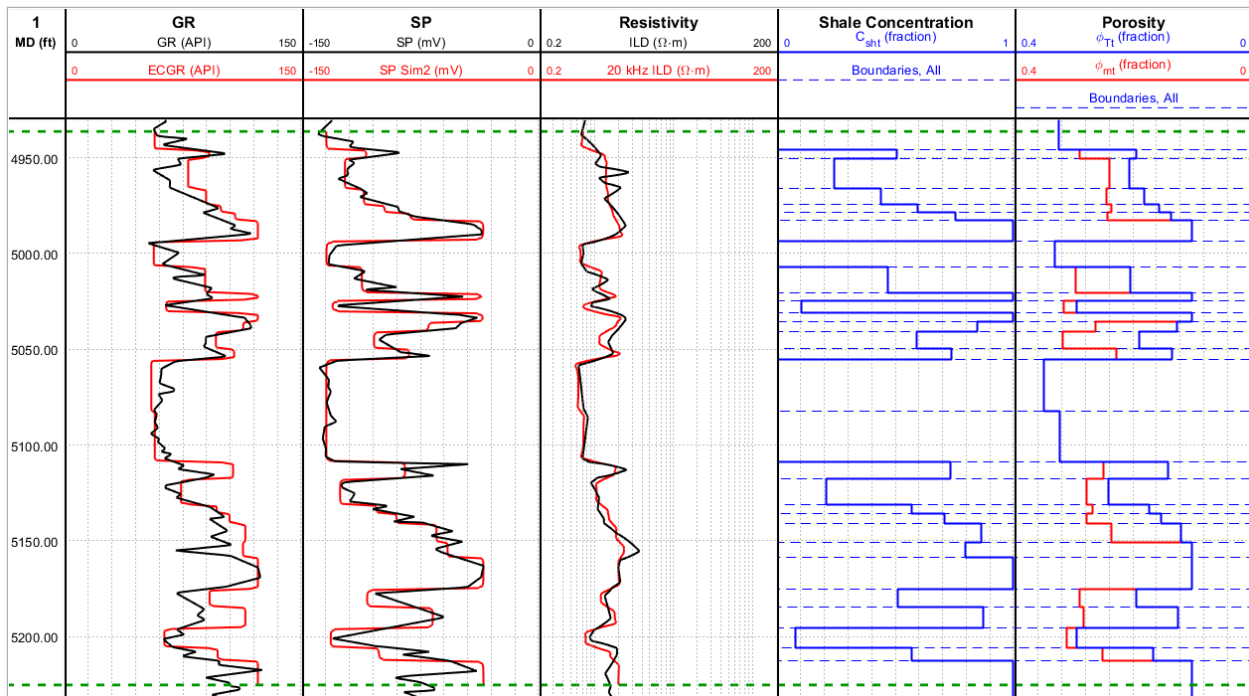


Figure 77. Well logs acquired in the Lower Wilcox formation in well #B04 within the 4950-5200 ft depth interval. Comparison of measured (black curves) and numerically simulated (red curves) gamma-ray, spontaneous potential, and deep-sensing resistivity logs. The blue dashed horizontal lines on Tracks 5 and 6 represent the petrophysical layer boundaries. Track 1: depth. Track 2: measured (black curve) and numerically simulated (red curve) gamma-ray logs. Track 3: measured (black curve) and numerically simulated (red curve) spontaneous potential logs. Track 4: measured (black curve) and numerically simulated (red curve) deep-sensing resistivity logs. Track 5: layer-by-layer volumetric concentration of shale. Track 6: layer-by-layer total (blue curve) and sandstone (red curve) porosity values.

Table 8. Summary of concentrations of potassium, thorium, and uranium assumed for the numerical simulation of GR log in the Lower Wilcox formation in well #B04.

Lithology	K (%)	Th (ppm)	U (ppm)
Clean Sandstones	0	0	13
Pure Shales	5.91	0	8

Numerical simulations within the 4400-4700 ft depth interval

The temperature of the Lower Wilcox formation at 4,628 ft is approximately 148 degrees F (**Equation 16**). **Figure 78** shows the well logs (GR, SP, and resistivity) acquired in this formation. The formation layer at 4,628 ft is assumed to be a shale-free (clean) sandstone because it exhibits low GR values (approximately 48 API). The formation layer at 5,168 ft is assumed to be pure shale because it exhibits relatively high GR values (approximately 121 API). UTAPWeLS is used to estimate porosity, formation water salinity, and shale concentration by numerically simulating GR, SP, and resistivity logs. First, a multilayer earth model is built with laminated shaly sandstones. The inflection points of well logs are used to detect the boundaries between petrophysical layers. Then, formation salinity and volumetric concentration of shale are estimated by numerically simulating the SP log. Track 2 of **Figure 78** shows a good agreement between measured (black curve) and numerically simulated (red curve) SP logs. The SP of clean sandstones and pure shales is -120 mV and -35 mV, respectively. The estimated formation water salinity (NaCl) is 23,000 parts per million (ppm). Track 5 of **Figure 78** shows the estimated layer-by-layer volumetric concentration of shale. Note that irreducible water saturation of shale-free (clean) sandstones is assumed to be negligible. Total and sandstone porosity values are estimated by numerically simulating the deep-sensing resistivity log. Layer-by-layer resistivity parallel to bedding planes (horizontal resistivity) is calculated using a parallel circuit model in which the resistivity of pure shales is assumed to be equal to 2.7 ohm-m. Based on core analysis, the porosity exponent is assumed equal to 1.85. Track 4 of **Figure 78** shows a good agreement between measured (black curve) and numerically simulated (red curve) deep-sensing resistivity logs. Track 6 of **Figure 78** shows the estimated layer-by-layer total (blue curve) and sandstone (red curve) porosity values. The porosity of pure shales is assumed to be equal to 0.1. The clean sandstone layer at 4,628 ft exhibits the largest porosity (approximately 0.35). Finally, the gamma ray log is numerically simulated. **Table 8** lists the assumed concentrations of potassium, thorium, and uranium in shale-free (clean) sandstones and pure shales. Track 2 of **Figure 78** compares the measured (black curve) and numerically simulated (red curve) GR logs.

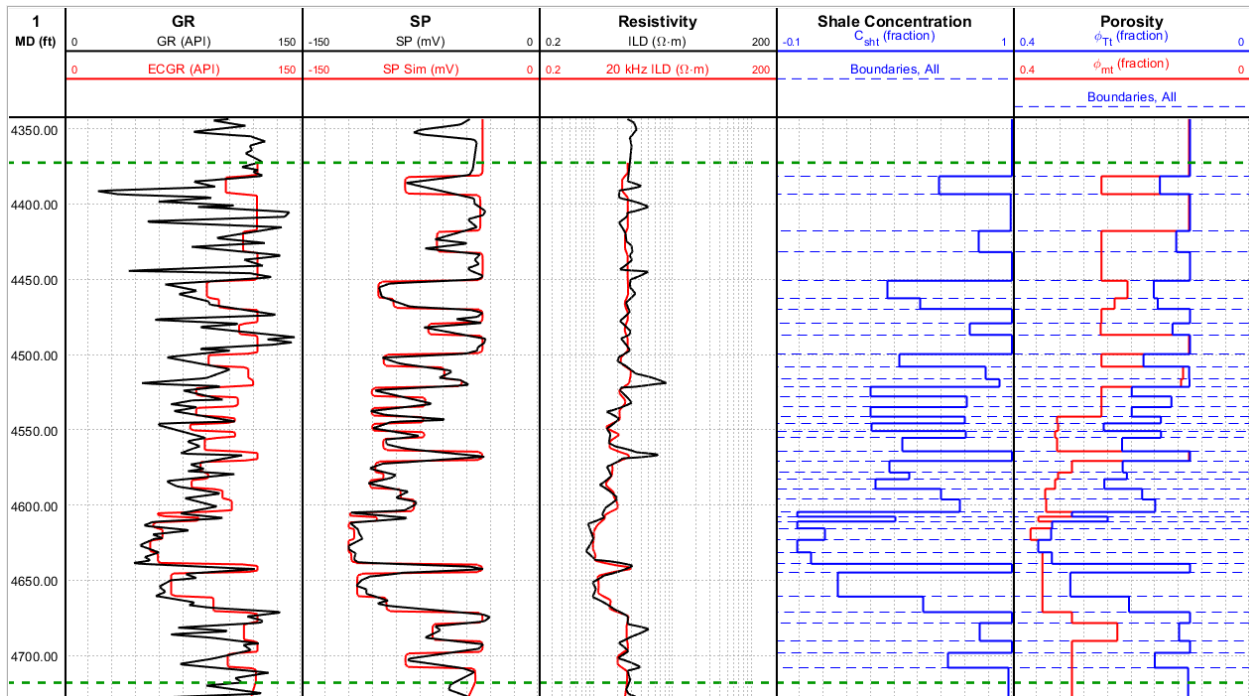


Figure 78. Well logs acquired in the Lower Wilcox formation in well #B04 within the 4950-5200 ft depth interval. Comparison of measured (black curves) and numerically simulated (red curves) gamma-ray, spontaneous potential, and deep-sensing resistivity logs. The blue dashed horizontal lines on Tacks 5 and 6 represent the petrophysical layer boundaries. Track 1: depth. Track 2: measured (black curve) and numerically simulated (red curve) gamma-ray logs. Track 3: measured (black curve) and numerically simulated (red curve) spontaneous potential logs. Track 4: measured (black curve) and numerically simulated (red curve) deep-sensing resistivity logs. Track 5: layer-by-layer volumetric concentration of shale. Track 6: layer-by-layer total (blue curve) and sandstone (red curve) porosity values.

6.8 Assessment of Porosity and Lithology in the Ellenburger and San Saba Formations in Well #A02

In well #A02, the neutron porosity log is expressed in limestone porosity units. **Figure 79** shows the relationship between neutron porosity (in limestone porosity units) and bulk density which indicates that the dominant lithology in the Ellenburger and San Saba formations is limestone because most of the blue markers fall on top of the limestone line. Accordingly, grain density, ρ_g , is assumed equal to 2.71 g/cc. Using the bulk density log, density porosity is given by:

$$\phi = \frac{\rho_g - \rho_b}{\rho_g - \rho_w} \quad (\text{Equation 30})$$

where ρ_b (g/cc) is bulk density (density log) and ρ_w is water density assumed equal to 1 g/cc. The estimated depth-by-depth porosity is displayed on the last track of **Figure 80**. The displayed porosity is calculated as an average of depth-by-depth density porosity and neutron porosity. The spikes observed in the calculated porosity log are interpreted as vuggy porosity. **Figure 81** shows the histogram of porosity in the Ellenburger and San Saba formations. Approximately 90% of porosity values are smaller than 0.06. Assessment of formation water salinity is not possible in this well because of the absence of resistivity and SP measurements.

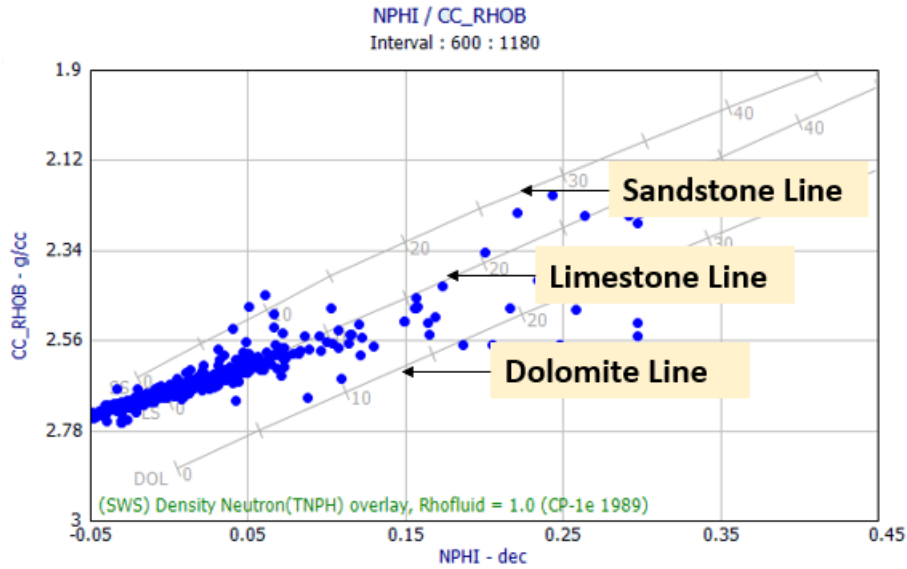


Figure 79. Relationship between neutron porosity and bulk density in well #A02. The dominant lithology is limestone.

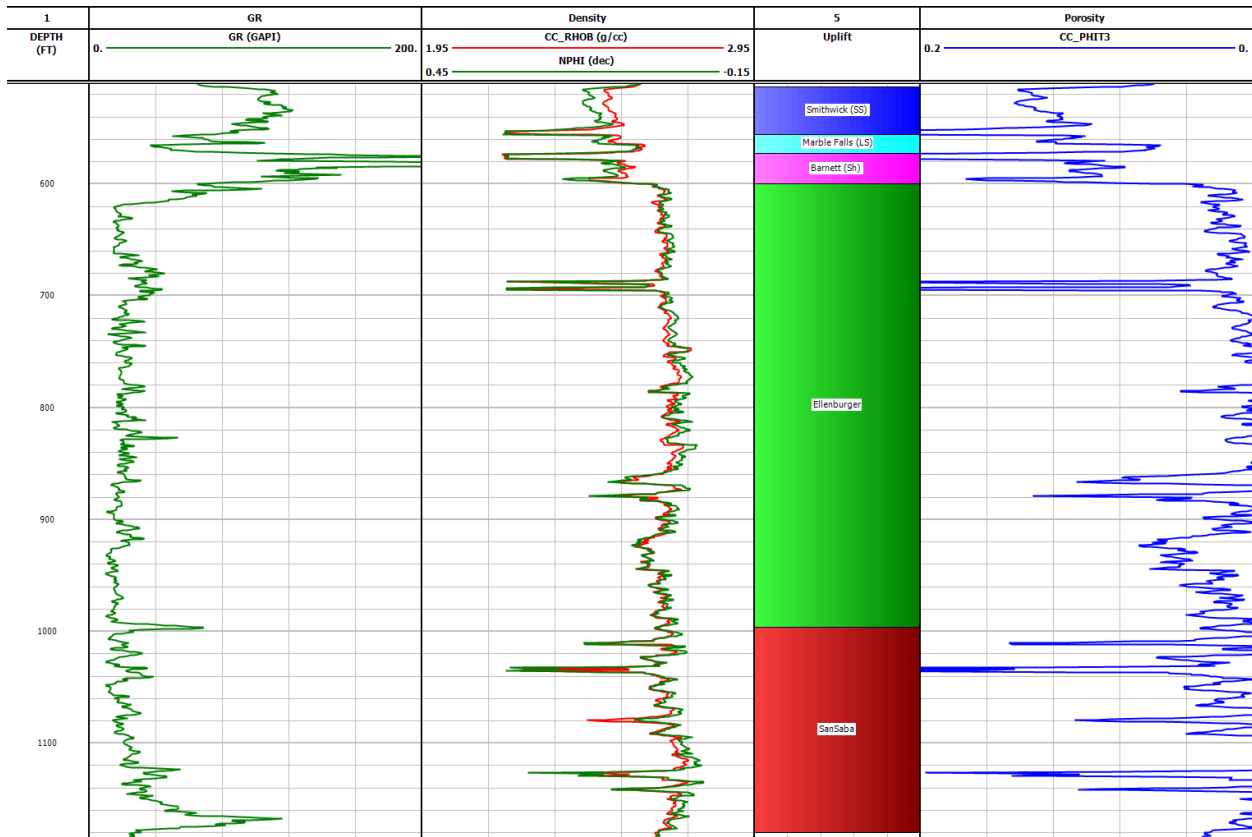


Figure 80. Well logs acquired in the Ellenburger and San Saba formations in well #A02. Track 1: depth. Track 2: GR log. Track 3: bulk density (red) and neutron porosity (green). Track 4: formation zones. Track 5: estimated porosity from density and neutron porosity logs.

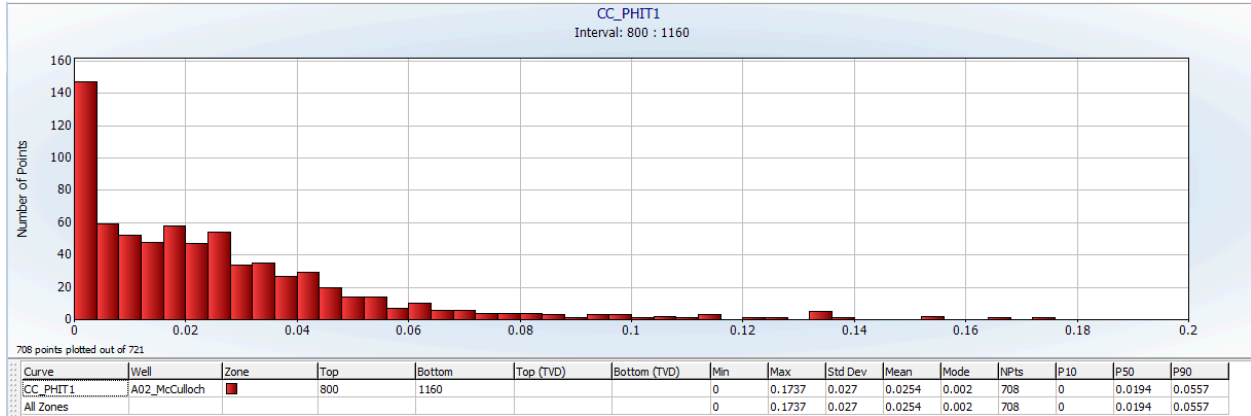


Figure 81. Histogram of porosity in the Ellenburger and San Saba formations in well #A02. Approximately 90% of porosity values are smaller than 0.06.

6.9 Assessment of Porosity and Lithology in the Ellenburger and San Saba Formations in Well #A03

The temperature of the Ellenburger and San Saba formations at 2,000 ft is approximately 85 degrees F in Well #A03 (**Equation 16**). The salinity of mud-filtrate is unknown because it was not recorded in the well log header. We assume that formation water resistivity is equal to 3 ohm-m at 85 degrees F, which corresponds to a salinity of 1,500 NaCl ppm. Depth-by-depth porosity is calculated using **Equation 29** where formation resistivity is assumed equal to the medium- (ILM) and deep-sensing (ILD) resistivity logs. The estimated depth-by-depth porosity is displayed on track 7 of **Figure 82** where the green and red curves were calculated using the ILM and ILD resistivity logs, respectively. **Figure 83** shows the histogram of porosity in the Ellenburger and San Saba formations. Approximately 90% of porosity values are smaller than 0.08. We noticed that the SP log values decreased with depth, and we applied a baseline shift as shown in **Figure 84**. Track 8 of **Figure 82** shows that the baseline-sifted SP log correlates with porosity where high porosity rocks exhibit large SSP values and tight rock exhibit low SSP values. Indeed, SP logs are sensitive to porosity and irreducible water saturation (the lower the porosity, the higher the irreducible water saturation, and the lower the SSP). This example shows that porous intervals of the Ellenburger and San Saba formations can be identified using the SP log.

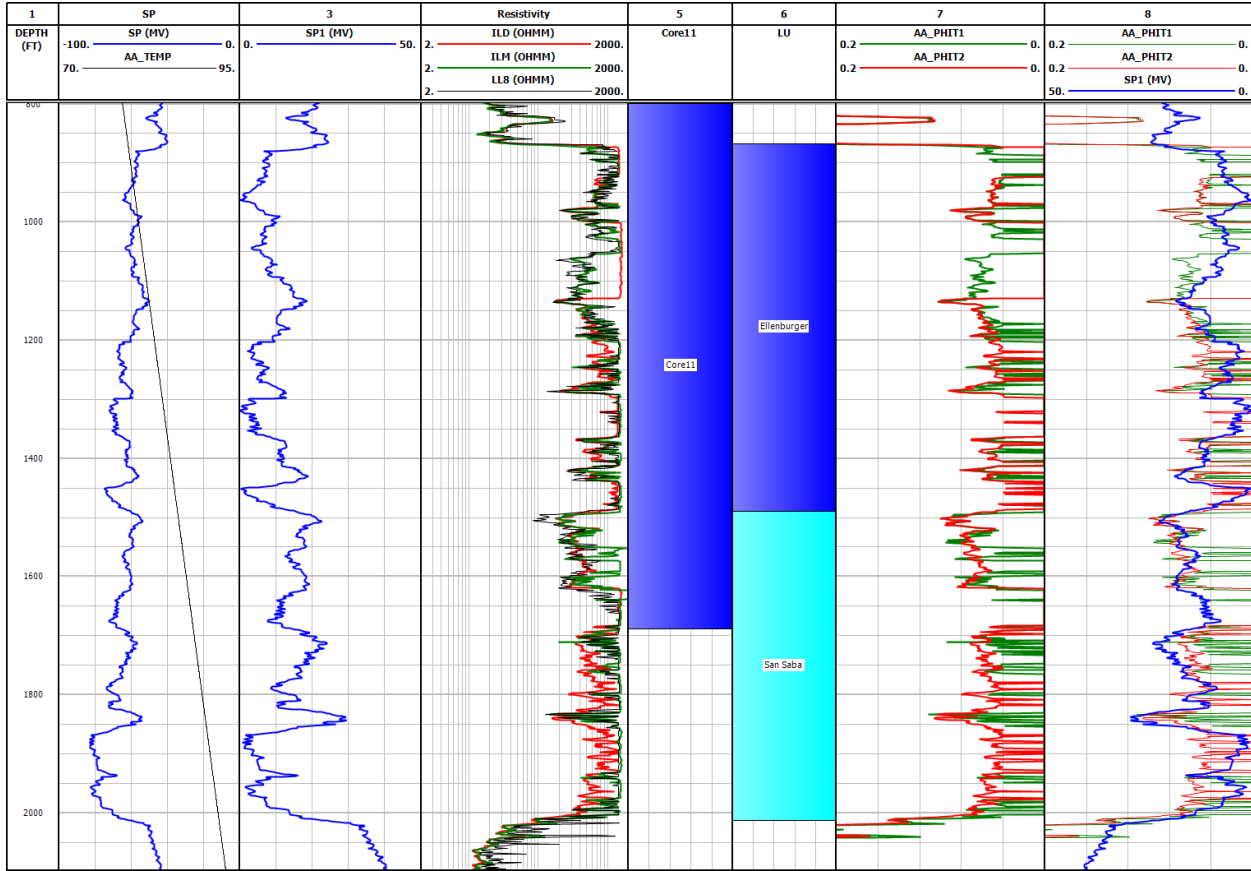


Figure 82. Well logs acquired in the Ellenburger and San Saba formations in well #A03. Track 1: depth. Track 2: SP log and formation temperature. Track 3: baseline-shifted SP log. Track 4: resistivity logs. Track 5: cored interval. Track 6: formation zones. Track 7: estimated porosity from ILM (green curve) and ILD (red curve) resistivity logs. Track 8: correlation between estimated porosity values (red and green curves) and baseline-shifted SP log.

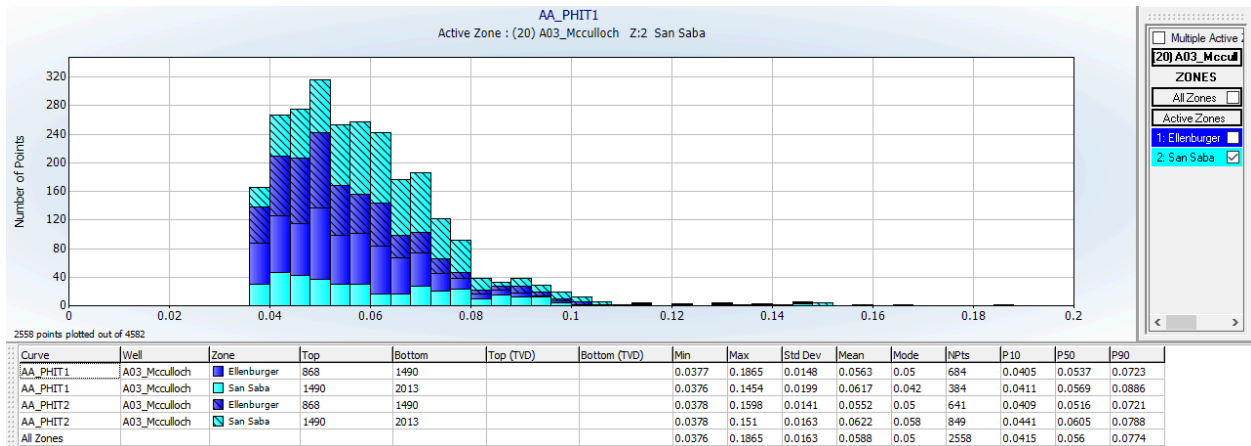


Figure 83. Histogram of porosity in the Ellenburger and San Saba formations in well #A03. Approximately 90% of porosity values are smaller than 0.06.

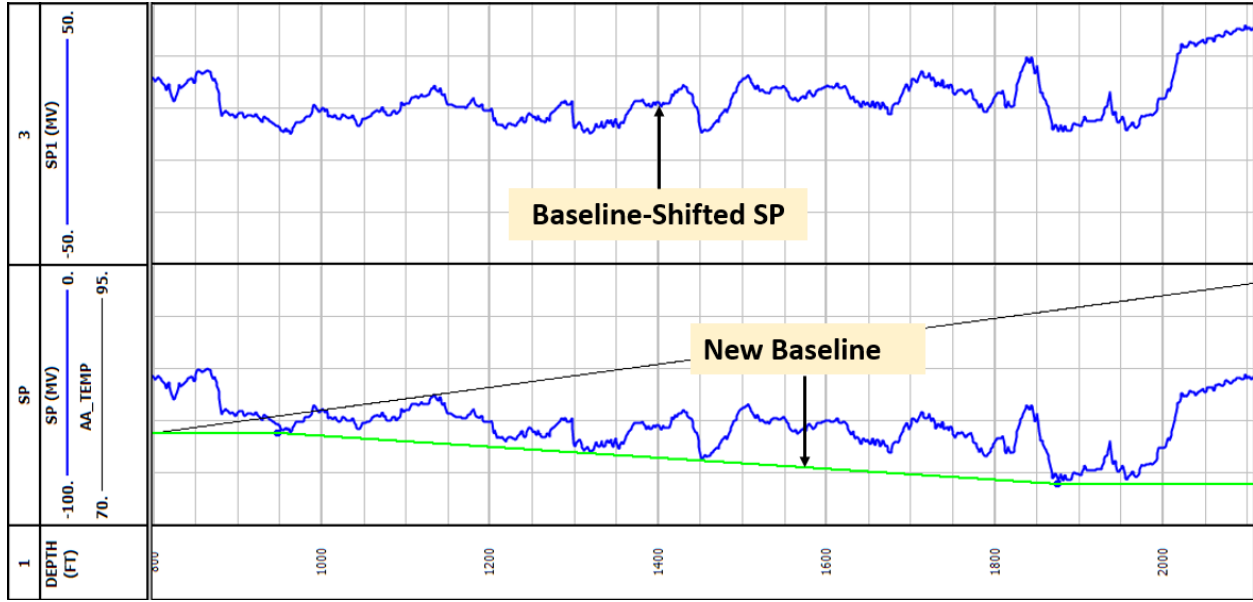


Figure 84. Baseline shift of the SP log acquired in the Ellenburger and San Saba formations in well #A03. Track 1: depth. Track 2: formation temperature (black curve), SP log (blue curve) and new SP baseline (green curve). Track 3: baseline-shifted SP log.

6.10 Assessment of Salinity and Porosity in the Hickory Formation in Well #A05

The temperature of the Hickory formation at 300 ft is approximately 73.3 degrees F in well #A05 (**Equation 16**). **Figure 85** shows the well logs acquired in this formation. Porosity in this formation is approximately 0.20 based on core analysis. We assume formation water resistivity equal to 2 ohm-m which corresponds to 2,673 NaCl ppm. Depth-by-depth porosity is calculated using **Equation 29**. The porosity exponent is equal to 1.77 based on core analysis. **Figure 86** shows that the average well-log-derived porosity is 0.21 with a standard deviation of 0.014. The mean porosity value is consistent with core-derived porosity and confirms the validity of the assumed formation water salinity.

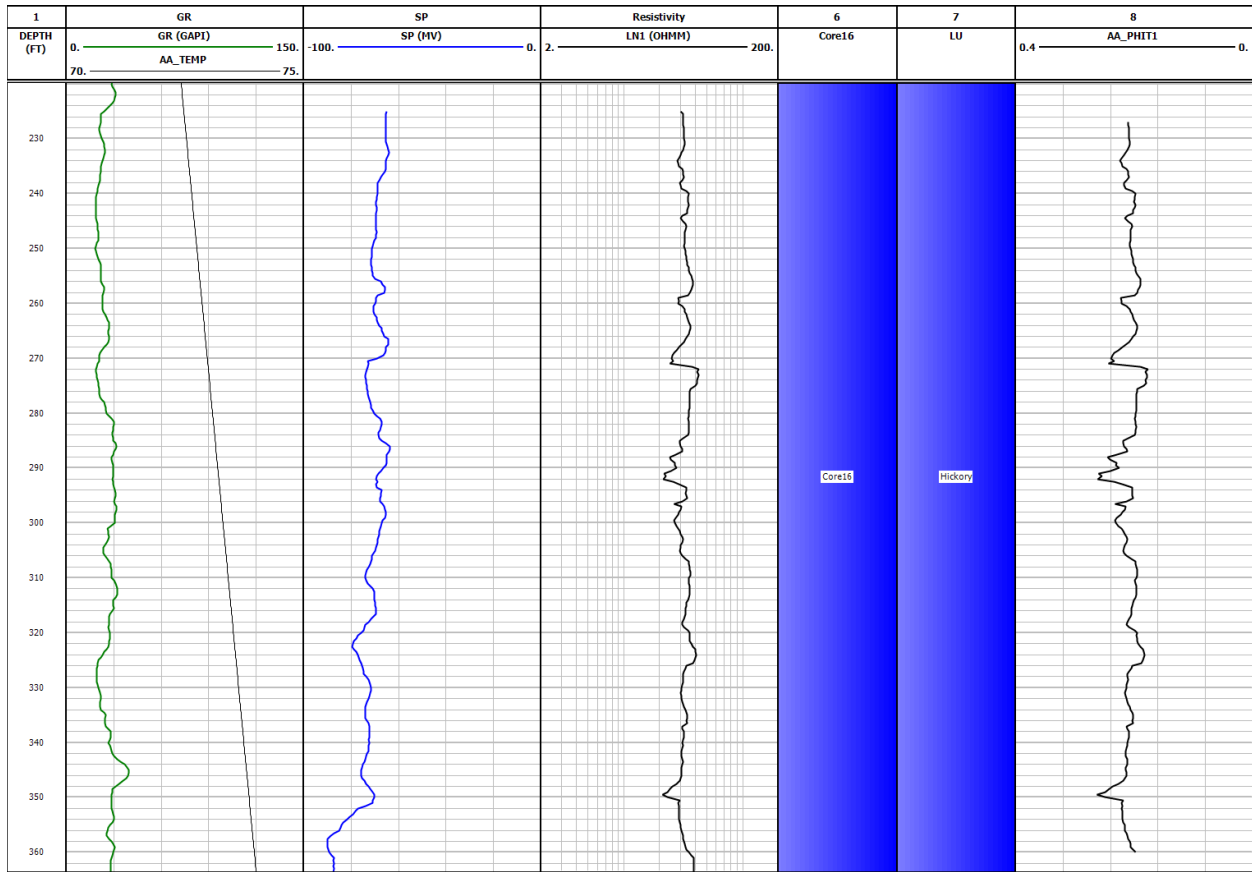


Figure 85. Well logs acquired in the Hickory formation in well #A05. Track 1: depth. Track 2: GR and formation temperature. Track 3: SP log. Track 4: resistivity log. Track 5: cored interval. Track 6: formation zones. Track 7: calculated porosity using the resistivity log.

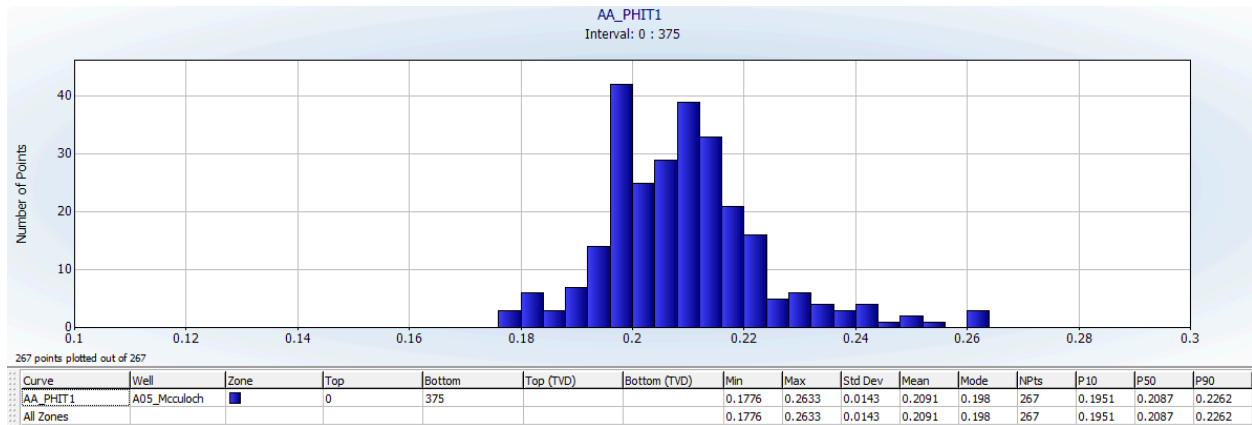


Figure 86. Histogram of porosity values in the Hickory formation in well #A05. The mean and standard deviation of porosity are equal to 0.21 and 0.14, respectively.

6.11 Assessment of Salinity, Porosity, and Shale Concentration in the Upper Wilcox Formation in Well #B06 Using Calculations

The SP values at 3,920 ft (clean sandstone) and 3,724 ft (pure shale) are equal to -80 mV and -30 mV, respectively. Thus, the SSP is equal to -50 mV. The formation temperature is equal to 130 degrees F (**Equation 16**). Mud-filtrate salinity is equal to 2,100 NaCl ppm. Based on **Equations 17, 18, 24** and **25**, formation water salinity is equal to 9,500 NaCl ppm and formation water resistivity is equal to 0.35 ohm-m. Depth-by-depth porosity is calculated using **Equation 29** using the ILD resistivity log. Note that Archie's equation is accurate in shale-free sandstones. More complex resistivity models, such as **Equation 27**, that incorporate shale resistivity should be used in shaly formations.

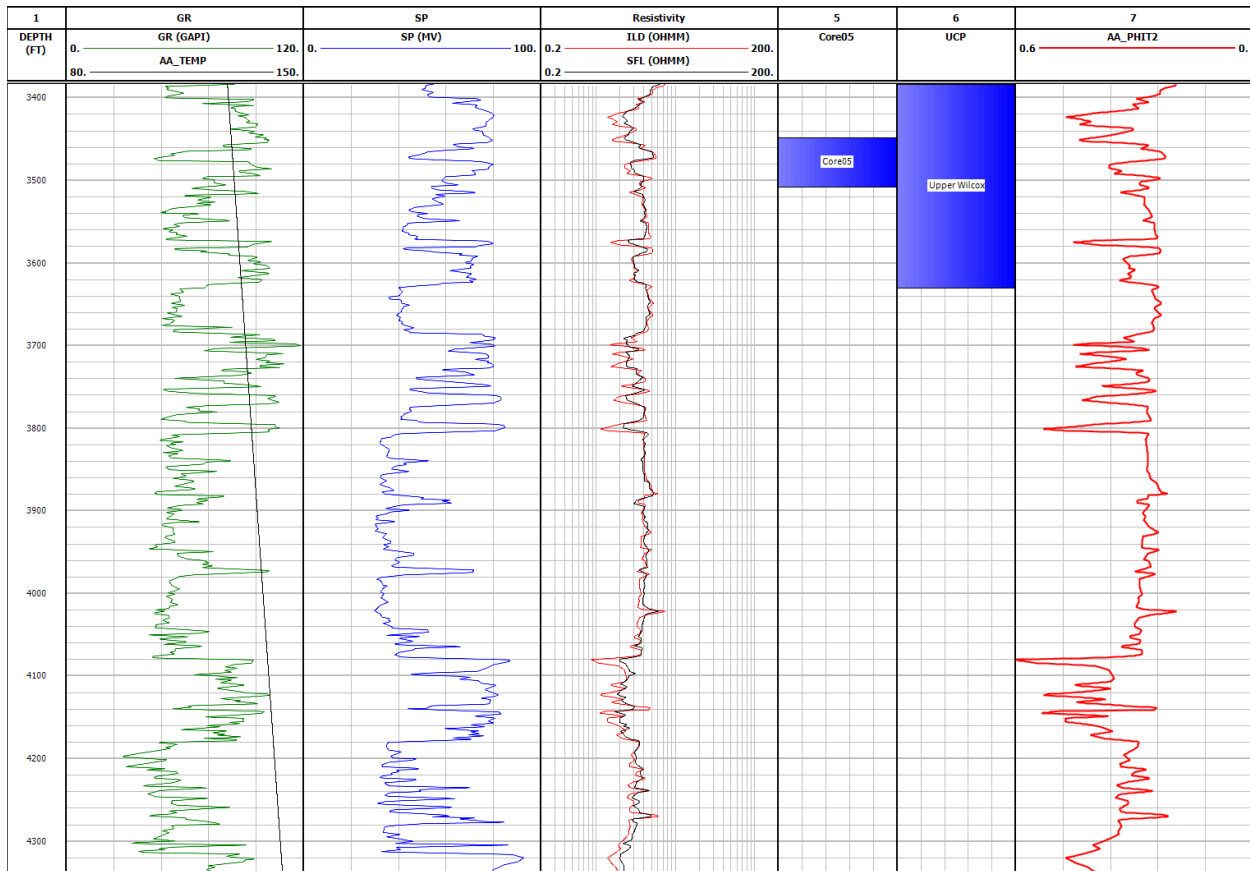


Figure 87. Well logs acquired in the Wilcox formation in well #B06. Track 1: depth. Track 2: GR and formation temperature. Track 3: SP log. Track 4: resistivity logs. Track 5: cored interval. Track 6: formation zones. Track 7: calculated porosity using ILD resistivity.

6.12 Assessment of Mineralogy in the Llano Uplift Based on Nuclear Logs in Well #A04

The interpretation of well logs in the Llano Uplift formations is challenging because of the presence of multiple minerals such as limestone (calcite), dolomite, sandstone (quartz), and shale. **Figure 88** shows the well logs acquired in well #A04. Neutron porosity (NPHI) and density porosity (DPHI) logs is displayed in limestone porosity units. In this section, we use the nuclear logs and Schlumberger charts to identify mineralogy. **Figure 88** shows the relationship between neutron porosity and bulk density in multiple formations. The sandstone, limestone, and dolomite lines are used as visual guides to identify mineralogy. Note that the data plotted corresponds to formation zones with negligible concentration of shale (relatively low GR). **Figure 89** shows the relationship between photoelectric factor and bulk density in multiple formations. The sandstone, limestone, and dolomite lines are used as visual guides to identify mineralogy. Note that the photoelectric factor (PEF) log is mostly sensitive to mineralogy and less sensitive to porosity. As expected, **Figures 89** and **90** indicate that the Hickory sandstones are composed of quartz, the Marble Falls limestones are composed of calcite, and the Ellenburger and San Saba formations are composed of limestone and dolomite.

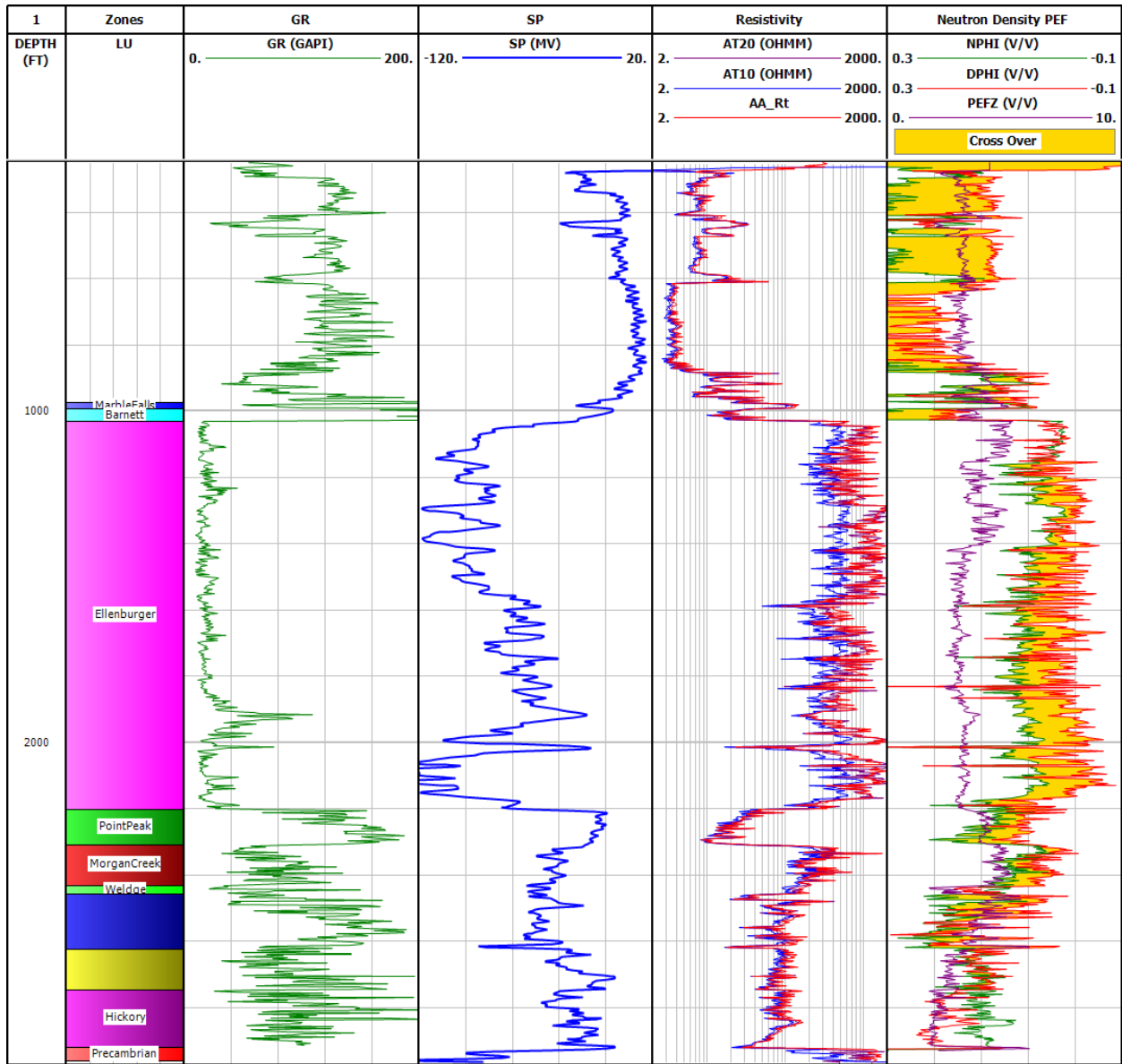


Figure 88. Well logs in well #A04. Track 1: depth. Track 2: formation zones. Track 3: GR log. Track 4: SP log. Track 5: resistivity logs. Track 6: PEF, density, and neutron porosity logs.

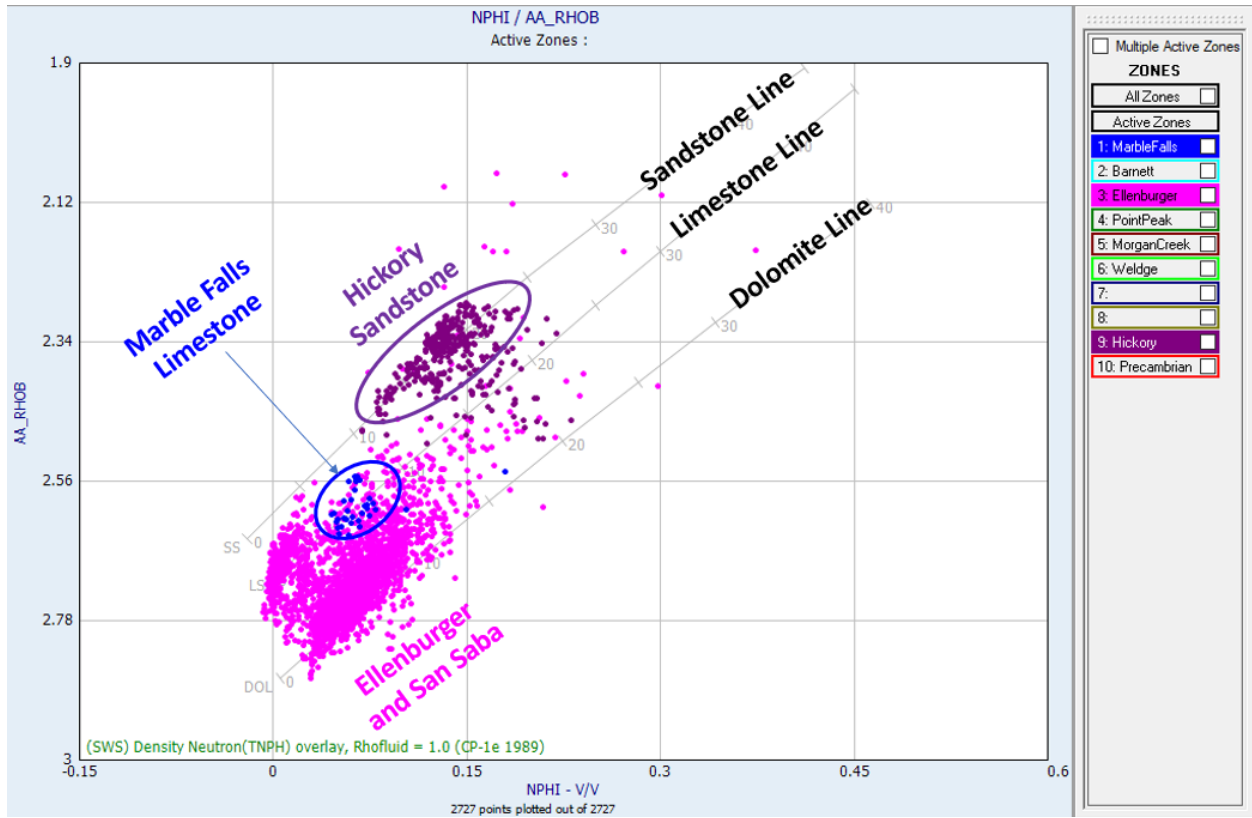


Figure 89. Relationship between neutron porosity and bulk density in well #A04. The sandstones, limestone, and dolomite lines are used as visual guides to identify mineralogy. The markers with different colors represent well log data from different formations: Hickory sandstones, Marble Falls limestones, Ellenburger and San Saba carbonate rocks.

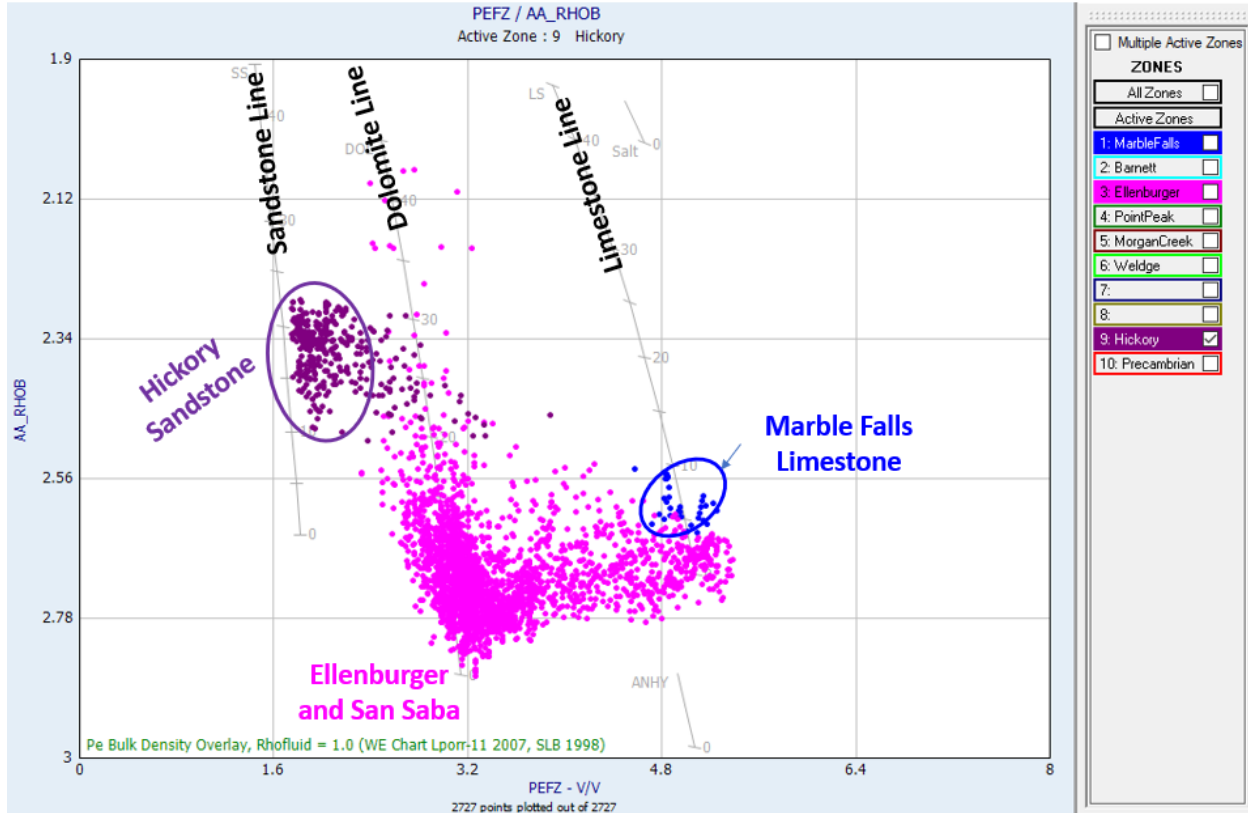


Figure 90. Relationship between photoelectric factor (PEF) and bulk density in well #A04. The sandstones, limestone, and dolomite lines are used as visual guides to identify mineralogy. The markers with different colors represent well log data from different formations: Hickory sandstones, Marble Falls limestones, Ellenburger and San Saba carbonate rocks.

6.13 Assessment of petrophysical properties of the Ellenburger and San Saba Formations in Well #A04

Assessment of mineralogy, porosity, and salinity in well #A04

The interpretation of well logs in the Ellenburger and San Saba formations is challenging because of the presence of multiple minerals such as calcite, dolomite, and chert (SiO_2). A multiminereral interpretation is conducted on the Interactive Petrophysics (IP) software. Track 7 of **Figure 91** shows the estimated porosity and mineralogy. Note that Calcite-rich layers are tight (porosity < 4%) and that dolomite-rich layers exhibit low porosity (porosity < 8%). Track 9 of **Figure 91** shows that porosity and SP logs are correlated (the larger the porosity, the greater the SSP deflection). Archie's porosity exponent is calculated based on porosity using **Equation 14** and it is displayed on the last track of **Figure 91**. Depth-by-depth temperature is calculated using **Equation 16**. Assuming that formation water salinity is equal to 1,500 ppm (NaCl), depth-by-depth formation water resistivity is calculated using **Equation 17**. The calculated formation temperature and formation water resistivity are displayed on the third track of **Figure 91** along with the GR log. Archie's porosity exponent is then calculated using **Equation 1**. Note that Archie's porosity exponent was calculated using two different methods (**Equations 1 and 14**) in this section. The last track of **Figure 91** compares estimates of Archie's porosity exponent using **Equations 1 and 14**. The good agreement between **Equations 1 and 14** indicates that the assumed formation water salinity, equal to 1,500 ppm (NaCl), is correct.

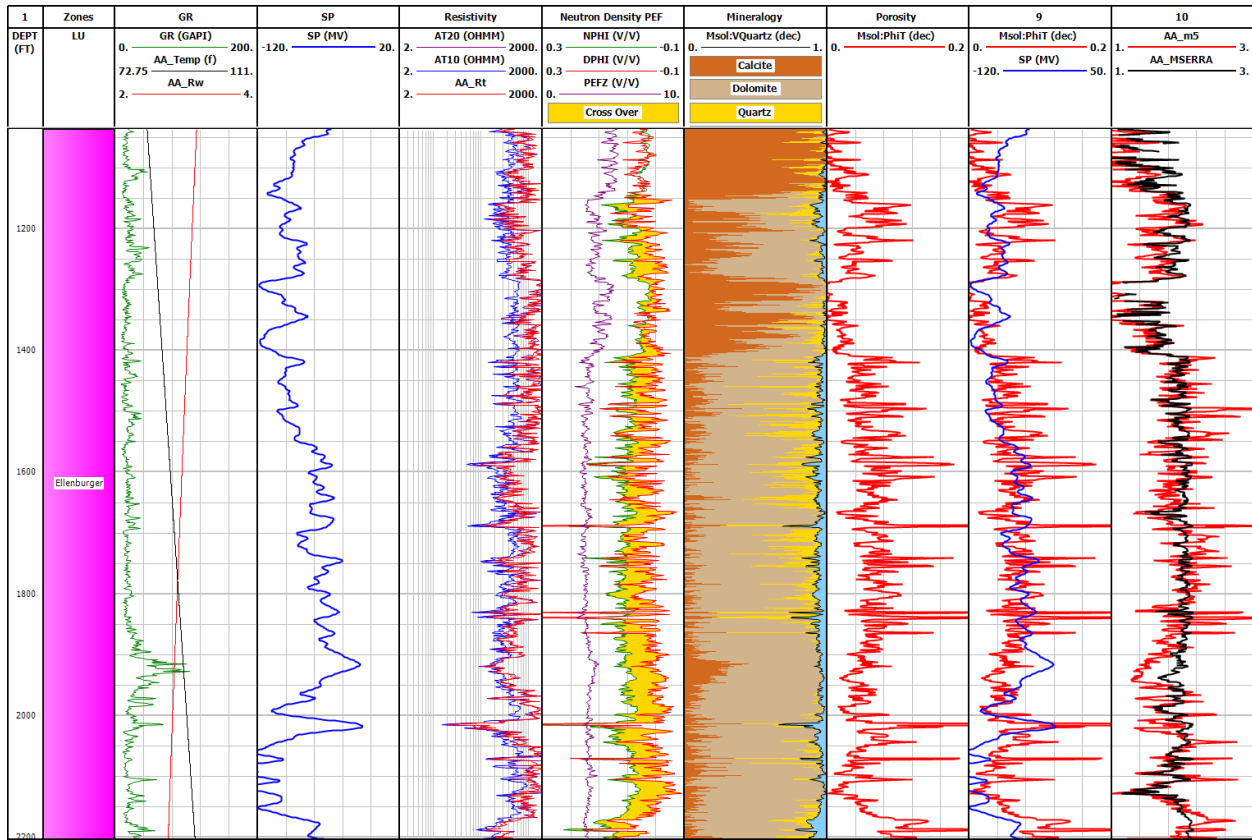


Figure 91. Multiminerational interpretation of well logs in well #A04. Track 1: depth. Track 2: formation zones. Track 3: GR log, formation temperature, and formation water resistivity. Track 4: SP log. Track 5: resistivity logs. Track 6: PEF, density, and neutron porosity logs. Track 7: porosity and mineralogy (quartz, calcite, and dolomite). Track 8: porosity. Track 9: porosity and SP log. Track 10: Archie's porosity exponent calculated using two different methods: Equations 1 and 14.

Numerical simulation of density and neutron porosity logs in well #A04 Using UTAPWeLS

The objective of this section is to invert (deconvolute) density and neutron porosity logs to estimate bed thicknesses and correct for shoulder-bed effects in the presence of thin beds. We assume a vertical well and horizontal layers. Layer boundaries are located at the inflection point of the density log. The estimation of layer-by-layer formation properties (bulk density and migration length) is obtained through an inversion method that implements the Markov-Chain Monte Carlo (MCMC) algorithm. Tracks 2 and 3 in **Figure 92** compare the available well logs (black curves) with their numerical simulations (red curves). The available well logs and their numerical simulation are in good agreement. The numerically simulated borehole density image (Track 4) exhibits thin laminations. The inverted layer-by-layer bulk density is displayed as a green blocky log on the last Track of **Figure 92**.

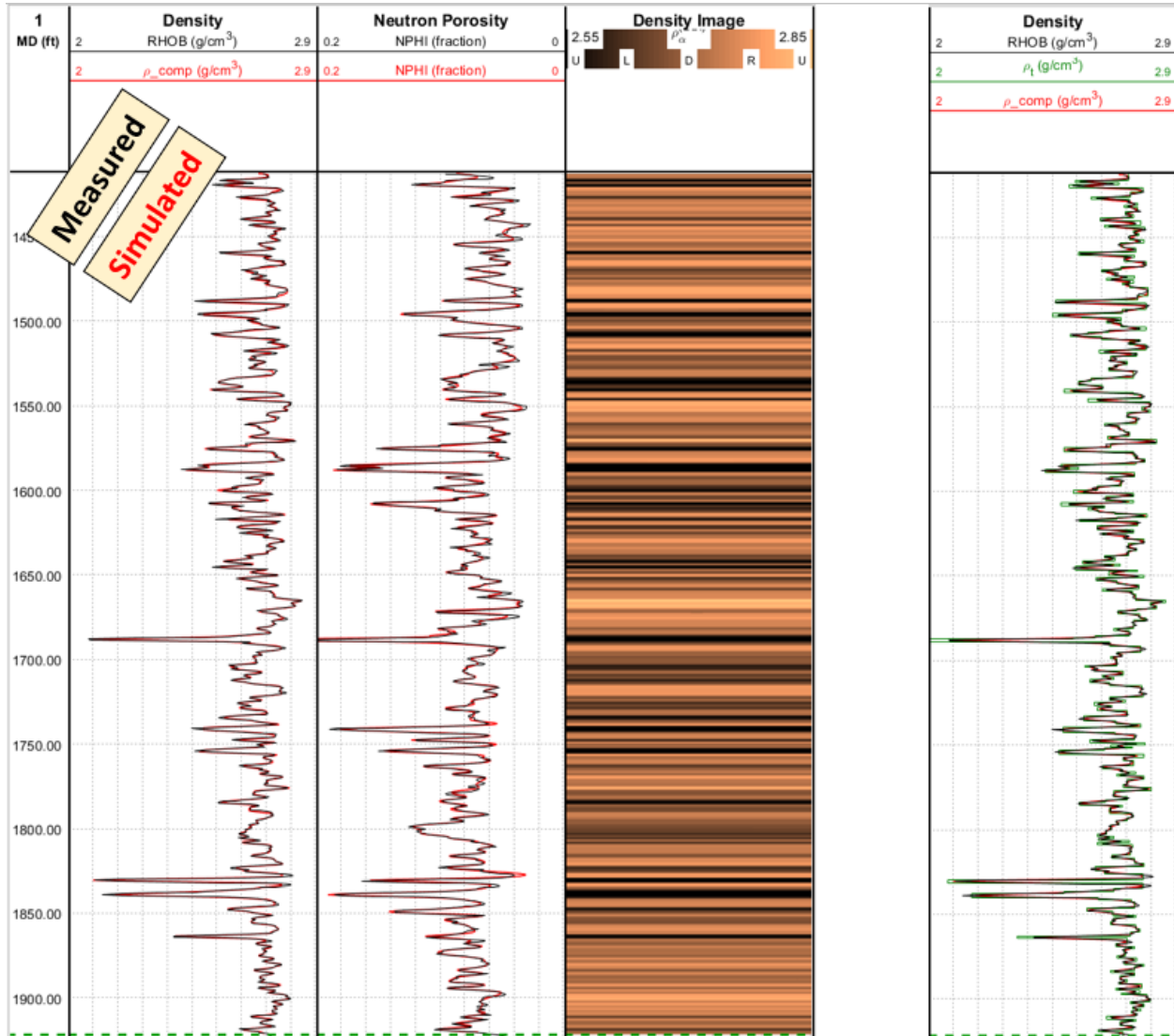


Figure 92. Numerical simulation of density and neutron porosity logs in well #A04. Track 1: depth. Track 2: measured and numerically simulated density logs. Track 3: measured and numerically simulated neutron porosity logs. Track 4: numerically simulated density image. Track 5: inverted layer-by-layer density.

Numerical simulation of resistivity logs in the presence of mud-filtrate invasion in well #A04 Using UTAPWeLS

Resistivity logs were acquired using Schlumberger's array induction tool (AIT). We assume a piston-like resistivity profile that can be described with three parameters: the radial length of invasion, the flushed zone resistivity, and virgin zone resistivity (Merletti et al., 2022; Merletti et al., 2023; Mohamed et al., 2023). Track 1 of **Figure 93** shows the estimated radial and vertical distributions of formation resistivity; the dark blue radial zone corresponds to the radius of the borehole (equal to 10 cm approximately), the light blue radial zone corresponds to the invaded zone, and the light blue to yellow zone corresponds to the virgin zone. Results of the numerical simulations indicate that the radial length of invasion is smaller than 10 cm. Track 2 of **Figure 93** shows the estimated layer -by-layer resistivity values in the flushed (black) and virgin (red curve) zones. Track 4 of **Figure 93** shows the numerically simulated resistivity logs, which are in good agreement with the measured well logs (Track 5).

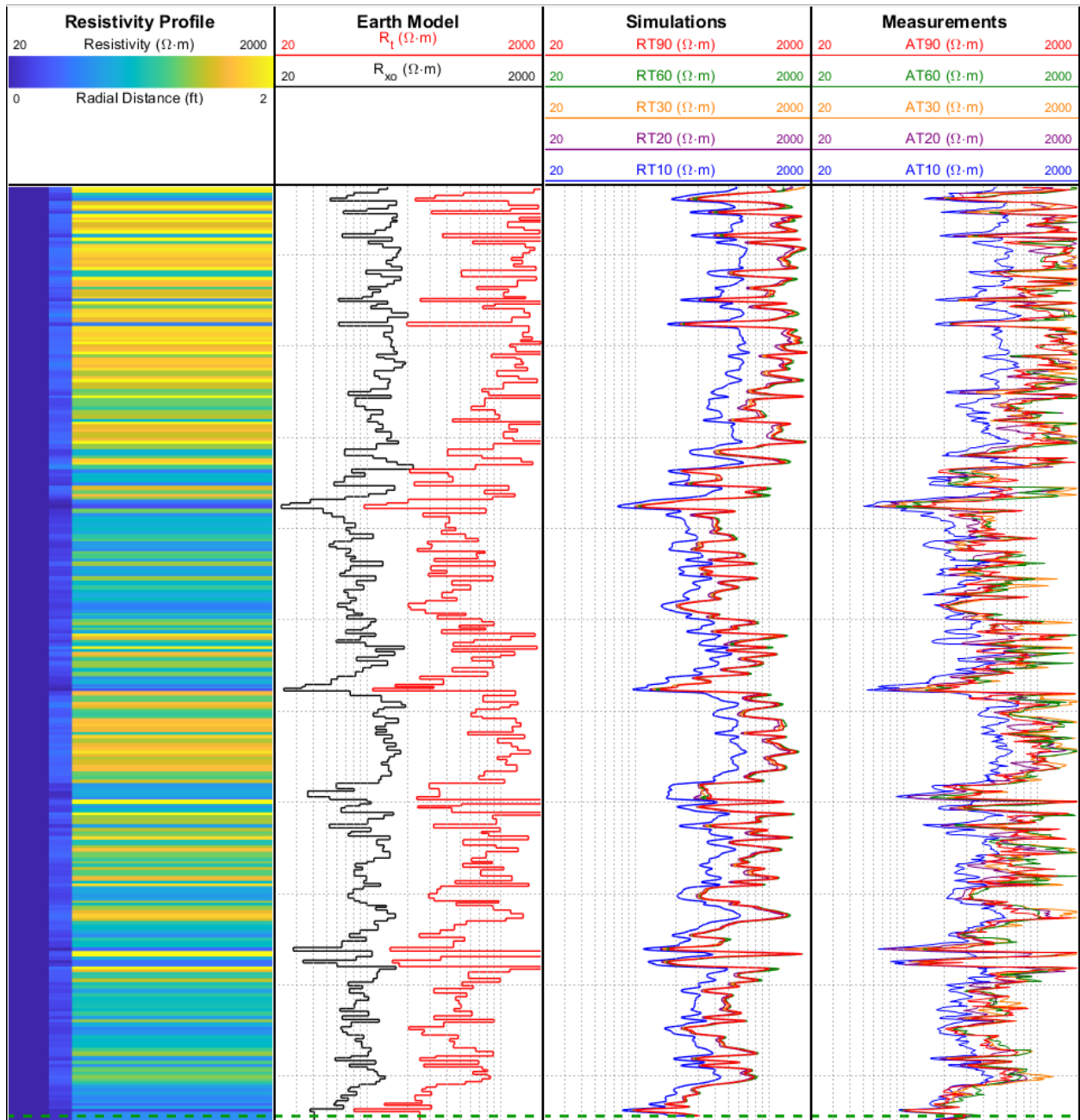


Figure 93. Numerical simulation of resistivity logs in well #A04. Track 1: radial profile of resistivity. Track 2: Layer-by-layer flushed- and virgin-zone resistivities. Track 3: numerically simulated resistivity logs. Track 4: available resistivity logs.

6.14 Assessment of the Radial Length of invasion in Oil-Bearing Carrizo Sandstones in well #B01 Using UTAPWeLS

The radial length of invasion in hydrocarbon-bearing formations can be used to infer flow-related properties of the rocks such as effective porosity and permeability (Bennis et al., 2019; Bennis et al., 2023c). The resistivity profile of the oil-bearing sandstones in well #B01 is modeled by matching resistivity logs with their numerical simulation. Resistivity logs were acquired using a deep-sensing

laterolog (lat_18) and a dual induction tool (SN and ILD). The last track of **Figure 94** compares the available resistivity logs (solid lines) with their numerical simulations (dashed lines). Track 5 of **Figure 94** shows the estimated layer-by-layer virgin-zone resistivity (in red) and flushed-zone resistivity (in black). Track 4 of **Figure 94** shows that permeable rocks exhibit a radial length of invasion equal to 1.5 m approximately. Note that a piston-like resistivity model is assumed. Low permeability rocks exhibit negligible separation between resistivity logs and negligible radial length of invasion.

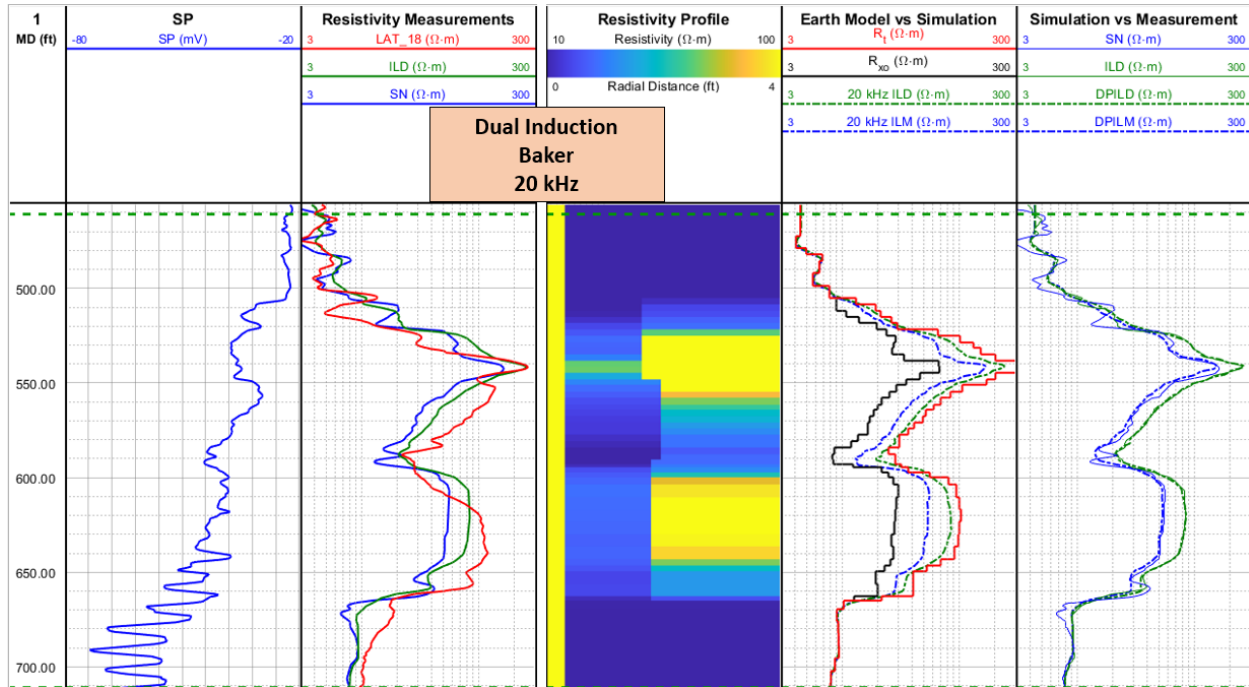


Figure 94. Numerical simulation of resistivity logs in well #B01. Track 1: depth. Track 2: SP log. Track 3: resistivity logs. Track 4: modeled radial and vertical variations of resistivity. Track 5: estimated flushed- and virgin-zone resistivity values and the numerically simulated dual induction resistivity logs. Track 6: measured (solid lines) and numerically simulated (dashed lines) resistivity logs.

7 CONCLUSIONS

In this study, we conducted numerical simulations of well logs and laboratory measurements on multiples samples from the Llano Uplift and Upper Coastal Plains aquifers to assess storage and flow properties of rocks. Laboratory measurements include porosity, permeability, porosity exponent (m), and nuclear magnetic resonance (NMR). Additionally, we measured grain density, NMR T_{2LM} , NMR $T_{2,Peak}$, and NMR irreducible water saturation. For rock samples with permeability greater than 1 mD, water permeability was measured using core flooding. For tight rocks, permeability was measured using a pulse decay permeameter. The parameters of multiple petrophysical models were calibrated using core data such as the SDR permeability model, the Timur-Coates permeability model, and the Timur permeability model. For each formation, relationships relating porosity, permeability and irreducible water saturation were derived.

In the Upper Coastal Plains, the Wilcox formation exhibits different facies such as coarse- and medium-grained sandstones, thinly laminated shaly sandstones, siderite nodules, and shales. The average porosity of shale-free sandstones is 30 percent. The porosity exponent, m , is equal to 1.95. Grain density is about 2.65 g/cc. Sandstones from core #1 representing the Queen City formation were extremely brittle, making core sampling not possible. Sampling from the Jackson and Yegua formations was not possible either because core #7 was constituted of small cuttings only.

In the Llano Uplift, the Hickory formation exhibits an interlayering of sandstones with different grain sizes. The average porosity of coarse-grained sandstones is 25 percent. The porosity exponent, m , is equal to 1.77. Grain density is about 2.65 g/cc. The Ellenburger and San Saba formations are composed of limestone, dolomite, and chert. Porosity is typically less than ten percent. There is no clear trend between porosity and permeability. The porosity exponent m increases with increasing porosity due to the presence of fractures and it is approximately equal to 1.95.

The assessment of storage and flow properties of aquifers is crucial for water resources management. Results from this study can also be used to assess the viability of geothermal energy generation and/or carbon capture and sequestration projects in Texas.

8 REFERENCES

- Aguilera, S., and Aguilera, R., 2003, Improved models for petrophysical analysis of dual porosity reservoirs: *Petrophysics*, **44**(01), 21-35.
- Aguilera, R., 1990, Extensions of Pickett Plots for the analysis of shaly formations by well logs: *The log Analyst*, **31**(05), 304-313.
- Archie, G.E., 1942, The electrical resistivity logs as an aid in determining some reservoir characteristics: *Trans. AIME*, **146**, 54-67.
- Bennis, M., and Torres-Verdín, C., 2019, Estimation of Dynamic Petrophysical Properties From Multiple Well Logs Using Machine Learning and Unsupervised Rock Classification, Paper KKKK, Transactions, SPWLA 60th Annual Logging Symposium, The Woodlands, Texas, USA, 15-19 June. DOI: [10.30632/T60ALS-2019_KKKK](https://doi.org/10.30632/T60ALS-2019_KKKK).
- Bennis, M., 2022, New Methods for the Interpretation of Borehole Geophysical Measurements and Core Data Acquired in Spatially Complex Rocks, PhD dissertation, The University of Texas at Austin, Austin, Texas. URL: <https://hdl.handle.net/2152/116968>. Accessed October 7, 2023.
- Bennis, M., and Torres-Verdín, C., 2023a, Petrophysical Interpretation of Logging-While-Drilling Borehole Measurements in the Presence of Electrical Anisotropy, Mud-Filtrate Invasion, Noise, and Well Deviation Effects, *Geophysics*, **88**(6), D371-D390. DOI: [10.1190/geo2023-0075.1](https://doi.org/10.1190/geo2023-0075.1).
- Bennis, M., and Torres-Verdín, C., 2023b, Numerical Simulation of Well Logs Based on Core Measurements: An Effective Method for Data Quality Control and Improved Petrophysical Interpretation, *Petrophysics*, **64**(5), 753-772. DOI: [10.30632/PJV64N5-2023a9](https://doi.org/10.30632/PJV64N5-2023a9).
- Bennis, M., and Torres-Verdín, C., 2023c, Automatic Multiwell Assessment of Flow-Related Petrophysical Properties of Tight Gas Sandstones Based on The Physics of Mud-Filtrate Invasion, Paper SPE-214668-PA, SPE Reservoir Evaluation & Engineering, **26**(3), 543-564. DOI: [10.2118/214668-PA](https://doi.org/10.2118/214668-PA).
- Ellis, D. V., and Singer, J. M., 2007, *Well logging for earth scientists*: Springer
- Jones, S. C., 1997, A technique for faster pulse-decay permeability measurements in tight rocks: *SPE Form Eval*, **12**(01), 19-25.
- Luycx, M., Bennis, M., Torres-Verdín, C., and Preeg, W., 2020, Simulation of Borehole Nuclear Measurements: A Practical Tutorial Guide for Implementation of Monte Carlo Methods and Approximations Based on Flux Sensitivity Functions, *Petrophysics*, **61**(1), 4-36. DOI: [10.30632/PJV61N1-2020T1](https://doi.org/10.30632/PJV61N1-2020T1).
- Merletti, G., Rabinovich, M., Al Hajri, S., Dawson, W., Farmer, R., Ambria, J., and Torres-Verdin, C., 2022, New Iterative Resistivity Modelling Workflow Reduces Uncertainty in the Assessment of Water Saturation in Deeply-Invaded Reservoirs, Paper 0057, Transactions, SPWLA 63rd Annual Logging Symposium, Stavanger, Norway, 11-15 June. DOI: [10.30632/SPWLA-2022-0057](https://doi.org/10.30632/SPWLA-2022-0057).
- Merletti, G., Al Hajri, S., Rabinovich, M., Farmer, R., Bennis, M., and Torres-Verdín, C., 2023, Assessment of True Formation Resistivity and Water Saturation in Deeply Invaded Tight-Gas Sandstones Based on the Combined Numerical Simulation of Mud-Filtrate Invasion and Resistivity Logs, *Petrophysics*, **64**(4), 502-517. DOI: [10.30632/PJV64N4-2023a2](https://doi.org/10.30632/PJV64N4-2023a2).
- Meyer, J. E., Croskrey, A. D., Suydam, A. K., van Oort, N., 2020, Brackish Groundwater in aquifers of the Upper Coastal Plains, Central Texas: TWDB report 385.

Texas Water Development Board Contract Number 2248302663

Final Report: Core Testing and Numerical Simulation of Well Logs for the Upper Coastal Plains and Llano Uplift Aquifers

- Mohamed, T. S., Bennis, M., Torres-Verdín, C., Merletti, G., and Gelvez, C., 2023, Using formation tester measurement to estimate depth of invasion and water saturation in deeply invaded tight-gas sandstones, SPWLA 64th Annual Logging Symposium, Lake Conroe, Texas, USA, 10-14 June.
- Timur, A., 1968, An investigation of porosity, permeability, & residual water saturation relationships for sandstone reservoirs: *The Log Analyst*, **9**, 8-17.
- Serra, O., 1989, Formation MicroScanner image interpretation: Schlumberger Educational Service, Houston, SMP-7028, 117.
- Standen, A., and Ruggiero, R., 2007, Llano Uplift aquifers structure and stratigraphy: TWDB contract number 0604830614.
- Voss, B., Torres-Verdín, C., Gandhi, A., Alabi, G., and Malek, L., 2009, Common stratigraphic framework to simulate well logs and to cross-validate static and dynamic petrophysical interpretations: Paper presented at the SPWLA 50th Annual Logging Symposium, The Woodlands, Texas, June 2009.

APPENDIX A - DIGITIZED WELL LOGS

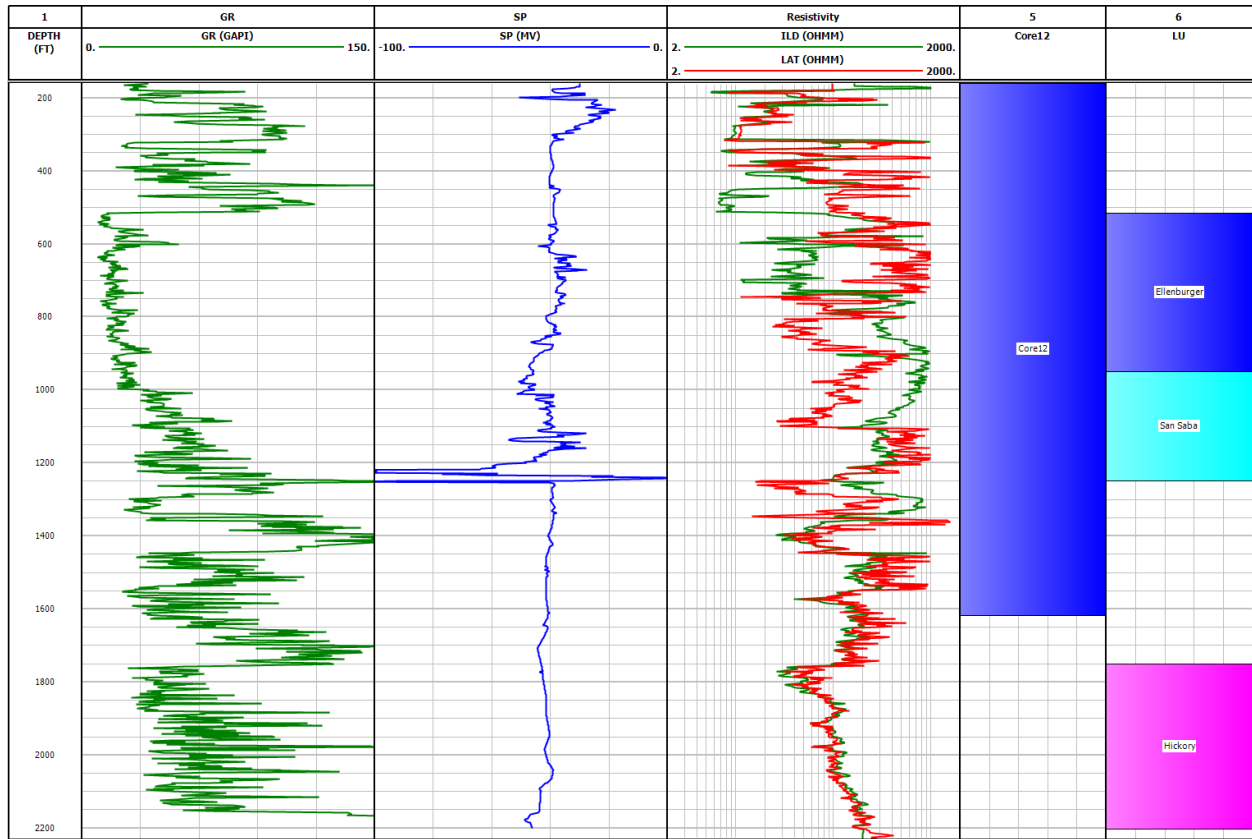


Figure 95. Well logs of well #A01. Track 1: depth. Track 2: SP log. Track 3: resistivity logs. Track 4: cored interval. Track 5: formation zones.

Texas Water Development Board Contract Number 2248302663
 Final Report: Core Testing and Numerical Simulation of Well Logs for the Upper Coastal Plains and Llano Uplift Aquifers

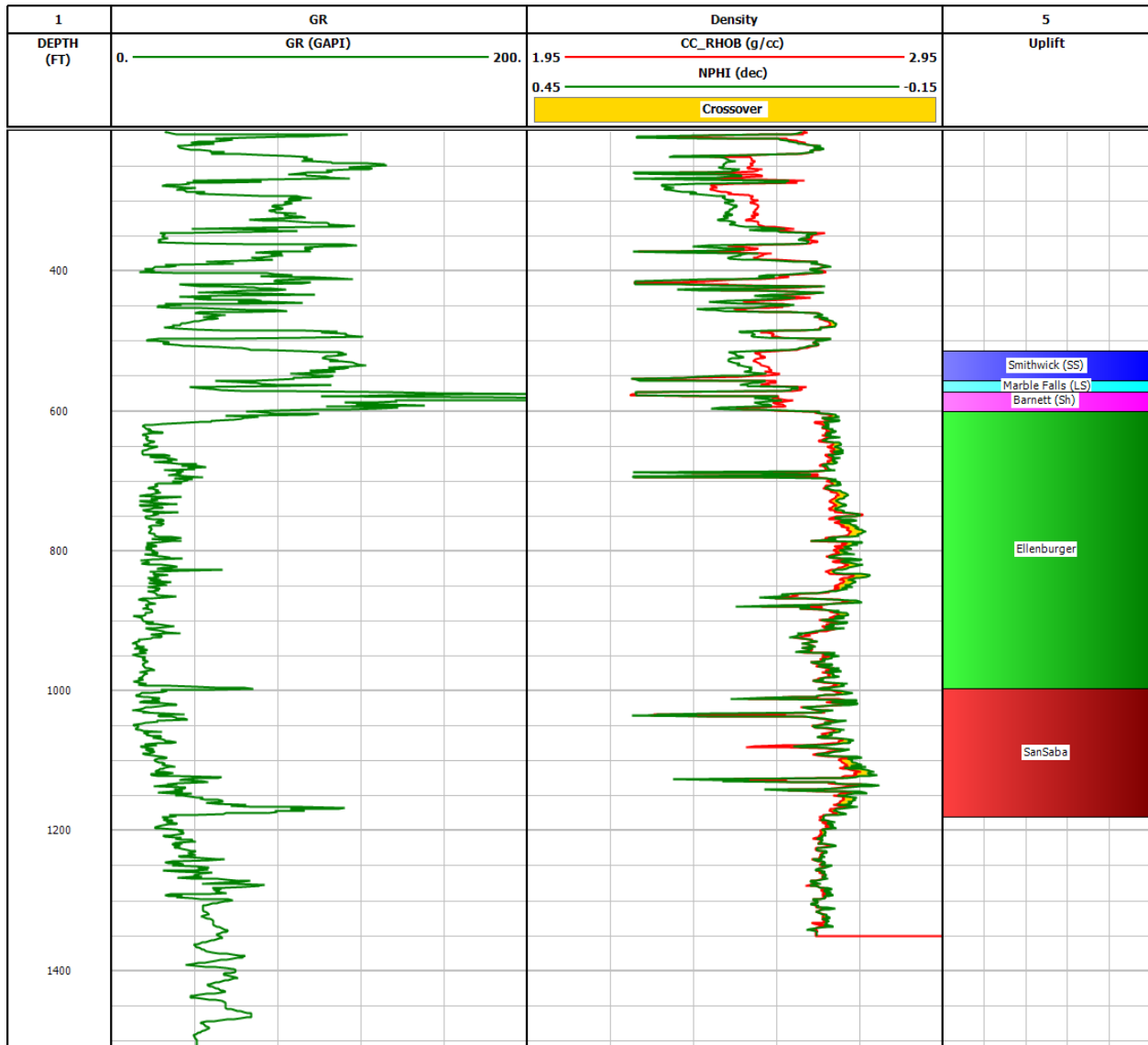


Figure 96. Well logs of well #A02. Track 1: depth. Track 2: GR log. Track 3: resistivity logs. Track 4: formation zones.

Texas Water Development Board Contract Number 2248302663

Final Report: Core Testing and Numerical Simulation of Well Logs for the Upper Coastal Plains and Llano Uplift Aquifers

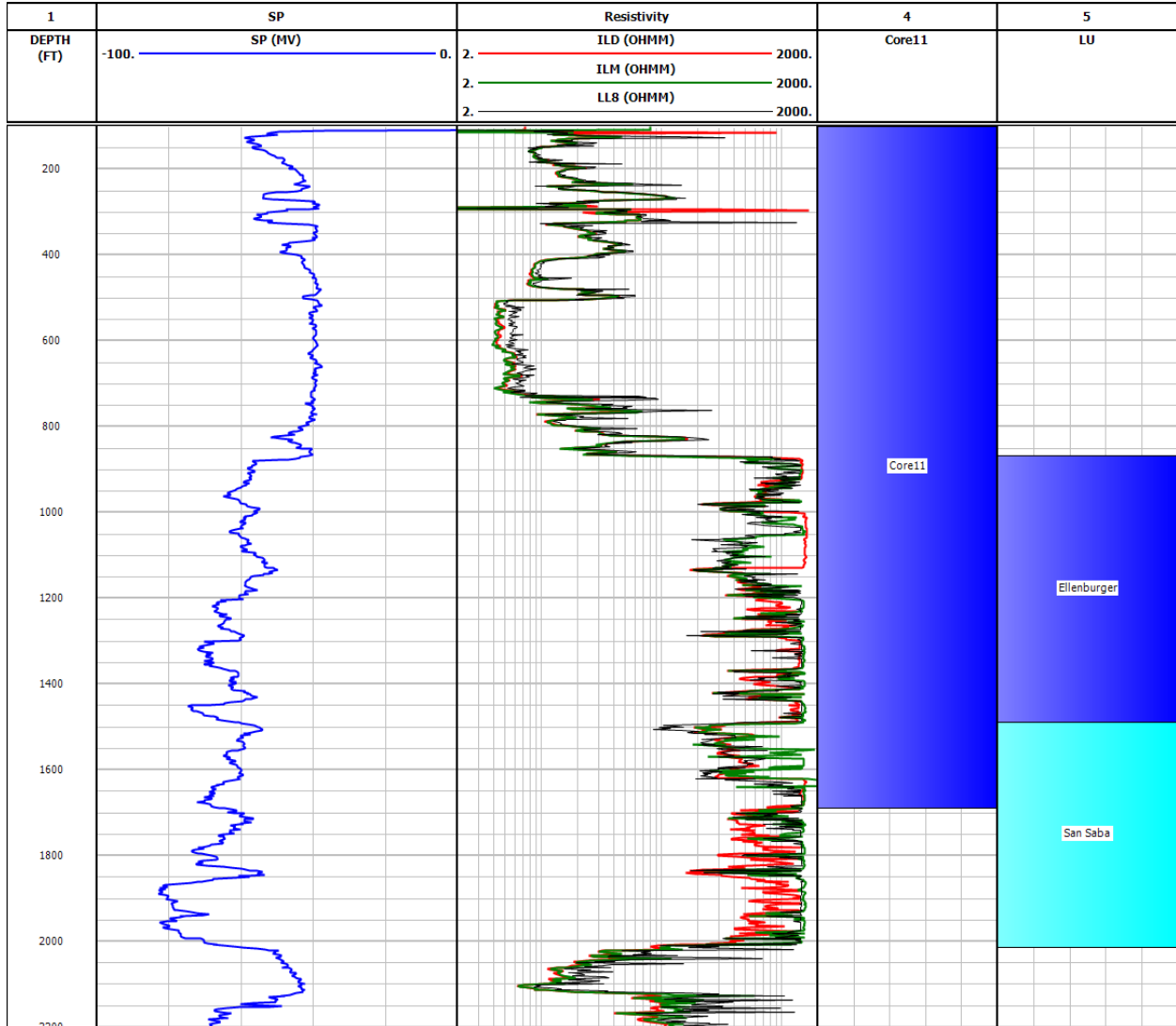


Figure 97. Well logs of well #A03. Track 1: depth. Track 2: SP log. Track 3: resistivity logs. Track 4: cored interval. Track 5: formation zones.

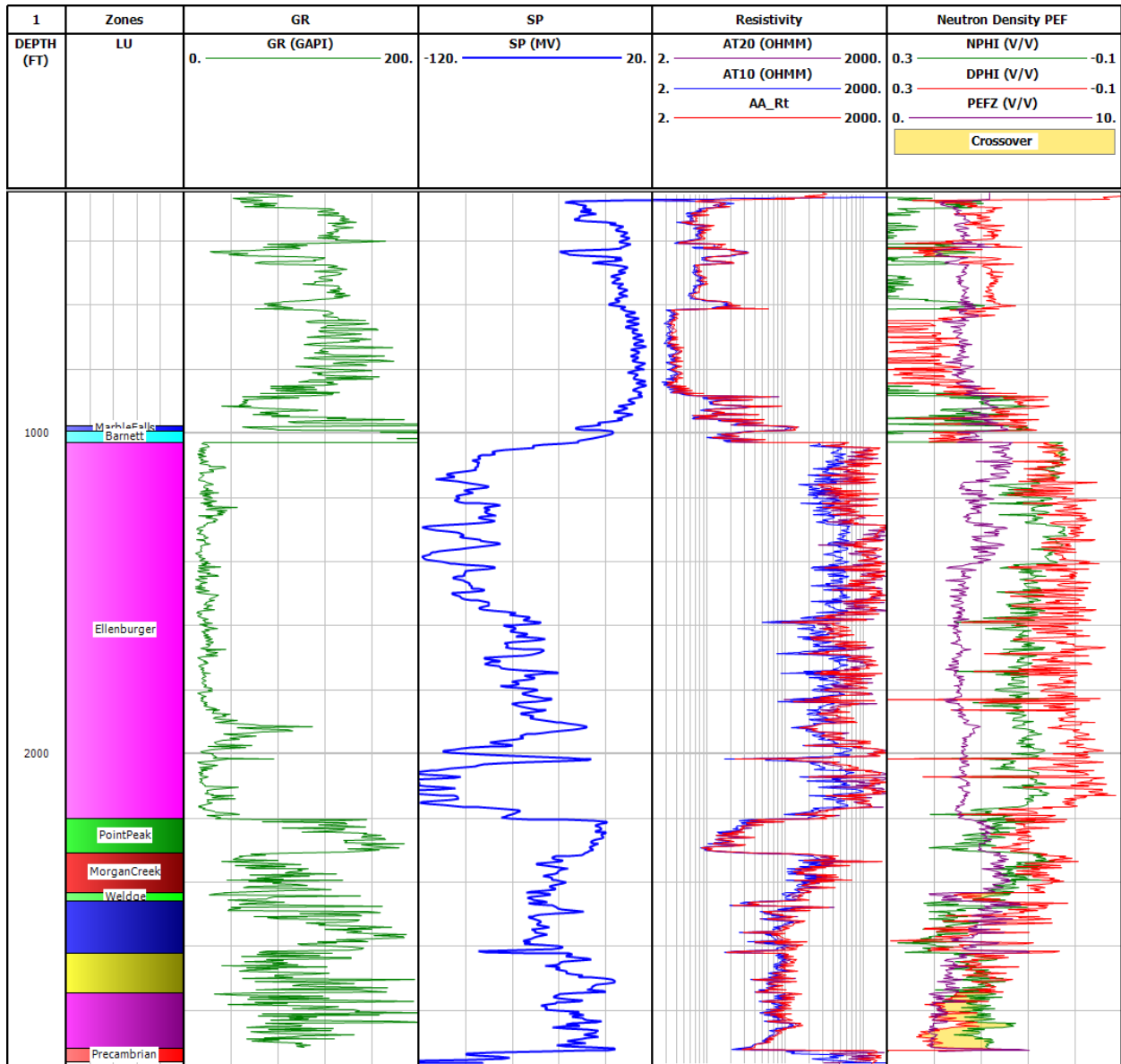


Figure 98. Well logs of well #A03. Track 1: depth. Track 2: formation zones. Track 3: GR log. Track 4: SP log. Track 5: resistivity logs. Track 6: nuclear logs.

Texas Water Development Board Contract Number 2248302663

Final Report: Core Testing and Numerical Simulation of Well Logs for the Upper Coastal Plains and Llano Uplift Aquifers

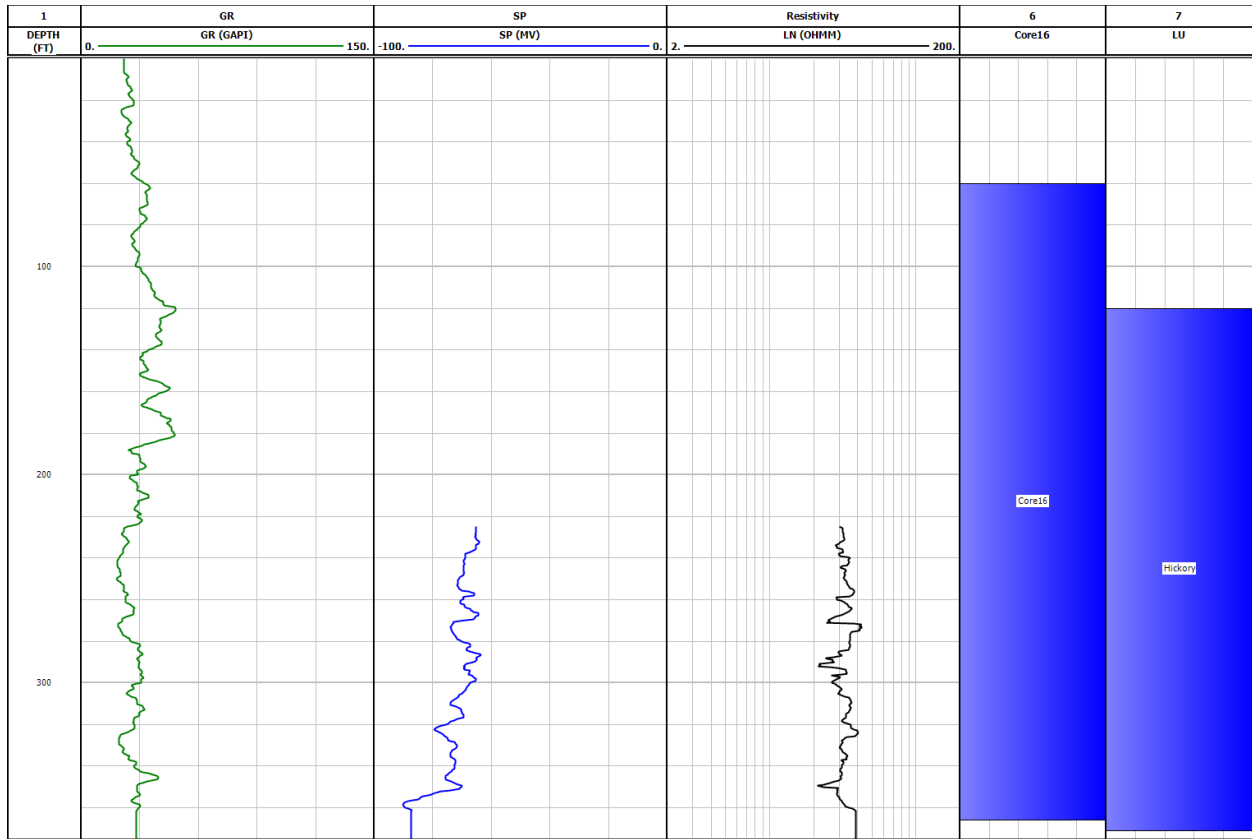


Figure 99. Well logs of well #A05. Track 1: depth. Track 2: GR log. Track 3: SP log. Track 4: resistivity logs. Track 5: cored interval. Track 6: formation zones.

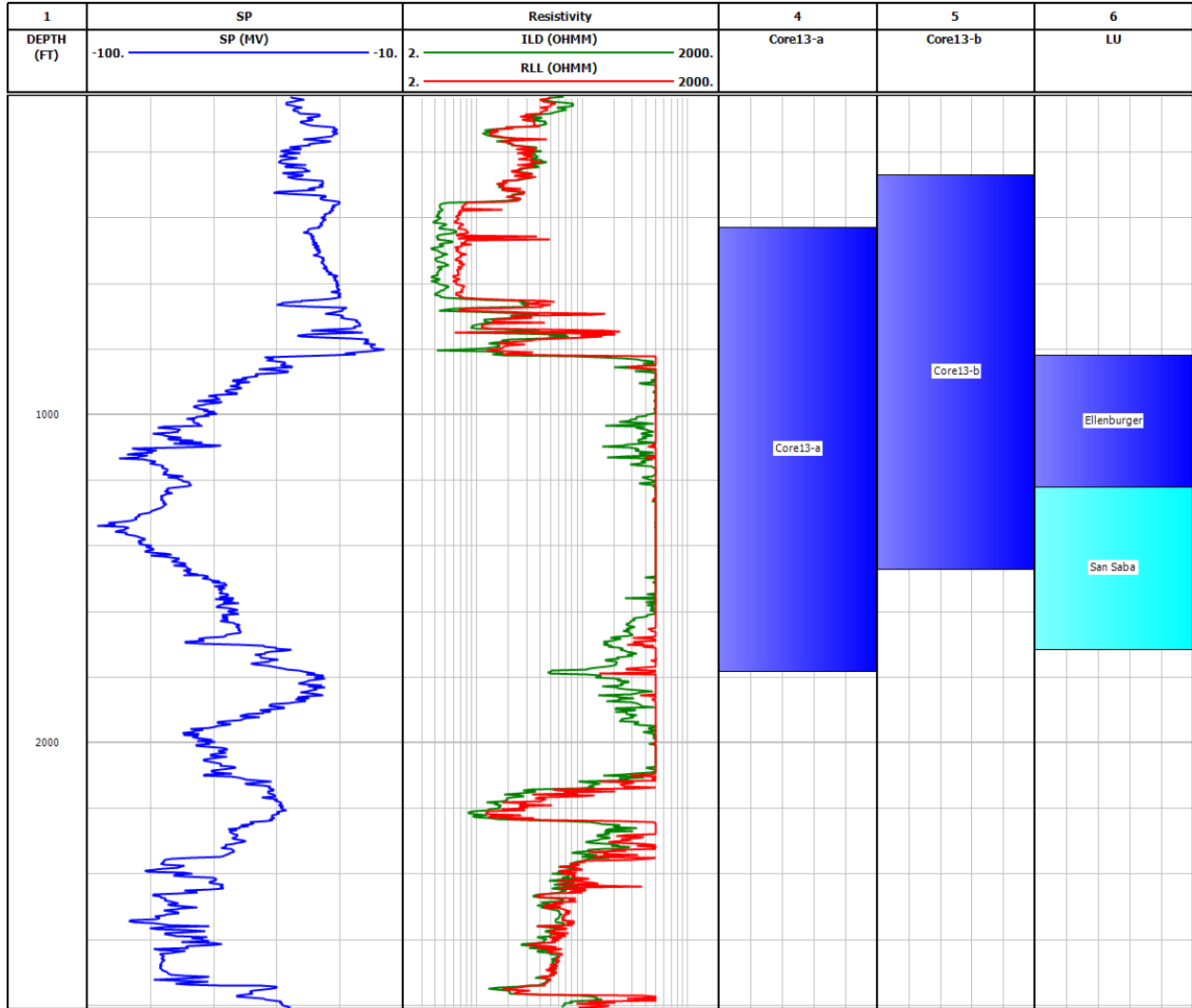


Figure 100. Well logs of well #A06. Track 1: depth. Track 2: SP log. Track 3: resistivity logs. Track 5: cored interval. Track 6: cored interval. Track 7: formation zones.

Texas Water Development Board Contract Number 2248302663

Final Report: Core Testing and Numerical Simulation of Well Logs for the Upper Coastal Plains and Llano Uplift Aquifers

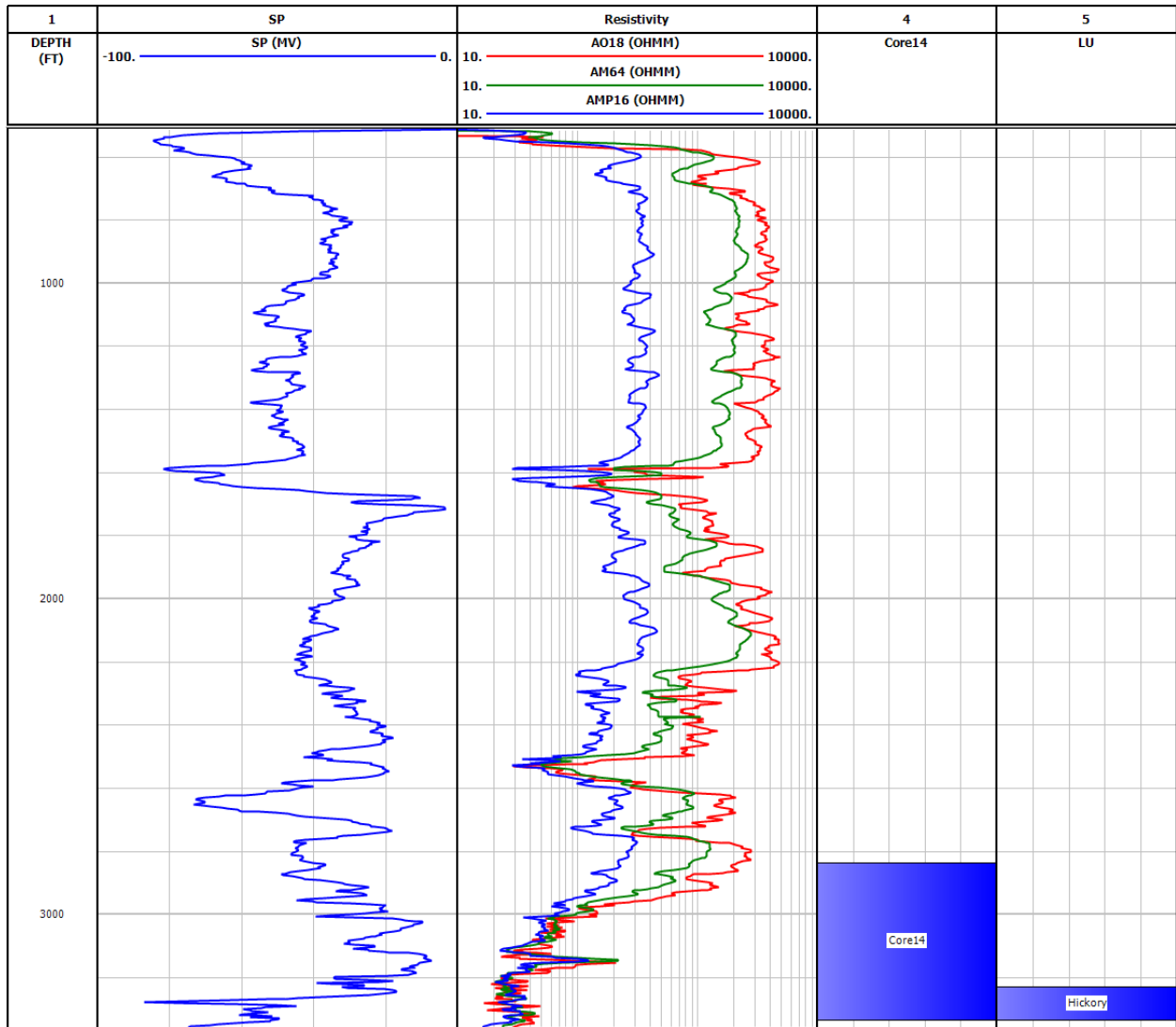


Figure 101. Well logs of well #A07. Track 1: depth. Track 2: SP log. Track 3: resistivity logs. Track 5: cored interval. Track 6: formation zones.

Texas Water Development Board Contract Number 2248302663

Final Report: Core Testing and Numerical Simulation of Well Logs for the Upper Coastal Plains and Llano Uplift Aquifers

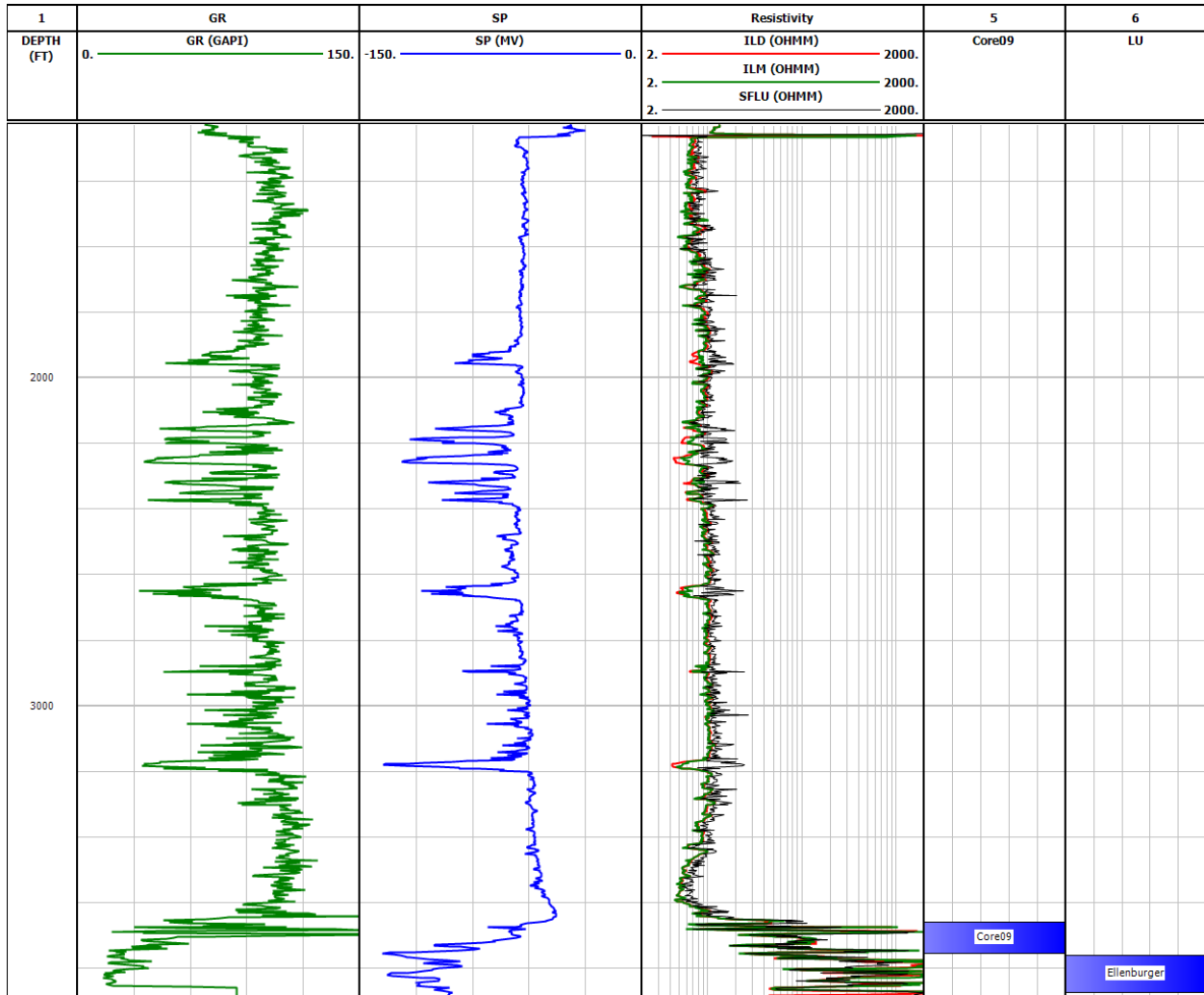


Figure 102. Well logs of well #A08. Track 1: depth. Track 2: GR log. Track 3: SP log. Track 4: resistivity logs. Track 5: cored interval. Track 6: formation zones.

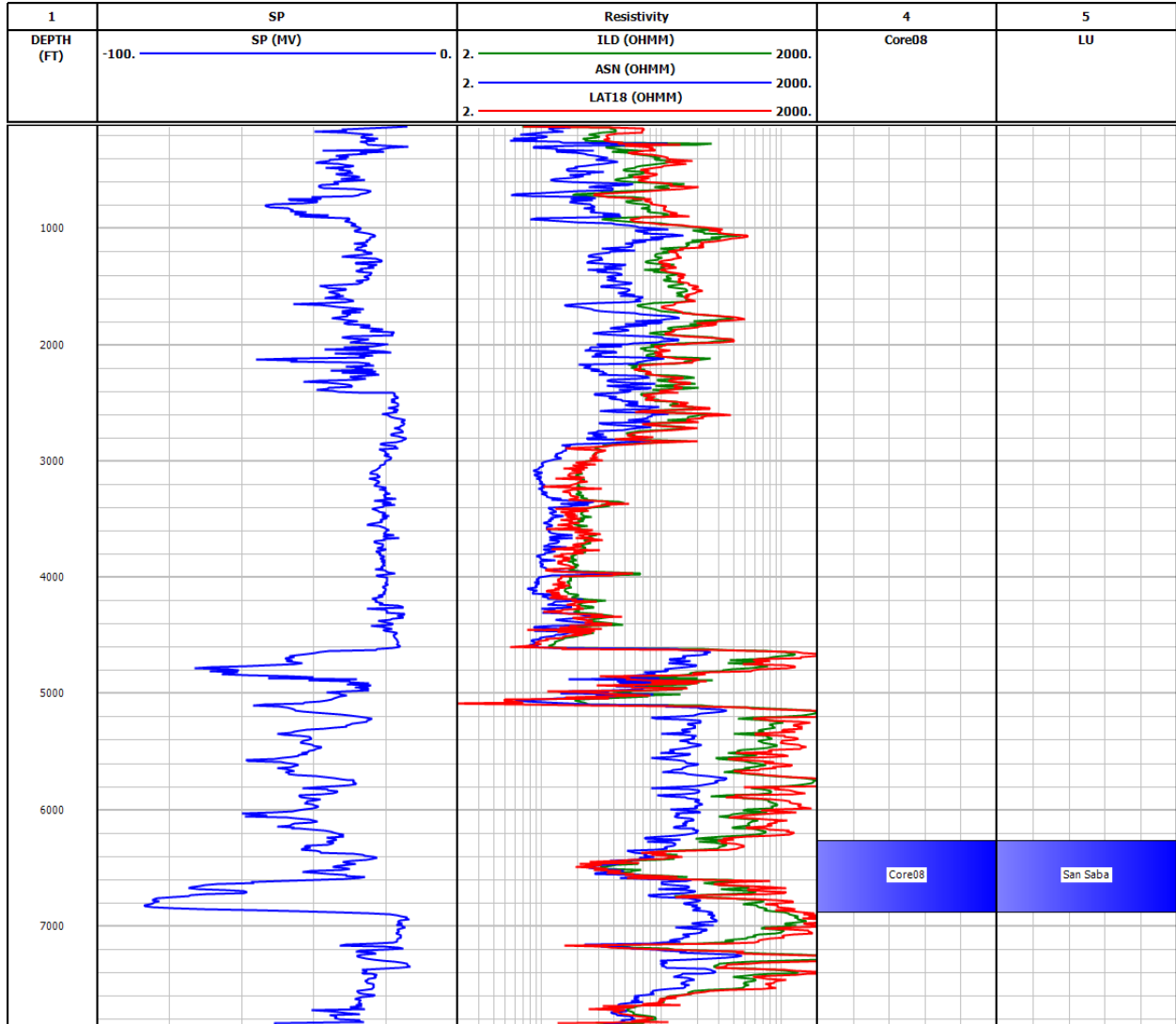


Figure 103. Well logs of well #A09. Track 1: depth. Track 2: SP log. Track 3: resistivity logs. Track 4: cored interval. Track 5: formation zones.

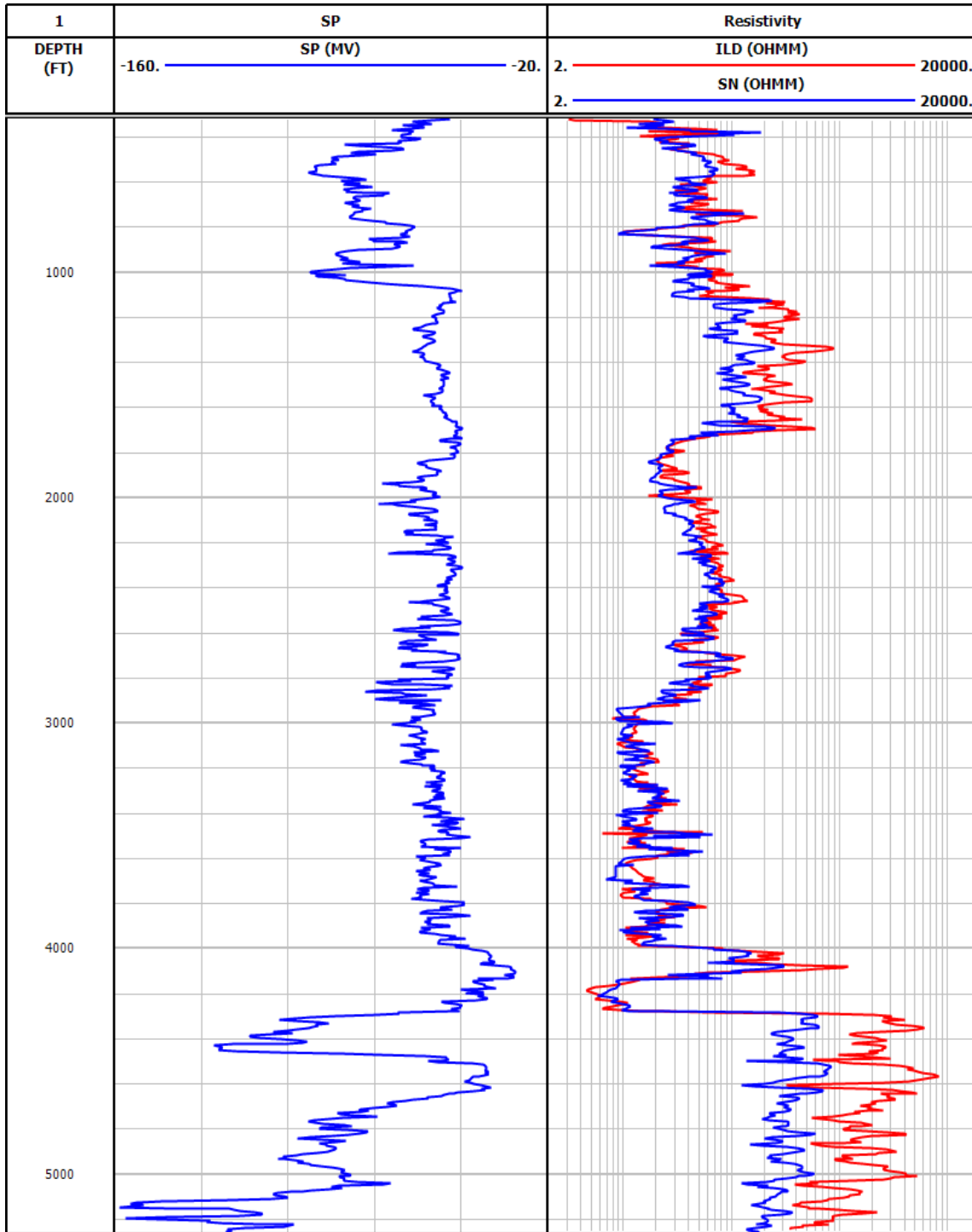


Figure 104. Well logs of well #A10. Track 1: depth. Track 2: SP log. Track 3: resistivity logs.

Texas Water Development Board Contract Number 2248302663

Final Report: Core Testing and Numerical Simulation of Well Logs for the Upper Coastal Plains and Llano Uplift Aquifers

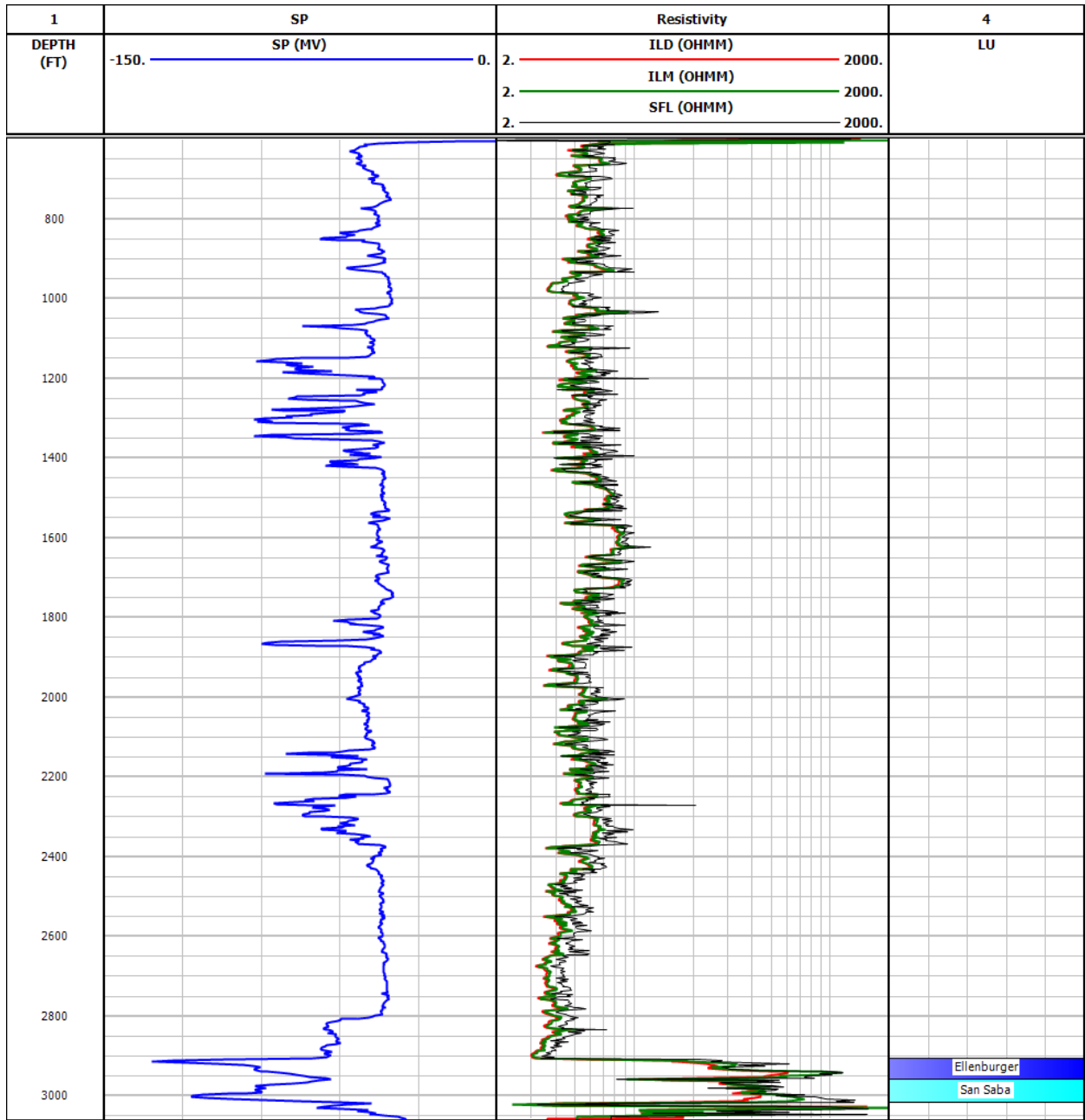


Figure 105. Well logs of well #A11. Track 1: depth. Track 2: SP log. Track 3: resistivity logs. Track 4: formation zones.

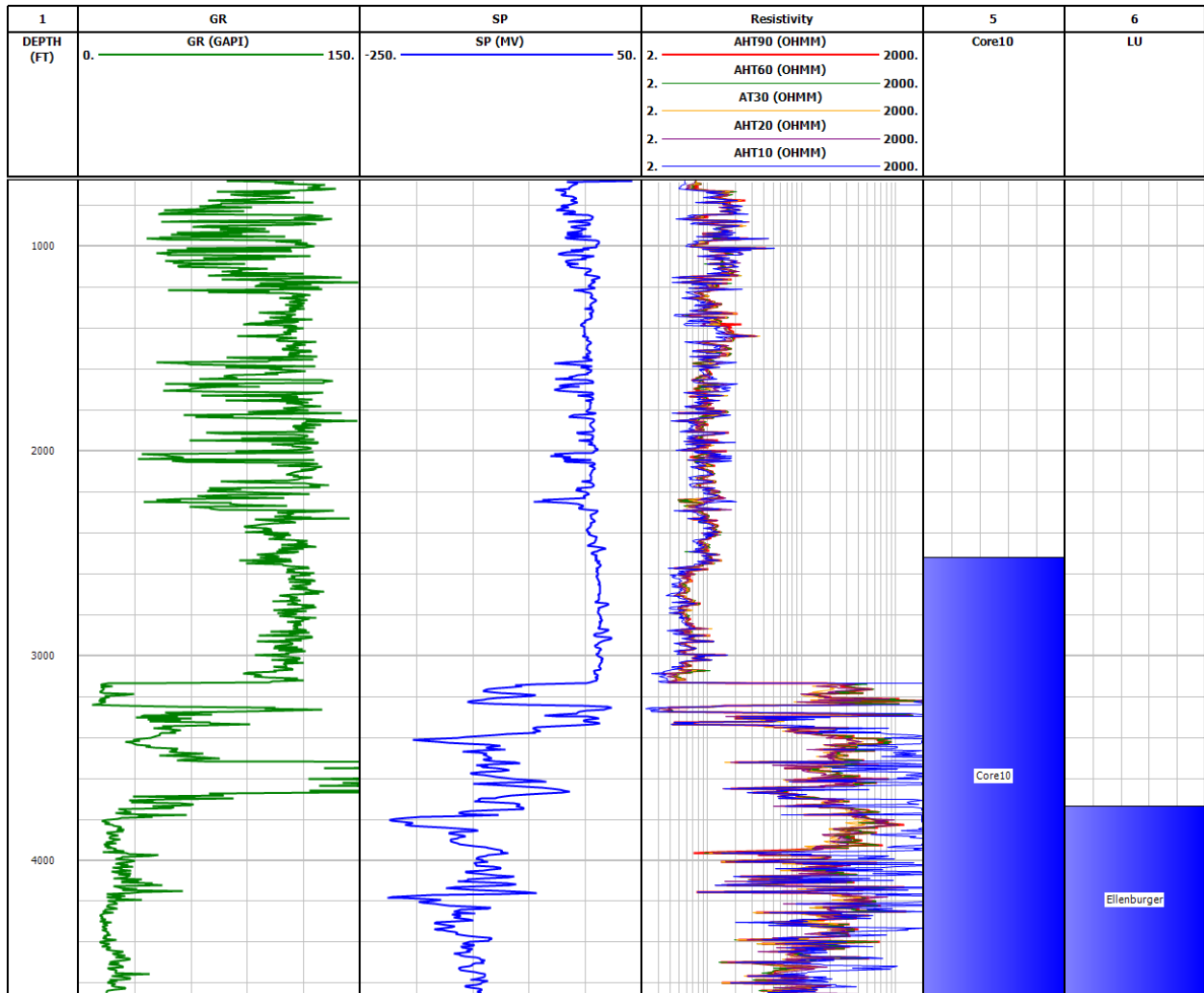


Figure 107. Well logs of well #A13. Track 1: depth. Track 2: GR log. Track 3: SP log. Track 4: resistivity logs. Track 5: cored interval. Track 6: formation zones.

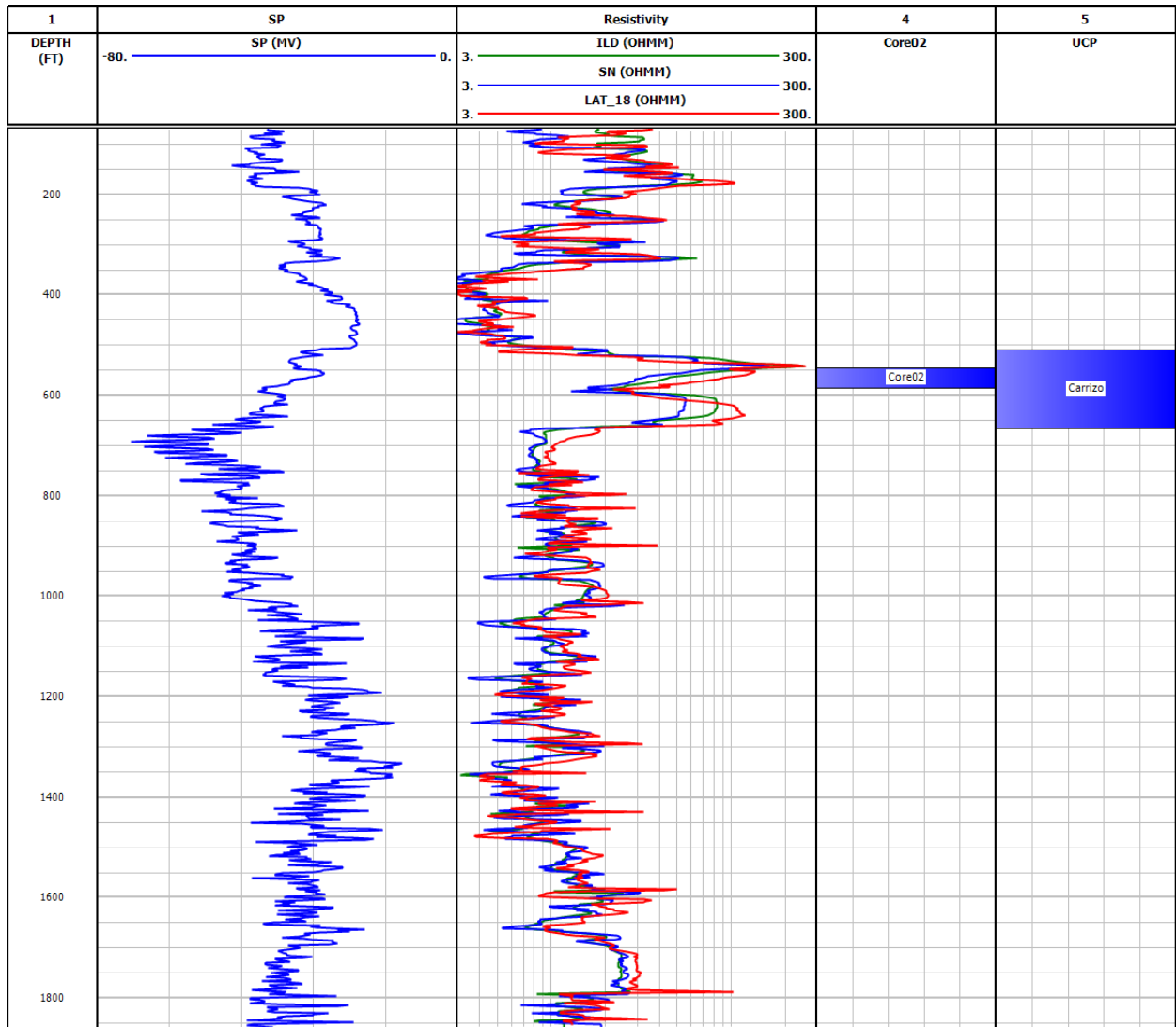


Figure 108. Well logs of well #B01. Track 1: depth. Track 2: SP log. Track 3: resistivity logs. Track 4: cored interval. Track 5: formation zones.

Texas Water Development Board Contract Number 2248302663

Final Report: Core Testing and Numerical Simulation of Well Logs for the Upper Coastal Plains and Llano Uplift Aquifers

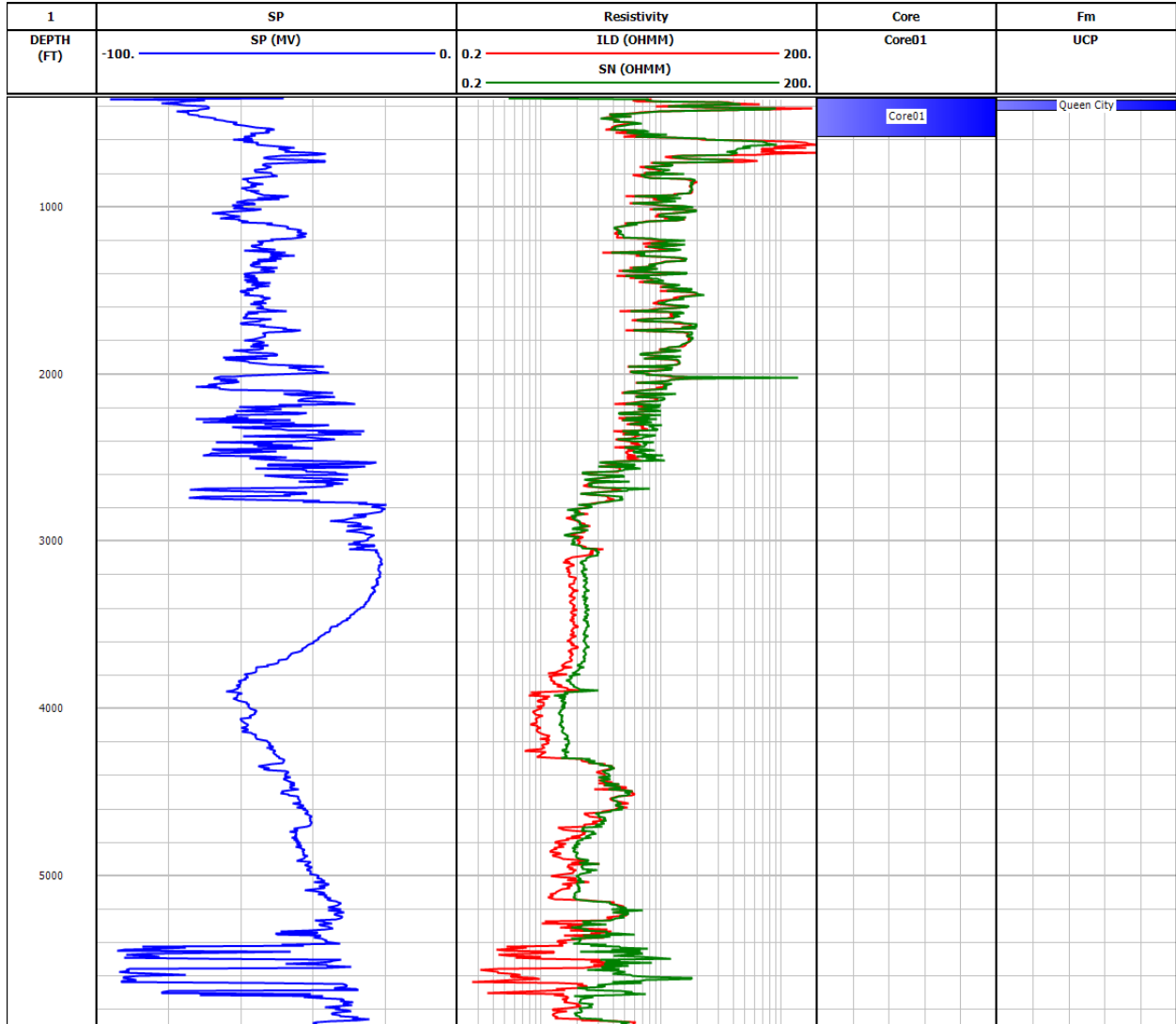


Figure 109. Well logs of well #B02. Track 1: depth. Track 2: SP log. Track 3: resistivity logs. Track 4: cored interval. Track 5: formation zones.

Texas Water Development Board Contract Number 2248302663

Final Report: Core Testing and Numerical Simulation of Well Logs for the Upper Coastal Plains and Llano Uplift Aquifers

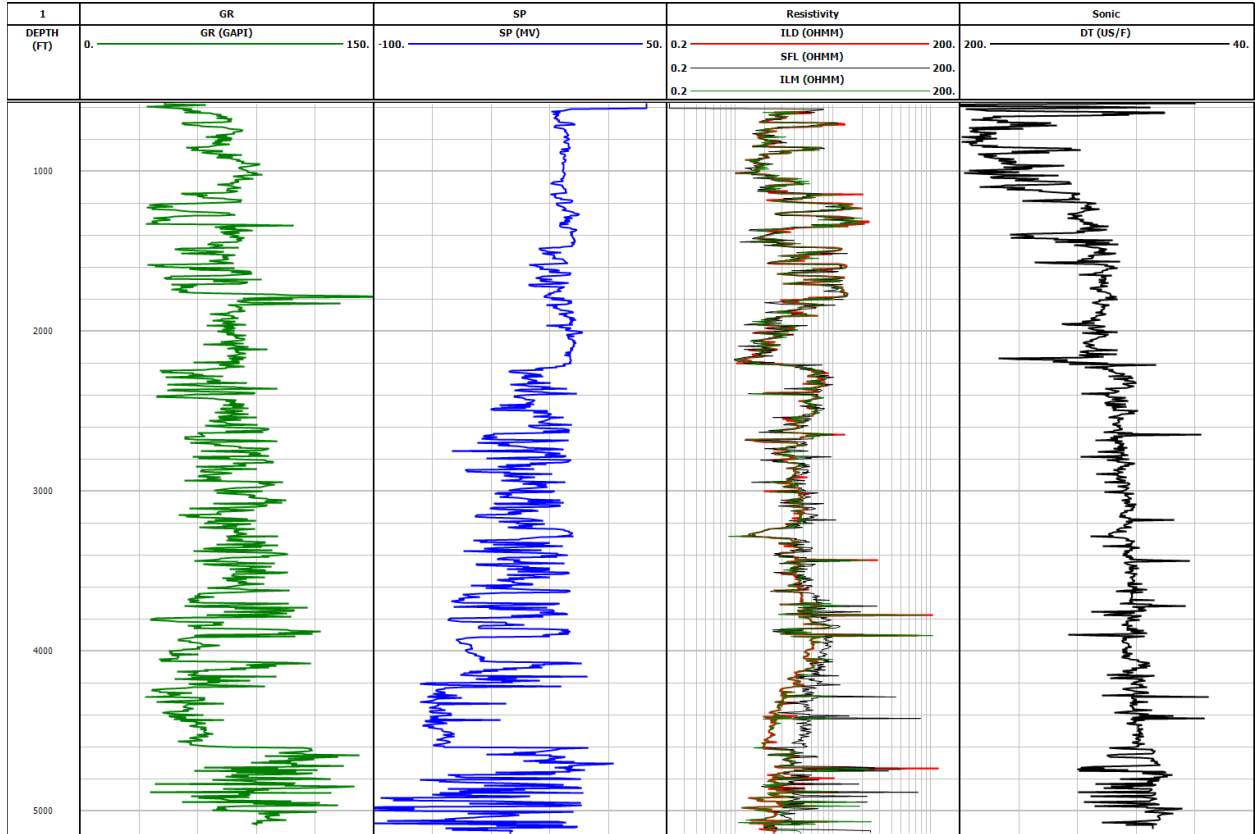


Figure 110. Well logs of well #B03. Track 1: depth. Track 2: GR log. Track 3: SP log. Track 3: resistivity logs. Track 4: sonic log.

Texas Water Development Board Contract Number 2248302663

Final Report: Core Testing and Numerical Simulation of Well Logs for the Upper Coastal Plains and Llano Uplift Aquifers

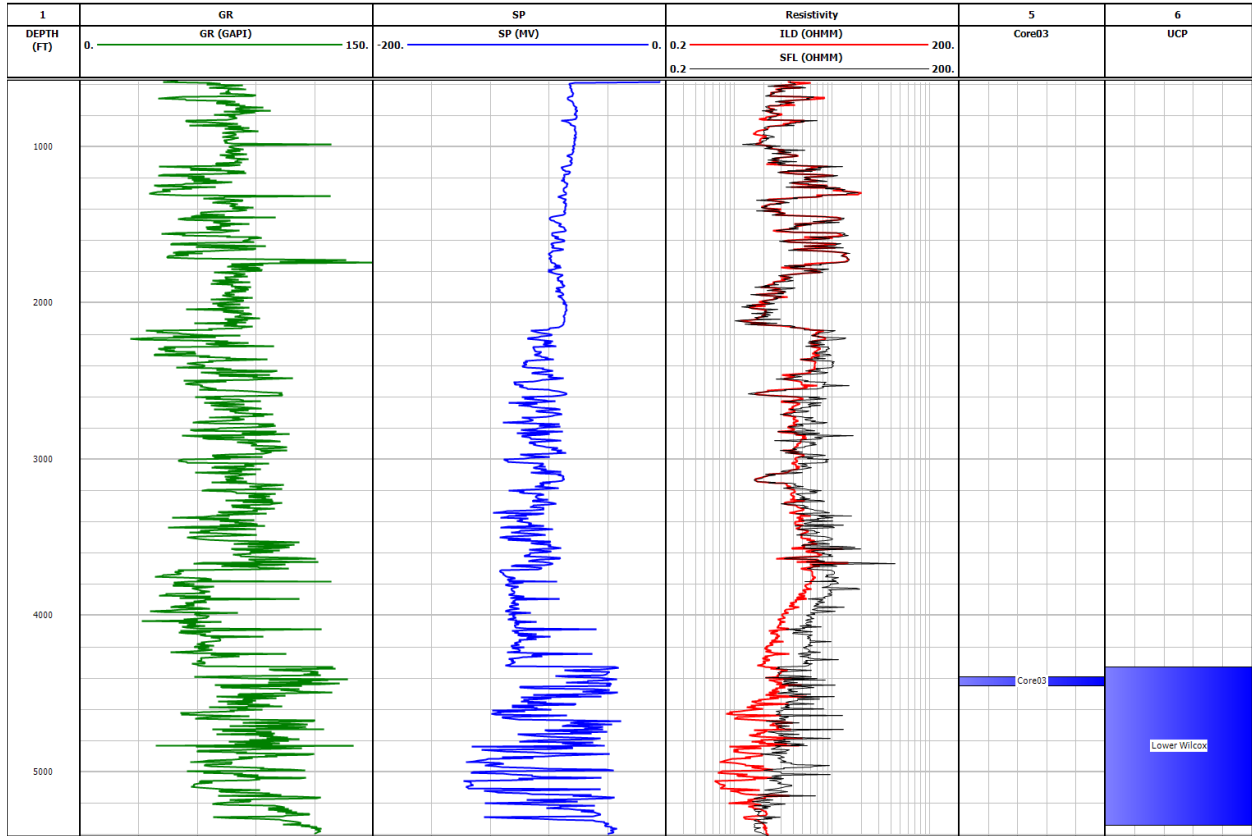


Figure 111. Well logs of well #B04. Track 1: depth. Track 2: GR log. Track 3: SP log. Track 4: resistivity logs. Track 5: cored interval. Track 6: formation zones.

Texas Water Development Board Contract Number 2248302663

Final Report: Core Testing and Numerical Simulation of Well Logs for the Upper Coastal Plains and Llano Uplift Aquifers

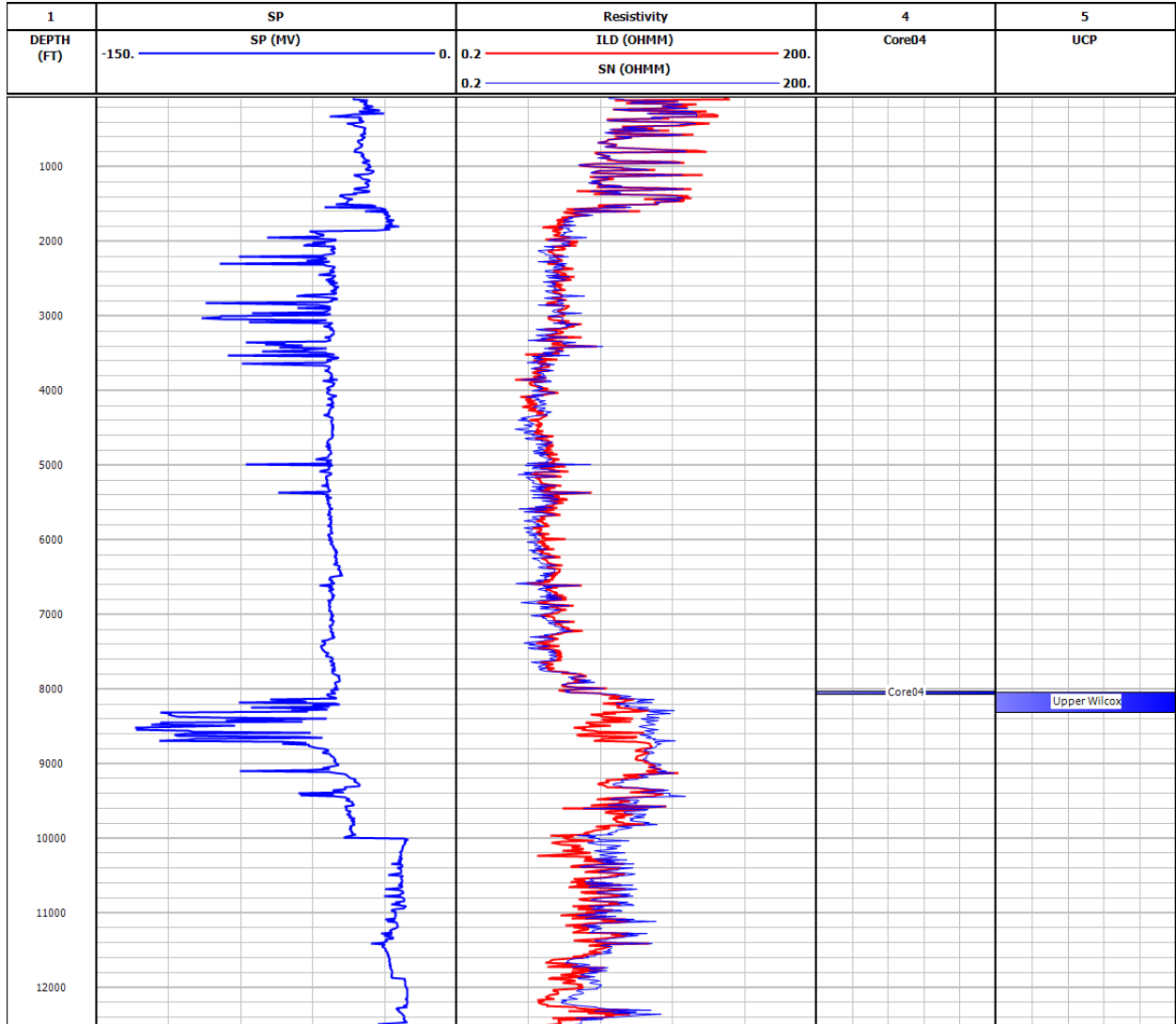


Figure 112. Well logs of well #B05. Track 1: depth. Track 2: SP log. Track 3: resistivity logs. Track 4: cored interval. Track 5: formation zones.

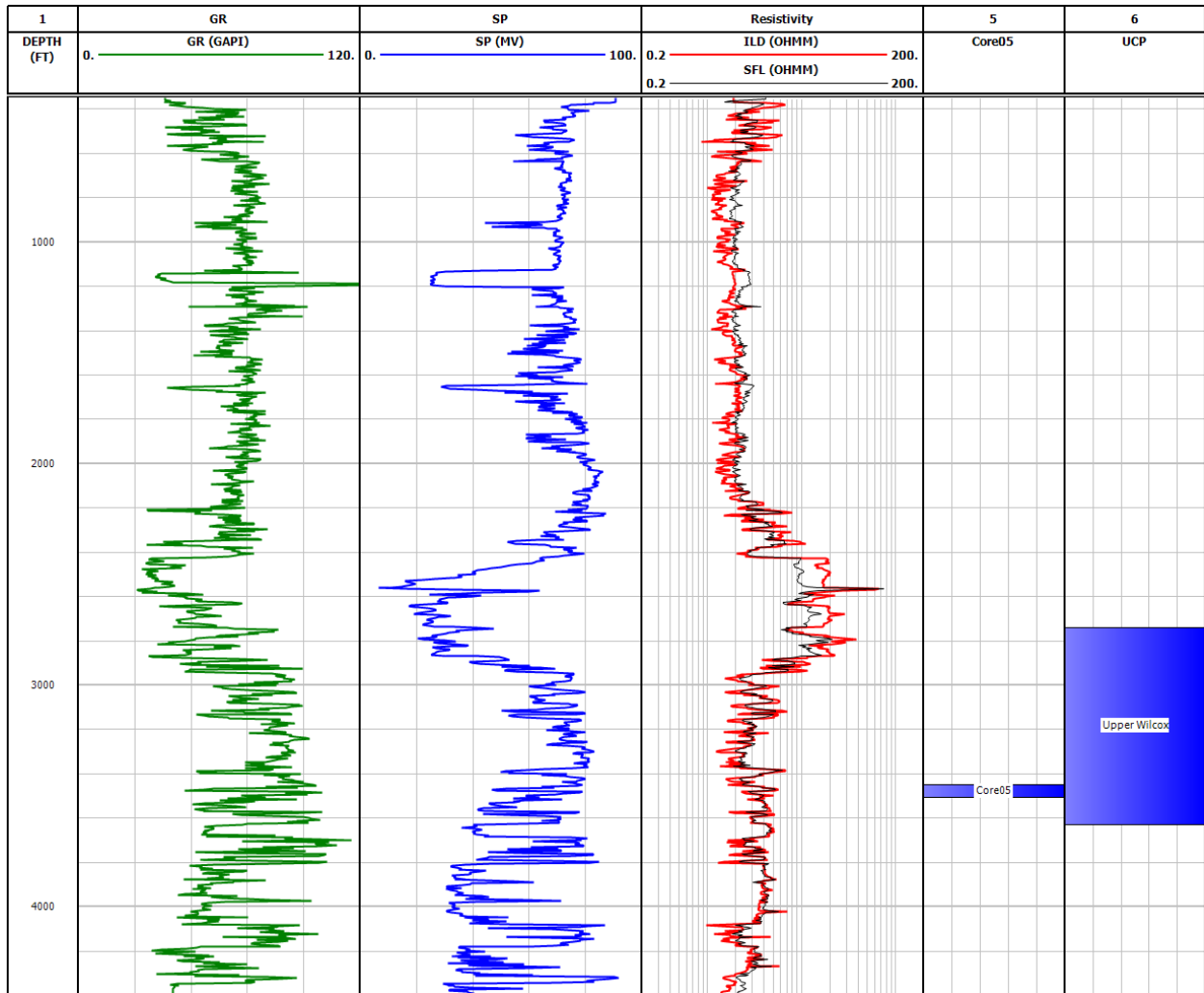


Figure 113. Well logs of well #B06. Track 1: depth. Track 2: GR log. Track 3: SP log. Track 4: resistivity logs. Track 5: cored interval. Track 6: formation zones.

Texas Water Development Board Contract Number 2248302663

Final Report: Core Testing and Numerical Simulation of Well Logs for the Upper Coastal Plains and Llano Uplift Aquifers

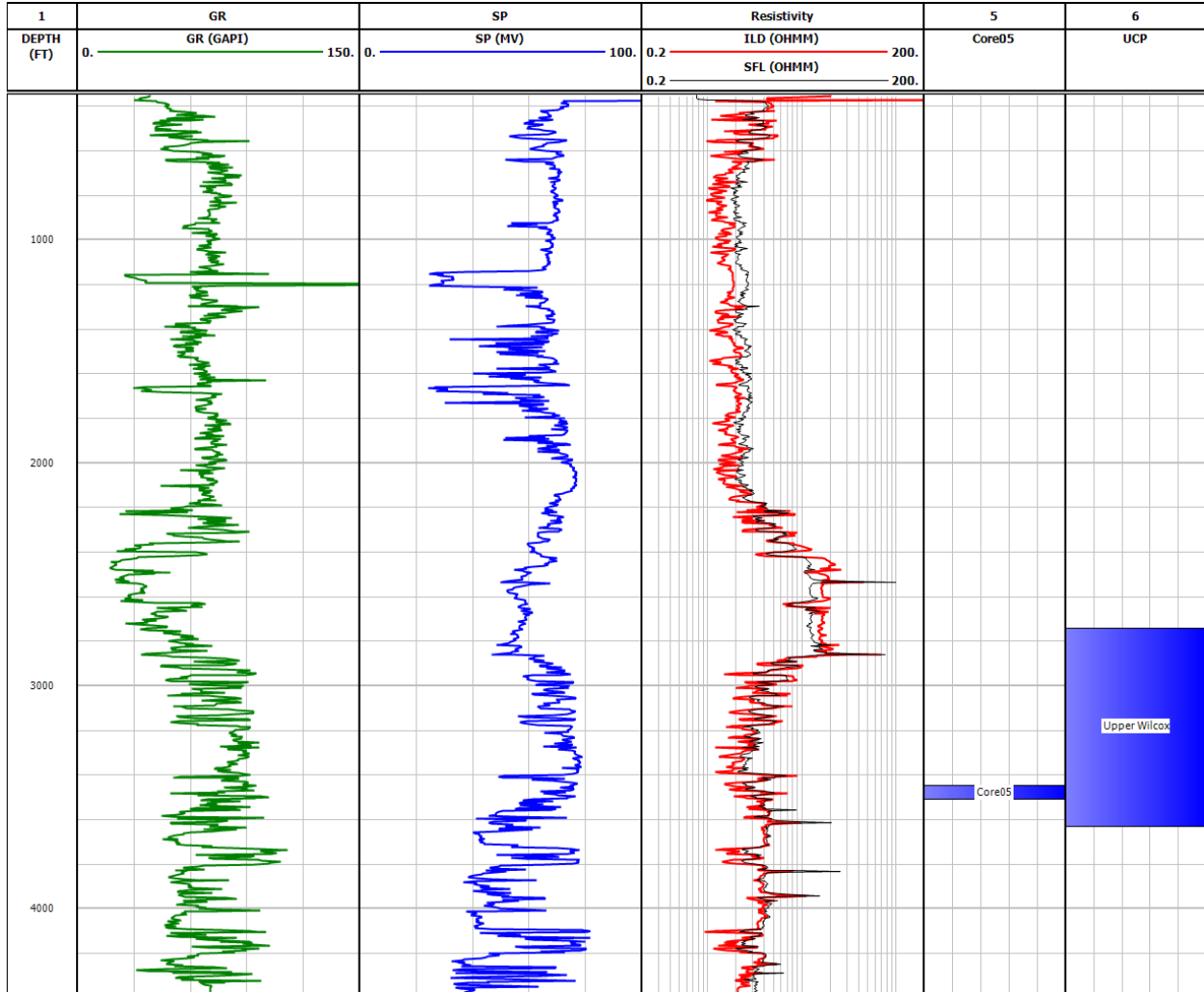


Figure 114. Well logs of well #B07. Track 1: depth. Track 2: GR log. Track 2: SP log. Track 3: resistivity logs. Track 4: cored interval. Track 5: formation zones.

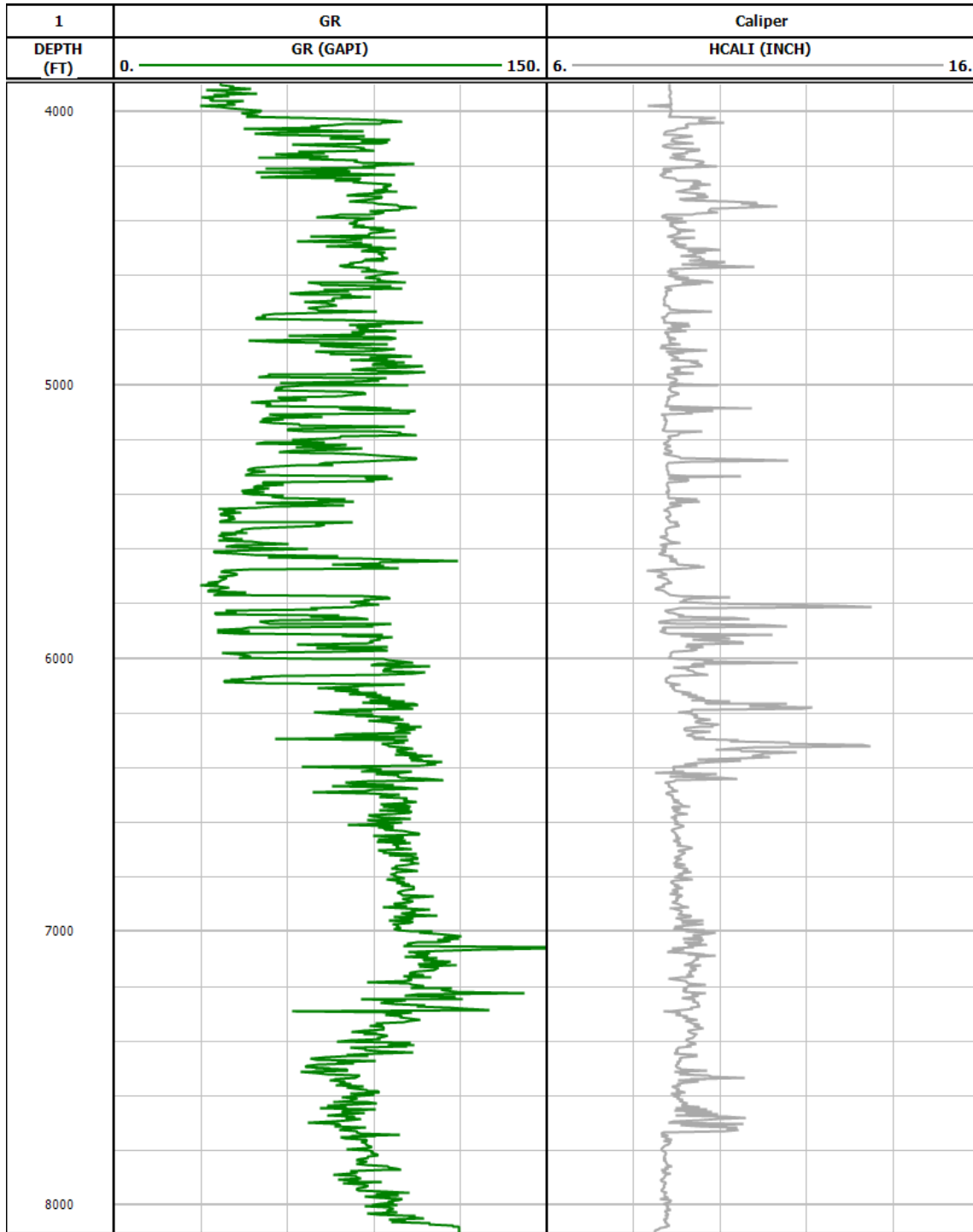


Figure 115. Well logs of well #B08. Track 1: depth. Track 2: GR log. Track 2: Caliper log.

Texas Water Development Board Contract Number 2248302663

Final Report: Core Testing and Numerical Simulation of Well Logs for the Upper Coastal Plains and Llano Uplift Aquifers

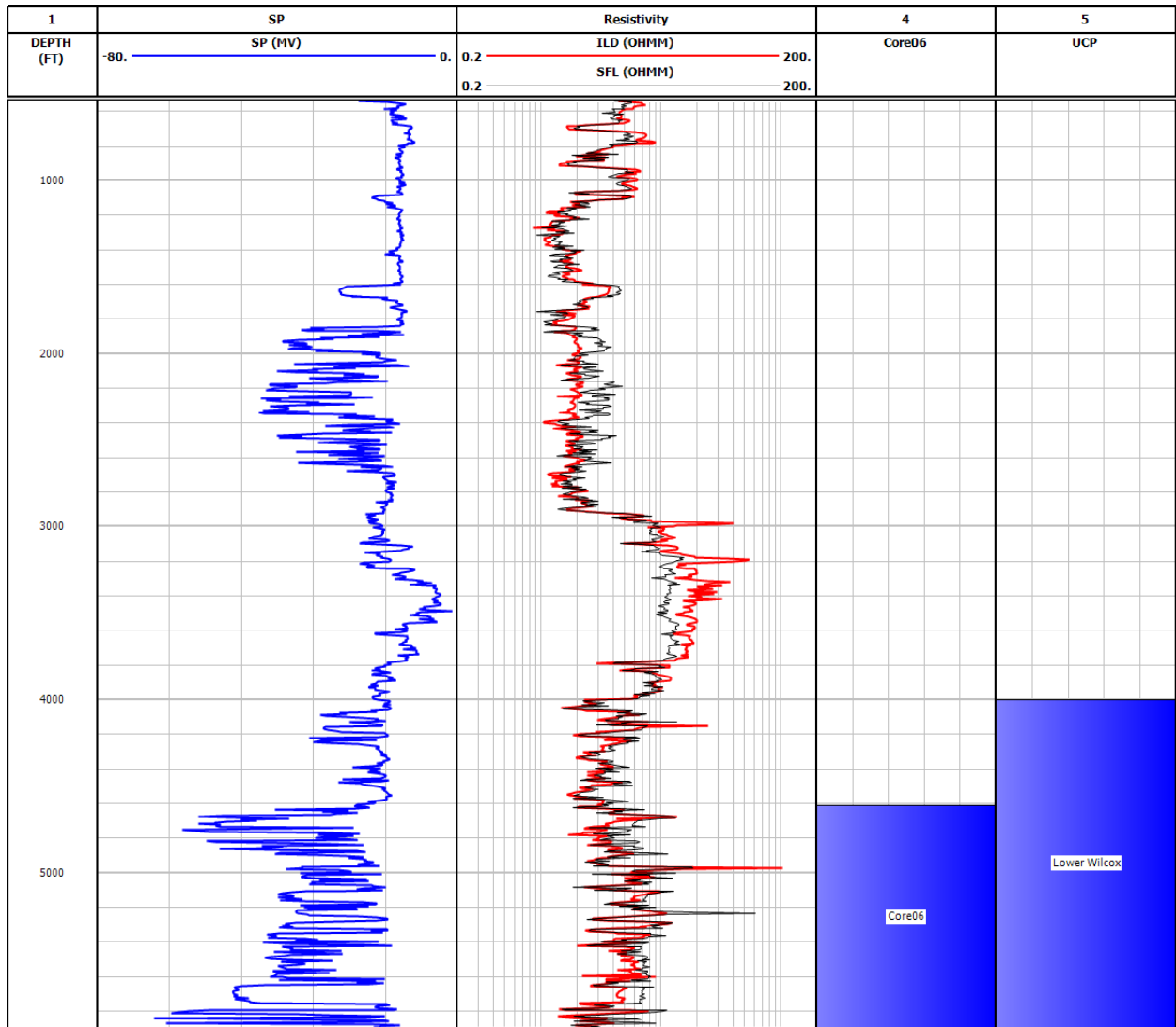


Figure 116. Well logs of well #B09. Track 1: depth. Track 2: SP log. Track 3: resistivity logs. Track 4: cored interval. Track 5: formation zones.

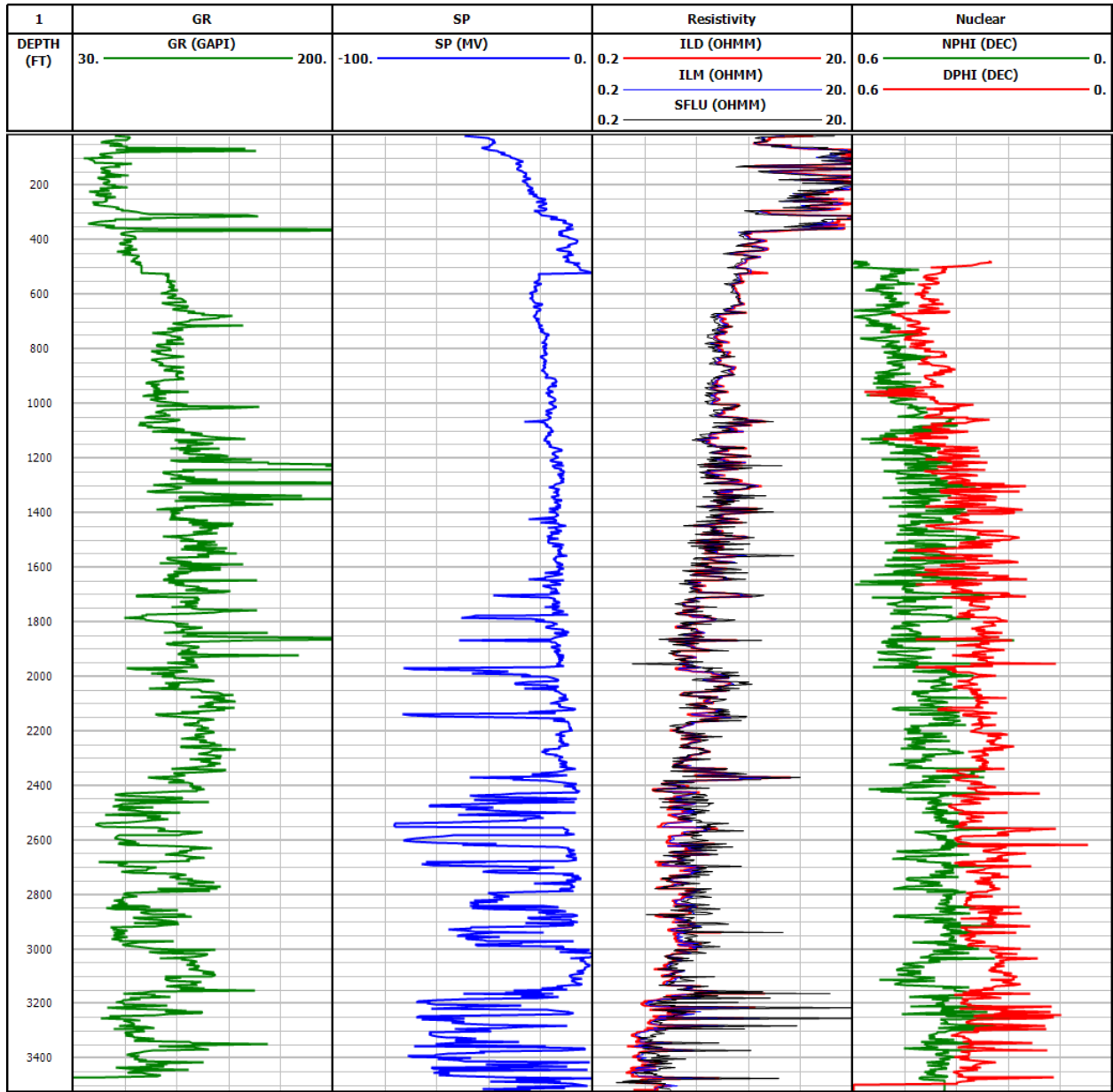


Figure 117. Well logs of well #B10. Track 1: depth. Track 2: GR log. Track 3: SP log. Track 4: resistivity logs. Track 5: density and neutron porosity logs calculated in sandstone porosity units.

APPENDIX B – PULSE DECAY PERMEABILITY MEASUREMENTS

Pulse-decay permeability experiments are performed for tight core samples. A new analytical solution is presented for the laboratory pulse-decay permeability problem. The decay of differential pressure over time is modeled as the sum of multiple exponentials, similar to decay of NMR magnetization. The pressure decay T_2 distribution is converted to a permeability distribution. Note that permeability is inversely proportional to T_2 . Conversely, the quicker the differential pressure decay, the low the T_2 , and the higher the permeability. The decay of differential pressure over time is typically characterized by a fast decay at early times and a slower decay at late times. Permeability is calculated from the late time decay rate of pressure. Early time decay rate of pressure is not of particular interest.

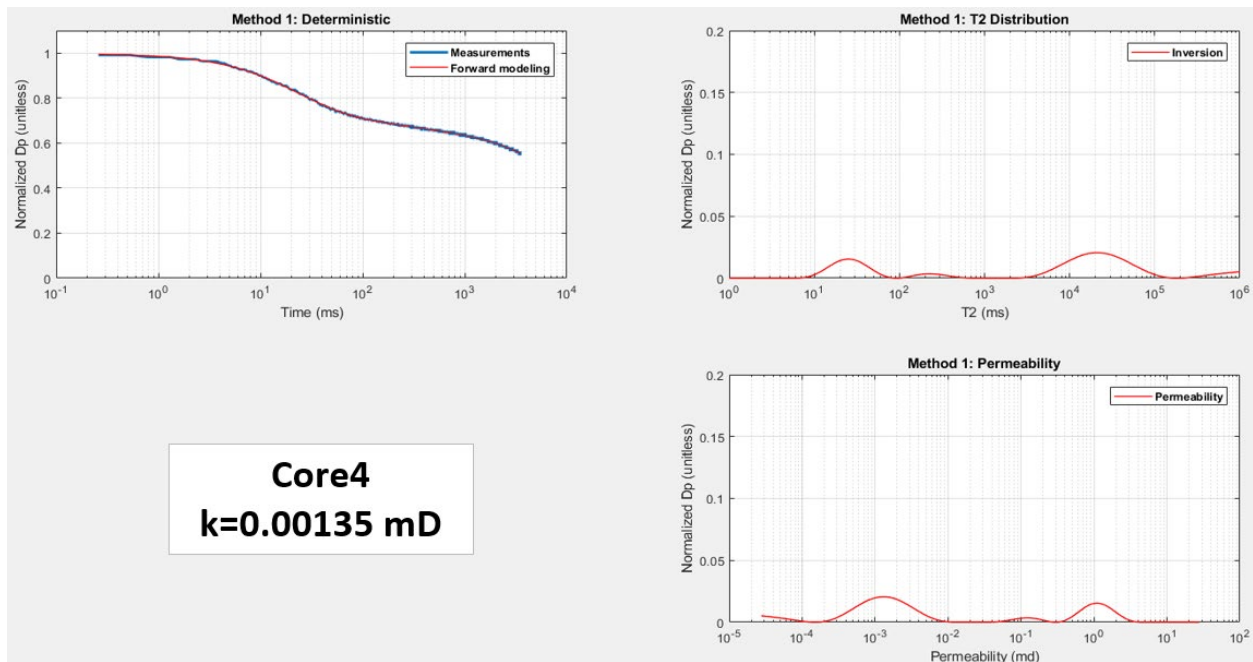


Figure 118. (Top left) Normalized differential pressure decay over time in seconds, (Top right) pressure decay T_2 distribution in seconds, and (Bottom right) permeability distribution in millidarcies of core sample #4.

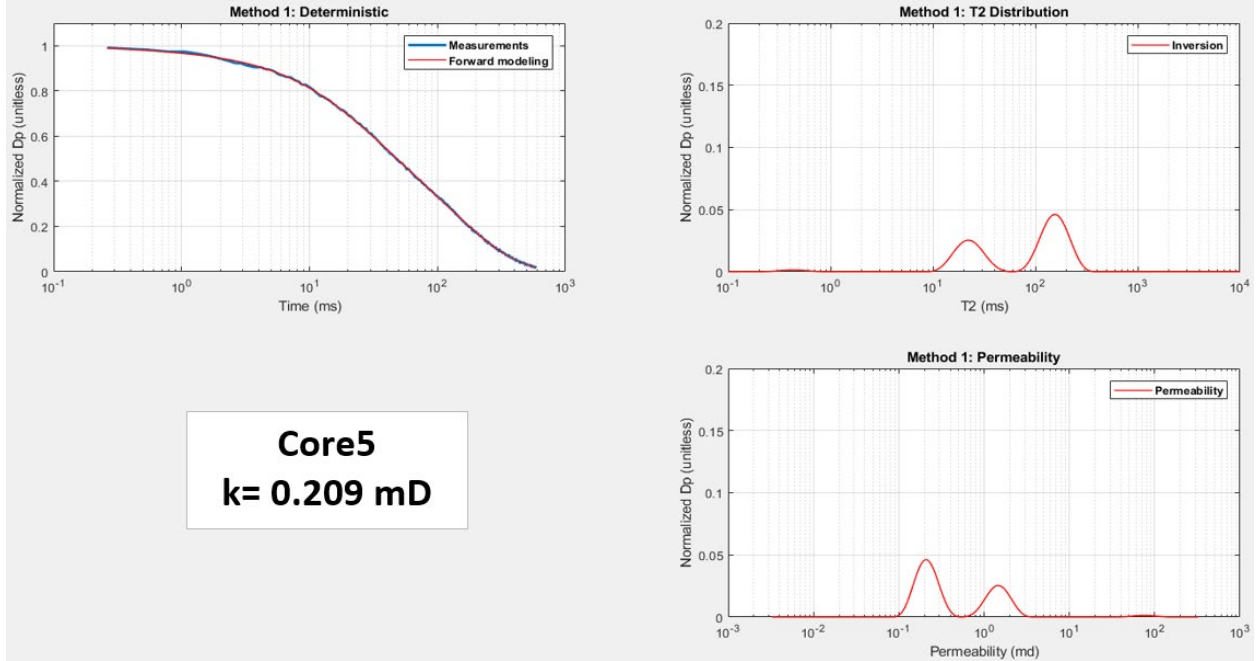


Figure 119. (Top left) Normalized differential pressure decay over time in seconds, (Top right) pressure decay T₂ distribution in seconds, and (Bottom right) permeability distribution in millidarcies of core sample #5.

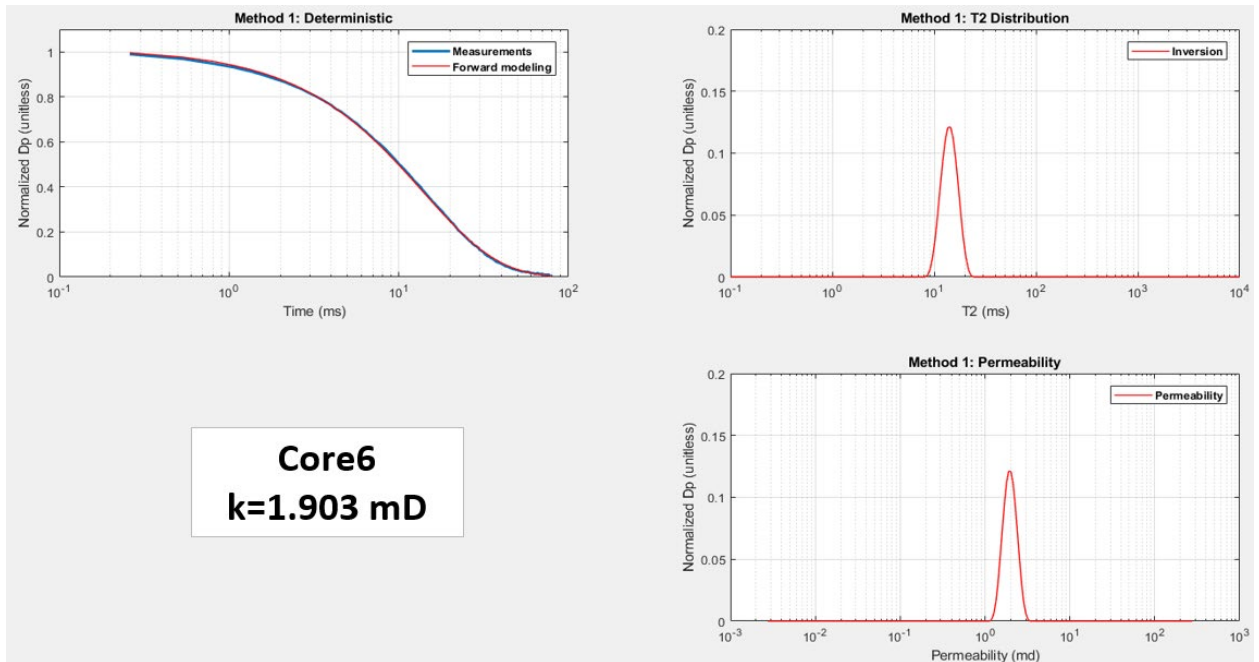


Figure 120. (Top left) Normalized differential pressure decay over time in seconds, (Top right) pressure decay T₂ distribution in seconds, and (Bottom right) permeability distribution in millidarcies of core sample #6.

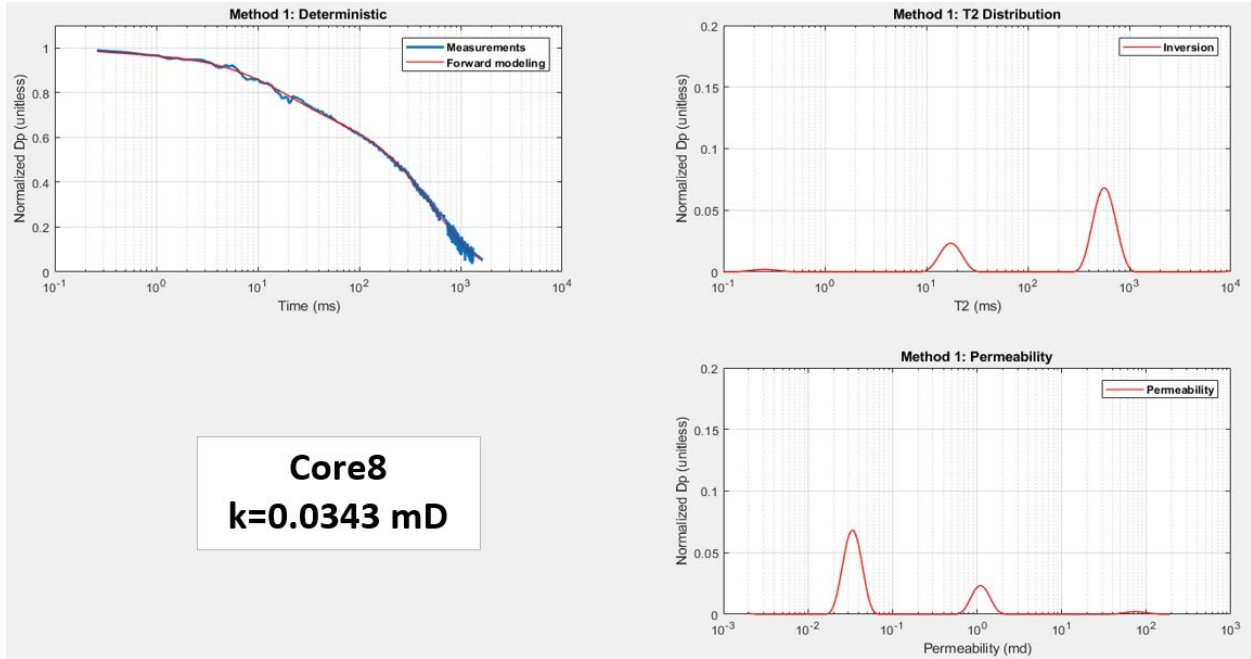


Figure 121. (Top left) Normalized differential pressure decay over time in seconds, (Top right) pressure decay T_2 distribution in seconds, and (Bottom right) permeability distribution in millidarcies of core sample #8.

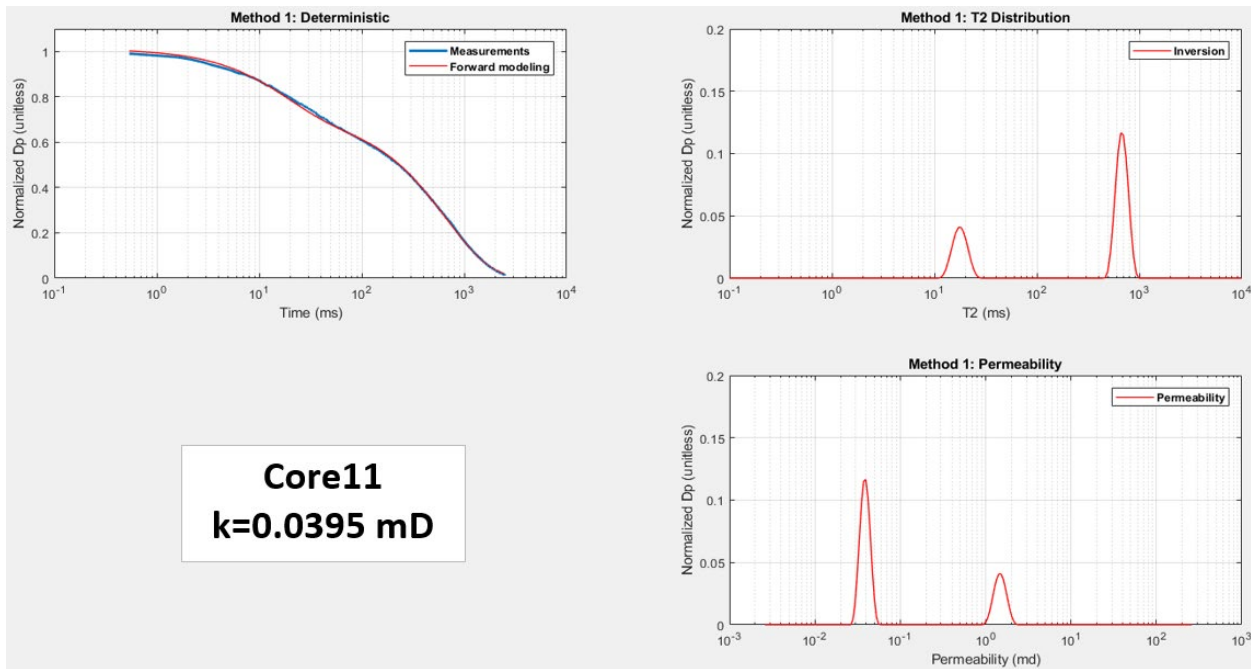


Figure 122. (Top left) Normalized differential pressure decay over time in seconds, (Top right) pressure decay T_2 distribution in seconds, and (Bottom right) permeability distribution in millidarcies of core sample #11.

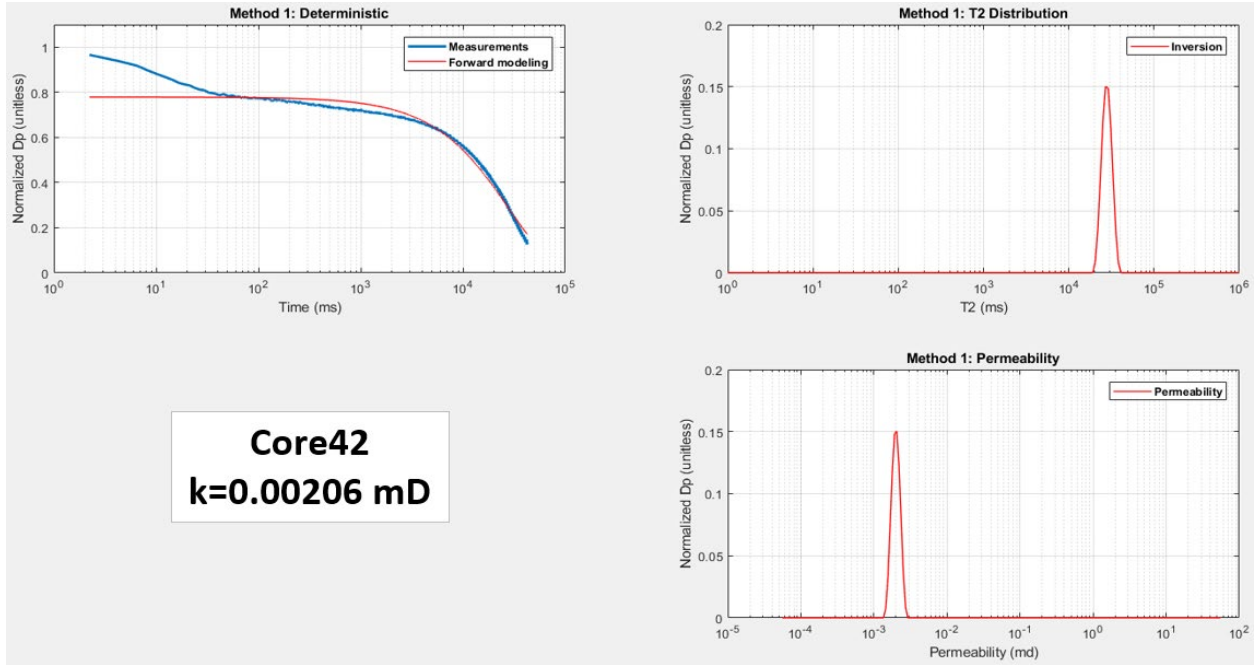


Figure 123. (Top left) Normalized differential pressure decay over time in seconds, (Top right) pressure decay T_2 distribution in seconds, and (Bottom right) permeability distribution in millidarcies of core sample #42.

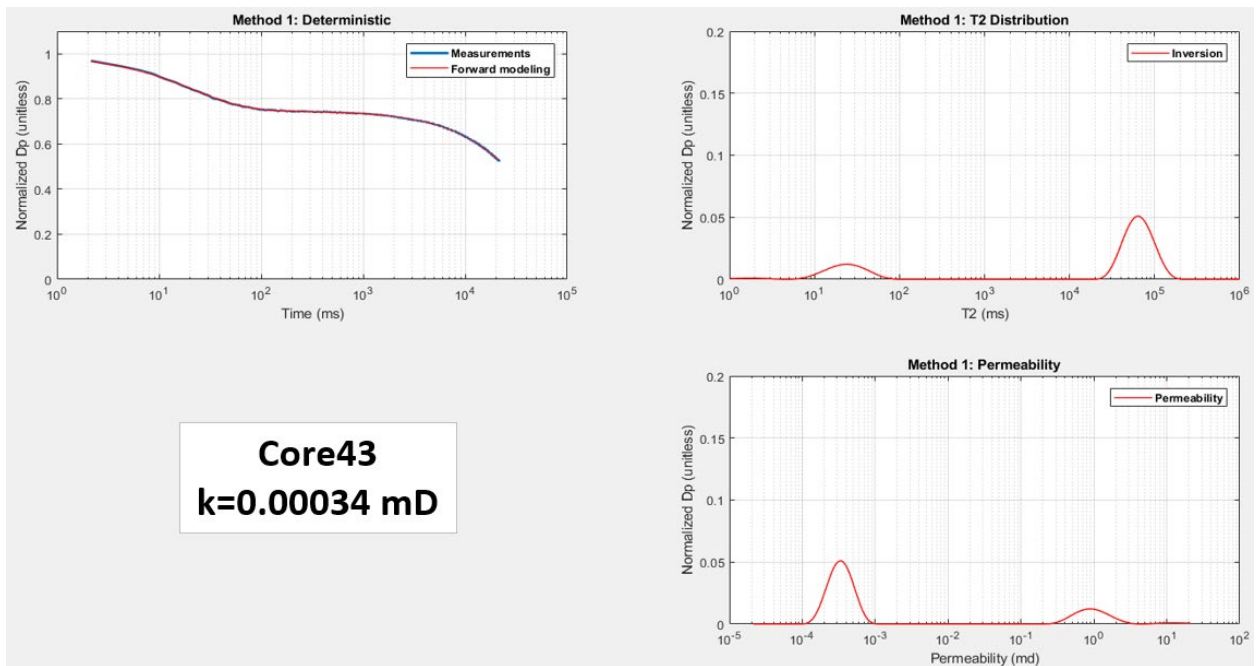


Figure 124. (Top left) Normalized differential pressure decay over time in seconds, (Top right) pressure decay T_2 distribution in seconds, and (Bottom right) permeability distribution in millidarcies of core sample #43.

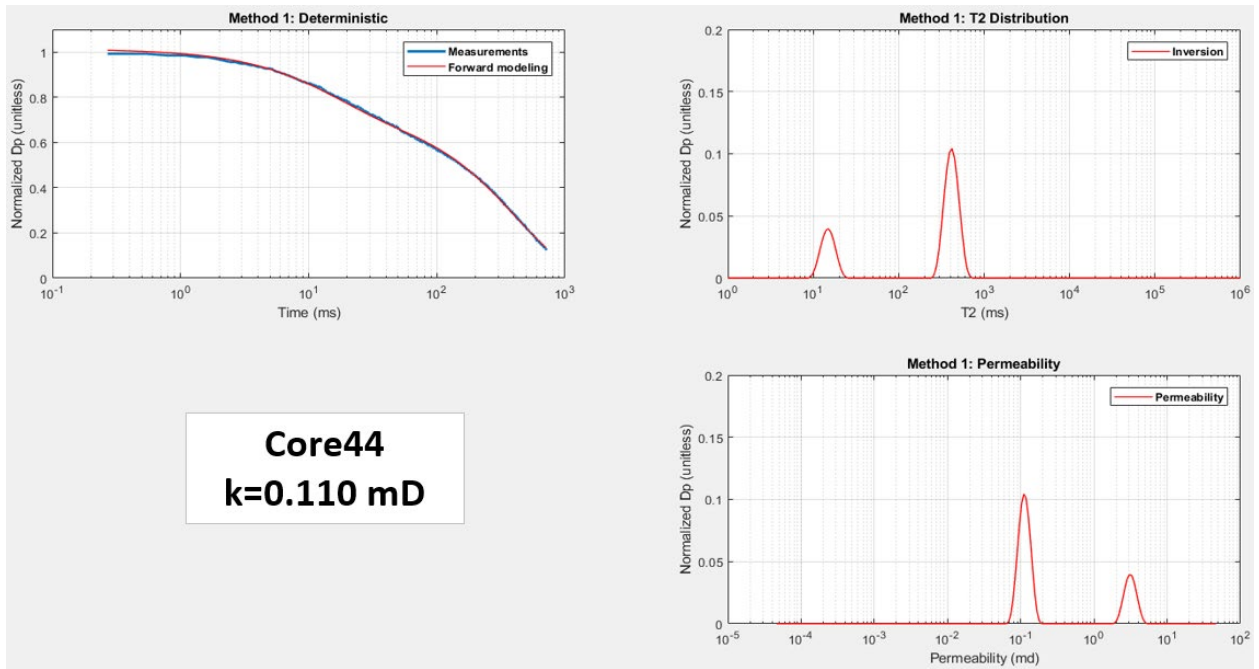


Figure 125. (Top left) Normalized differential pressure decay over time in seconds, (Top right) pressure decay T_2 distribution in seconds, and (Bottom right) permeability distribution in millidarcies of core sample #44.

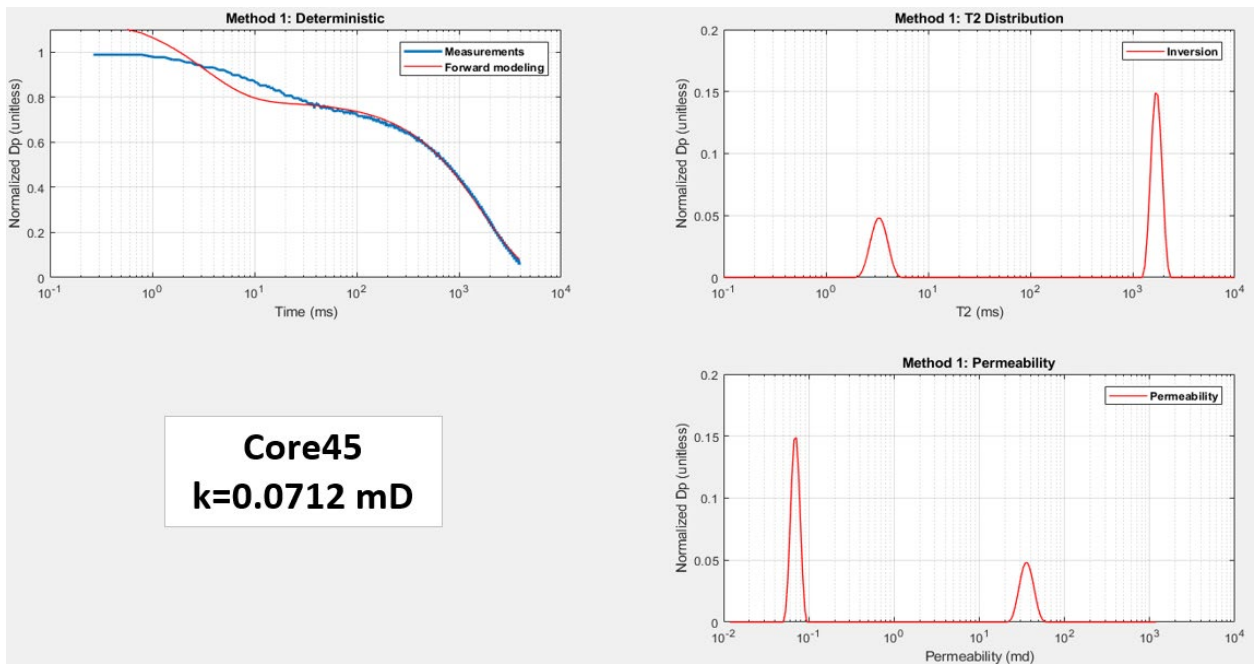


Figure 126. (Top left) Normalized differential pressure decay over time in seconds, (Top right) pressure decay T_2 distribution in seconds, and (Bottom right) permeability distribution in millidarcies of core sample #45.

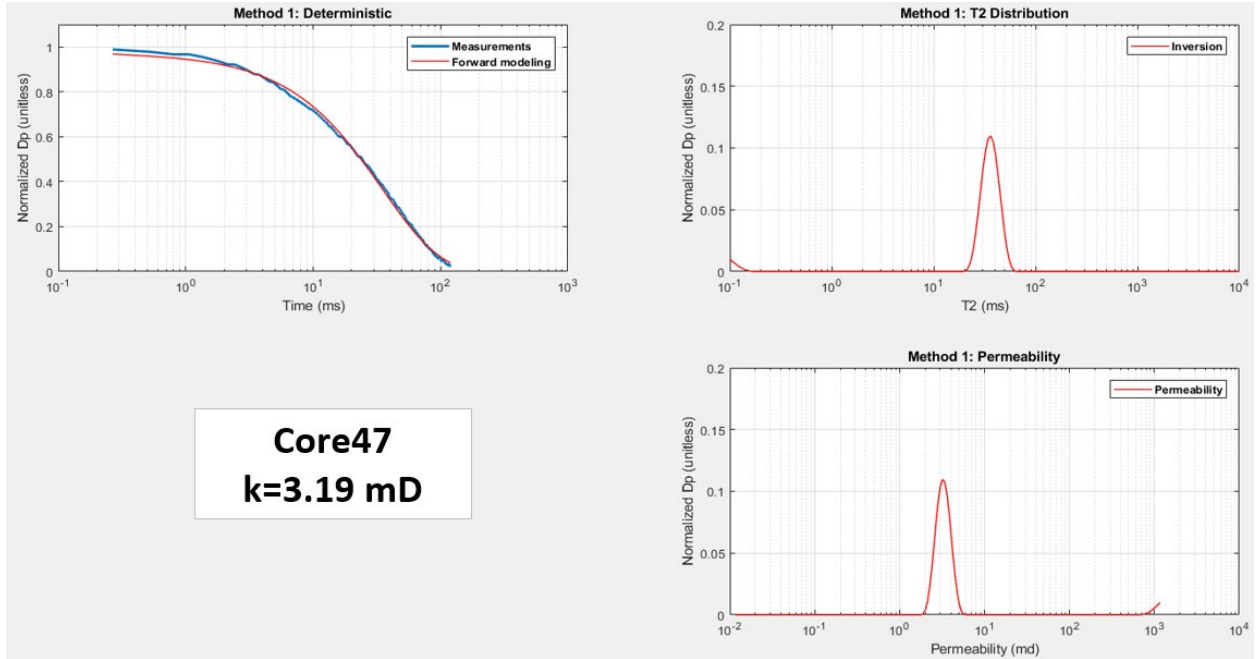


Figure 127. (Top left) Normalized differential pressure decay over time in seconds, (Top right) pressure decay T_2 distribution in seconds, and (Bottom right) permeability distribution in millidarcies of core sample #47.

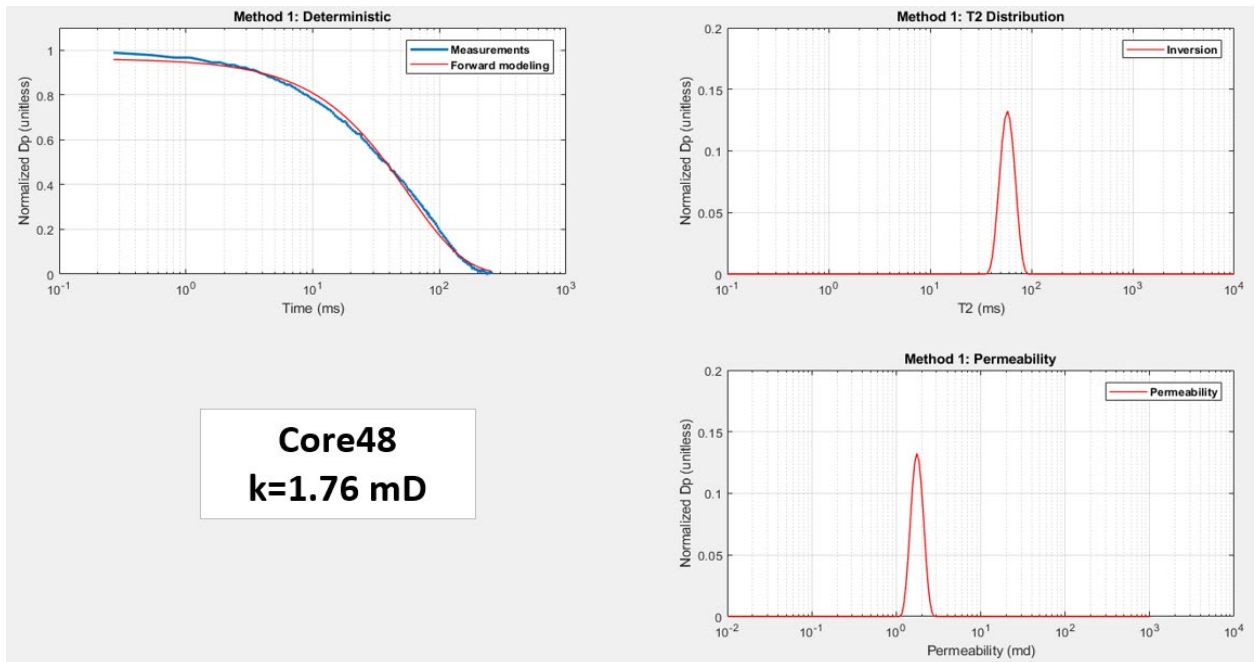


Figure 128. (Top left) Normalized differential pressure decay over time in seconds, (Top right) pressure decay T_2 distribution in seconds, and (Bottom right) permeability distribution in millidarcies of core sample #48.

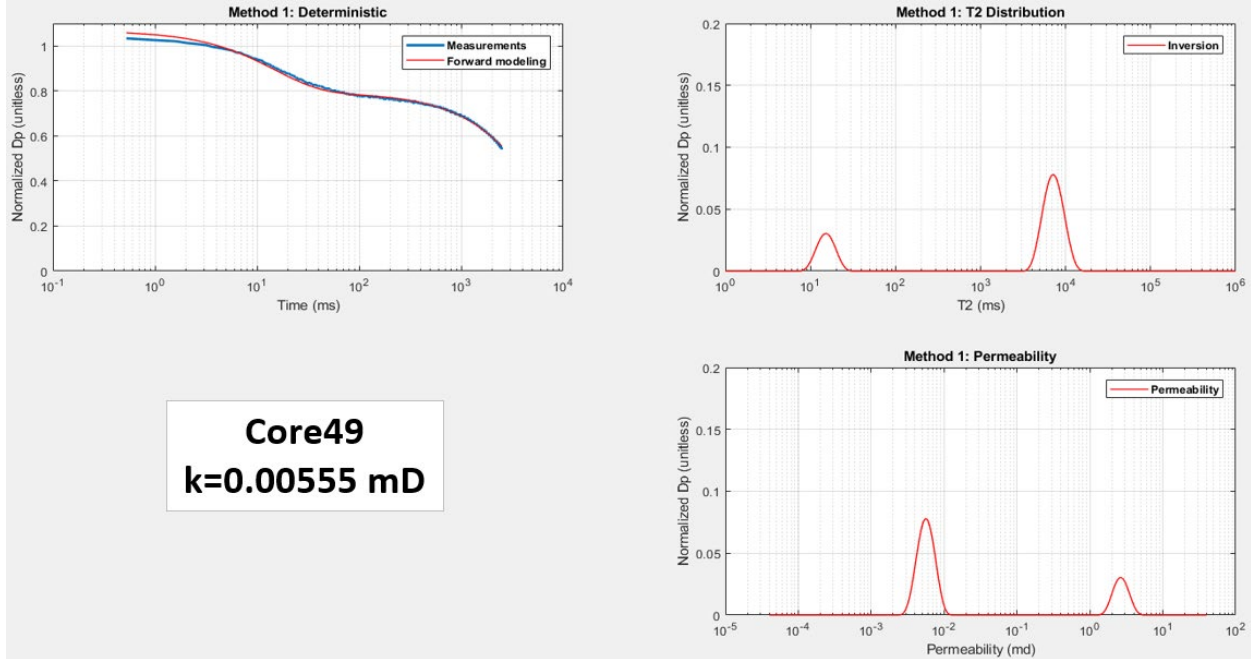


Figure 129. (Top left) Normalized differential pressure decay over time in seconds, (Top right) pressure decay T₂ distribution in seconds, and (Bottom right) permeability distribution in millidarcies of core sample #49.

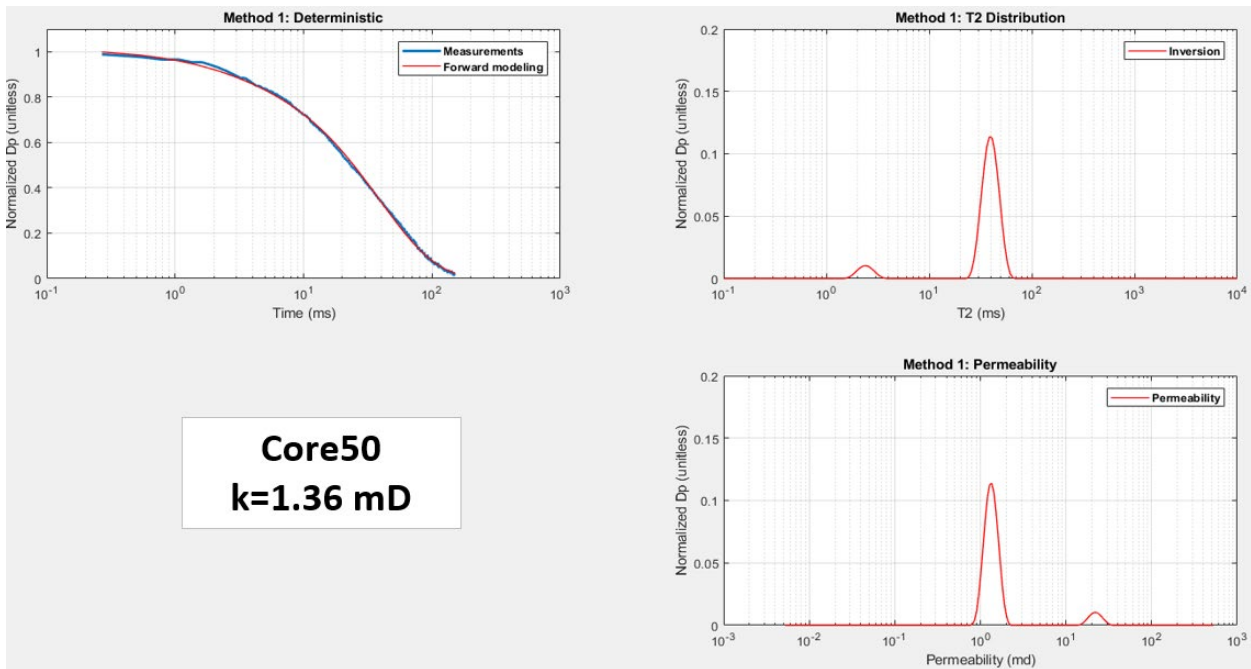


Figure 130. (Top left) Normalized differential pressure decay over time in seconds, (Top right) pressure decay T₂ distribution in seconds, and (Bottom right) permeability distribution in millidarcies of core sample #50.

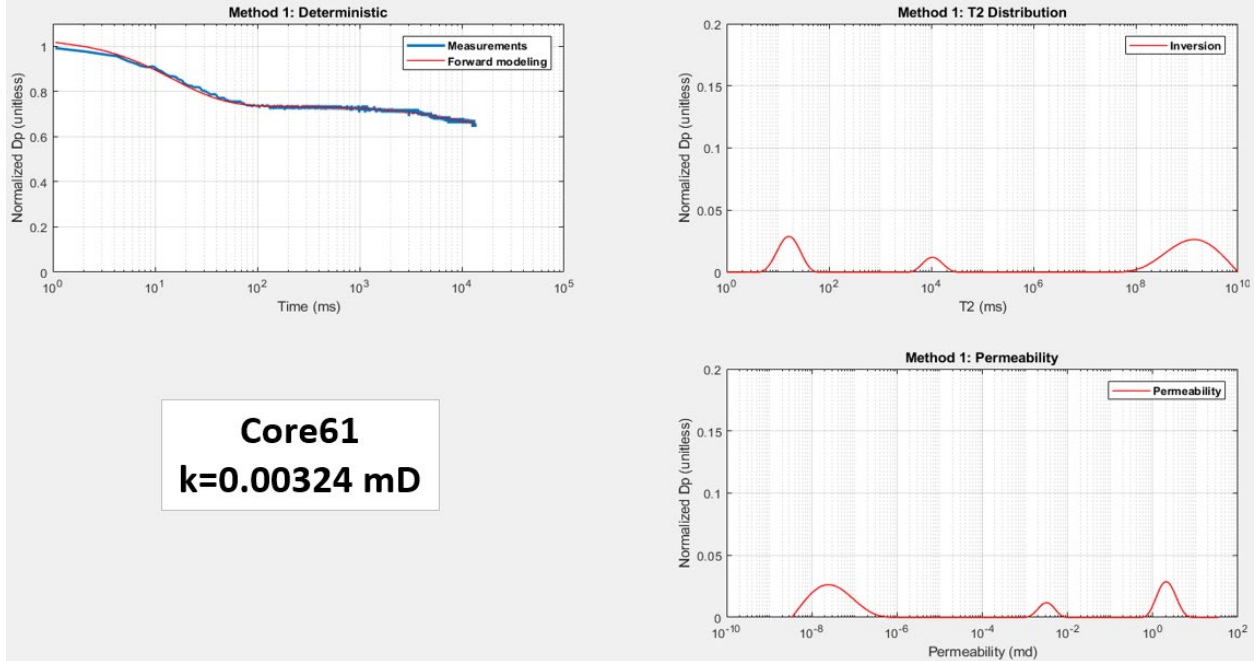


Figure 131. (Top left) Normalized differential pressure decay over time in seconds, (Top right) pressure decay T_2 distribution in seconds, and (Bottom right) permeability distribution in millidarcies of core sample #61.

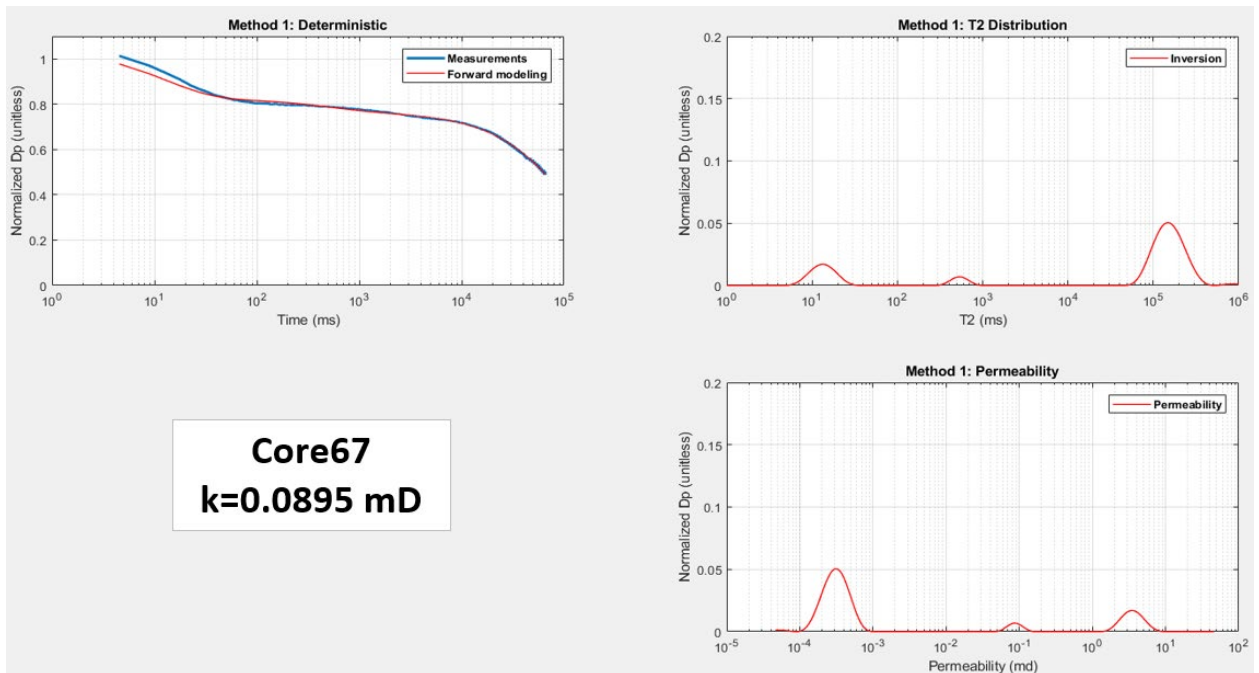


Figure 132. (Top left) Normalized differential pressure decay over time in seconds, (Top right) pressure decay T_2 distribution in seconds, and (Bottom right) permeability distribution in millidarcies of core sample #67.

APPENDIX C – NORMALIZED MAGNETIZATION DECAY MEASUREMENTS AND NMR T₂ DISTRIBUTIONS

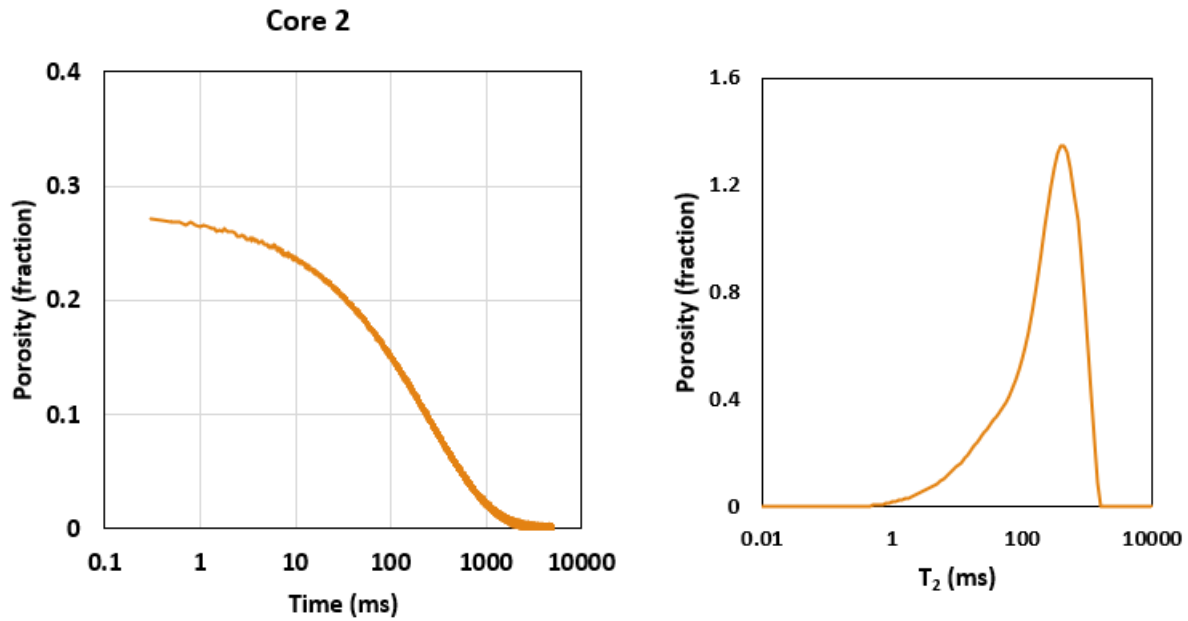


Figure 133. (Left) Normalized magnetization decay measurement and (Right) NMR T₂ distribution of core sample #2.

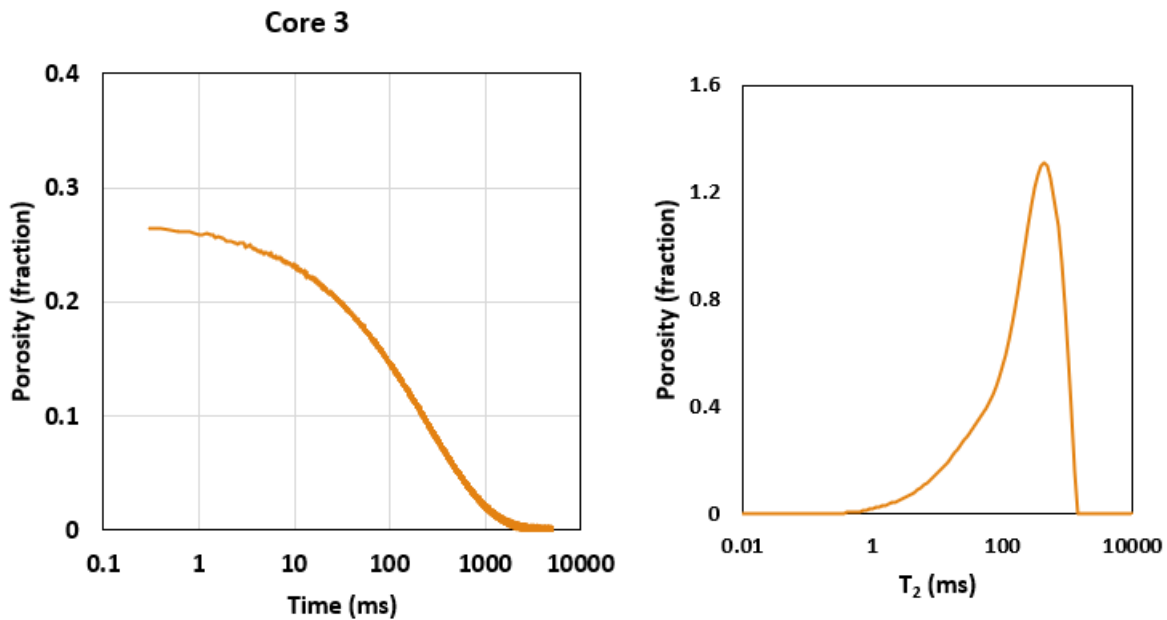


Figure 134. (Left) Normalized magnetization decay measurement and (Right) NMR T₂ distribution of core sample #3.

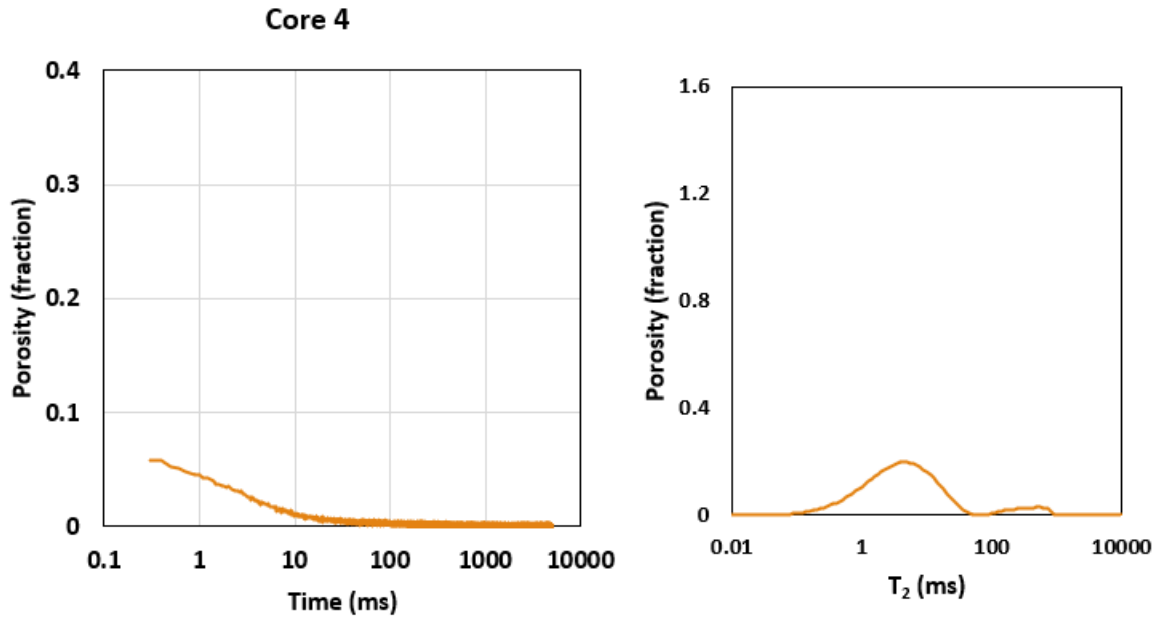


Figure 135. (Left) Normalized magnetization decay measurement and (Right) NMR T₂ distribution of core sample #4.

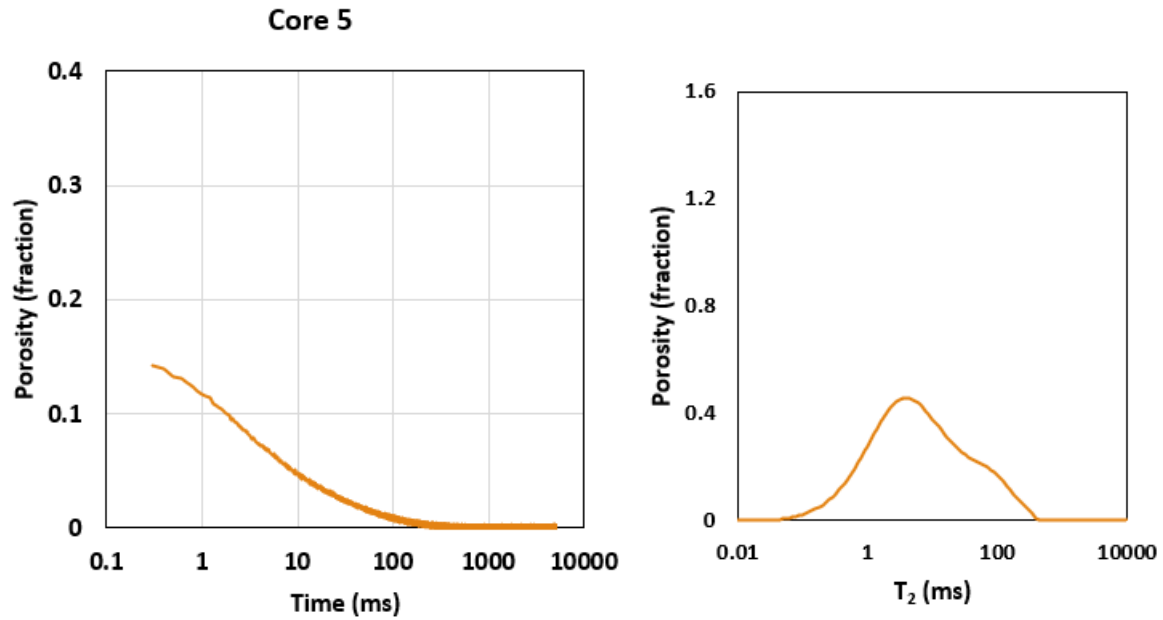


Figure 136. (Left) Normalized magnetization decay measurement and (Right) NMR T₂ distribution of core sample #5.

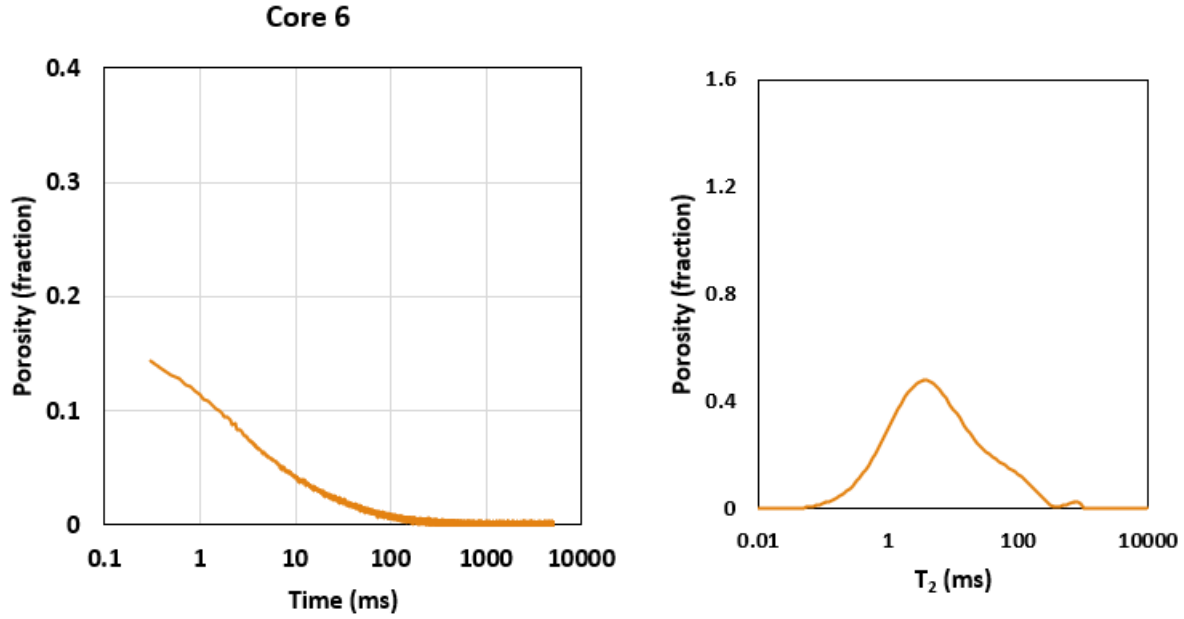


Figure 137. (Left) Normalized magnetization decay measurement and (Right) NMR T₂ distribution of core sample #6.

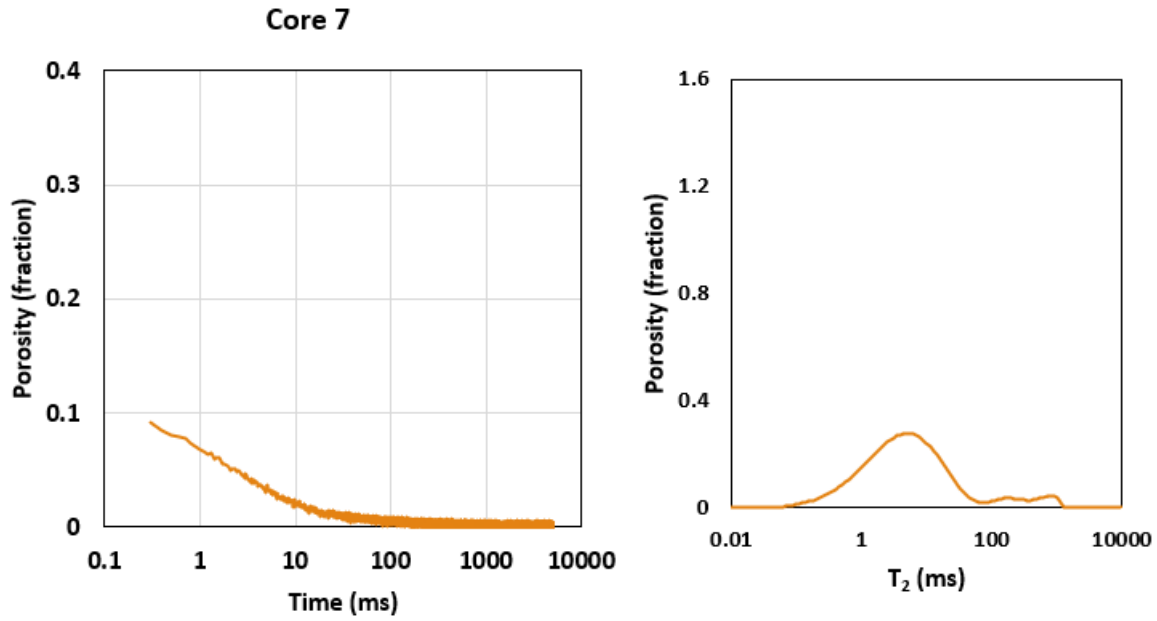


Figure 138. (Left) Normalized magnetization decay measurement and (Right) NMR T₂ distribution of core sample #7.

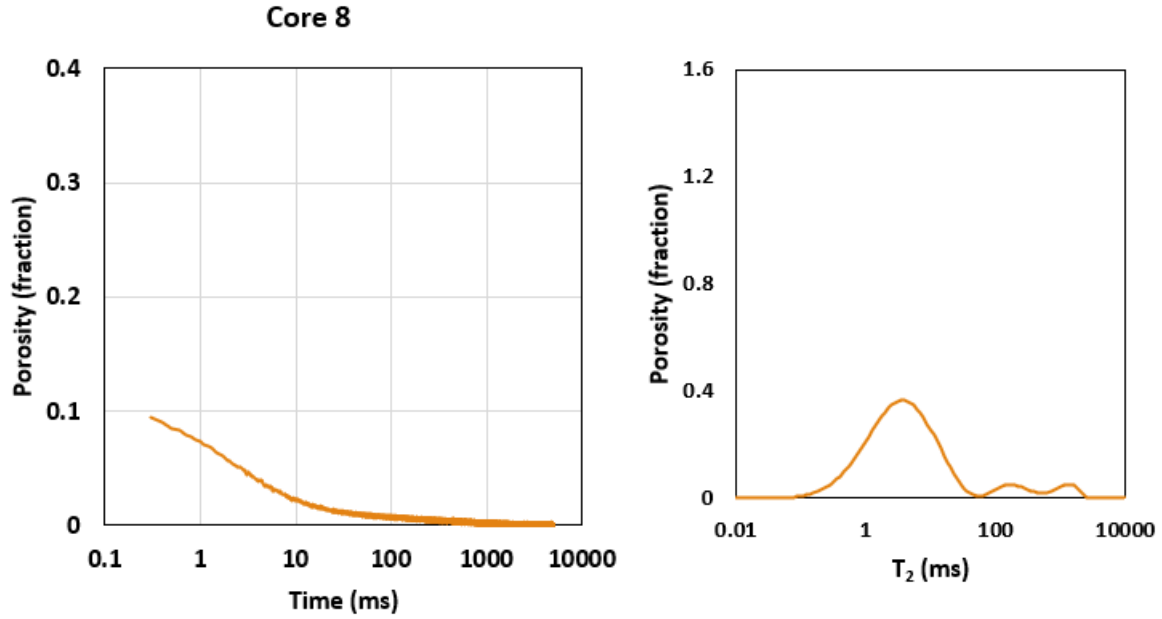


Figure 139. (Left) Normalized magnetization decay measurement and (Right) NMR T_2 distribution of core sample #8.

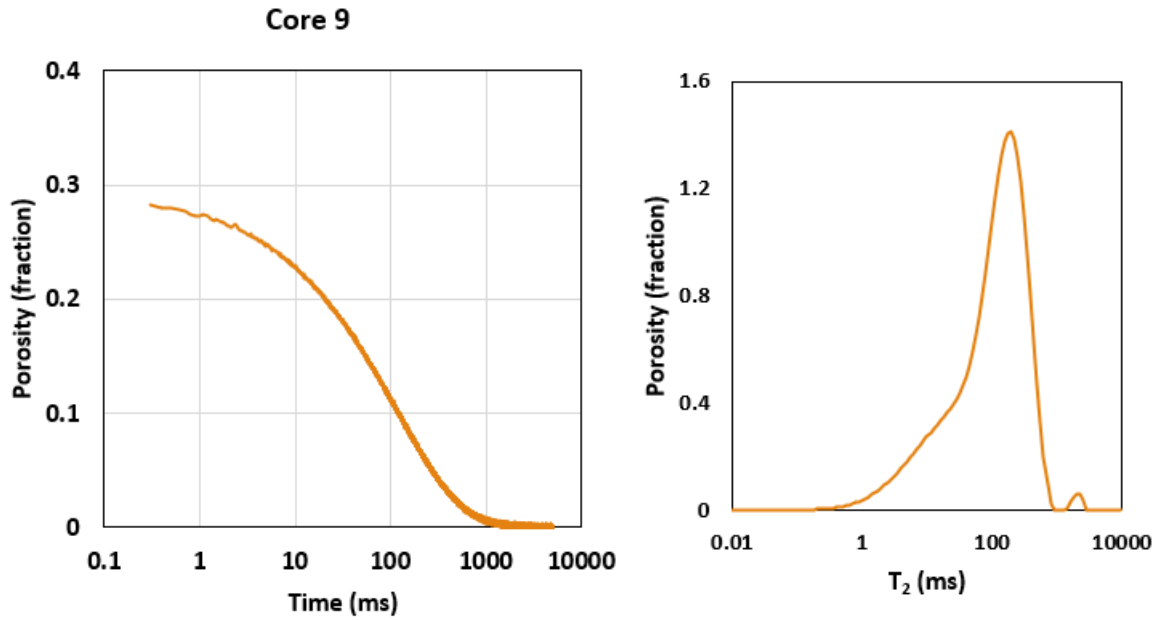


Figure 140. (Left) Normalized magnetization decay measurement and (Right) NMR T_2 distribution of core sample #9.

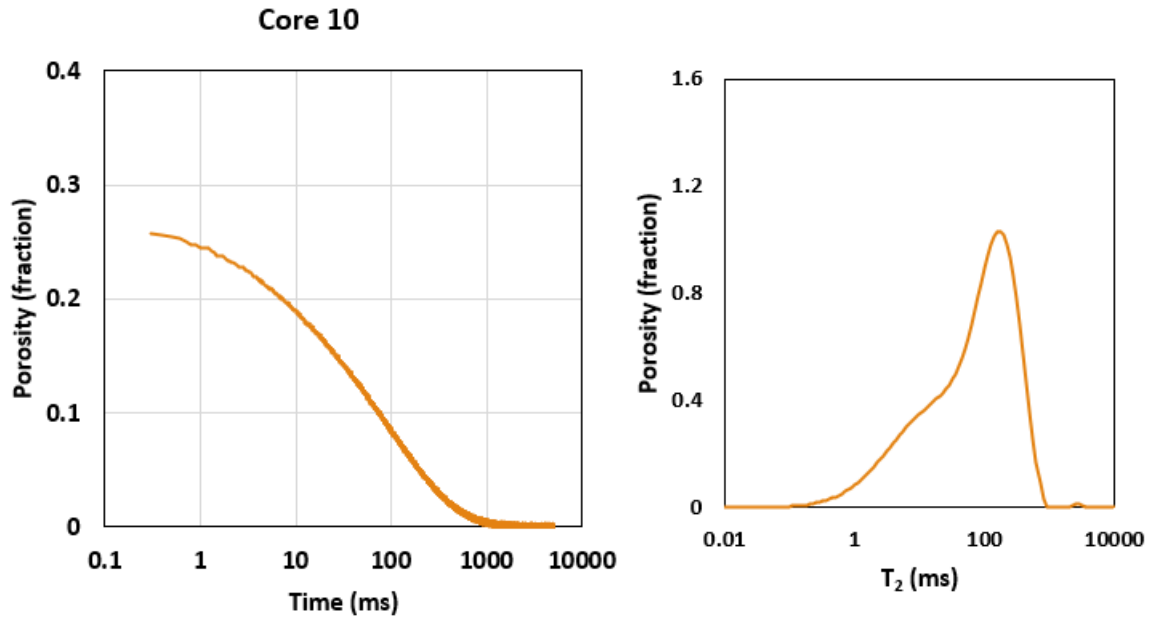


Figure 141. (Left) Normalized magnetization decay measurement and (Right) NMR T_2 distribution of core sample #10.

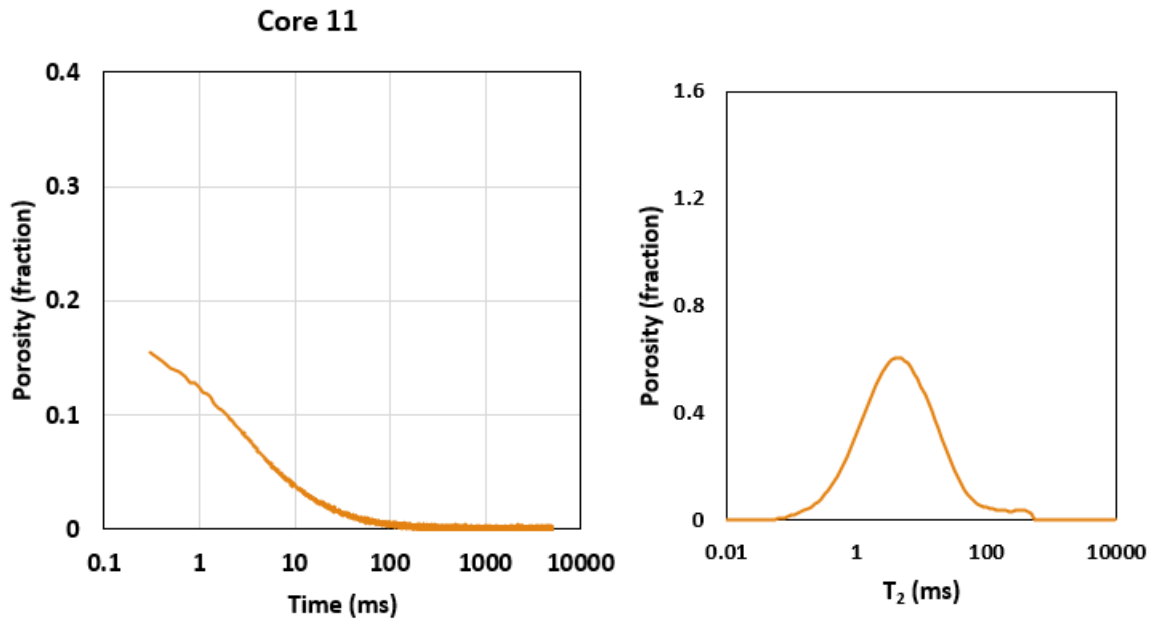


Figure 142. (Left) Normalized magnetization decay measurement and (Right) NMR T_2 distribution of core sample #11.

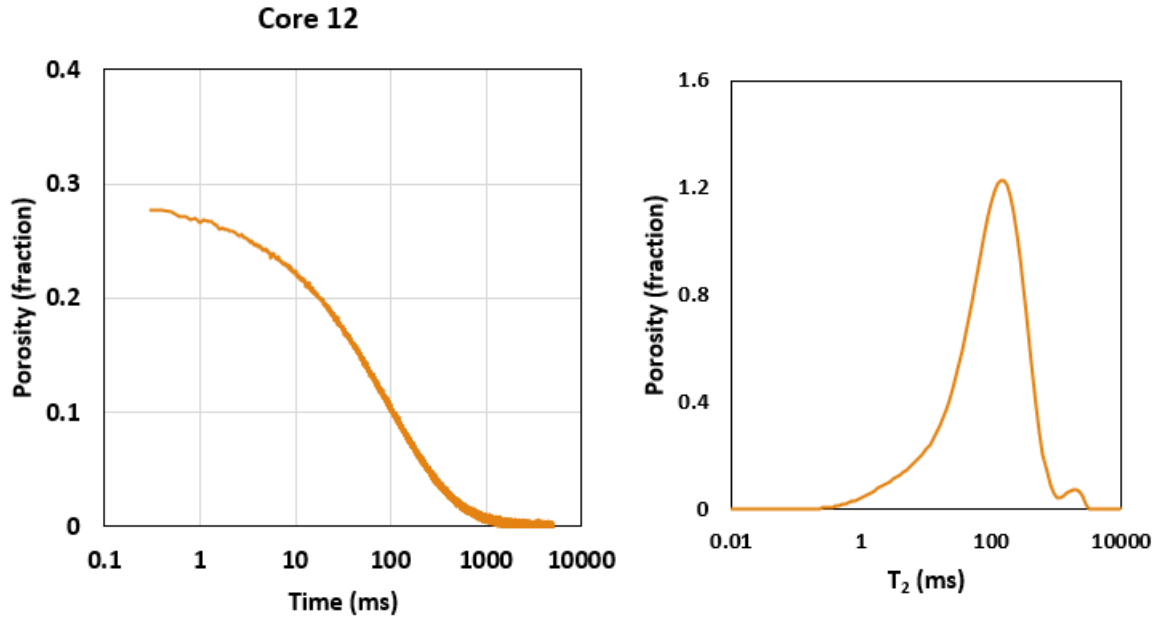


Figure 143. (Left) Normalized magnetization decay measurement and (Right) NMR T_2 distribution of core sample #12.

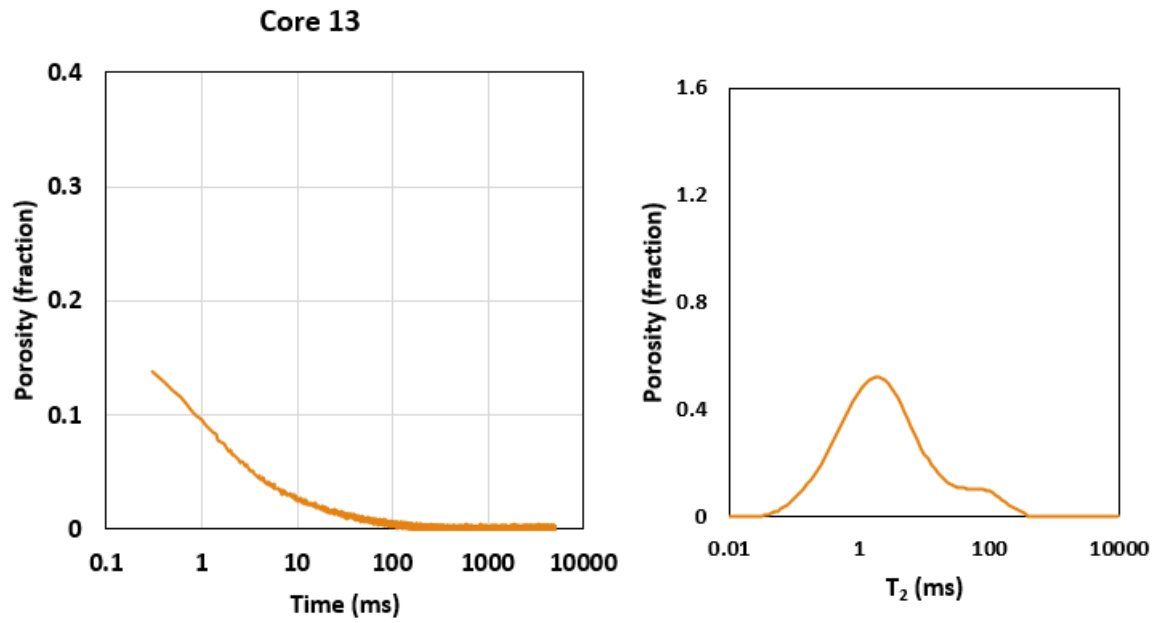


Figure 144. (Left) Normalized magnetization decay measurement and (Right) NMR T_2 distribution of core sample #13.

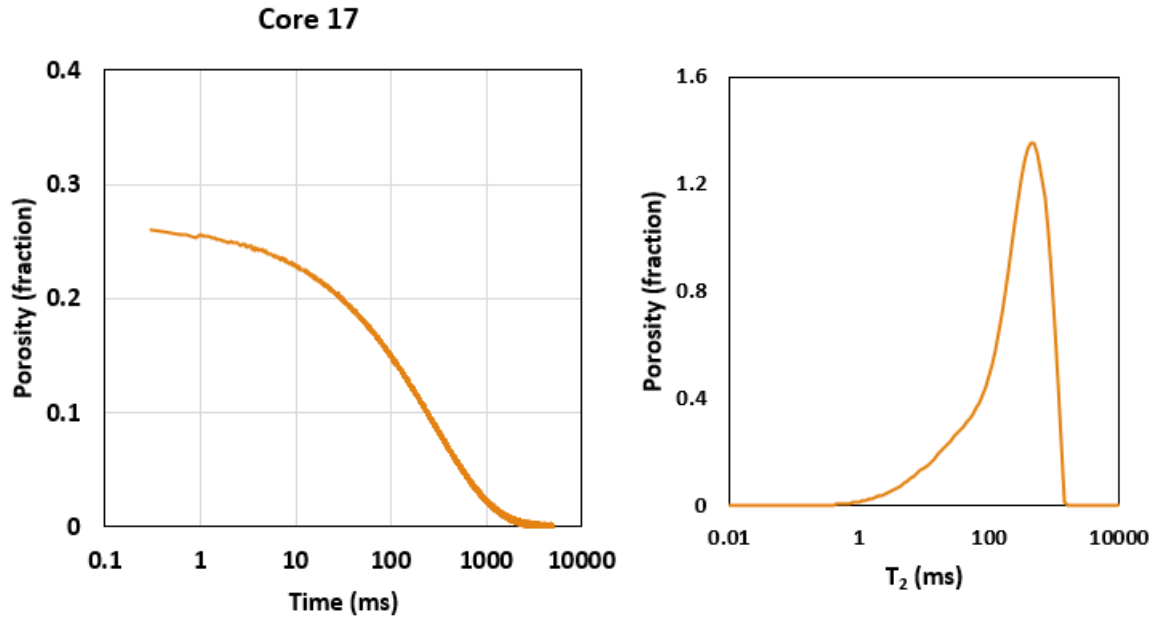


Figure 145. (Left) Normalized magnetization decay measurement and (Right) NMR T_2 distribution of core sample #17.

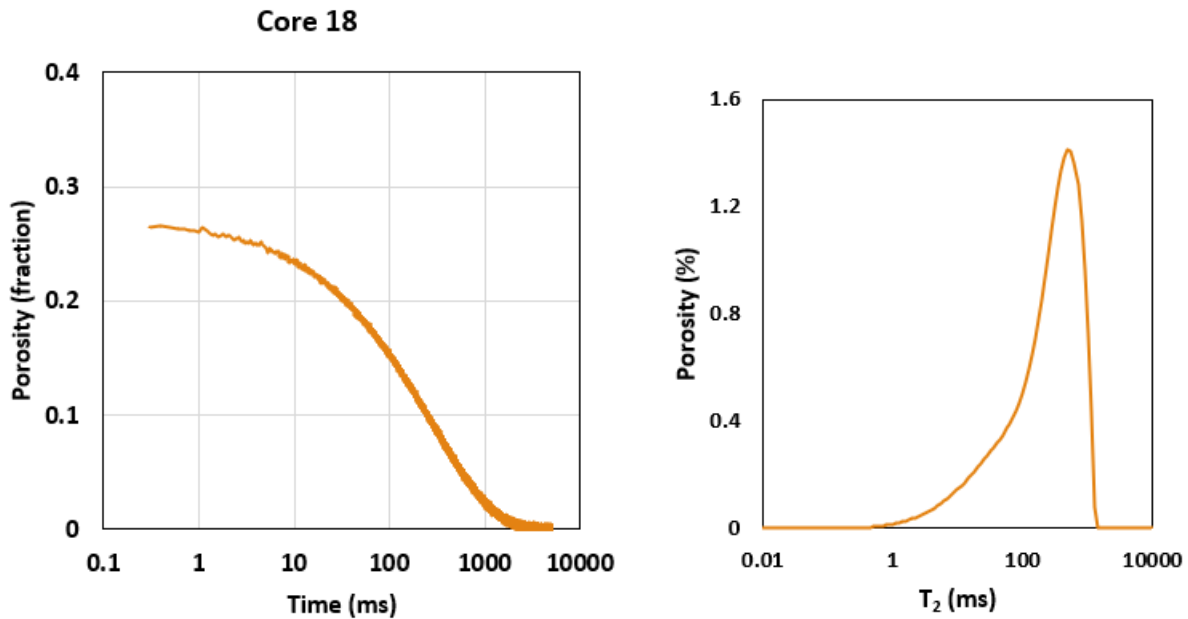


Figure 146. (Left) Normalized magnetization decay measurement and (Right) NMR T_2 distribution of core sample #18.

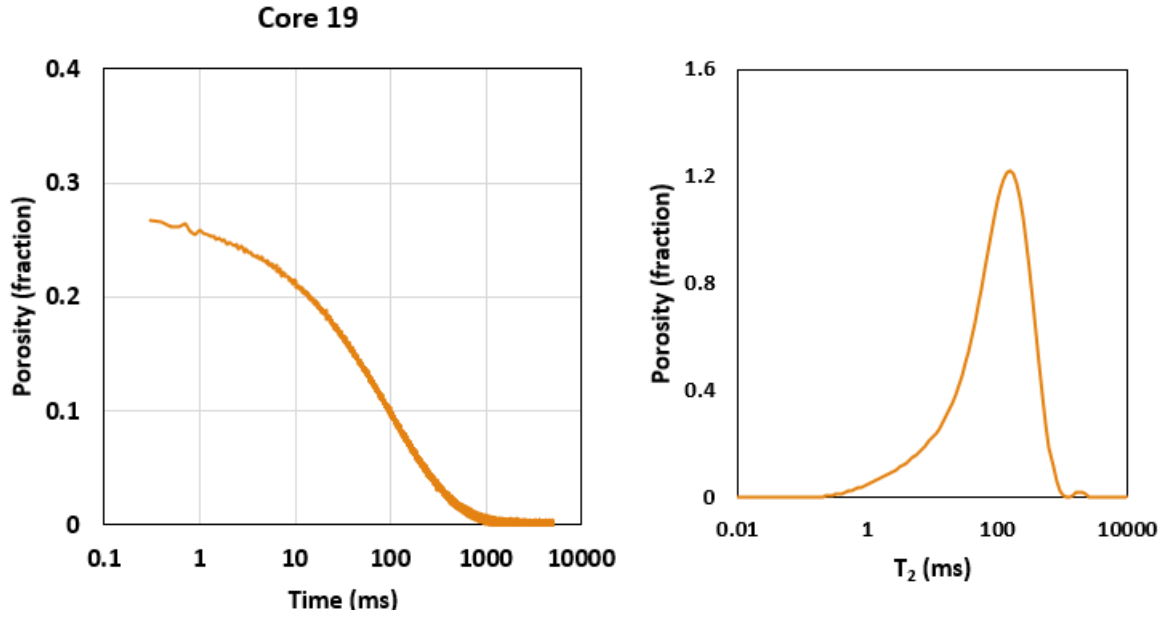


Figure 147. (Left) Normalized magnetization decay measurement and (Right) NMR T_2 distribution of core sample #19.

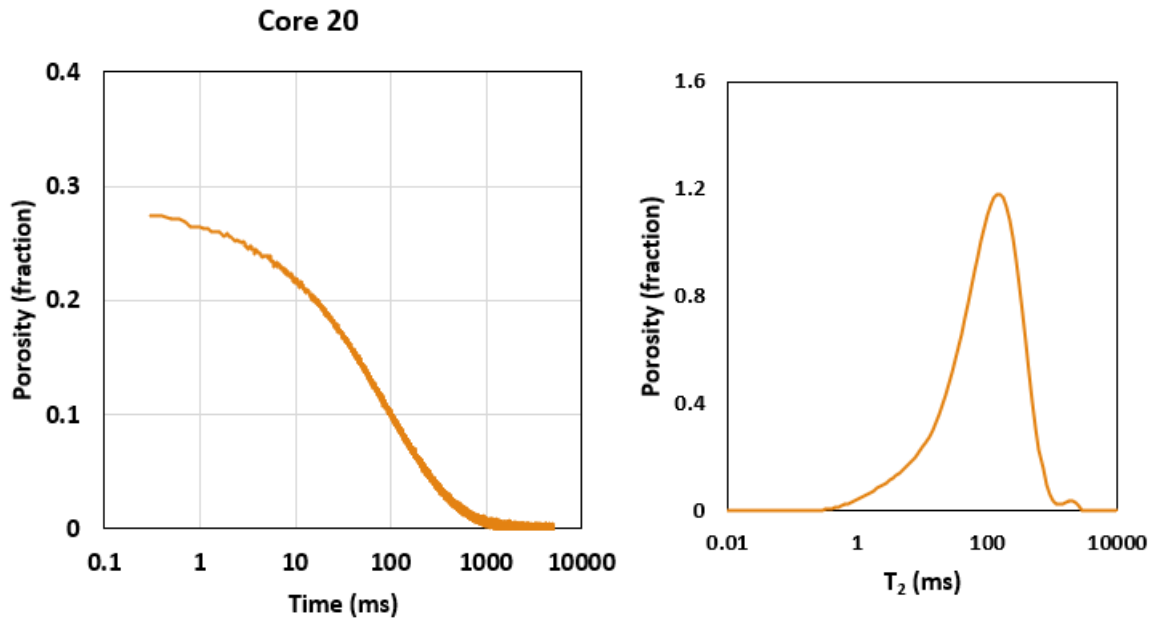


Figure 148. (Left) Normalized magnetization decay measurement and (Right) NMR T_2 distribution of core sample #20.

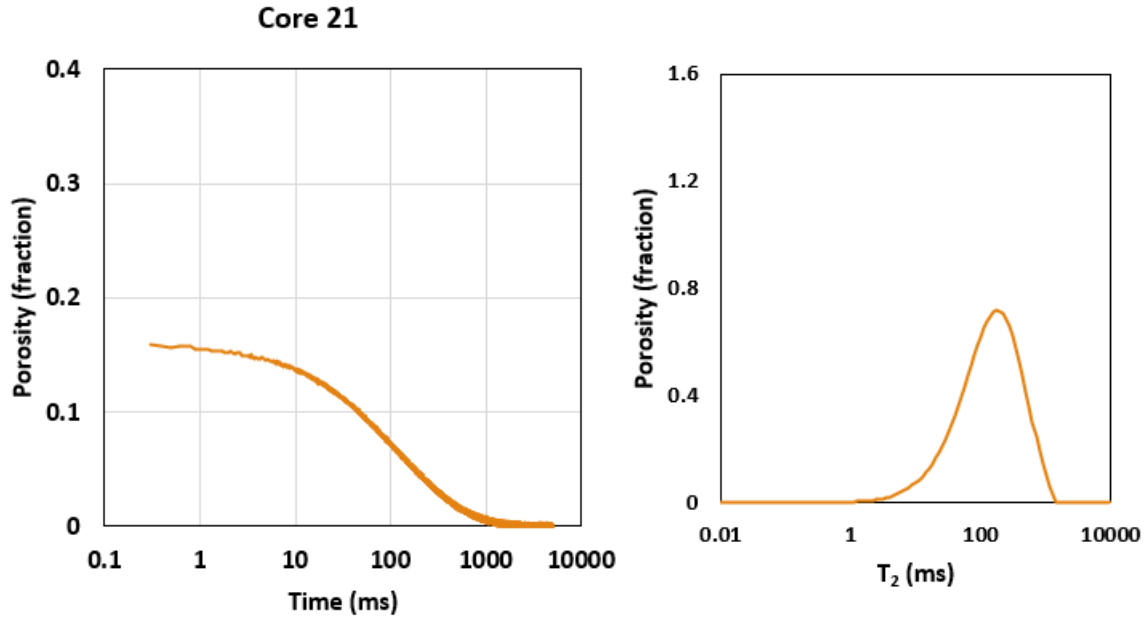


Figure 149. (Left) Normalized magnetization decay measurement and (Right) NMR T_2 distribution of core sample #21.

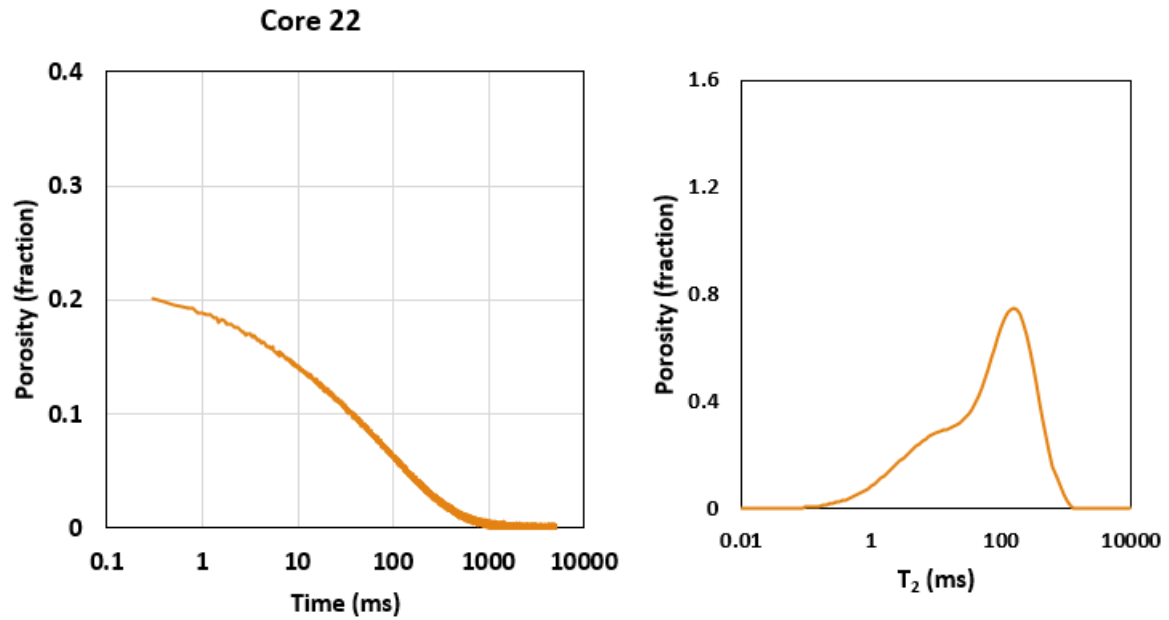


Figure 150. (Left) Normalized magnetization decay measurement and (Right) NMR T_2 distribution of core sample #22.

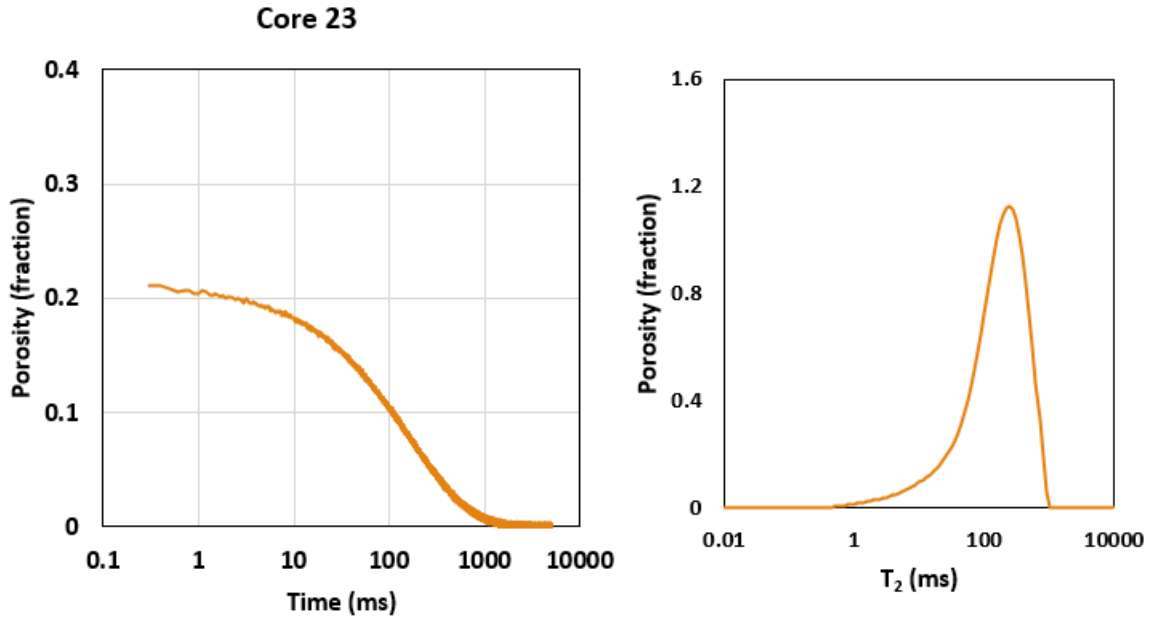


Figure 151. (Left) Normalized magnetization decay measurement and (Right) NMR T_2 distribution of core sample #23.

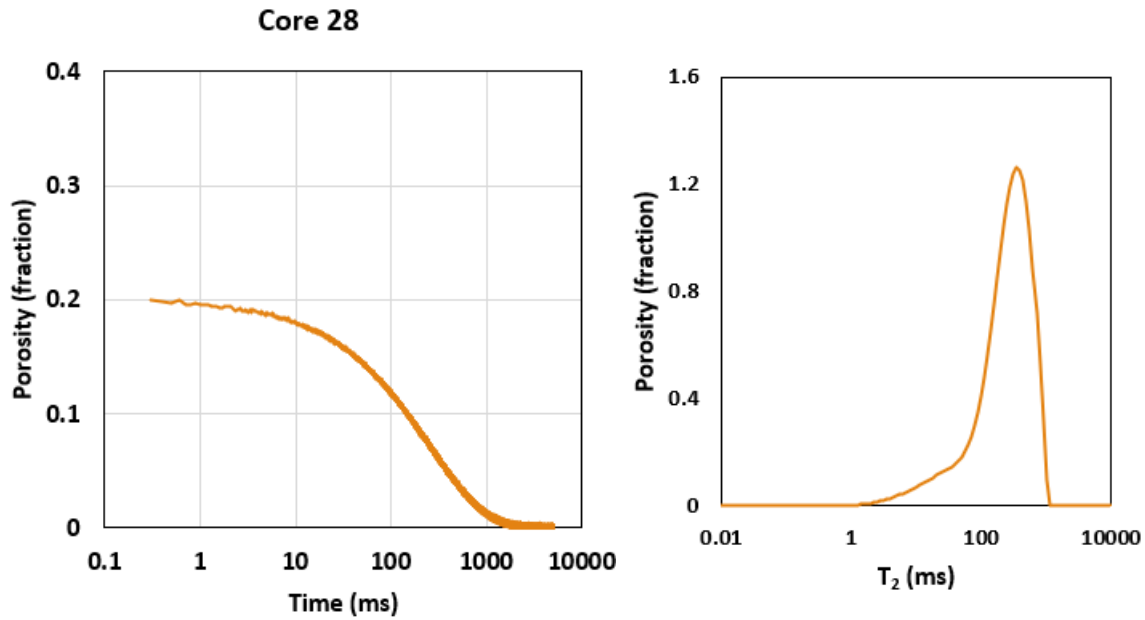


Figure 152. (Left) Normalized magnetization decay measurement and (Right) NMR T_2 distribution of core sample #28.

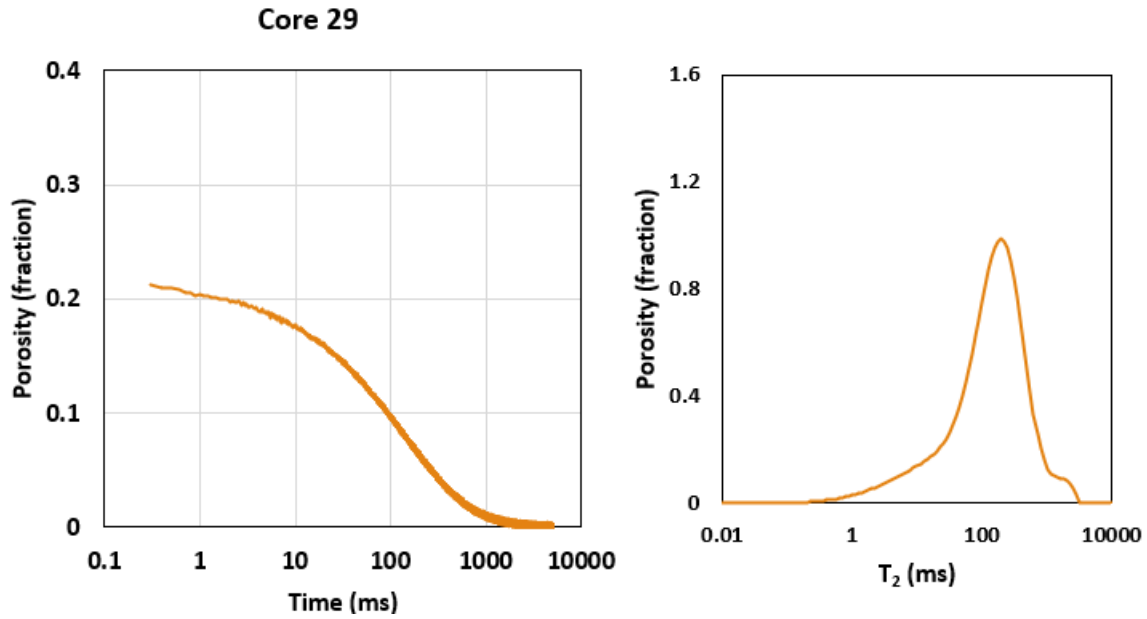


Figure 153. (Left) Normalized magnetization decay measurement and (Right) NMR T_2 distribution of core sample #29.

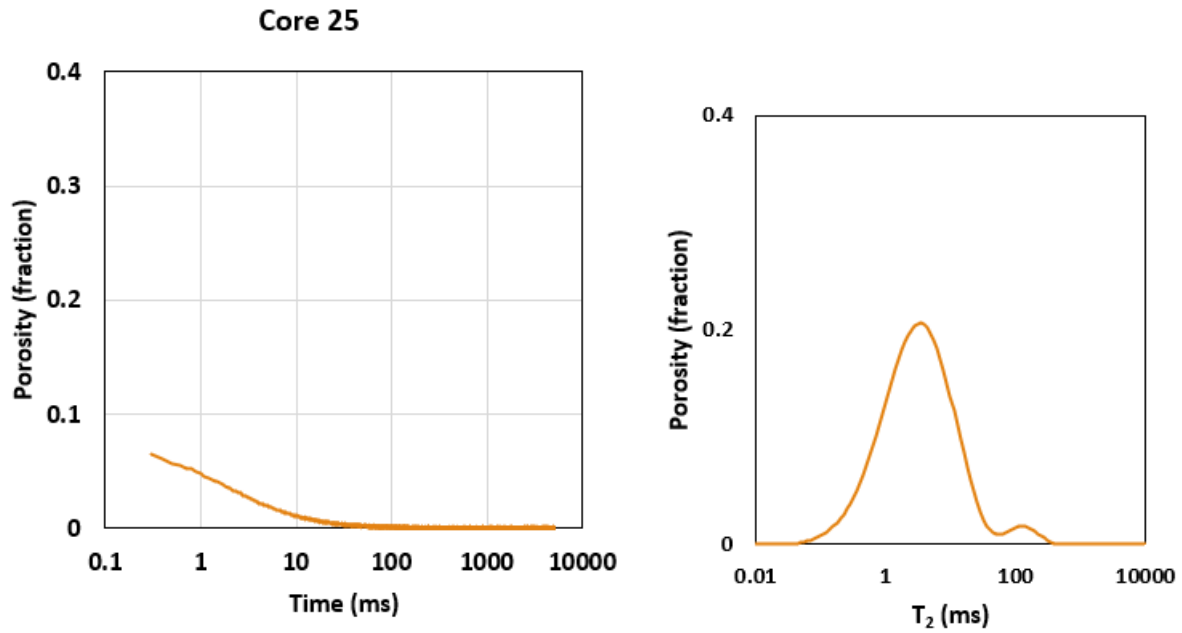


Figure 154. (Left) Normalized magnetization decay measurement and (Right) NMR T_2 distribution of core sample #25.

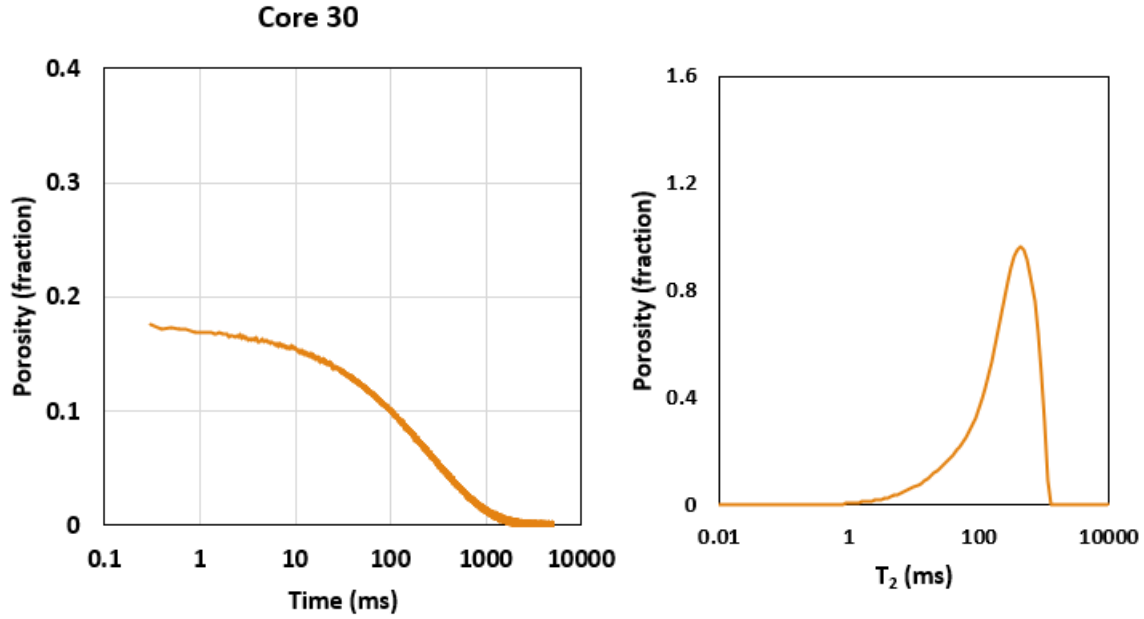


Figure 155. (Left) Normalized magnetization decay measurement and (Right) NMR T₂ distribution of core sample #30.

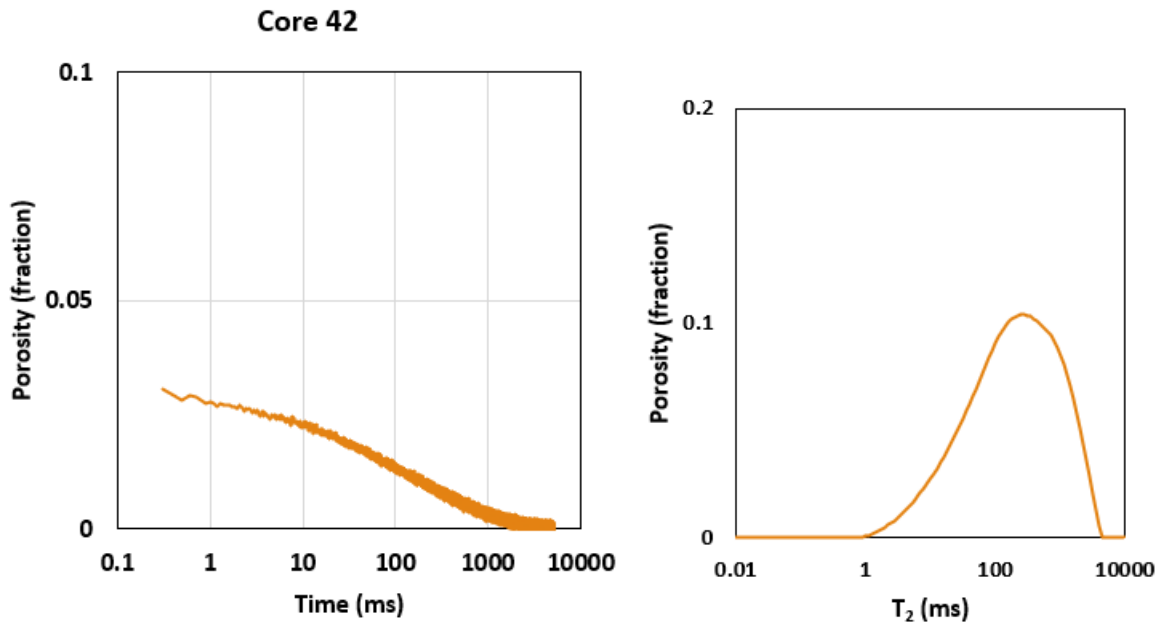


Figure 156. (Left) Normalized magnetization decay measurement and (Right) NMR T₂ distribution of core sample #42.

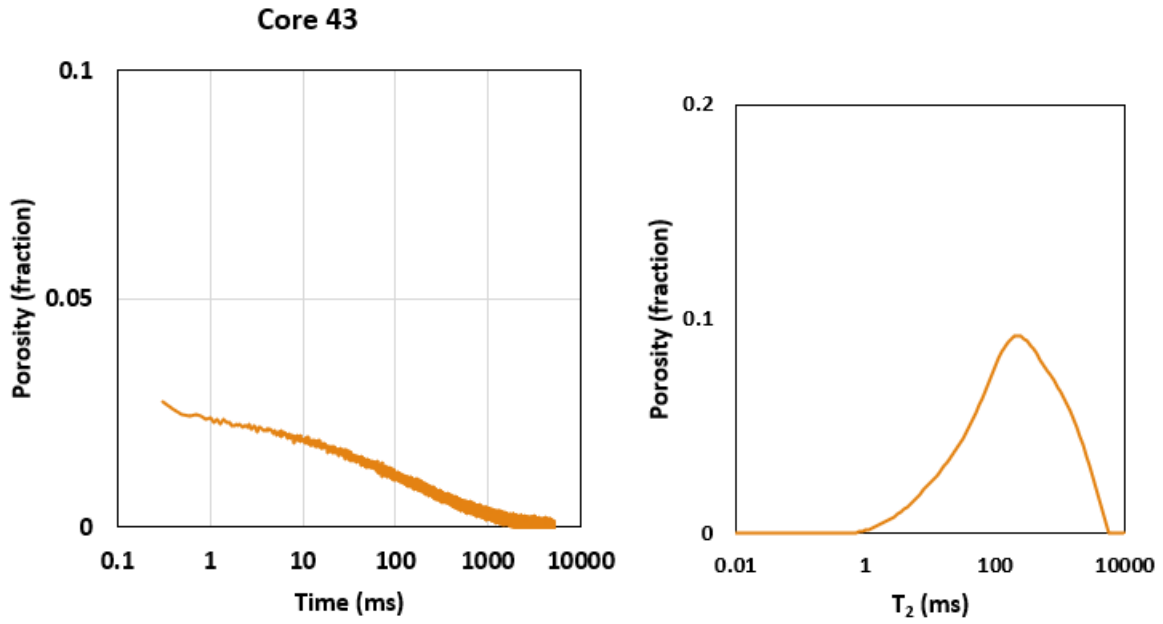


Figure 157. (Left) Normalized magnetization decay measurement and (Right) NMR T_2 distribution of core sample #43.

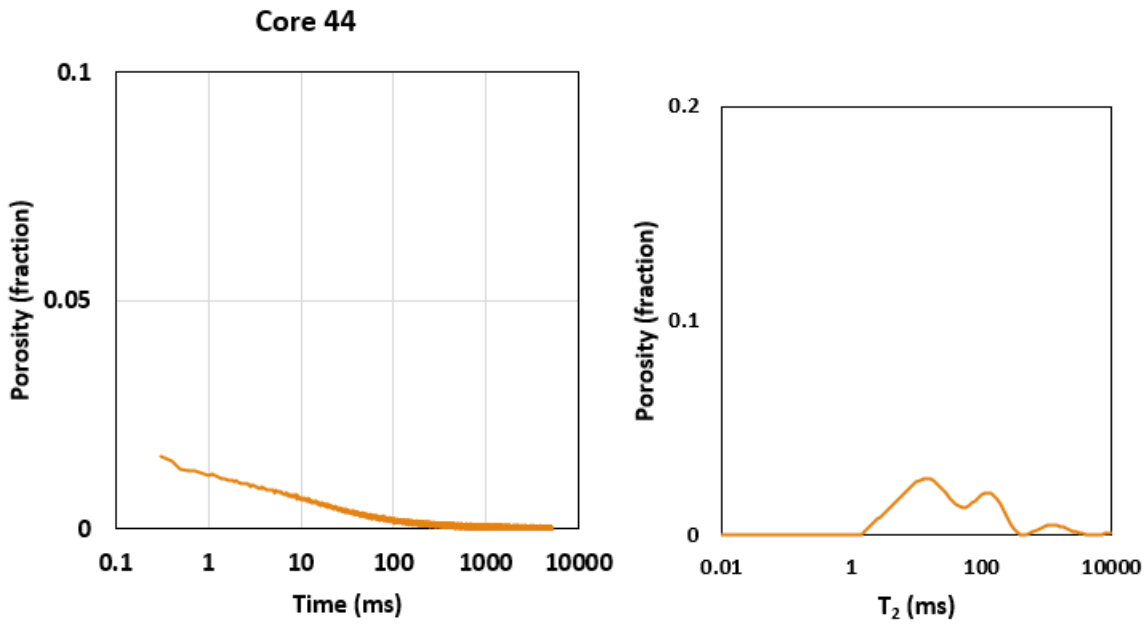


Figure 158. (Left) Normalized magnetization decay measurement and (Right) NMR T_2 distribution of core sample #44.

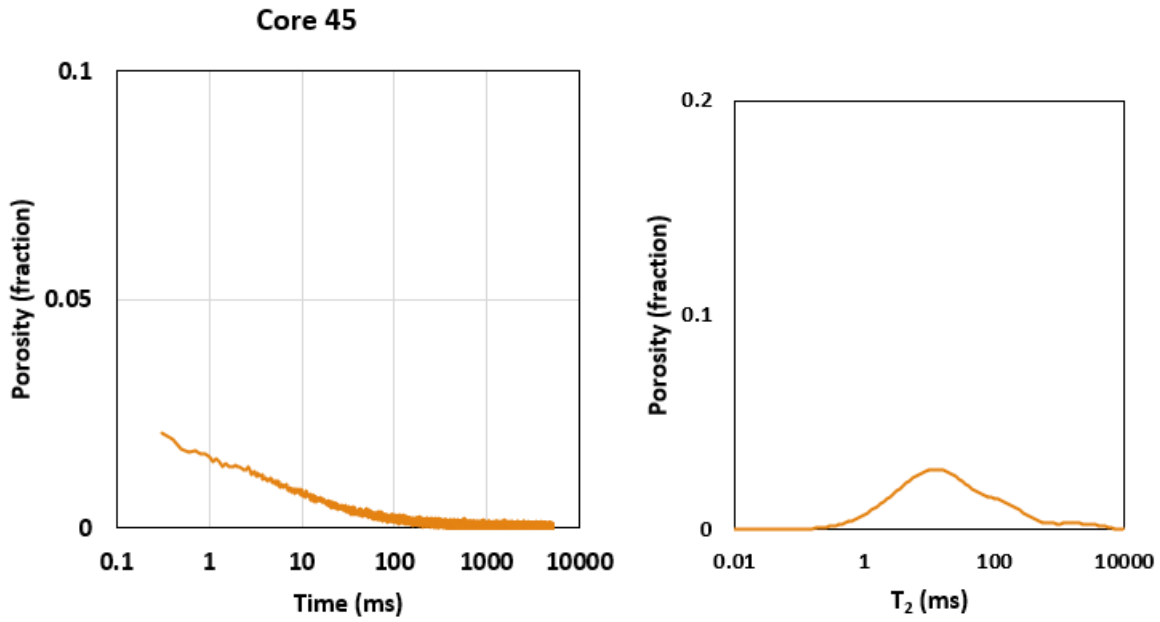


Figure 159. (Left) Normalized magnetization decay measurement and (Right) NMR T_2 distribution of core sample #45.

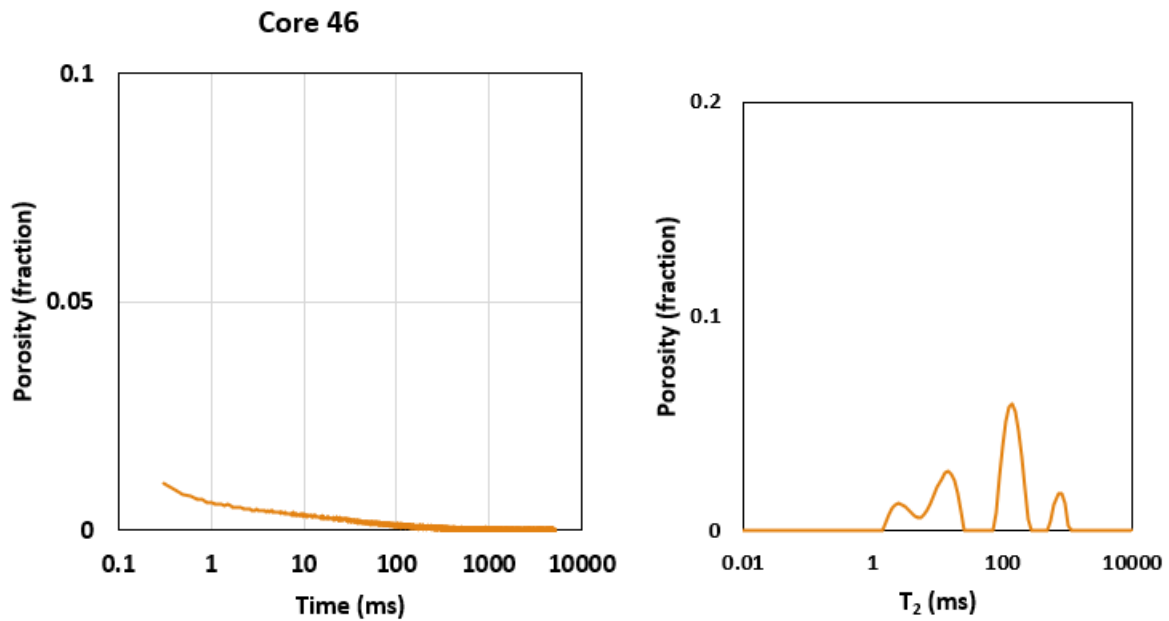


Figure 160. (Left) Normalized magnetization decay measurement and (Right) NMR T_2 distribution of core sample #46.

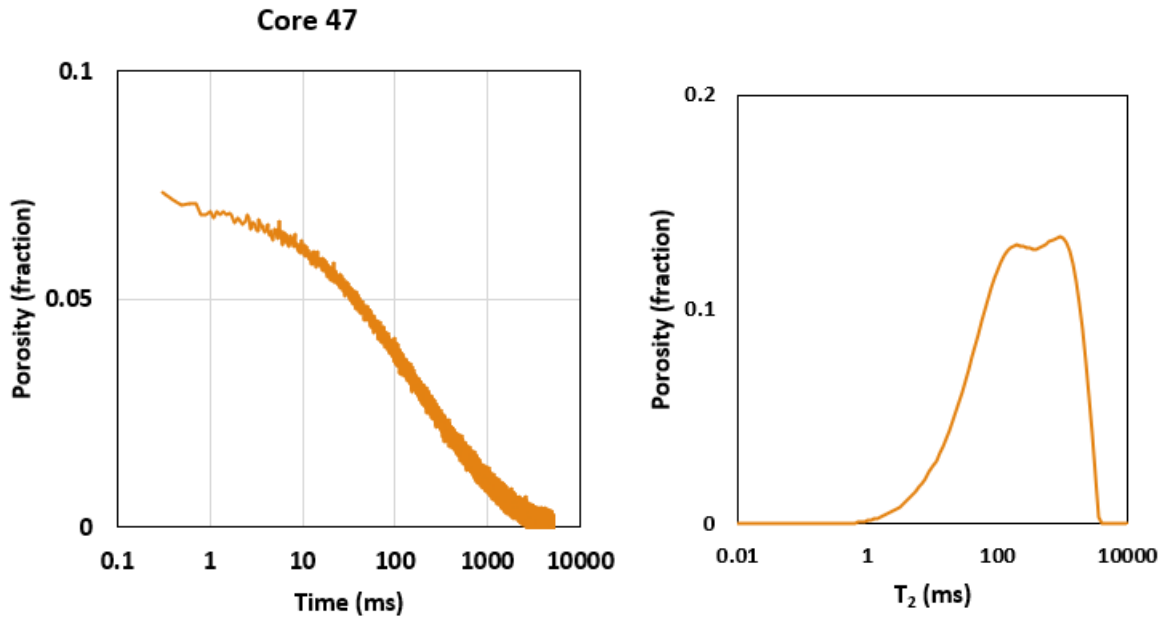


Figure 161. (Left) Normalized magnetization decay measurement and (Right) NMR T_2 distribution of core sample #47.

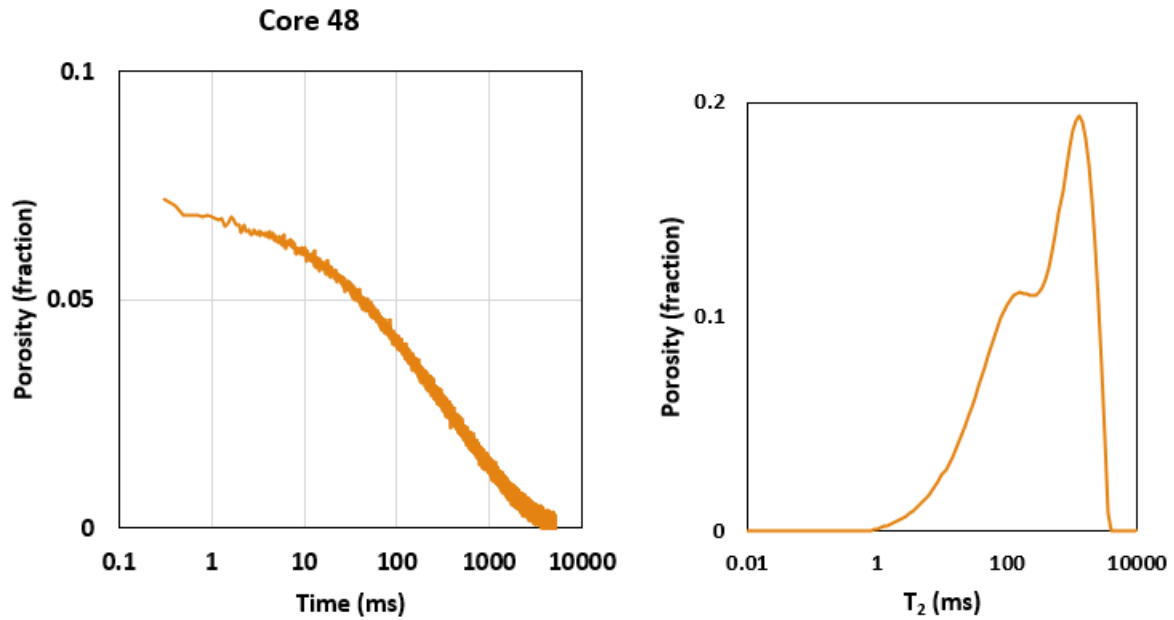


Figure 162. (Left) Normalized magnetization decay measurement and (Right) NMR T_2 distribution of core sample #48.

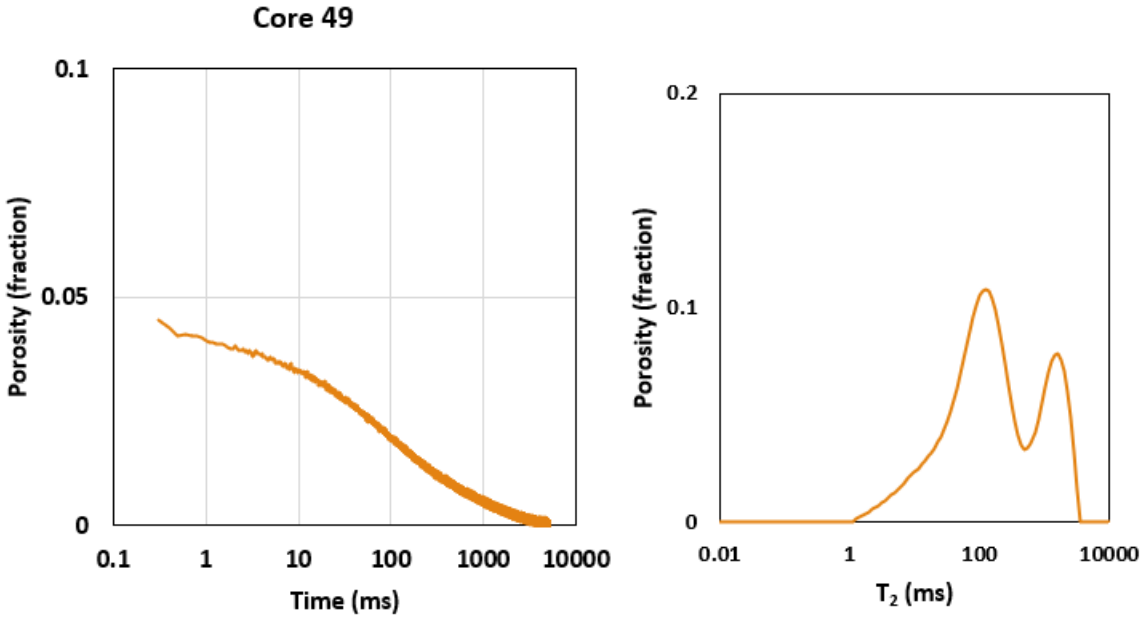


Figure 163. (Left) Normalized magnetization decay measurement and (Right) NMR T_2 distribution of core sample #49.

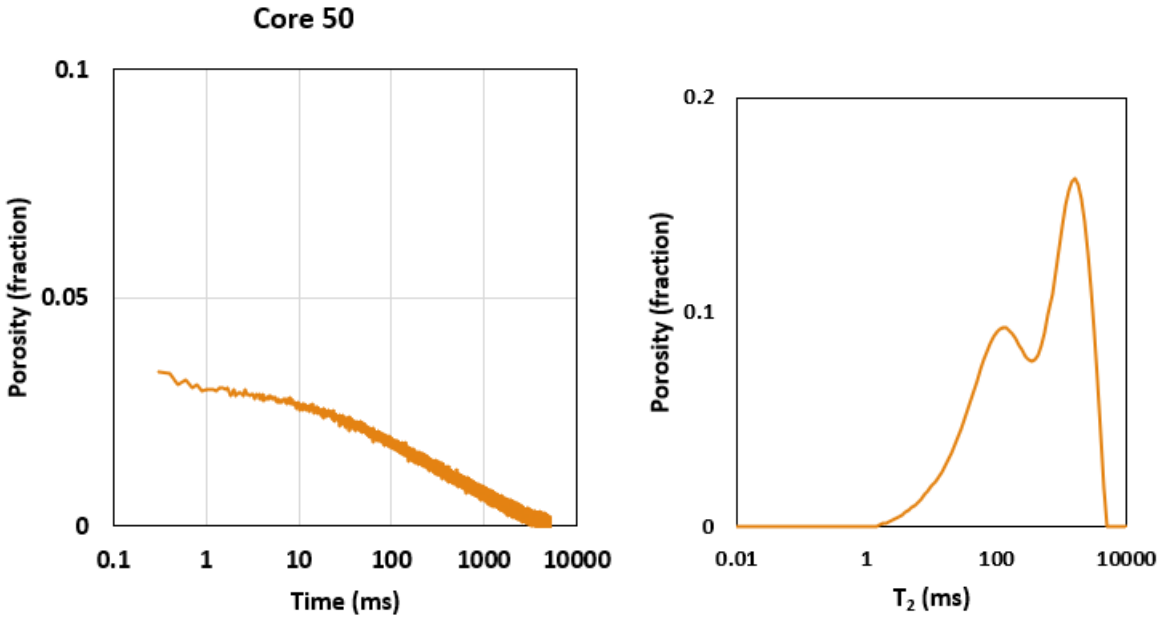


Figure 164. (Left) Normalized magnetization decay measurement and (Right) NMR T_2 distribution of core sample #50.

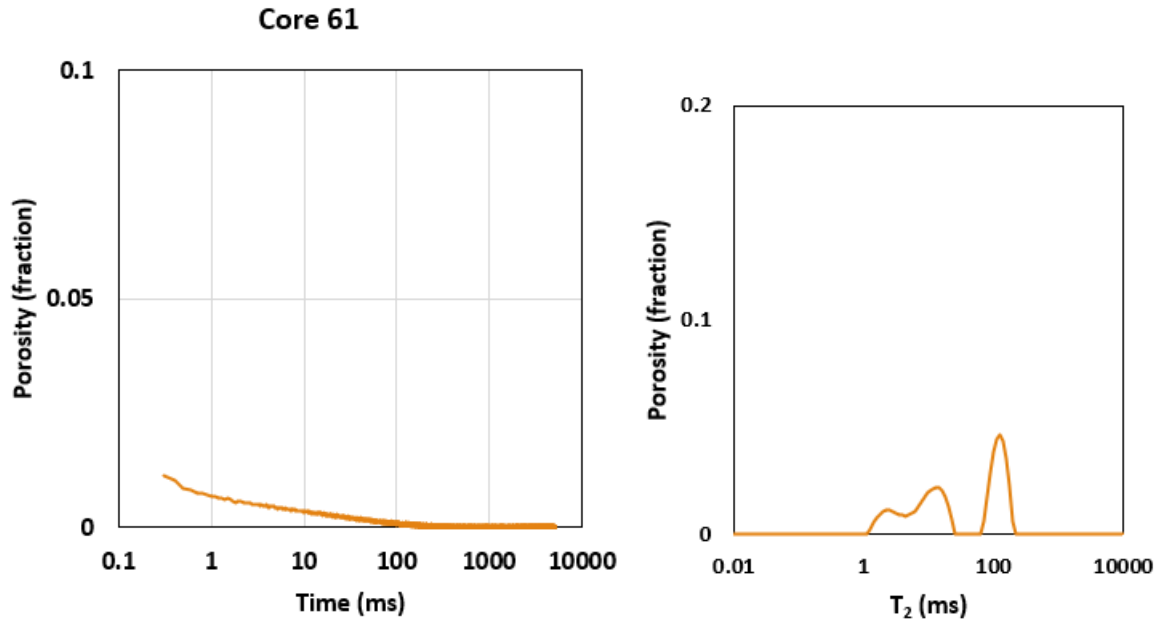


Figure 165. (Left) Normalized magnetization decay measurement and (Right) NMR T₂ distribution of core sample #61.

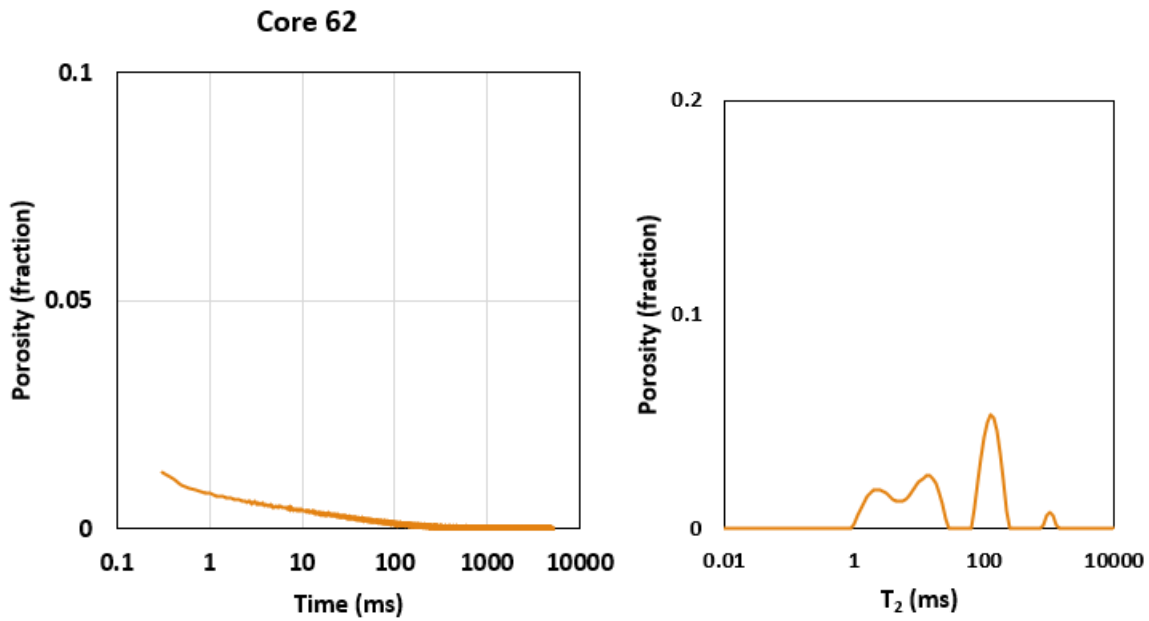


Figure 166. (Left) Normalized magnetization decay measurement and (Right) NMR T₂ distribution of core sample #62.

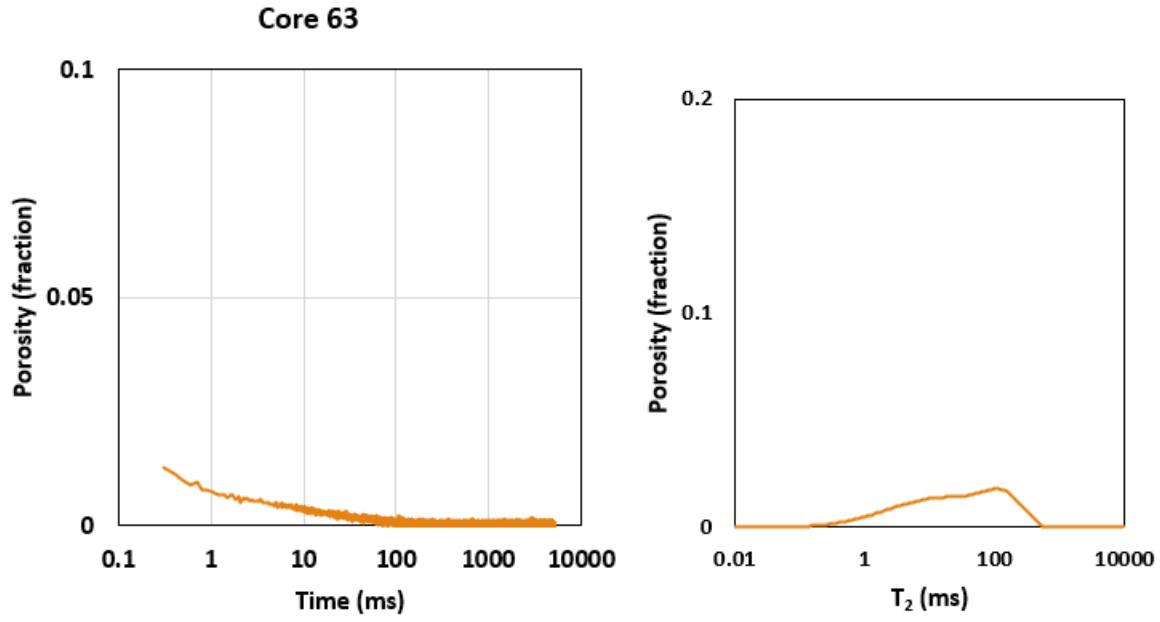


Figure 167. (Left) Normalized magnetization decay measurement and (Right) NMR T_2 distribution of core sample #63.

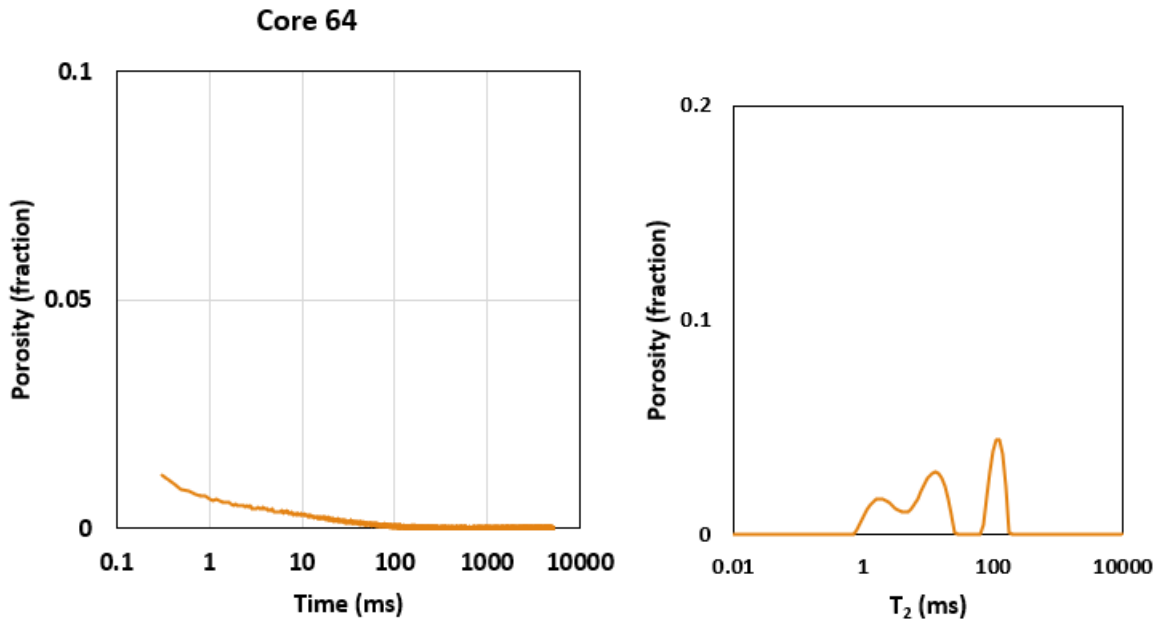


Figure 168. (Left) Normalized magnetization decay measurement and (Right) NMR T_2 distribution of core sample #64.

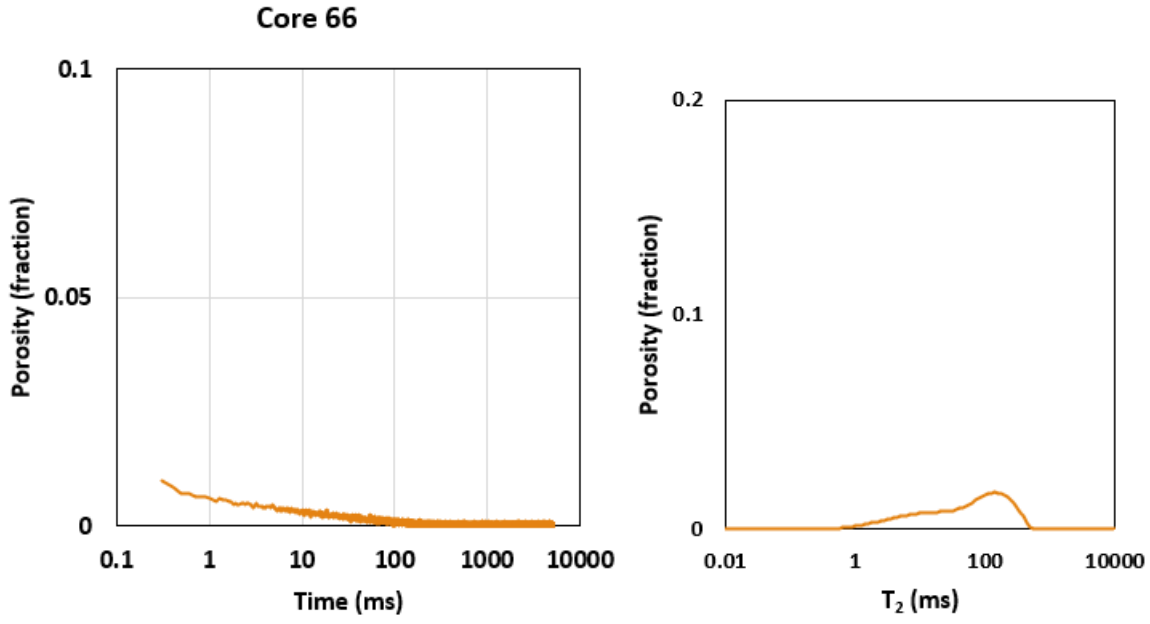


Figure 169. (Left) Normalized magnetization decay measurement and (Right) NMR T_2 distribution of core sample #66.

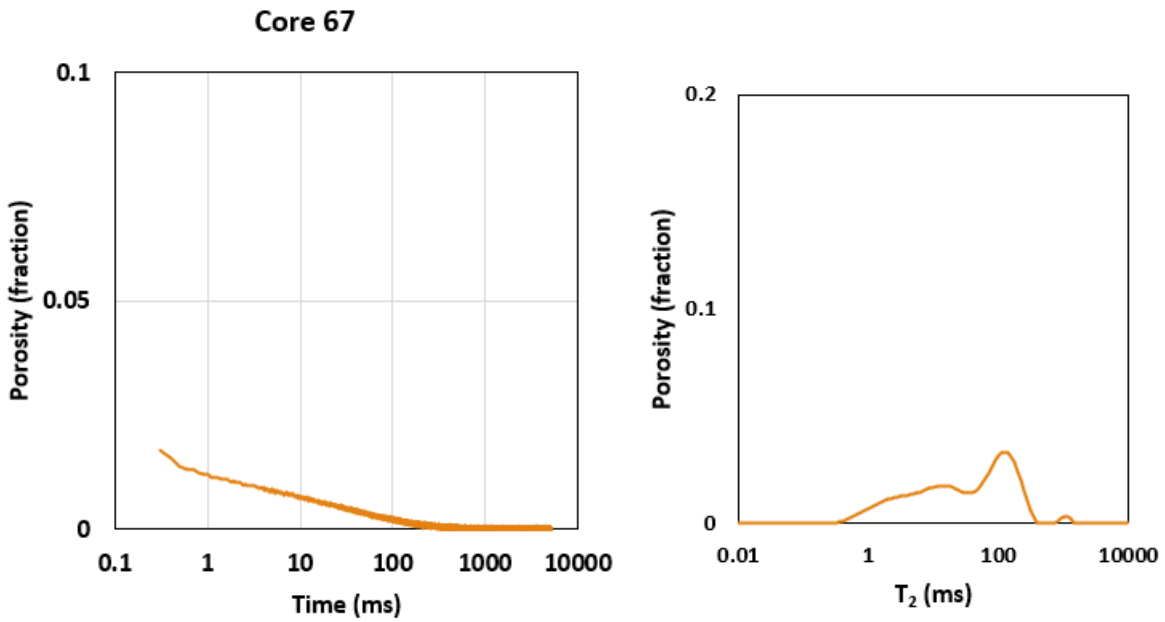


Figure 170. (Left) Normalized magnetization decay measurement and (Right) NMR T_2 distribution of core sample #67.

APPENDIX D – WATER PERMEABILITY MEASUREMENTS

Permeability to water is estimated using Darcy's equation. For a given core sample, different levels of pressure difference are applied to the corresponding flow rate is measured. According to Darcy's law, flow rate varies linearly with respect to differential pressure where the slope is proportional to permeability. 3 wt.% KCl brine was used to conduct flow experiments.

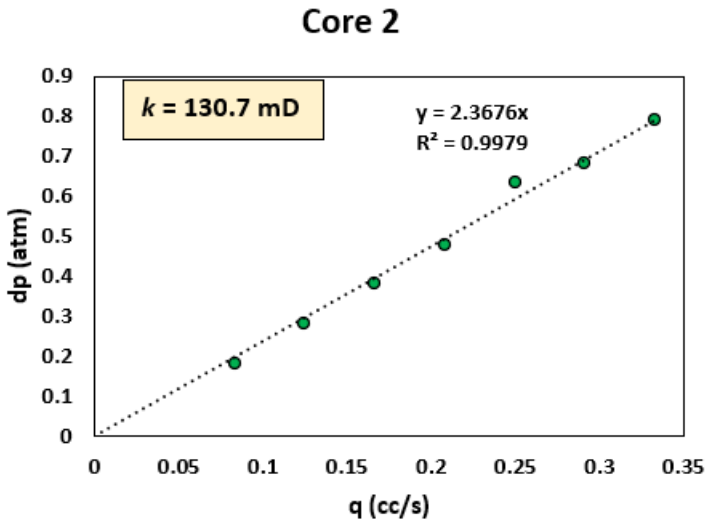


Figure 171. Permeability assessment for core sample #2. This plot shows the measured flow rate of water at different levels of pressure difference applied to the core sample. Dot line is the slope which is used to estimate permeability.

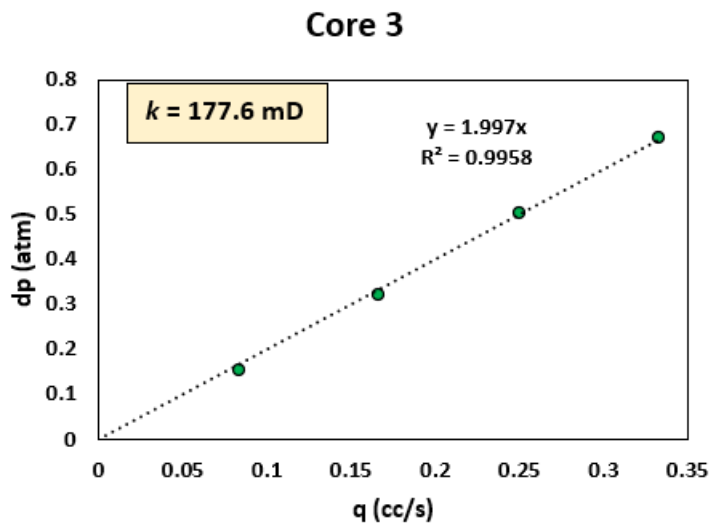


Figure 172. Permeability assessment for core sample #3. This plot shows the measured flow rate of water at different levels of pressure difference applied to the core sample. 3 wt.% KCl brine is used to conduct flow experiments. Dot line is the slope which is used to estimate permeability.

Core 9

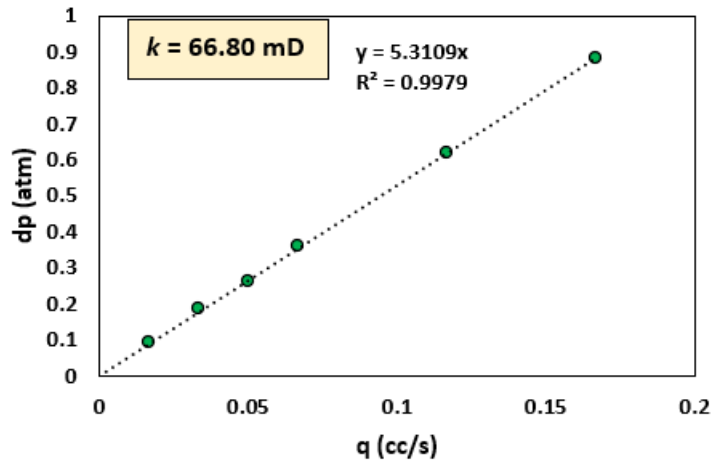


Figure 173. Permeability assessment for core sample #9. This plot shows the measured flow rate of water at different levels of pressure difference applied to the core sample. 3 wt.% KCl brine is used to conduct flow experiments. Dot line is the slope which is used to estimate permeability.

Core 10

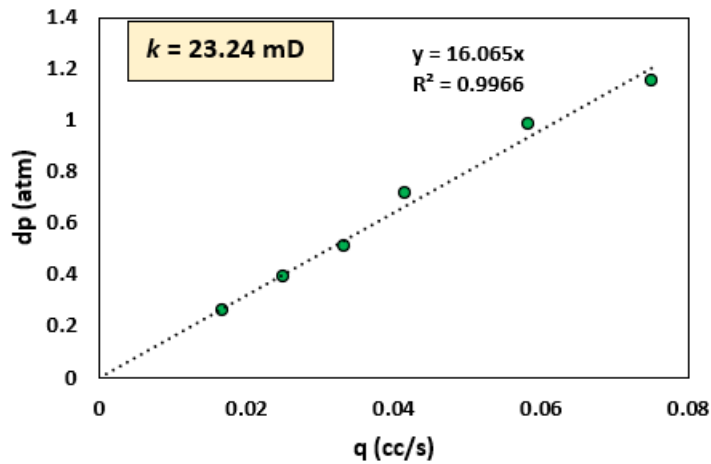


Figure 174. Permeability assessment for core sample #10. This plot shows the measured flow rate of water at different levels of pressure difference applied to the core sample. 3 wt.% KCl brine is used to conduct flow experiments. Dot line is the slope which is used to estimate permeability.

Core 12

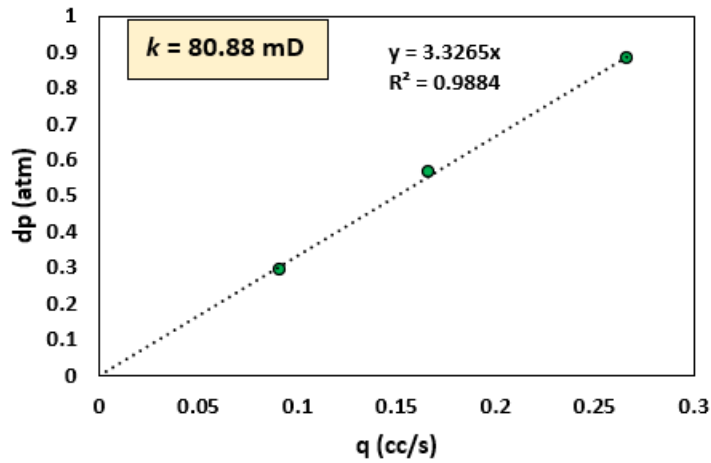


Figure 175. Permeability assessment for core sample #12. This plot shows the measured flow rate of water at different levels of pressure difference applied to the core sample. 3 wt.% KCl brine is used to conduct flow experiments. Dot line is the slope which is used to estimate permeability.

Core 17

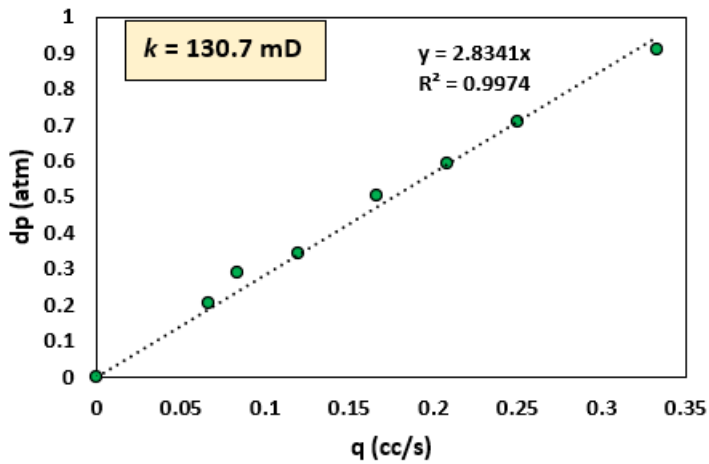


Figure 176. Permeability assessment for core sample #17. This plot shows the measured flow rate of water at different levels of pressure difference applied to the core sample. 3 wt.% KCl brine is used to conduct flow experiments. Dot line is the slope which is used to estimate permeability.

Core 18

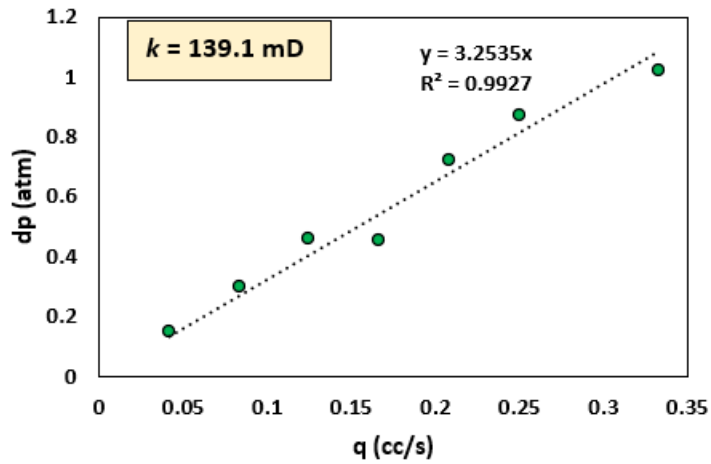


Figure 177. Permeability assessment for core sample #18. This plot shows the measured flow rate of water at different levels of pressure difference applied to the core sample. 3 wt.% KCl brine is used to conduct flow experiments. Dot line is the slope which is used to estimate permeability.

Core 19

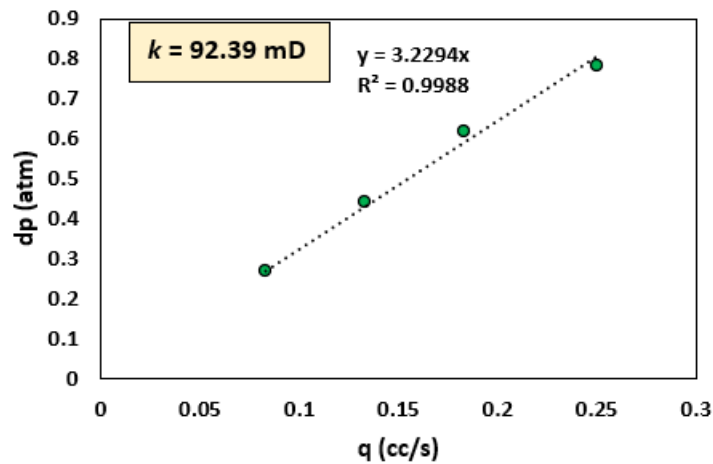


Figure 178. Permeability assessment for core sample #19. This plot shows the measured flow rate of water at different levels of pressure difference applied to the core sample. 3 wt.% KCl brine is used to conduct flow experiments. Dot line is the slope which is used to estimate permeability.

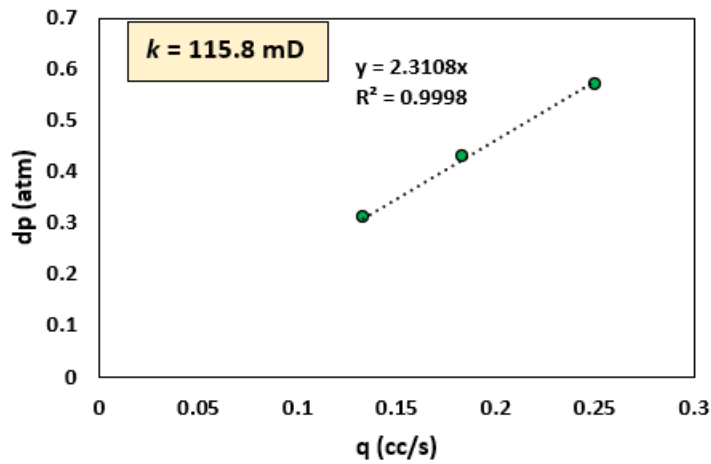
Core 20

Figure 179. Permeability assessment for core sample #20. This plot shows the measured flow rate of water at different levels of pressure difference applied to the core sample. 3 wt.% KCl brine is used to conduct flow experiments. Dot line is the slope which is used to estimate permeability.

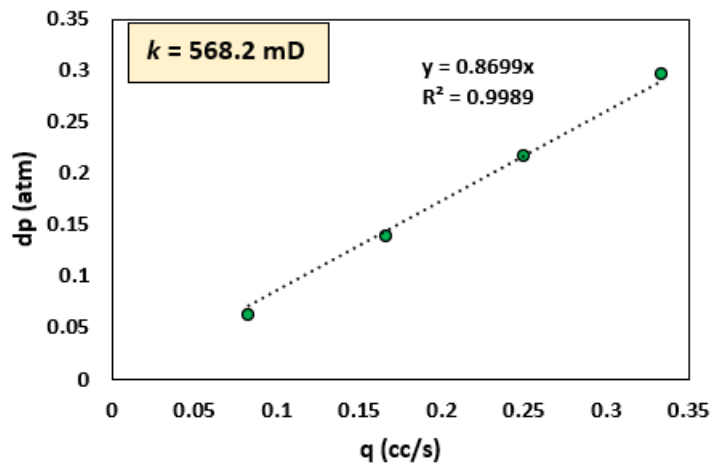
Core 21

Figure 180. Permeability assessment for core sample #21. This plot shows the measured flow rate of water at different levels of pressure difference applied to the core sample. 3 wt.% KCl brine is used to conduct flow experiments. Dot line is the slope which is used to estimate permeability.

Core 22

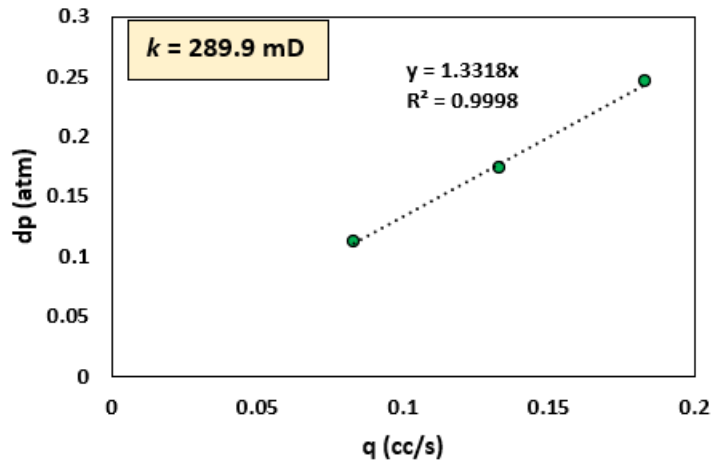


Figure 181. Permeability assessment for core sample #22. This plot shows the measured flow rate of water at different levels of pressure difference applied to the core sample. 3 wt.% KCl brine is used to conduct flow experiments. Dot line is the slope which is used to estimate permeability.

Core 29

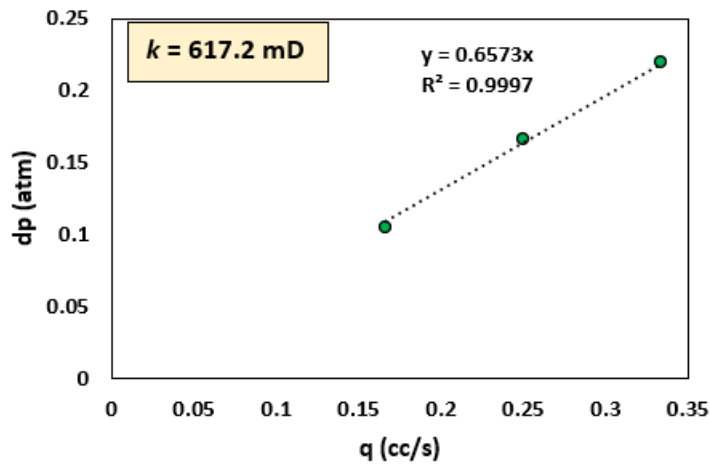


Figure 182. Permeability assessment for core sample #29. This plot shows the measured flow rate of water at different levels of pressure difference applied to the core sample. 3 wt.% KCl brine is used to conduct flow experiments. Dot line is the slope which is used to estimate permeability.

APPENDIX E – A SIMPLE CORRELATION BETWEEN T₂ CUTOFF AND T_{2LM}

The NMR T₂ distribution contains valuable information related to porosity, pore size distribution, and saturating fluids. Accurate estimation of irreducible water saturation from NMR measurement is crucial for the assessment of storage and flow properties of rocks such as effective porosity and permeability. The application of a threshold relaxation time, T₂ cutoff, to NMR T₂ distributions to estimate irreducible water saturation assumes that bound water occupies small pores while free fluid occupies large ones. Therefore, irreducible water saturates the pores with a T₂ value less than the T₂ cutoff whereas the fluids in pores with a T₂ value greater than the T₂ cutoff are mobile. Based on empirical data, the T₂ cutoff of sandstones and limestones is often assumed to be equal to 33 and 92 ms, respectively. However, multiple studies have shown that the simple assumption of a constant T₂ cutoff value per lithology classification may yield inaccurate estimates of irreducible water saturation. Therefore, it is not advisable to evaluate the physical properties of rock samples with a constant T₂ cutoff value.

In this section, we derive a simple empirical relationship to estimate the T₂ cutoff from T_{2LM}. First, we collected data including T₂ cutoff, porosity, permeability, irreducible water saturation, and T_{2LM}. The data covered a wide range of petrophysical properties and common lithologies (siltstones, sandstones, and carbonate rocks). Considering that porosity and T_{2LM} are derived from NMR measurements, we investigate the correlation between these properties and T₂ cutoff. Note that this approach is inspired by the SDR permeability model. **Figure 183** shows a good correlation between the T₂ cutoff and T_{2LM} values on a log-log scale where the correlation number is equal to R²=0.66. T₂ cutoff increases with an increase of T_{2LM}. **Figure 184** shows a weak correlation between the T₂ cutoff and porosity on a log-log scale where the correlation number is equal to R²=0.03. Therefore, the relationship between T₂ cutoff and T_{2LM} derived from this dataset is given by:

$$T_{2,cutoff} = 2.97 * T_{2LM}^{0.686} \quad (\text{Equation E-1})$$

Figure 185 shows the relationship between measured and predicted T₂ cutoff. The average percentage error is 14%.

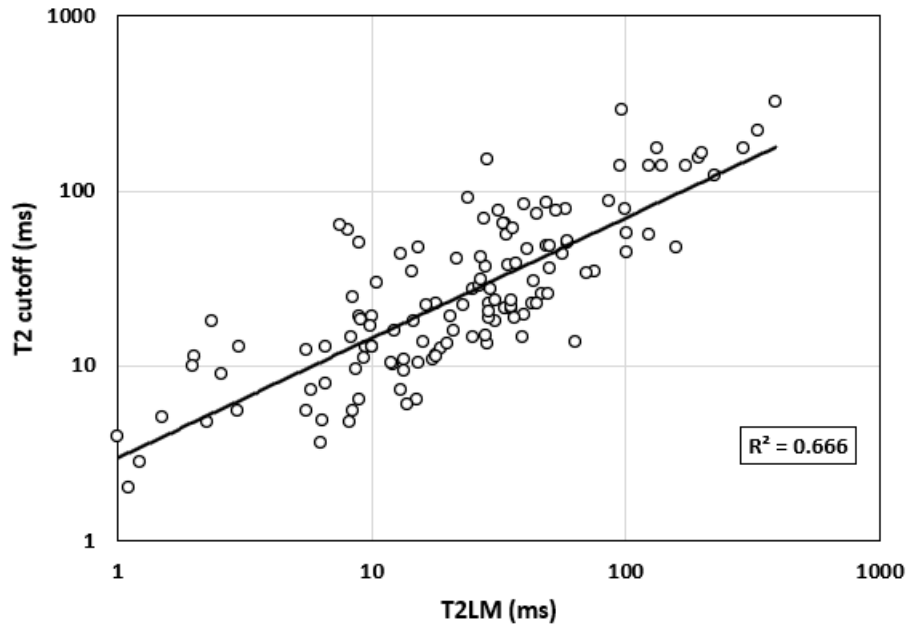


Figure 183. Correlation between T_{2LM} and T₂ cutoff for a dataset comprised of samples with a wide range petrophysical properties and common lithologies (siltstones, sandstones, and carbonate rocks). The correlation number is equal to R²=0.67.

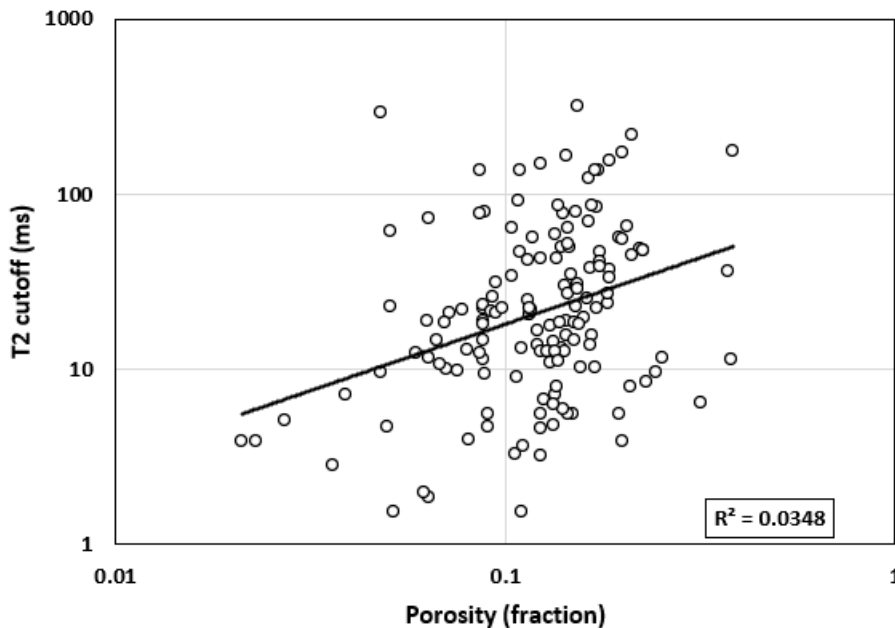


Figure 184. Correlation between porosity and T₂ cutoff for a dataset comprised of samples with a wide range petrophysical properties and common lithologies (siltstones, sandstones, and carbonate rocks). The correlation number is equal to R²=0.03.

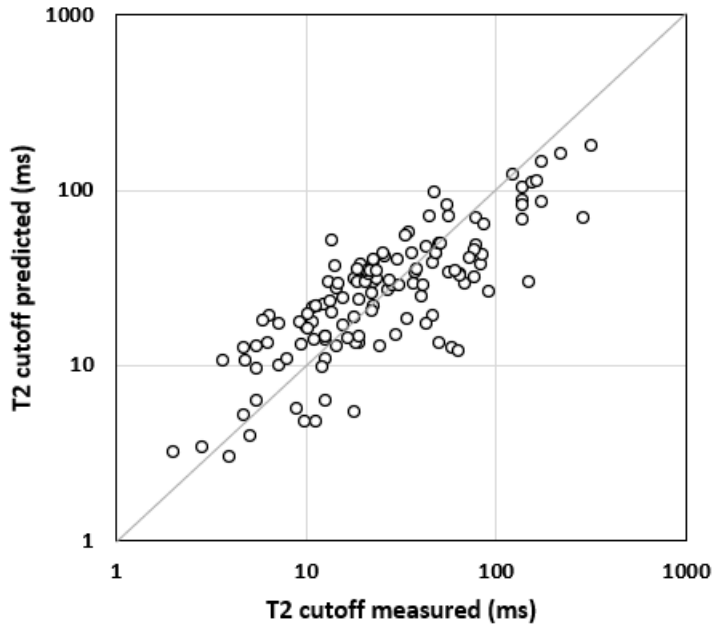


Figure 185. Comparison of measured T_2 cutoff and predicted values using Equation D-1. The average percentage error is 14%.

APPENDIX F – ARCHIE’S POROSITY EXPONENT OF DUAL POROSITY ROCKS

The estimation of Archie's porosity exponent, m , is of great importance in determining water salinity in aquifers and water saturation in hydrocarbon-saturated reservoirs, particularly in vuggy and naturally fractured rocks. Several studies have investigated the relationships between m and various porosity components, such as non-connected vuggy porosity and fracture porosity. The aim is to understand the influence of these specific porosity types on the electrical resistivity measurements and subsequently on the estimation of salinity and water saturation. To estimate the porosity exponent in such rocks, researchers often employ experimental methods, numerical simulations, or empirical correlations based on well log data and core analysis. These approaches involve characterizing the different porosity components, measuring the electrical properties of the rock, and analyzing the relationships between m and the relevant porosity parameters.

For reservoirs with natural fractures or connected vugs, Serra's (1989) model is given by:

$$m = \frac{\log((\phi - \phi_2)^{m_b} + \phi_2^{m_f})}{\log(\phi)} \quad (\text{F-1})$$

where ϕ is total porosity, ϕ_2 is porosity of fractures or connected vugs, m_b is porosity exponent of the matrix, and m_f is porosity exponent of the fractures or connected vugs. For reservoirs with non-connected vugs, Serra's (1989) model is given by:

$$m = \frac{m_b \log(\phi - \phi_{nc})}{\log(\phi)} \quad (\text{F-2})$$

where ϕ_{nc} is non-connected porosity. The above equations apply the porosity exponent of the matrix, m_b , to the difference $(\phi - \phi_2)$ in **Equation F-1** and $(\phi - \phi_{nc})$ in **Equation F-2**. These differences correspond to matrix porosity, ϕ_m , equal to void space within the matrix divided by the bulk volume of the “composite system” (bulk volume of the matrix plus bulk volume of the non-connected vugs). Aguilera (2003) showed that the Serra (1989) model fails when porosity is greater than approximately 0.4. However, Aguilera (2003) showed that for most cases of practical importance, the Serra (1989) model provides reasonable results as long as m_f is assumed equal to one.

Matrix porosity, ϕ_b , defined by Aguilera (2003) is different from the matrix porosity, ϕ_m , used by Serra (1989). Matrix porosity, ϕ_b , is equal to void space within the matrix divided by the bulk volume of the “matrix system” and is given by:

$$\phi_b = \frac{\phi - \phi_2}{1 - \phi_2} \quad (\text{F-3})$$

Aguilera (2003) modeled rocks with matrix porosity and natural fractures or connected vugs with a parallel resistance network. The corresponding porosity exponent is given by:

$$m = \frac{\log((1 - \phi_2) \phi_b^{m_b} + \phi_2)}{\log(\phi)} \quad (\text{F-4})$$

Aguilera et al. (2003) modeled rocks with matrix porosity and non-connected vugs with a series resistance network. The corresponding porosity exponent is given by:

$$m = \frac{-\log((1 - \phi_{nc}) \phi_b^{-m_b} + \phi_{nc})}{\log(\phi)} \quad (\text{F-5})$$

Figures 185 show negligible differences between Serra's (1989) models and Aguilera's (2003) models for rocks with non-connected vugs and for rocks with natural fractures or connected vugs. Note that total porosity is displayed on a logarithmic scale on the x-axis of **Figure 185**.

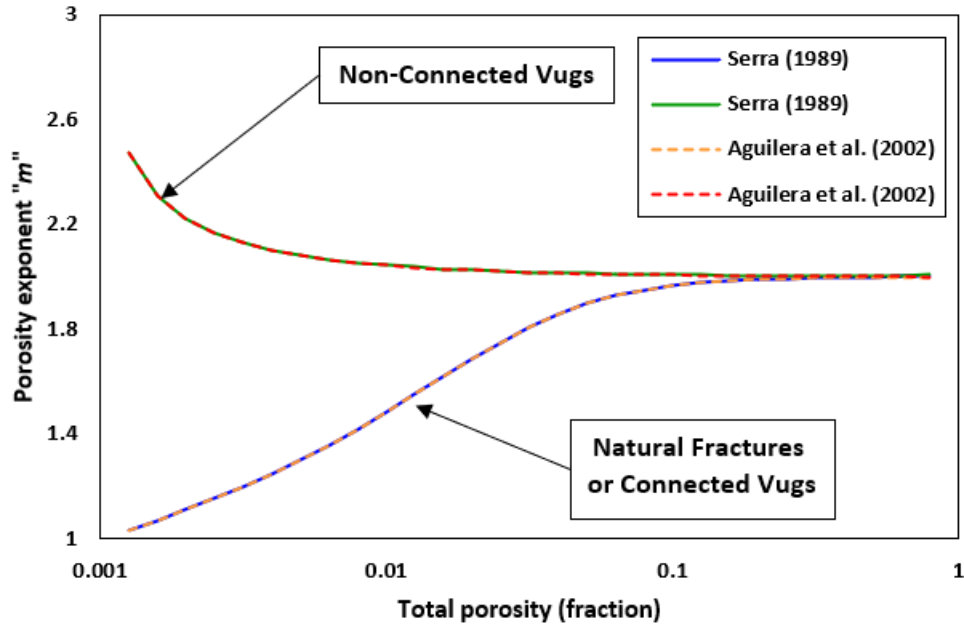


Figure 186. Relationship between total porosity and porosity exponent “m” of carbonate rocks with non-connected vugs (green and red lines), and natural fractures or connected vugs (blue and oranges lines). The models are described by Serra (1989) and Aguilera (2003).